Plasma Physics Reports, Vol. 28, No. 5, 2002, pp. 367–381. Translated from Fizika Plazmy, Vol. 28, No. 5, 2002, pp. 403–418.

TOKAMAKS

Jump in Transport Coefficients in Discharges with ECR Heating in the T-10 Tokamak

V. F. Andreev, Yu. N. Dnestrovskij, K. A. Razumova, and A. V. Sushkov

Russian Research Centre Kurchatov Institute, pl. Kurchatova 1, Moscow, 123182 Russia

Received October 18, 2001

Abstract—Transient processes after off-axis ECR heating in the T-10 tokamak is switched on or off are analyzed. It is found that the transient processes have the following two characteristic features. First, transport coefficients undergo a jump, thereby driving the evolution of the initial steady-state distributions of the plasma parameters. Second, the evolution of the original configuration is accompanied by ECR heating of the plasma. A mathematical model is proposed that takes into account the jump in transport coefficients over the entire cross section of the plasma column and adequately describes this transient process. An analysis of the experimental data confirms the validity of the model equations formulated here. It is shown that, without invoking the jump in transport coefficients after off-axis ECR heating is switched on or off, it is impossible to describe the experimentally observed opposite-sign changes in the electron temperature at the center of the plasma column and in the ECR heating region. *© 2002 MAIK "Nauka/Interperiodica".*

1. INTRODUCTION

At present, there is much experimental evidence for the very fast response (on time scales shorter than the diffusion time calculated from the energy balance) of the electron transport to various perturbations, specifically, (i) the propagation of sawtooth oscillations [1], (ii) modulated on-axis ECR heating (ECRH) in the W7-AS stellarator [2], (iii) L–H and H–L transitions in the JET tokamak [3], (iv) the injection of impurities that cool the peripheral plasma in the TFTR device [4, 5], and (v) the peripheral pellet injection in the RTP [6] and Tore Supra [7] tokamaks.

This effect was first observed during laser ablation of pellets, accompanied by peripheral plasma cooling, in experiments on the TEXT tokamak [8, 9], in which the central electron temperature increased rapidly in response to plasma cooling at the periphery. These experiments are remarkable in that they are characterized by electron temperature inversion. An opposite effect was observed during heating of the peripheral plasma in the TEXT tokamak [10] and during modulated ECRH in the RTP tokamak [11].

In the experiments carried out in [8, 9], two results appear to be paradoxical: (i) the so-called nonlocal response of the plasma to an external action (i.e., a rapid change in the local plasma parameters at a large distance from the plasma region upon which an external action is performed) and (ii) the heating of the central plasma in response to the peripheral plasma cooling. Note that the response time is about $\tau_d \approx 1$–3 ms, which is one–two orders of magnitude shorter than the energy confinement time τ_E and two–three orders of magnitude shorter than the resistive time τ_S of the current redistribution. Consequently, the heating of the central plasma cannot be explained by the peaking of the current density and the change in the Z_{eff} profile.

The nonlocal response of the plasma to an external action can be explained, e.g., by the simultaneous change in the electron heat diffusivity χ_e over the entire cross section of the plasma column during the delay time τ_d [8, 9]. In this case, in order to describe the experiments of [8, 9], it is necessary that the electron heat diffusivity χ_e decrease by about 25–50% in the plasma core and increase at the plasma boundary. The experiments on the peripheral plasma heating [10, 11], in which the electron temperature was observed to decrease in the central plasma region, can also be explained by a rapid change in χ_e, but this change is opposite in sign to that in the experiments [8, 9]. A detailed analysis of the L–H and H–L transitions [12–14] showed that not only χ_e but also χ_i should change in a jumplike fashion, in which case the delay time τ_d is of the same order as that during the cooling or heating of the peripheral plasma. Note that the physical nature of such a rapid change in transport coefficients is still unclear.

In [15], the processes of the peripheral plasma cooling and heating of the core plasma in the experiments of [8, 9] were described using the canonical profile transport model [16, 17]. A comprehensive review of the models used to explain the nonlocal plasma response to an external action can be found in [18].

In our earlier papers [19–24], a new method was developed that makes it possible to determine transport coefficients for the transient processes that occur, e.g., in response to ECRH. The method may be outlined as follows. The transient process is described by transport equations with the unknown coefficients that are to be

1063-780X/02/2805-0367$22.00

reconstructed by solving the corresponding inverse problem. The electron temperature is assumed to be known at several radial points and at several times. The heat diffusivity, heat convection velocity, and ECRH power profile are determined from the condition for the discrepancy functional (the difference between the temperature values measured experimentally and those obtained theoretically by solving the heat-conduction equation) to be at minimum.

The objectives of this study are to analyze the transient processes after off-axis ECRH is switched on or off, develop a mathematical model describing the nonlocal plasma response to ECRH, and to reconstruct transport coefficients both in the steady state and during the transient process.

2. MATHEMATICAL MODEL

The transient process after ECRH is switched on will be described as follows (the transient process after ECRH is switched off can be described in a similar way). We write the heat-conduction equation, the boundary and initial conditions for the electron temperature $T^S(r)$ corresponding to the quasi-steady plasma without ECRH, and the heat-conduction equation for the electron temperature $T(r, t)$ corresponding to the transient process after ECRH is switched on:

$$\begin{aligned}
&\frac{3}{2}\frac{\partial}{\partial t}(n^S T^S) = \frac{1}{r}\frac{\partial}{\partial r}\left(r n^S \chi_e^S \frac{\partial T^S}{\partial r}\right) \\
&\quad - \frac{1}{r}\frac{\partial}{\partial r}(r n^S u_e^S T^S) + P_{OH}^S + Q^S, \qquad (1)\\
&\frac{\partial T^S}{\partial r}(r = 0, t) = 0, \quad T^S(r = 1, t) = T_0,
\end{aligned}$$

$$\begin{aligned}
&\frac{3}{2}\frac{\partial}{\partial t}(nT) = \frac{1}{r}\frac{\partial}{\partial r}\left(r n \chi_e \frac{\partial T}{\partial r}\right) - \frac{1}{r}\frac{\partial}{\partial r}(r n u_e T) \\
&\quad + P_{OH} + Q + P_{EC}, \\
&\frac{\partial T}{\partial r}(r = 0, t) = 0, \quad T(r = 1, t) = T_0, \quad t > t_S, \qquad (2)\\
&T(r, t = t_S) = T^S(r), \quad 0 < r < 1.
\end{aligned}$$

Here, we have introduced the following notation: t_S is the time at which ECRH is switched on, P_{EC} is the ECRH power, T_0 is the electron temperature at the plasma boundary, $n^S(r)$ is the steady-state electron density, $T^S(r)$ is the steady-state electron temperature, P_{OH}^S is the steady-state ohmic heating power, the term Q^S describes the steady-state heat sinks, $n(r, t)$ is the electron density, $T(r, t)$ is the electron temperature, P_{OH} is the ohmic heating power, and the term Q describes the heat sinks during the transient process after ECRH is switched on.

In heat-conduction equations (1) and (2), the total heat flux W is assumed to be the sum of the diffusive and convective components:

$$W = -n\chi_e \frac{\partial T}{\partial r} + n u_e T, \qquad (3)$$

where χ_e is the electron heat diffusivity and u_e is the heat convection velocity. Hence, Eqs. (1) and (2) allow for the convective heat flux $5/2\Gamma_n T$, where Γ_n is the particle flux.

Subtracting Eq. (1) from Eq. (2), we obtain

$$\begin{aligned}
&\frac{3}{2}\frac{\partial}{\partial t}(nT - n^S T^S) = \frac{1}{r}\frac{\partial}{\partial r}\left[r\left(n\chi_e \frac{\partial T}{\partial r} - n^S \chi_e^S \frac{\partial T^S}{\partial r}\right)\right] \\
&\quad - \frac{1}{r}\frac{\partial}{\partial r}[r(n u_e T - n^S u_e^S T^S)] + (P_{OH} - P_{OH}^S) \\
&\quad + (Q - Q^S) + P_{EC}, \\
&\frac{\partial}{\partial r}[T(r = 0, t) - T^S(r = 0)] = 0, \qquad (4)\\
&[T(r = 1, t) - T^S(r = 1)] = 0, \quad t > t_S, \\
&[T(r, t = t_S) - T^S(r)] = 0, \quad 0 < r < 1.
\end{aligned}$$

We represent the density $n(r, t)$ and temperature $T(r, t)$ for the transient process as the sums of the steady-state values $n^S(r)$ and $T^S(r)$ and the variations $\tilde{n}(r, t)$ and $\tilde{T}(r, t)$:

$$\begin{aligned}
n(r, t) &= n^S(r) + \tilde{n}(r, t), \\
T(r, t) &= T^S(r) + \tilde{T}(r, t). \qquad (5)
\end{aligned}$$

After ECRH is switched on, the power is mainly deposited in the electron plasma component; consequently, the electron temperature changes at a much faster rate than the electron density does. As a consequence, the relative density variation $\tilde{n}$ is much smaller than the relative temperature variation $\tilde{T}$. In this paper, we are considering the transient process that occur on time scales of 10–20 ms, which allows us to neglect the electron density variations, i.e., to assume that

$$\frac{\tilde{n}}{n^S} \ll \frac{\tilde{T}}{T^S}, \quad \frac{\tilde{n}}{n^S} \ll 1. \qquad (6)$$

Setting $n(r, t) = n^S(r)$ in Eqs. (4), we obtain

$$\begin{aligned}
&nT - n^S T^S \approx n^S \tilde{T}, \\
&n\chi_e \nabla T - n^S \chi_e^S \nabla T^S \approx n^S(\chi_e \nabla T - \chi_e^S \nabla T^S) \\
&\quad = n^S(\chi_e - \chi_e^S)\nabla T^S + n^S \chi_e \nabla \tilde{T}, \qquad (7)\\
&n u_e T - n^S u_e^S T^S \approx n^S(u_e T - u_e^S T^S)
\end{aligned}$$

$$= n^S(u_e - u_e^S)T^S + n^S u_e \tilde{T},$$

where $\nabla f = \frac{\partial f}{\partial r}$.

Note that, up to this point, we did not assume that the ratios $(\chi_e - \chi_e^S)/\chi_e^S$ and $(u_e - u_e^S)/u_e^S$ are small.

Finally, Eq. (4) reduces to

$$\frac{3}{2}\frac{\partial}{\partial t}(n^S\tilde{T}) = \frac{1}{r}\frac{\partial}{\partial r}\left(rn^S\chi_e\frac{\partial\tilde{T}}{\partial r}\right) - \frac{1}{r}\frac{\partial}{\partial r}(rn^S u_e\tilde{T}) + P_{EC}$$

$$+ [(P_{OH} - P_{OH}^S) + (Q - Q^S)]$$

$$+ \frac{1}{r}\frac{\partial}{\partial r}\left[rn^S(\chi_e - \chi_e^S)\frac{\partial T^S}{\partial r}\right] - \frac{1}{r}\frac{\partial}{\partial r}[rn^S(u_e - u_e^S)T^S], \quad (8)$$

$$\frac{\partial\tilde{T}}{\partial r}(r = 0, t) = 0, \quad \tilde{T}(r = 1, t) = 0, \quad t > t_S,$$

$$\tilde{T}(r, t = t_S) = 0, \quad 0 < r < 1.$$

In the inverse problem for Eq. (8), which describes the transient process after ECRH is switched on, the unknowns are the transport coefficients χ_e^S, u_e^S, χ_e, and u_e and the ECRH power profile P_{EC}. The ohmic heating power profiles P_{OH}^S and P_{OH}, as well as the profiles Q^S and Q of the power of electron–ion energy exchange, are described by standard formulas expressing the profiles in terms of the plasma density and plasma temperature.

In order to formulate the inverse problem of reconstructing the transport coefficients, it is necessary to choose a particular model for each of them. Here, we will analyze the following two models of transport coefficients.

(i) The first is the model in which the transport coefficients χ_e and u_e depend on the local values of the plasma parameters, specifically, the electron density $n(r, t)$ and electron temperature $T(r, t)$ and their gradients. In this model, the transport coefficients χ_e and u_e can change in a local region of the plasma column only when the local density and local temperature both change in the vicinity of this region.

(ii) The second is the model in which the transport coefficients χ_e and u_e are nonlocal functions of the plasma parameters. This indicates that, in any local region of the plasma column, the coefficients χ_e and u_e can change even when the local density and temperature in this region remain unchanged.

For each of the models, we will write out the heat-conduction equation for describing the transient process after ECRH is switched on or off and will formulate the inverse problem of reconstructing the transport coefficients χ_e and u_e and the ECRH power profile P_{EC}. Note that, in the steady stage, the problem of determining χ_e and u_e is degenerate: it is possible to find only flux (3) rather than its diffusive and convective components. It is for this reason that the transport coefficients χ_e and u_e can be determined separately only by analyzing the transient process.

3. LOCAL DEPENDENCE OF THE TRANSPORT COEFFICIENTS χ_e AND u_e ON THE PLASMA PARAMETERS

The transport coefficients χ_e and u_e in Eq. (8) can depend on many local plasma parameters. In our analysis, we restrict ourselves to considering the problem in a simplified formulation. We assume that the electron heat diffusivity χ_e and heat convection velocity u_e are functions of the following local parameters: the electron density, the electron temperature, and their gradients. In other words, we assume that

$$\begin{aligned}\chi_e &= \chi_e(n, T, \nabla n, \nabla T),\\ u_e &= u_e(n, T, \nabla n, \nabla T).\end{aligned} \quad (9)$$

Below, for brevity, assumption (9) will be referred to as a local model.

Small perturbations of the plasma parameters satisfy the following relationships, which will be used below to linearize the heat-conduction equation (8):

$$\frac{\tilde{T}}{T^S} \ll \frac{\nabla\tilde{T}}{\nabla T^S}, \quad \frac{\nabla\tilde{T}}{\nabla T^S} \ll \frac{\nabla^2\tilde{T}}{\nabla^2 T^S}, \quad (10)$$

where $\nabla^2 f = \frac{\partial^2 f}{\partial r^2}$.

In order to describe the transient process, we expand the transport coefficients χ_e and u_e (9) in the increments in the independent variables T and ∇T in the vicinities of the steady-state values of the density n^S and temperature T^S. We also neglect the terms of the second order in the temperature variation $\tilde{T}$. Taking into account relationships (6) and (10), we obtain the expressions

$$\begin{aligned}\chi_e &\approx \chi_e^S + \left(\frac{\partial\chi_e}{\partial T}\right)^S\tilde{T} + \left(\frac{\partial\chi_e}{\partial\nabla T}\right)^S\nabla\tilde{T},\\ u_e &\approx u_e^S + \left(\frac{\partial u_e}{\partial T}\right)^S\tilde{T} + \left(\frac{\partial u_e}{\partial\nabla T}\right)^S\nabla\tilde{T}.\end{aligned} \quad (11)$$

Analogously, we expand the ohmic heating power P_{OH} and heat loss Q during the transient process in the vicinity of the steady state and neglect the corresponding second-order terms. As a result, we obtain

$$P_{OH} - P_{OH}^S \approx \left(\frac{\partial P_{OH}}{\partial T}\right)^S\tilde{T}, \quad Q - Q^S \approx \left(\frac{\partial Q}{\partial T}\right)^S\tilde{T}. \quad (12)$$

Substituting formulas (11) and (12) into Eq. (8), we arrive at the following linearized equation for the electron temperature variation $\tilde{T}(r, t)$:

$$\frac{3}{2}\frac{\partial}{\partial t}(n^S\tilde{T}) = \frac{1}{r}\frac{\partial}{\partial r}\left(rK\frac{\partial\tilde{T}}{\partial r}\right) - \frac{1}{r}\frac{\partial}{\partial r}(rV\tilde{T}) + P_{EC} + \left[\left(\frac{\partial P_{OH}}{\partial T}\right)^S + \left(\frac{\partial Q}{\partial T}\right)^S\right]\tilde{T}.$$
$$\frac{\partial\tilde{T}}{\partial r}(r = 0, t) = 0, \quad \tilde{T}(r = 1, t) = 0, \quad t > t_S, \tag{13}$$
$$\tilde{T}(r, t_S) = 0, \quad 0 < r < 1.$$

Here, we have introduced the notation

$$K = n^S\left[\chi_e^S + \left(\frac{\partial\chi_e}{\partial\nabla T}\right)^S\nabla T^S + \left(\frac{\partial u_e}{\partial\nabla T}\right)^S T^S\right],$$
$$V = n^S\left[u_e^S + \left(\frac{\partial u_e}{\partial T}\right)^S T^S + \left(\frac{\partial\chi_e}{\partial T}\right)^S\nabla T^S\right]. \tag{14}$$

In the local model of transport coefficients [25], the most important of the characteristic features of Eq. (13) and relationships (14) are as follows.

(i) The transport coefficients (14) in the transient process differ from those in the steady stage.

(ii) If the coefficient χ_e is a function of the electron temperature T only, then the linearized equation (13) always contains the convective term, even when the convective heat flux does not enter the basic equations (1) and (2) ($u_e^S \equiv 0$).

(iii) The coefficients K and V in the linearized equation (13) are functions of the steady-state plasma parameters; i.e., they are determined only by the steady-state density and temperature distributions.

4. NONLOCAL DEPENDENCE OF THE TRANSPORT COEFFICIENTS χ_e AND u_e ON THE PLASMA PARAMETERS

In this model, the transient process after ECRH is switched on or off is described by assuming that the dependence of transport coefficients on the plasma parameters is nonlocal. Let us clarify what is meant here by the nonlocal dependence. The electron heat diffusivity χ_e and heat convection velocity u_e in the transient process can be represented as

$$\chi_e(r, t) = \chi_e^S(r) + \tilde{\chi}_e(r, t), \quad u_e(r, t) = u_e^S(r) + \tilde{u}_e(r, t),$$
$$\tilde{\chi}_e(r, t) = \begin{cases} 0, & t \le t_S \\ \tilde{\chi}_e(r), & t > t_S \end{cases}, \quad \tilde{u}_e(r, t) = \begin{cases} 0, & t \le t_S \\ \tilde{u}_e(r), & t > t_S. \end{cases} \tag{15}$$

In fact, representations (15) assume that the variations $\tilde{\chi}_e$ and $\tilde{u}_e$ occur on time scales much shorter than the diffusion time, which is characteristic of the transient process in question. In addition, it is not assumed that the ratios $\tilde{\chi}_e/\chi_e^S$ and $\tilde{u}_e/u_e^S$ are smaller than unity. Below, representations (15) will be referred to as a nonlocal model of transport coefficients.

Substituting representations (15) into Eq. (8) yields the equation

$$\frac{3}{2}\frac{\partial}{\partial t}(n^S\tilde{T}) = \frac{1}{r}\frac{\partial}{\partial r}\left(rK\frac{\partial\tilde{T}}{\partial r}\right) - \frac{1}{r}\frac{\partial}{\partial r}(rV\tilde{T}) + P_{EC} + \left[\left(\frac{\partial P_{OH}}{\partial T}\right)^S + \left(\frac{\partial Q}{\partial T}\right)^S\right]\tilde{T} + \frac{1}{r}\frac{\partial}{\partial r}\left(r\tilde{K}\frac{\partial T^S}{\partial r}\right) - \frac{1}{r}\frac{\partial}{\partial r}(r\tilde{V}T^S), \tag{16}$$
$$\frac{\partial\tilde{T}}{\partial r}(r = 0, t) = 0, \quad \tilde{T}(r = 1, t) = 0, \quad t > t_S,$$
$$\tilde{T}(r, t = t_S) = 0, \quad 0 < r < 1.$$

When deriving this equation, we assumed that expansions (12) are valid. We also introduced the notation

$$K = K^S + \tilde{K}, \quad V = V^S + \tilde{V},$$
$$K^S = K^S(r) = n^S(r)\chi_e^S(r),$$
$$\tilde{K} = \tilde{K}(r) = n^S(r)\tilde{\chi}_e(r), \tag{17}$$
$$V^S = V^S(r) = n^S(r)u_e^S(r),$$
$$\tilde{V} = \tilde{V}(r) = n^S(r)\tilde{u}_e(r).$$

In the formulation of the inverse problem, the unknowns in Eq. (16) are the electron heat diffusivity χ_e^S and heat convection velocity u_e^S in the steady state, the variations $\tilde{\chi}_e$ and $\tilde{u}_e$ in the transient process after ECRH is switched on or off, and the ECRH power profile $P_{\mathrm{EC}}(r)$.

Note that, in the inverse problem for the linearized equation (13), there are only two unknown functions, K and V, but the relationship between these functions and the steady-state coefficients χ_e^S and u_e^S (14) is undetermined. Now, Eq. (16) contains four unknown functions, namely, K, $\tilde{K}$, V, and $\tilde{V}$, with which, however, the four sought-for functions χ_e^S, u_e^S, χ_e, and u_e can easily be found from formulas (17).

Equations (16) with relationships (17) will be used to describe the transient process after ECRH is switched on or off in the model of the nonlocal dependence of transport coefficients on the plasma parameters.

5. FORMULATION OF THE INVERSE PROBLEM AND NUMERICAL ALGORITHM FOR SOLVING IT

Here, we formulate the inverse problems of reconstructing the transport coefficients for problem (13) and (14) and for problem (16) and (17). Let the transient process after ECRH is switched on or off be described by Eq. (13) with relationships (14) or by Eq. (16) with relationships (17), and let the coefficients K and V as well as the coefficients $\tilde{K}$ and $\tilde{V}$ in Eq. (16) be time-independent. The known quantities are the electron temperature variations f_i^k measured experimentally at N radial points r_i ($i = 1, \ldots, N$) at M times t_k ($k = 1, \ldots, M$) and some of the global plasma parameters, namely, the major and minor radii of the plasma column, the total plasma current, the ohmic heating power, and the ECRH power.

We begin by writing the discrepancy functional:

$$J = \frac{1}{2}\sum_{k=1}^{M}\sum_{i=1}^{N}\gamma_i[\tilde{T}(r_i, t_k) - f_i^k]^2 / \sum_{k=1}^{M}\sum_{i=1}^{N}\gamma_i[f_i^k]^2, \quad (18)$$

where the weighting factors γ_i are to be chosen in accordance with the reliability of information from different measurement channels.

The inverse problem is formulated as follows. It is necessary to determine the ECRH power profile $P_{EC}(r)$, the heat diffusivity $K(r)$, the heat convection velocity $V(r)$, and also, for Eq. (16), the variations $\tilde{K}(r)$ and $\tilde{V}(r)$ with which the solution $\tilde{T}(r, t)$ to the heat-conduction equation (13) or (16) minimizes the discrepancy functional (18).

The method for solving the inverse problem assumes a parametric representation of the sought-for functions. We expand the unknown functions $K(r)$, $\tilde{K}(r)$, $V(r)$, $\tilde{V}(r)$, and $P_{EC}(r)$ in certain basis polynomial functions [19–24]:

$$K(r) = \sum_{j=1}^{M_K} k_j \varphi_j^K(r), \quad \tilde{K}(r) = \sum_{j=1}^{M_{\tilde{K}}} \tilde{k}_j \tilde{\varphi}_j^{\tilde{K}}(r),$$

$$V(r) = \sum_{j=1}^{M_V} v_j \varphi_j^V(r), \quad \tilde{V}(r) = \sum_{j=1}^{M_{\tilde{V}}} \tilde{v}_j \tilde{\varphi}_j^{\tilde{V}}(r), \quad (19)$$

$$P_{EC}(r) = A\exp\left[-\beta\left(\frac{r - r_0}{2w}\right)^{\alpha}\right], \quad \beta = 2^{\alpha}\ln 2.$$

Here, φ_j^K, φ_j^V, $\tilde{\varphi}_j^{\tilde{K}}$, and $\tilde{\varphi}_j^{\tilde{V}} = \{1, r, r^2, r^3, \ldots\}$ are polynomials; r_0 is the position of the center of the ECRH power profile; w is its half-width; and the constants A and α determine the amplitude, profile, and total ECRH power.

Hence, the solution of the inverse problem reduces to the determination of the vector of the unknown parameters

$$\mathbf{P} = \{k_j, j = 1, \ldots, M_K, \tilde{k}_j, j = 1, \ldots, M_{\tilde{K}}, v_j, j = 1, \ldots, M_V, \tilde{v}_j, j = 1, \ldots, M_{\tilde{V}}, A, r_0, w, \alpha\} \quad (20)$$

from the condition for the discrepancy functional (18) to be at minimum.

The inverse problem is solved by the method of iterative regularization [26], which consists of the following steps: (i) the initial vector $\mathbf{P}^s$ ($s = 1$) of the sought-for parameters is specified and Eq. (13) or (16) is solved, (ii) the gradient ∇J^S of the discrepancy functional (18) and the descent depth vector $\mathbf{h}^S$ are calculated, and (iii) the new approximation for the sought-for parameters is determined from the relationship $P_i^{s+1} = P_i^s + h_i^s\frac{\partial J^s}{\partial P_i}$. This iteration procedure (i)–(iii) minimizes the discrepancy functional (18), thereby giving the desired solution to the inverse problem (13), (14), and (18)–(20) or the inverse problem (16), (17), and (18)–(20).

The accuracy with which the transport coefficients and the right-hand sides of the equations of the inverse problem can be reconstructed was thoroughly discussed in [19], in which the numerical results of "quasi-real" experiments were presented and the reconstruction accuracy was estimated as a function of the uncertainties in the input parameters (i.e., errors in measuring the electron temperature). That is why we do not discuss this question in detail here.

6. NUMERICAL RESULTS

Here, we describe numerical results obtained for the T-10 tokamak. Since the spatial resolution of the system for measuring the electron temperature from the second harmonic of EC emission in T-10 was insufficient for our purposes, the numerical algorithm proposed here was based on the data from soft X-ray (SXR) diagnostics. In T-10, the SXR intensity I_{SXR} is recorded from 40 viewing chords with the spatial resolution Δr = 1–1.5 cm and the temporal resolution Δt = 40 μs. Having solved the abelianization problem, we obtain the radial SXR intensity profile $J_{SXR}(r)$, from which we can determine the electron temperature profile by solving the transcendental equation

$$J_{SXR} \propto f(Z_{eff})\frac{n^2}{\sqrt{T_e}}\int_0^{\infty}\exp\left(\frac{-E}{T_e}\right)\eta(E)dE, \quad (21)$$

where $\eta(E)$ is the sensitivity function of the detector.

In Eq. (21), the sensitivity function $\eta(E)$ was calculated for a Maxwellian electron distribution function. When calculating the electron temperature, we also

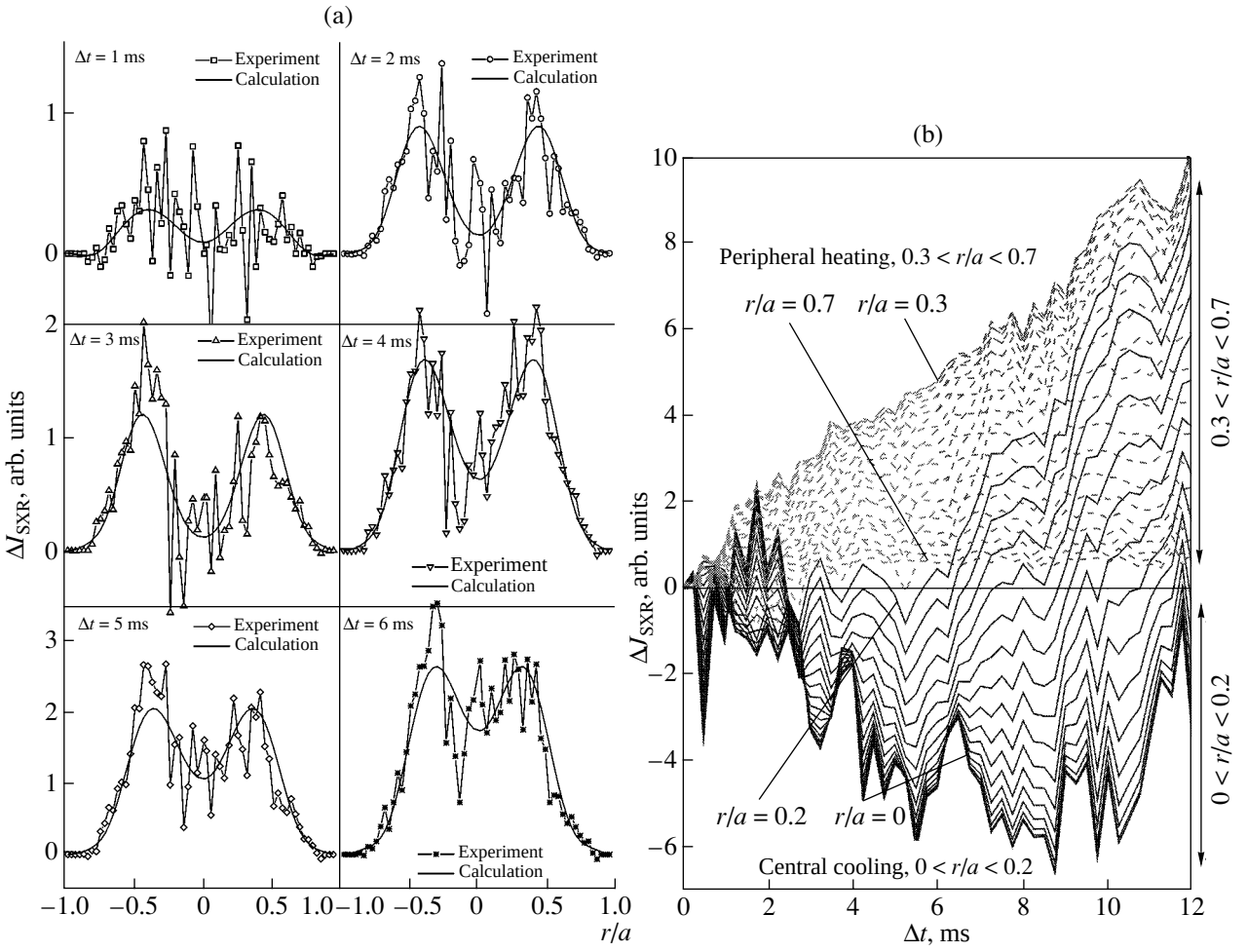

Fig. 1. (a) Radial profiles of the change $\Delta I_{SXR}(r)$ in the chord SXR signal at different times after off-axis ECRH in shot no. 29614 is switched on (t = 670 ms). The symbols are for the experimental SXR intensities, and the solid curves are for the integral of the local SXR intensity, ΔJ_{SXR}, obtained by solving the problem of the abelianization of the SXR signal ΔI_{SXR}. (b) Time evolution of the local SXR intensity $\Delta J_{SXR}(t)$ at different radii after off-axis ECRH in shot no. 29614 is switched on (t = 670 ms). The solid curves correspond to the radial points in the central plasma region $0 < r/a < 0.2$, and the dashed curves refer to the ECRH power deposition region $0.3 < r/a < 0.7$. The quantity ΔJ_{SXR} was determined from the abelianization of the measured signal ΔI_{SXR}.

assumed that the electron density $n(r, t)$ and profile $Z_{eff}(r, t)$ both remained unchanged during the transient process. The SXR detectors were calibrated with the help of the electron temperature profile measured by the Thomson scattering technique in the steady discharge stage before ECRH is switched on or off.

Figure 1a shows the radial profiles of the change $\Delta I_{SXR}(r)$ in the chord SXR signal intensity at different times after off-axis ECRH in shot no. 29614 is switched on (t = 6470 ms). The symbols denote the experimental SXR intensities, and the solid curves correspond to the integral of the local SXR intensity, ΔJ_{SXR}, which was obtained by solving the problem of the abelianization of the SXR signal ΔI_{SXR}.

Figure 1b shows the time evolution of the local SXR intensity $\Delta J_{SXR}(t)$ at different radii after off-axis ECRH in the same discharge (shot no. 29614) is switched on (t = 670 ms). The solid curves correspond to the radial points in the central plasma region $0 < r/a < 0.2$, and the dashed curves refer to the ECRH power deposition region $0.3 < r/a < 0.7$. The quantity ΔJ_{SXR} was determined from the abelianization of the measured signal ΔI_{SXR}.

In moving along the viewing chords from the plasma boundary toward the center of the plasma column, each next signal is the sum of the preceding signal and the integral of the signals from the inner region between two neighboring measurement channels. Note that, in the direction from the plasma boundary to the plasma center, the viewing chords become even longer. There is a possibility that the SXR signal intensity decreases starting from a certain measurement channel (as is the case in Figs. 1a and 2a). This indicates that the change in the SXR intensity in the ECRH power depo-

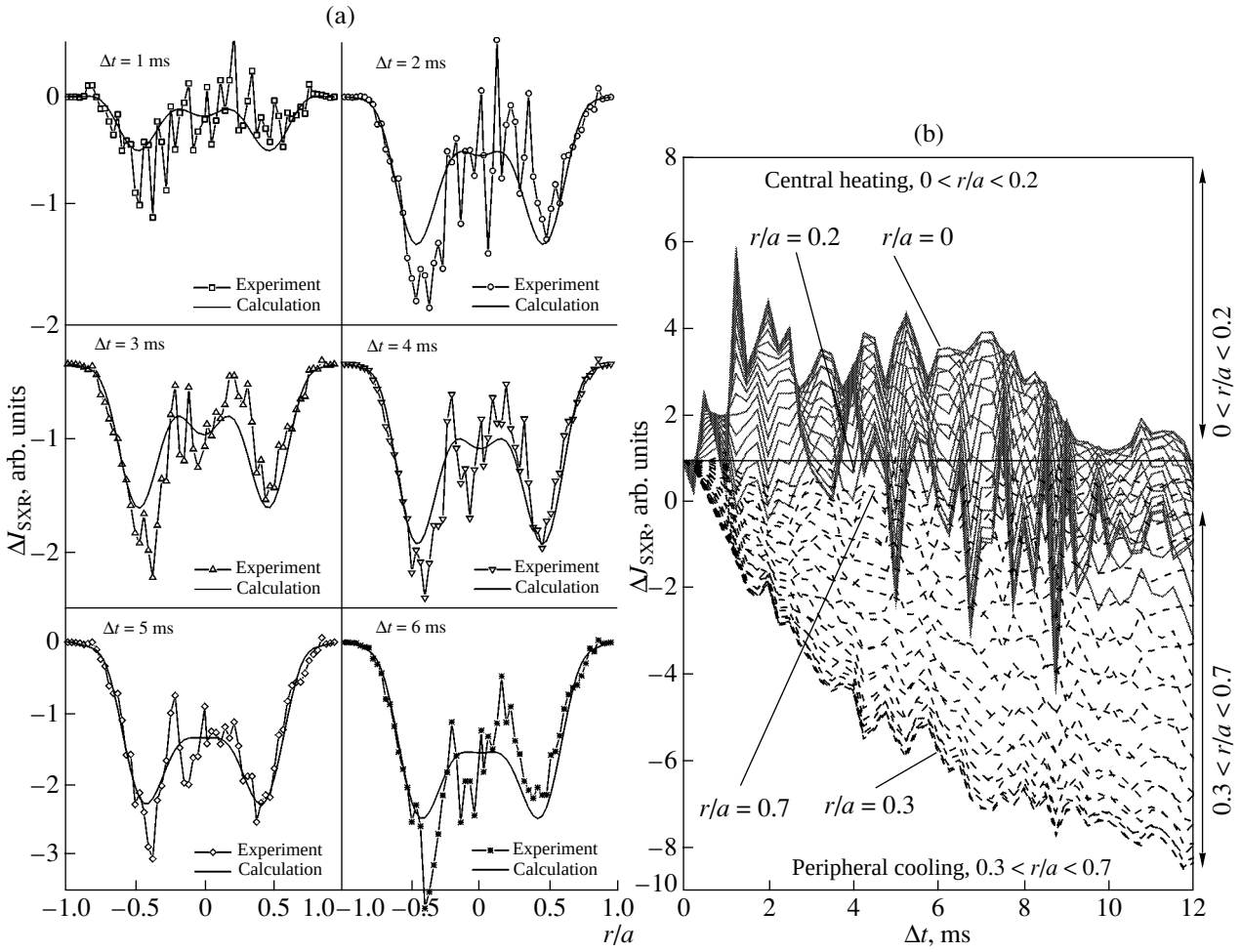

Fig. 2. (a) Radial profiles of the change $\Delta I_{SXR}(r)$ in the chord SXR signal at different times after off-axis ECRH in shot no. 29614 is switched off (t = 750 ms). The symbols are for the experimental SXR intensities, and the solid curves are for the integral of the local SXR intensity, ΔJ_{SXR}, obtained by solving the problem of the abelianization of the SXR signal ΔI_{SXR}. (b) Time evolution of the local SXR intensity $\Delta J_{SXR}(t)$ at different radii after off-axis ECRH in shot no. 29614 is switched off (t = 750 ms). The solid curves correspond to the radial points in the central plasma region $0 < r/a < 0.2$, and the dashed curves refer to the ECRH power deposition region $0.3 < r/a < 0.7$.

sition region is opposite in sign to the change in the SXR intensity at the center of the plasma column. This effect is also confirmed by the solution to the abelianization problem of reconstructing the radial profile of the local SXR signal intensity.

Figure 2a shows the radial profiles of the change $\Delta I_{SXR}(r)$ in the chord SXR signal at different times after off-axis ECRH in shot no. 29614 is switched off (t = 750 ms). The symbols denote the experimental SXR intensities, and the solid curves correspond to the integral of the local SXR intensity, ΔJ_{SXR}, which was obtained by solving the problem of the abelianization of the SXR signal ΔI_{SXR}.

Figure 2b shows the time evolution of the local SXR intensity $\Delta I_{SXR}(t)$ at different radii after off-axis ECRH in the same discharge as in Fig. 2a (shot no. 29614) is switched off (t = 750 ms). The solid curves correspond to the radial points in the central plasma region $0 < r/a < 0.2$, and the dashed curves refer to the ECRH power deposition region $0.3 < r/a < 0.7$.

One can readily see that, during the first ten milliseconds, the change in the local intensity ΔJ_{SXR} in the central region is opposite in sign to the change in ΔJ_{SXR} in the ECRH power deposition region. In other words, after ECRH is switched on, the central temperature decreases, while, after ECRH is switched off, the central temperature increases. Hence, the transient process after off-axis ECRH is switched on or off is an example of the nonlocal plasma response to an external action.

Now, we turn to the solution of the inverse problems. First, we present the results of a numerical solution of the inverse problem (13) and (14). Here, we analyze discharges in which the changes in the ohmic heating power P_{OH} and heat loss Q are both much smaller

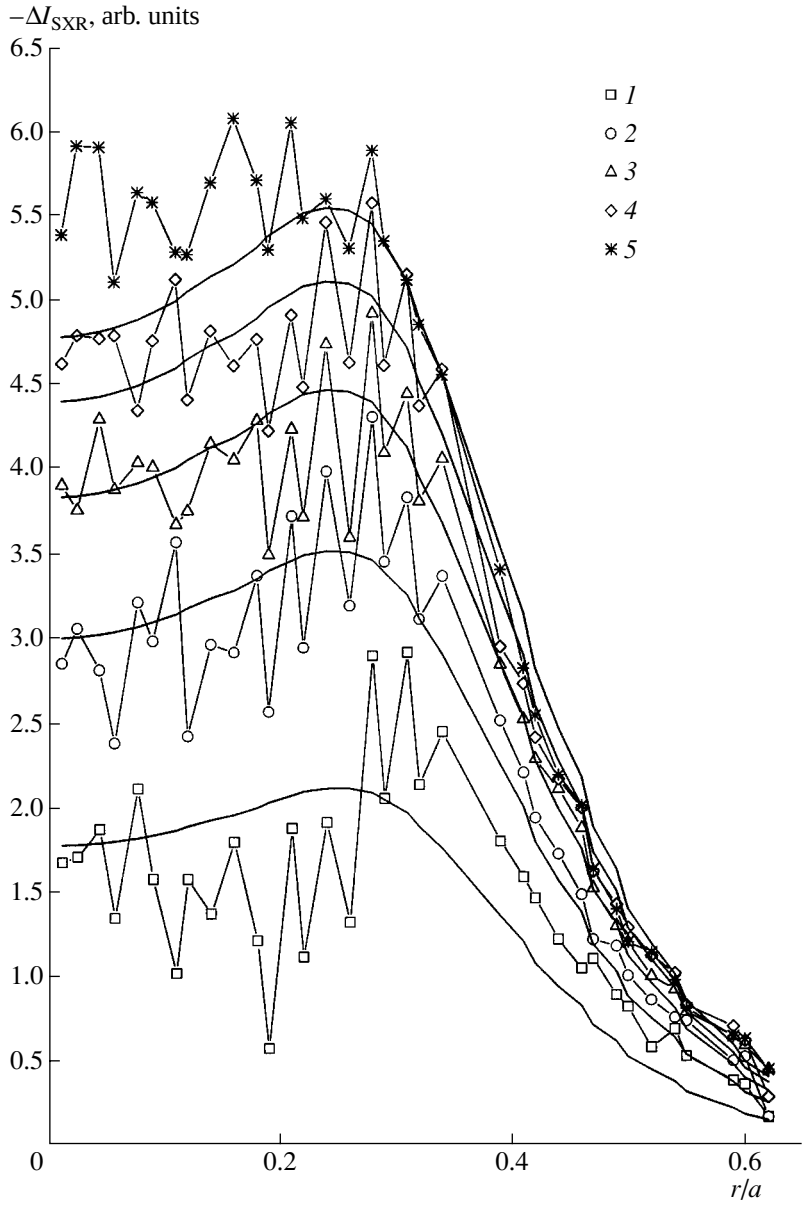

Fig. 3. Radial profiles of the change $\Delta I_{SXR}(r)$ in the chord SXR signal at different times after off-axis ECRH in shot no. 23281 is switched off (t = 800.5 ms): *1* – Δt = (*1*) 2, (*2*) 4, (*3*) 6, (*4*) 8, and (*5*) 10 ms. The symbols are for the experimental SXR signal intensities, and the solid curves are for the integral of the local SXR intensity, ΔJ_{SXR}, obtained by solving the abelianization problem.

than the ECRH power P_{EC}; consequently, in Eq. (13), we can neglect the terms with $(\partial P_{OH}/\partial T)^S$ and $(\partial Q/\partial T)^S$.

The relevant experimental data and the results of their numerical processing for the transient process after off-axis ECRH in shot no. 23281 is switched off (t = 800.5 ms) are illustrated in Figs. 3–6.

Figure 3 shows the radial profiles of the change $\Delta I_{SXR}(r)$ in the chord SXR signal at different times after off-axis ECRH is switched off. The symbols denote the experimental SXR signal intensities, and the solid curves correspond to the integral of the local SXR intensity, ΔJ_{SXR}, which was obtained by solving the abelianization problem.

Figure 4 shows the radial profiles of the electron temperature variation $\tilde{T}(r, t)$ at different times after off-axis ECRH is switched off.

The results of solving the inverse problem (13), (14) and (18)–(20) are illustrated in Fig. 5, which shows the radial profiles of the effective electron heat diffusivity $\chi_e^{\text{eff}}(r) = K(r)/n^S(r)$, effective heat convection velocity $u_e^{\text{eff}}(r) = V(r)/n^S(r)$, and ECRH power $P_{EC}(r)$. The P_{EC}

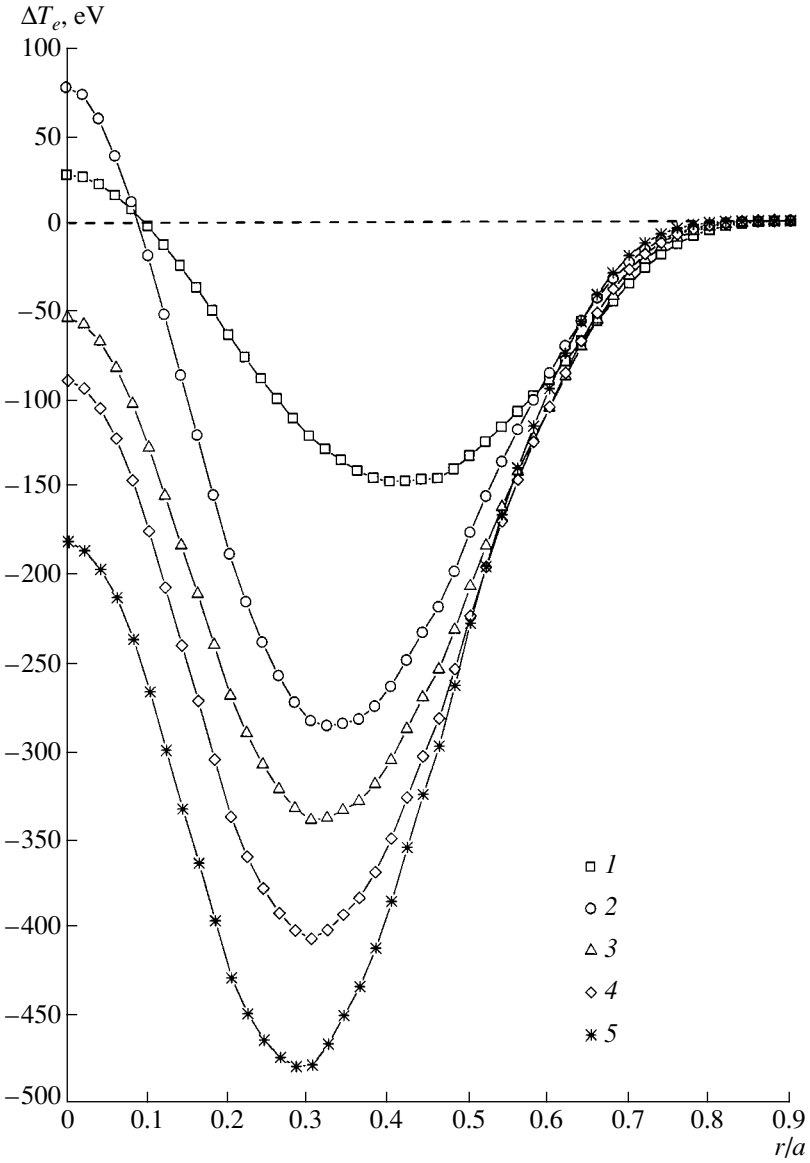

Fig. 4. Radial profiles of the electron temperature variation at different times after off-axis ECRH in shot no. 23281 is switched off (t = 800.5 ms): Δt = (*1*) 2, (*2*) 4, (*3*) 6, (*4*) 8, and (*5*) 10 ms.

profile shown by the solid curve is obtained by solving the inverse problem with the parameters $r_0/a = 0.34$, $w/a = 0.16$, and $\alpha = 2$. When solving the inverse problem, we fixed the last parameter, $\alpha = 2$, set the total ECRH power at 0.65 MW, and searched for the parameters r_0 and w. In Fig. 5, the dashed curve is the radial profile of the normalized input power, calculated by the method of ray trajectories with the TORAY code [27].

The ECRH power profile obtained from our model is seen to coincide fairly closely with that calculated by the TORAY code. The discrepancies between the profiles can be explained by the fact that, in reality, the transport coefficients may be both temperature- and time-dependent, which is not taken into account in our model equation (13) with relationships (14).

Figure 6 shows the radial profiles of the change in the heat flux components at different times after ECRH is switched off, namely, the diffusive component $\Delta W_{\text{diff}} = -K\partial\tilde{T}/\partial r$ and the convective component $\Delta W_{\text{conv}} = V\tilde{T}$, calculated by solving the inverse problem.

We point out the following characteristic feature of the results obtained. Figure 4 clearly shows that, on the time scales under consideration (5–10 ms), the variation $\tilde{T}(r, t)$ in the electron temperature profile spreads out slowly (in comparison with the diffusion time) but the increment in the temperature gradient does not decrease. An analogous effect was mentioned in [23, 28–30]. According to Fig. 5, the effective heat convec-

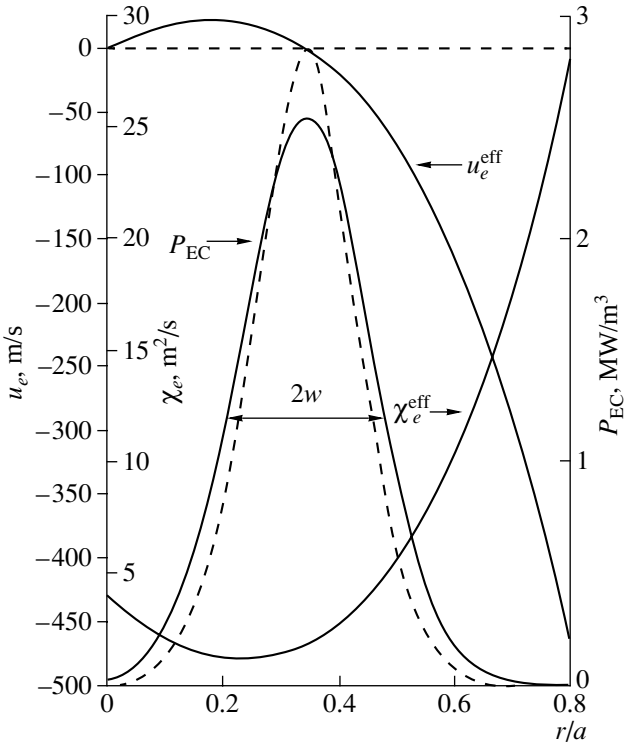

Fig. 5. Solution to the inverse problem (13), (14) and (18)–(20) for shot no. 23281. Shown are the radial profiles of the effective electron heat diffusivity $\chi_e^{\text{eff}}(r) = K(r)/n^S(r)$, effective heat convection velocity $u_e^{\text{eff}}(r) = V(r)/n^S(r)$, and ECRH power $P_{\text{EC}}(r)$. The P_{EC} profile shown by the solid curve is obtained by solving the inverse problem with the following parameters: the total ECRH power is 0.65 MW, $r_0/a = 0.34$, $w/a = 0.16$, and $\alpha = 2$. The dashed curve is the radial profile of the normalized input power, calculated by the method of ray trajectories with the TORAY code.

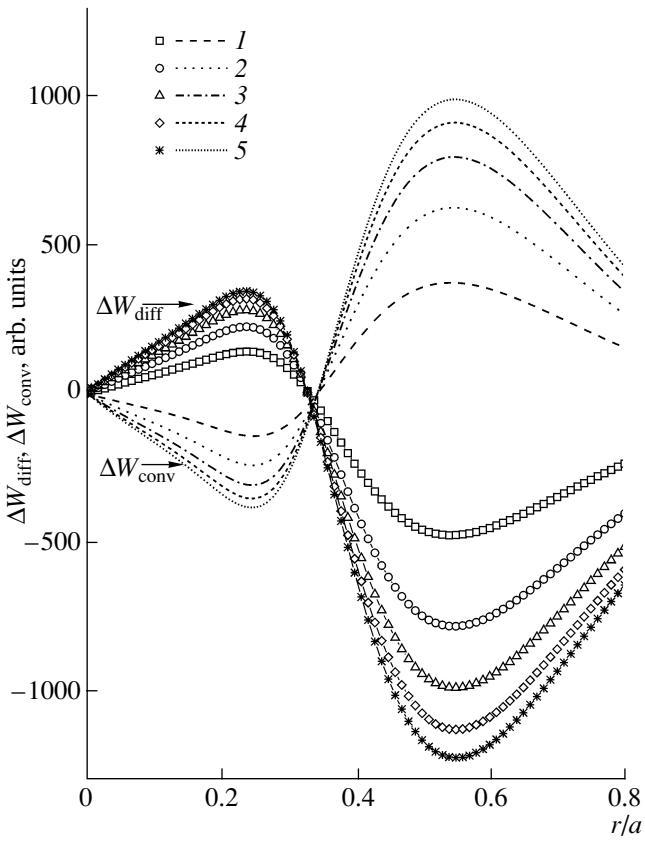

Fig. 6. Radial profiles of the changes in the heat flux components for shot no. 23281 at different times after off-axis ECRH is switched off (t = 800.5 ms), namely, the diffusive component $\Delta W_{\text{diff}} = -K\partial\tilde{T}/\partial r$ and the convective component $\Delta W_{\text{conv}} = V\tilde{T}$, calculated by solving the inverse problem: Δt = (*1*) 2, (*2*) 4, (*3*) 6, (*4*) 8, and (*5*) 10 ms.

tion velocity $u_e^{\text{eff}}(r)$ changes its sign near the center of the ECRH power deposition region. This indicates that, to the left and to the right of the power deposition region, the convective heat flux is directed toward the diffusive heat flux (Fig. 6). The presence of the convective heat flux with such a structure prevents the electron temperature profile from being spread out.

Now, we turn to the results obtained from the nonlocal model (15) and (16). Recall that, in the inverse problem (15), (16), and (18)–(20), it is necessary to reconstruct five unknown profiles, namely, $K(r)$, $V(r)$, $\tilde{K}(r)$, $\tilde{V}(r)$, and $P_{\text{EC}}(r)$, which is, however, a fairly difficult task because it requires low-noise experimental data. Since the noise level in discharges illustrated in Fig. 1a, 2a, and 3 was very high, we consider the following two simplified versions of the inverse problem.

Problem A. We assume that the total heat flux (3) in the steady state only has the diffusive component; i.e., $u_e^S(r) \equiv 0$. Additionally, we assume that, during the transient processes after ECRH is switched on or off, only the electron heat diffusivity changes, $\tilde{\chi}_e(r, t) \neq 0$, while $\tilde{u}_e(r, t) \equiv 0$.

In this version of the inverse problem (15), (16), and (18)–(20), it is necessary to reconstruct the coefficients $K(r) = K^S(r) + \tilde{K}(r)$ and $\tilde{K}(r)$ and the ECRH power profile $P_{\text{EC}}(r)$.

Problem B. We again assume that the total heat flux (3) in the steady state only has the diffusive component; i.e., $u_e^S(r) \equiv 0$. Additionally, we assume that, during the transient processes after ECRH is switched on or off, the total heat flux acquires a convective component, while its diffusive component remains unchanged; i.e., $\tilde{\chi}_e(r, t) \equiv 0$ and $\tilde{u}_e(r, t) \neq 0$.

In this version of inverse problem (15), (16), and (18)–(20), it is necessary to reconstruct the coefficients

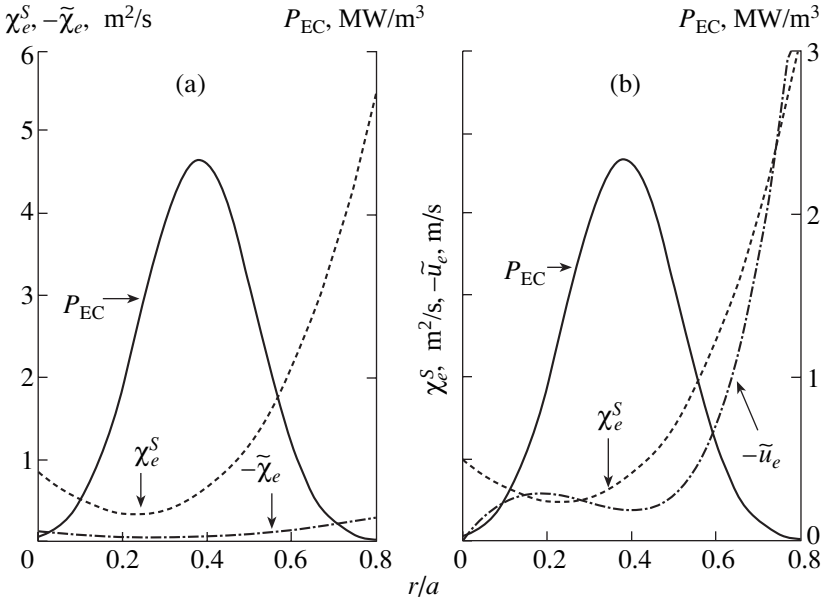

Fig. 7. (a) Solution to inverse problem (15), (16), and (18)–(20) in formulation A for the transient process after ECRH in shot no. 23281 is switched off. The dashed curve is for the steady-state electron heat diffusivity $\chi_e^S(r) = \chi_e(r) - \tilde{\chi}_e(r)$, the dashed-and-dotted curve is for the jump $\tilde{\chi}_e(r)$ in the electron heat diffusivity, and the solid curve is the ECRH power profile $P_{EC}(r)$ with the parameters $r_0/a = 0.38$ and $w/a = 0.17$. (b) Solution to inverse problem (15), (16), and (18)–(20) in formulation B for the transient process after ECRH in shot no. 23281 is switched off. The dashed curve is for the steady-state electron heat diffusivity $\chi_e^S(r)$, the dashed-and-dotted curve is for the jump $\tilde{u}_e(r)$ in the heat convection velocity, and the solid curve is the ECRH power profile $P_{EC}(r)$ with the parameters $r_0/a = 0.38$ and $w/a = 0.17$.

$K(r) = K^S(r)$ and $\tilde{V}(r)$ and the ECRH power profile $P_{EC}(r)$.

Note that, when solving these two simplified inverse problems, we fixed the parameters $\alpha = 2$ and $P_{EC} = 0.65$ MW and searched for the parameters r_0 and w.

Figure 7a illustrates the solution to inverse problem (15), (16), and (18)–(20) in formulation A. The dashed curve corresponds to the steady-state electron heat diffusivity $\chi_e^S(r) = \chi_e(r) - \tilde{\chi}_e(r)$, the dashed-and-dotted curve refers to the jump $\tilde{\chi}_e(r)$ in the electron heat diffusivity, and the solid curve is the ECRH power profile $P_{EC}(r)$ with the parameters $r_0/a = 0.38$ and $w/a = 0.17$.

Figure 7b illustrates the solution to inverse problem (15), (16), and (18)–(20) in formulation B. The dashed curve corresponds to the steady-state electron heat diffusivity $\chi_e^S(r)$, the dashed-and-dotted curve refers to the jump $\tilde{u}_e(r)$ in the heat convection velocity, and the solid curve is the ECRH power profile $P_{EC}(r)$ with the parameters $r_0/a = 0.38$ and $w/a = 0.17$.

Figure 8 shows the time evolution of the variation in the electron temperature at several radii (version A). The solid curves correspond to the electron temperature calculated by solving transcendental equation (21) after solving the abelianization problem. The dashed curves refer to the solution of inverse problem (15), (16), and (18)–(20) in formulation A. We can see that this version of the model describes well an increase in the electron temperature in the central region of the plasma column and a decrease in the electron temperature in the ECRH power deposition region.

Figure 9 shows the radial profiles of the changes in the heat flux components at different times after off-axis ECRH is switched off (version B). The solid curve reflects the jump in heat flux, $\Delta W_{jump} = n^S \tilde{u}_e T^S$, which is associated with the jumps in transport coefficients. The symbols stand for the perturbation $\Delta W_{diff} = -n^S \chi_e^S \frac{\partial \tilde{T}}{\partial r}$ of the diffusive heat flux, and the dashed curves correspond to the perturbation $\Delta W_{conv} = n^S \tilde{u}_e \tilde{T}$ of the convective heat flux. The perturbed convective heat flux is seen to be about one order of magnitude smaller than the perturbed diffusive heat flux.

Note that, at this stage of investigation, we are not able to choose one of the two solutions obtained by solving the inverse problem in formulations A and B, because the input experimental data were obtained from discharges with a fairly high noise level. In order

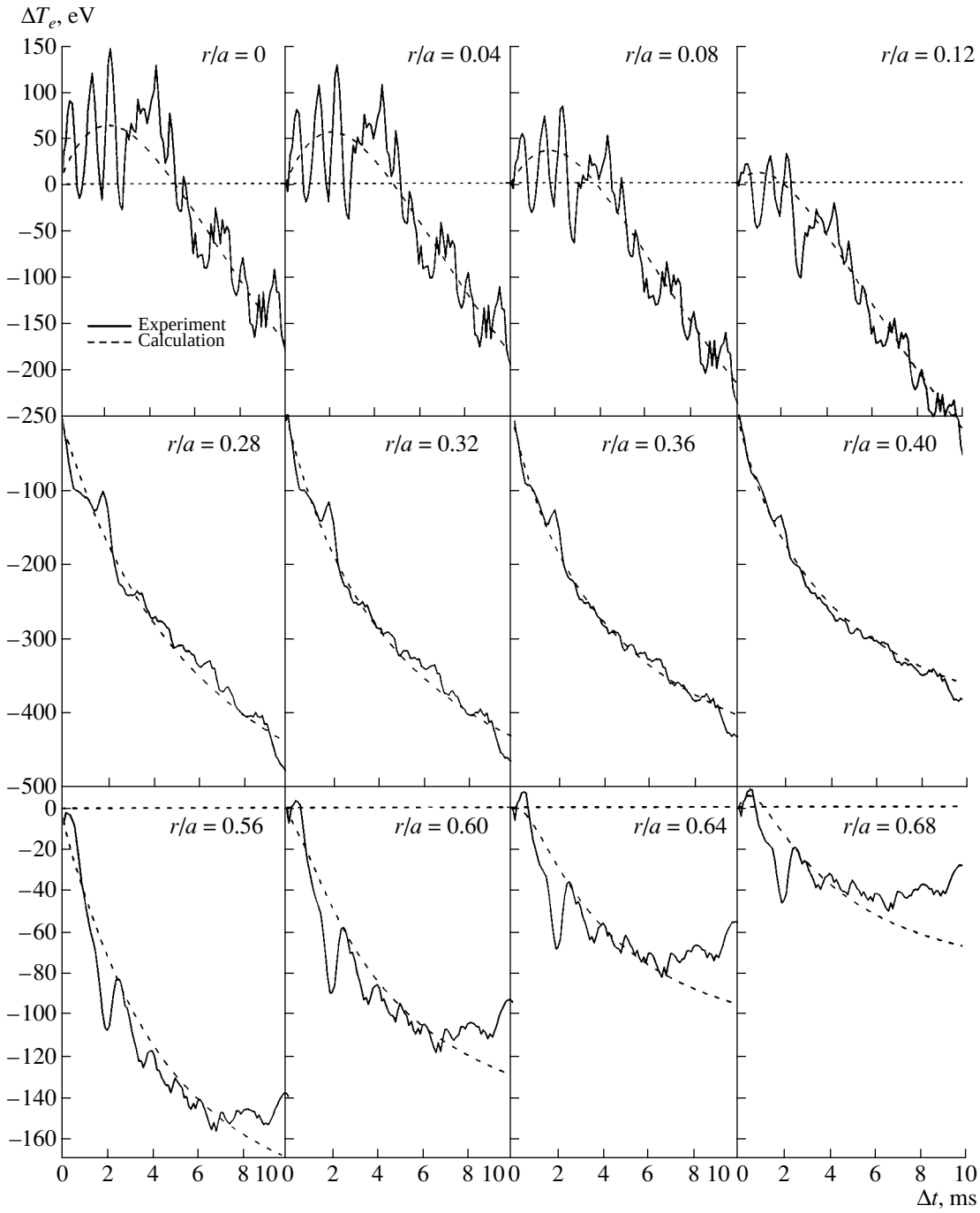

Fig. 8. Time evolution of the electron temperature variation (version A) at several radii in the transient process after ECRH in shot no. 23281 is switched off. The solid curves correspond to the electron temperature calculated by solving transcendental equation (21) after solving the abelianization problem. The dashed curves refer to the solution of inverse problem (15), (16), and (18)–(20).

to choose one of these solutions, it is necessary to involve additional experimental information. Thus, it is well known that, after ECRH is switched on, the plasma is partially expelled from the central region. This effect can be explained as the onset of an additional radial convective flux directed outward from the center (version B). However, in order to obtain the final answer to this question, it is necessary to have more detailed experimental information about the behavior of the plasma density and to solve the equation describing its evolution.

7. DISCUSSION

In this paper, we have described transient processes after ECRH is switched on or off by using two models of transport coefficients. For each of the model, we have derived the transport equation and have formulated the inverse problem. By solving the inverse problems, we have reconstructed the transport coefficients and the ECRH power profile. Let us compare the numerical results obtained from these two models.

(i) First, we consider how each of the models describes opposite-sign changes in the electron temperature in the central region of the plasma column and in the power deposition region during off-axis ECRH (see Figs. 1b, 2b, and also papers [2, 8–11]).

The nonlocal model of transport coefficients reliably describes a decrease (or increase) in the temperature at the plasma center. After ECRH is switched on (or off), the electron heat diffusivity increases (or decreases) simultaneously over the entire cross section of the plasma column in a jumplike manner. This indicates that the central electron temperature begins to change before the perturbations from ECRH reach the central region.

The local model of transport coefficients is incapable of describing opposite-sign changes in the electron temperature in the central region of the plasma column and in the ECRH power deposition region. In Eq. (13), the heat sink term (which describes changes in both the ohmic heating power and the power of electron–ion energy exchange) comes into play only when the central temperature changes; however, this change in the temperature is a consequence of the propagation of perturbations from ECRH. In this case, the sinks can only slow down the rate at which the temperature changes, so that the heat sink term fails to describe the temperature decrease in the central region of the plasma column.

(ii) Second, we consider how the models describe the experimentally observed retarded spreading of the variation $\tilde{T}(r,t)$ in the electron temperature profile on a time scale longer than the diffusive time (see Fig. 4 and also papers [22, 28–30]).

The nonlocal model describes this effect as follows. At each radial point, there are two competing processes: a decrease in the temperature because of the jumplike increase in the electron heat diffusivity and an increase in the temperature due to ECRH. As a result, the temperature changes at a slower rate, thereby leading to the observed effect of the retarded spreading of the radial electron temperature profile.

The local model describes this effect in a different way. The heat convection velocity $u_e^{\text{eff}}(r)$ evaluated by solving the corresponding inverse problem has the following feature: it changes its sign near the center of the ECRH power deposition region (Fig. 5). As a result, to the left and right of the power deposition region, the convective heat flux $\Delta W_{\text{conv}} = V\tilde{T}$ is directed toward the diffusive heat flux $\Delta W_{\text{diff}} = -K\partial\tilde{T}/\partial r$. It is this structure of the convective flux that prevents the electron temperature profile from being spread out.

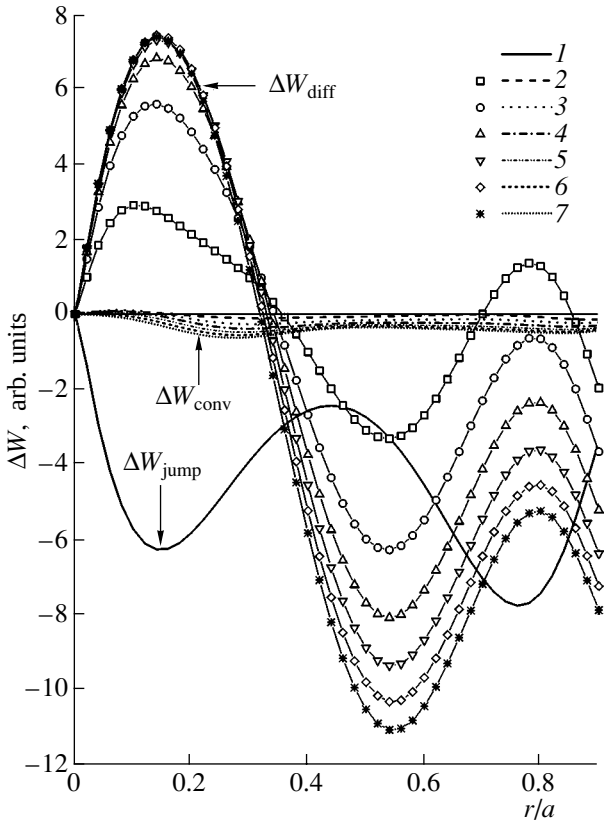

Fig. 9. Radial profiles of the changes in the heat flux components (version B) at different times after off-axis ECRH in shot no. 23281 is switched off: (*2*) Δt = 0.5 ms, (*3*) Δt = 1.5 ms, (*4*) Δt = 2.5 ms, (*5*) Δt = 3.5 ms, (*6*) Δt = 4.5 ms, and (*7*) Δt = 5.5 ms. Solid curve *1* is for the jump in the heat flux, $\Delta W_{\text{jump}} = n^S \tilde{u}_e T^S$, which is associated with the jumps in transport coefficients. The symbols stand for the perturbed diffusive heat flux $\Delta W_{\text{diff}} = -n^S \chi_e^S \frac{\partial \tilde{T}}{\partial r}$, and the dashed curves are for the perturbed convective heat flux $\Delta W_{\text{conv}} = n^S \tilde{u}_e \tilde{T}$.

This analysis indicates that the effective heat convection velocity $u_e^{\text{eff}}(r)$ depends not only on the local plasma parameters but also on the position of the region where the ECRH power is deposited, i.e., on the parameters of the transient process (in the case at hand, on the ECRH power profile $P_{\text{EC}}(r)$). However, formula (14), which was obtained for $u_e^{\text{eff}}(r)$ in deriving linearized equation (13), implies that the heat convection velocity $u_e^{\text{eff}}(r)$ should depend only on the steady-state distributions of the plasma density and plasma temperature. For

this reason, the solution $u_e^{\text{eff}}(r)$ obtained above contradicts the assumptions made in deriving linearized equation (13).

(iii) Third, we point out one more feature of the solutions to the inverse problems in the two models of transport coefficients.

In the local model, the perturbations of the diffusive ($\Delta W_{\text{diff}} = -K\partial\tilde{T}/\partial r$) and convective ($\Delta W_{\text{conv}} = V\tilde{T}$) heat fluxes cancel one another to a large extent (Fig. 6). In this case, the required heat convection velocity in the ECRH power deposition region is high, $u_e^{\text{eff}} \approx 50$ m/s (Fig. 5). This indicates that, in order to determine the heat flux from the solution to inverse problem (13), (14), and (18)–(20), it is necessary to determine the difference of two large quantities, which is as small as 10–20% of the diffusive heat flux. As a result, in the local model, the inverse problem turns out to be ill-conditioned, which may lead to a large error in the resulting solutions.

The nonlocal model gives another pattern of the heat fluxes (Fig. 9). The temporal evolution of the change in the total heat flux is characterized by the jump $\Delta W_{\text{jump}} = n^S\tilde{u}_e T^S$ or $\Delta W_{\text{jump}} = -n^S\tilde{\chi}_e\partial T^S/\partial r$ in the heat flux (this jump is associated with the jumps in transport coefficients), the jump $\Delta W_{\text{diff}} = -n^S\chi_e^S\partial\tilde{T}/\partial r$ in the diffusive heat flux component (this jump is determined by the change in the electron temperature), and the jump $\Delta W_{\text{conv}} = n^S\tilde{u}_e\tilde{T}$ in the convective heat flux component (this jump, however, plays an insignificant role in the evolutionary pattern, because the heat convection velocity is as low as $\tilde{u}_e \approx 2$ m/s, see Fig. 7b). Consequently, in the nonlocal problem as formulated, the inverse problem is well-conditioned and the resulting solutions are sufficiently exact.

(iv) Finally, we compare the two models in the context of the value of the discrepancy functional (18). In the local model (9), the discrepancy functional (18) determined from the solution to inverse problem (13), (14) and (18)–(20) is approximately equal to $J \approx 8.89 \times 10^{-3}$. In nonlocal model (15), the solution to inverse problem (15), (16), and (18)–(20) yields $J \approx 5.63 \times 10^{-3}$. As a result, the discrepancy functional in the nonlocal model (15) is a factor of about 1.5 smaller than that in local model (9). This circumstance is an additional argument in favor of the nonlocal model.

Hence, the above analysis of the numerical results obtained from two different models of transport coefficients allows us to draw the following conclusions:

(i) The use of the nonlocal model (15) (specifically, the introduction of the jumps in transport coefficients) provides a reasonable accuracy in the description of transient processes after ECRH is switched on or off.

(ii) In contrast, the local model (11) fails to describe these transient processes with a sufficient accuracy and yields results contradicting the underlying assumptions of the model.

8. CONCLUSIONS

The transient processes after ECRH is switched on or off have the following characteristic features. First, the transport coefficients change in a jumplike manner, thereby driving the evolution of the initial steady-state distributions of the plasma parameters. Second, the evolution of the original configuration is accompanied by ECRH of the plasma. Consequently, in numerical modeling and in a theoretical analysis, it is necessary to use the equations that are capable of describing both of these transient processes simultaneously.

The mathematical model proposed here takes into account the jump in transport coefficients over the entire cross section of the plasma column and adequately describes the transient processes under consideration. An analysis of the experimental data confirms the validity of the model equations formulated here. Numerical calculations show that, under the ECRH conditions in the T-10 tokamak, the jump $\tilde{\chi}_e$ in the electron heat diffusivity amounts to approximately 15–20% of the steady-state value χ_e^S. Note that, without invoking the jump in transport coefficients after off-axis ECRH is switched on or off, it is impossible to describe opposite-sign changes in the electron temperature in the central region of the plasma column and in the ECRH power deposition region.

The proposed nonlocal model of transport coefficients can be used to analyze the results from experiments in which the peripheral discharge plasma is cooled by injecting pellets or impurities and from experiments in which the peripheral plasma is heated as the total plasma current is rapidly ramped up.

ACKNOWLEDGMENTS

We are grateful to A.M. Stefanovskiĭ for valuable discussions that stimulated the development of the nonlocal model of transport coefficients. This work was supported in part by the Russian Foundation for Basic Research, project nos. 00-15-96536 and 01-02-17483.

REFERENCES

1. E. D. Frederickson, K. McGuire, A. Cavallo, *et al.*, Phys. Rev. Lett. **65**, 2869 (1990).
2. U. Stroth, L. Giannone, H. J. Hartfuss, *et al.*, in *Proceedings of the International Workshop on Plasma Physics "Local Transport in Hot Plasmas," Varenna, 1993*, p. 161.
3. J. G. Cordey, D. G. Muir, S. V. Neudatchin, *et al.*, Plasma Phys. Controlled Fusion **36**, A267 (1994).

4. M. W. Kissick, E. D. Fredrickson, J. D. Callen, *et al.*, Nucl. Fusion **34**, 349 (1994).
5. M. W. Kissick, J. D. Callen, and E. D. Fredrickson, Nucl. Fusion **36**, 1691 (1996).
6. P. Mantica, G. Gorini, G. M. D. Hogeweij, *et al.*, in *Proceedings of the 24th European Conference on Controlled Fusion and Plasma Physics, Berchtesgaden, 1997*, ECA, Vol. 21A, Part IV, p. 1853.
7. X. L. Zou, M. Erba, A. Geraud, *et al.*, in *Proceedings of the 25th European Conference on Control Fusion and Plasma Physics, Prague, 1998*, ECA, Vol. 22C, p. 655.
8. K. W. Gentle, W. L. Rowan, R. V. Bravenec, *et al.*, Phys. Rev. Lett. **74**, 3620 (1995).
9. K. W. Gentle, R. V. Bravenec, G. Cima, *et al.*, Phys. Plasmas **2**, 2292 (1995).
10. K. W. Gentle, W. L. Rowan, R. V. Bravenec, *et al.*, Phys. Plasmas **4**, 3599 (1997).
11. P. Galli, G. Gorini, P. Mantica, *et al.*, Nucl. Fusion **39**, 1355 (1999).
12. S. V. Neudatchin, J. G. Cordey, D. G. Muir, *et al.*, in *Proceedings of the 20th EPS Conference on Controlled Fusion and Plasma Physics, Lisbon, 1993*, ECA, Vol. 17C, Part I, p. 83.
13. J. G. Cordey, D. G. Muir, S. V. Neudatchin, *et al.*, Nucl. Fusion **35**, 101 (1995).
14. S. V. Neudatchin, H. Shirai, T. Takizuka, *et al.*, in *Proceedings of the 22nd European Conference on Controlled Fusion and Plasma Physics, Bournemouth, 1995*, ECA, Vol. 19C, Part III, p. 29.
15. Yu. N. Dnestrovskij, S. V. Cherkasov, S. E. Lysenko, and K. N. Tarasyan, Nucl. Fusion **38**, 373 (1998).
16. Yu. N. Dnestrovskij, E. L. Berezovskij, S. E. Lysenko, *et al.*, Nucl. Fusion **31**, 1877 (1991).
17. Yu. N. Dnestrovskij, S. E. Lysenko, and K. N. Tarasyan, Nucl. Fusion **35**, 1047 (1995).
18. J. D. Callen and M. W. Kissick, Plasma Phys. Controlled Fusion **39**, B173 (1997).
19. V. F. Andreev, Yu. N. Dnestrovskij, and A. M. Popov, Nucl. Fusion **33**, 499 (1993).
20. V. F. Andreev, Yu. N. Dnestrovskij, K. A. Razumova, and A. V. Sushkov, in *Proceedings of the 24th European Conference on Controlled Fusion and Plasma Physics, Berchtesgaden, 1997*, ECA, Vol. 21A, Part II, p. 937.
21. V. F. Andreev, Yu. N. Dnestrovskij, S. E. Lysenko, *et al.*, in *Proceedings of the 26th European Conference on Controlled Fusion and Plasma Physics, Maastricht, 1999*, ECA, Vol. 23J, p. 853.
22. V. F. Andreev, A. V. Sushkov, Yu. N. Dnestrovskij, *et al.*, in *Proceedings of the 27th European Conference on Controlled Fusion and Plasma Physics, Budapest, 2000*, ECA, Vol. 24B, p. 812.
23. V. F. Andreev, Yu. N. Dnestrovskij, S. E. Lysenko, *et al.*, Vopr. At. Nauki Tekh., Ser. Termoyad. Sintez, No. 1, 116 (2000).
24. V. F. Andreev, Yu. N. Dnestrovskij, K. A. Razumova, and A. V. Sushkov, in *Proceedings of the 28th European Conference on Controlled Fusion and Plasma Physics, Funchal, 2001*, ECA, Vol. 25A, p. 1173.
25. N. J. Lopes Cardozo, Plasma Phys. Controlled Fusion **37**, 799 (1995).
26. O. M. Alifanov, E. A. Artyukhov, and S. V. Rumyantsev, *Extremal Methods for Solving Ill-Posed Problems* (Nauka, Moscow, 1988).
27. R. H. Cohen, Phys. Fluids **30**, 2442 (1987).
28. C. Sozzi, S. Cirant, A. Airoldi, *et al.*, in *Proceedings of the 18th IAEA Fusion Energy Conference, Sorento, 2000*, p. 200.
29. F. Leuterer, A. G. Peeters, G. Pereverzev, and F. Ryter, in *Proceedings of the 24th European Conference on Controlled Fusion and Plasma Physics, Berchtesgaden, 1997*, ECA, Vol. 21A, Part IV, p. 1533.
30. P. Mantica, G. Gorini, G. M. D. Hogeweij, *et al.*, Phys. Rev. Lett. **82**, 5048 (1999).

Translated by I. A. Kalabalyk

Plasma Physics Reports, Vol. 28, No. 5, 2002, pp. 382–394. Translated from Fizika Plazmy, Vol. 28, No. 5, 2002, pp. 419–431.

MAGNETIC CONFINEMENT SYSTEMS

Physical Nature of the Electric Current Produced by the Asymmetry of Particle Motion in Toroidal Magnetic Confinement Systems

Yu. V. Gott and É. I. Yurchenko

Nuclear Fusion Institute, Russian Research Centre Kurchatov Institute, pl. Kurchatova 1, Moscow, 123182 Russia

Received October 29, 2001; in final form, November 22, 2001

Abstract—A new type of longitudinal electric current is revealed by analyzing the drift trajectories of charged particles in a tokamak—the current that may be referred to as the asymmetry current because it is associated with the asymmetry of the boundary between trapped and transit particles in phase space. The generation of this current is explained by the fact that the motions of the particles that cross the magnetic surface at a given point in opposite directions are qualitatively different. The asymmetry current results from the toroidal variations of the magnetic field and is maintained by the radial momentum flux of transit particles. The contribution of the particles of different species to the asymmetry current density is proportional to their pressure, is independent of the gradients of the plasma parameters, is maximum at the magnetic axis, and decreases toward the plasma periphery. In contrast to standard neoclassical theory, the asymmetry current can be found only from exact particle trajectories. The asymmetry current is calculated for tokamaks with differently shaped magnetic surfaces and for a model stellarator. By exploiting the newly revealed asymmetry current, together with the bootstrap current, it may be possible to substantially simplify the problem of creating a tokamak reactor. © *2002 MAIK "Nauka/Interperiodica".*

1. INTRODUCTION

The concept of a steady-state tokamak-based fusion reactor was introduced as early as 1971 by Bickerton, Connor, and Taylor [1] and independently by Kadomtsev and Shafranov [2]. Their ideas originated from Galeev and Sagdeev's theoretical discovery (in 1967) of "banana" diffusion, which generates the bootstrap current [3, 4]. In 1987, the bootstrap current was observed experimentally by Havryluk *et al.* [5]. The bootstrap current density is proportional to the plasma-density and plasma-temperature gradients, and the neoclassical bootstrap current vanishes near the magnetic axis. Because of this, it was proposed to use an external current source in order to maintain the central region of the tokamak plasma in a steady state. However, exact calculations of the drift trajectories show that the near-axis bootstrap current density is actually nonzero: for typical plasma parameters, it is about 18% of the maximum radial current density [6–9]. It has been estimated that this level of the bootstrap current density is capable of ensuring the steady-state operation only of a tokamak reactor with a highly elongated plasma [10], while the creation and stable confinement of such a plasma is a fairly complicated technical problem, which has not yet been conclusively resolved. In this context, it is of interest to discuss a new natural mechanism for generating a steady-state longitudinal current near the magnetic axis. This mechanism operates in a narrow region in phase space and is governed by a qualitative difference in the motions of charged particles that cross a given magnetic surface in opposite directions. The magnitude of this new current—the asymmetry current—is determined by the density of such *transit* particles that are responsible for the asymmetry of the boundary between transit and trapped particles in phase space. In toroidal magnetic confinement systems, the asymmetry current is generated by the magnetic field gradient. The magnitude of the asymmetry current is proportional to the total plasma pressure, and its density is maximum at the magnetic axis of the device.

To the best of our knowledge, there are two papers devoted to experimental studies of the radial distribution of the noninductive current density: these are experiments on the Proto-Cleo stellarator [11] and the CDX-U tokamak [12]. In those papers, the near-axis current density was found to be far greater than its neoclassical value. The analysis carried out in [13–17] showed that, in a tokamak, the current near the magnetic axis may be so high that it cannot be described by neoclassical theory; moreover, this current has the same direction as the ohmic current. As was asserted in [13, 14], the existence of such a current follows from the conservation of the generalized momentum (the toroidal canonical momentum) of a particle. The self-generation of the current in a tokamak with an additional vertical (poloidal) magnetic field was considered by Chu [15], who showed that the trapped particle loss cone in velocity space is asymmetric with respect to the sign of

1063-780X/02/2805-0382$22.00

the toroidal particle velocity. The current generated by a specific group of particles in a standard tokamak magnetic field was for the first time predicted theoretically in our papers [16, 17], where this current was called the "asymmetry current." In [18], we analyzed for the first time the question of whether the asymmetry current can actually exist in stellarators.

Since an asymmetry of the boundary region between trapped and transit particles in phase space stems from the characteristic features of the drift motion of particles in the magnetic field of a closed confinement system and since these features themselves are associated with the conservation of the toroidal canonical momentum, we can state that the currents predicted in [13–18] are produced by essentially the same mechanism.

However, in all papers devoted to the investigation of plasma behavior near the magnetic axis (including papers [6–10], which were aimed, in particular, at calculating the on-axis current), the authors found only corrections to the bootstrap current and revealed no asymmetry current, although, at the magnetic axis, the asymmetry current is substantially higher than the bootstrap current.

Here, we quantitatively estimate the asymmetry current in tokamaks with circular and noncircular magnetic surfaces. The asymmetry current in stellarators is considered by using a simplified model, which provides only qualitative estimates. We compare these qualitative predictions with the experimental data from the Proto-Cleo stellarator [11].

2. ASYMMETRY CURRENT (QUALITATIVE ANALYSIS)

We consider the motion of charged particles in a tokamak magnetic field in the drift approximation [19] and represent the magnetic field as

$$\mathbf{B} = \frac{B_0}{h}\left(0, \frac{B_\theta}{B_0}, 1\right), \tag{1}$$

where B_0 is the toroidal magnetic field, $h = 1 + \varepsilon\cos\theta$, $\varepsilon = r/R$, r is the radius of a magnetic surface, R is the tokamak major radius, θ is the poloidal angle, and B_θ is the poloidal magnetic field. In order to simplify the analysis of the drift trajectories, we assume that the ratio B_θ/B_0 is small and neglect the changes in the safety factor q, plasma density n, and temperature T along the particle trajectories. In this case, the drift equations [20] yield

$$\psi - J = \zeta\frac{v_\parallel}{v}h, \tag{2}$$

$$v_\parallel = \sigma_v v\sqrt{G + \varepsilon\cos\theta}\,h^{-1/2}. \tag{3}$$

Here, the poloidal magnetic flux $\psi = \psi_0 2q/(B_0R^2)$ is normalized in such a way that, for circular magnetic surfaces, it is equal to $\psi = \varepsilon^2$; $J = J_0\zeta/(mv)$ is the normalized toroidal component of the generalized momentum; the parameter $\zeta = 2q\rho/R$ is proportional to the Larmor radius ρ of a particle moving with the velocity v; $G = 1 - \mu B_0/E$ is the invariant quantity expressed in terms of the magnetic moment $\mu = mv_\perp^2 h/2B_0$ of a particle; $v_\parallel$ and $v_\perp$ are the particle velocities parallel and perpendicular to the magnetic field; and $\sigma_v = \pm 1$ is the sign of the particle velocity at a point with the coordinates ε and θ on the particle trajectory.

From Eqs. (2) and (3) for a tokamak with circular magnetic surfaces ($\psi = \varepsilon^2 = \text{const}$), we obtain the following expression, which is to be the subject of our analysis:

$$\begin{aligned}\varepsilon^2 - \varepsilon_s^2 + \sigma_s\zeta\sqrt{h_s}\sqrt{G + \varepsilon_s\cos\theta_s} \\ = \sigma_v\zeta\sqrt{h}\sqrt{G + \varepsilon\cos\theta}.\end{aligned} \tag{4}$$

In order to understand the physical nature of the asymmetry current, it is sufficient to thoroughly examine how the character of the particle motion changes depending on the value of the quantity G and the sign of the quantity σ_s. The value $\sigma_s = +1$ determines the sign of the velocity of a particle whose trajectory intersects the magnetic surface $\varepsilon = \varepsilon_s$ at the point ($\varepsilon = \varepsilon_s$, $\theta = \theta_s$); the current of such particles increases the rotational transform. The value $\sigma_s = -1$ corresponds to the sign of the velocity of a particle that crosses this magnetic surface at the same point but in the opposite direction. Note that, in a tokamak, a particle with $\sigma_s = +1$ moves in the direction of the ohmic current. We also stress that, in contrast to σ_v, the quantity σ_s is an integral of motion.

Expression (4) implies that, first, the drift trajectories of the particles with $\sigma_s = +1$ that start from a magnetic surface of radius $\varepsilon_s > \zeta^{2/3}$ at $\theta_s = 0$ remain inside this magnetic surface and, second, the drift trajectories of the particles with $\sigma_s = -1$ remain outside this surface, provided that the toroidal magnetic field points in the direction of the ohmic current. Since the topology of the drift trajectories in a small region $0 < \varepsilon_s < \zeta^{2/3}$ around the magnetic axis is very complicated [21], this region requires separate treatment and will be investigated numerically. In order to qualitatively analyze the types of drift trajectories, it is expedient to divide the full range of changes of the invariant G, $-\varepsilon_s\cos\theta_s \le G \le 1$, into three characteristic subranges: (i) $-\varepsilon_s\cos\theta_s \le G < G_+$, (ii) $G_+ \le G \le G_-$, and (iii) $G_- < G \le 1$ [16, 17]. The boundaries between these subranges, G_+ and G_-, can be determined qualitatively from the condition for the longitudinal velocity component to vanish (at $\theta = \pi$) on the inner and outer drift trajectories, respectively. The coordinates ε_0 and θ_0 of the point at which the longitudinal

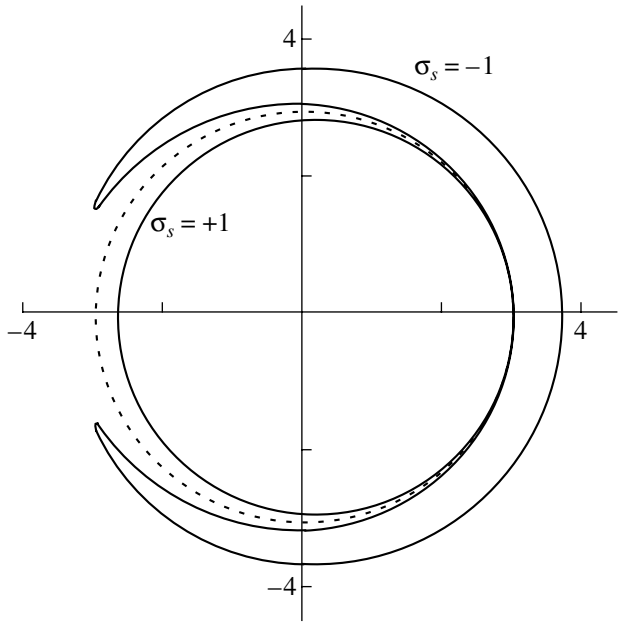

Fig. 1. Particle trajectories in the phase space region $G_+ \le G \le G_-$ ($G^* = 3$). The magnetic surface is shown by the dashed curve.

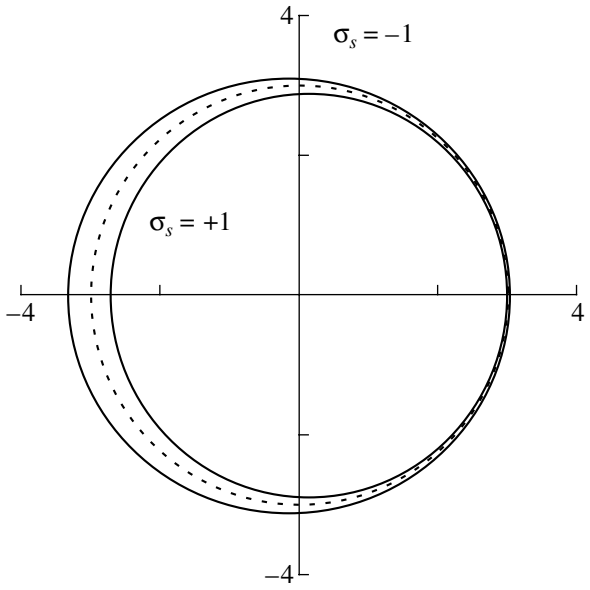

Fig. 2. Particle trajectories in the phase space region $G_- < G \le 1$ ($G^* = 3.5$). The magnetic surface is shown by the dashed curve.

particle velocity vanishes on the trajectory can be found from the set of equations

$$\varepsilon_0^2 - \varepsilon_s^2 = -\sigma_s \zeta \sqrt{G + \varepsilon_s \cos\theta_s}, \tag{5}$$

$$\cos\theta_0 = -\frac{G}{\varepsilon_0}. \tag{6}$$

Setting $\theta_0 = \pi$ in Eqs. (5) and (6) yields the following equation for $G_\pm$:

$$G_\pm = \sqrt{\varepsilon_s^2 - \sigma_s \zeta \sqrt{G_\pm + \varepsilon_s \cos\theta_s}}. \tag{7}$$

It is a straightforward matter to find a solution for $\varepsilon_s = 0$. For $\varepsilon_s > \zeta^{2/3}$, Eq. (7) can be solved by the method of successive approximations. In the first approximation, we set $G_\pm = \varepsilon_s$ under the square root sign and expand the right-hand side in a series to obtain

$$G_+ = 0 \quad \text{and} \quad G_- = \zeta^{2/3} \quad \text{for} \quad \varepsilon_s = 0, \tag{8}$$

$$G_\pm \approx \varepsilon_s - \sigma_s \zeta \frac{\sqrt{1 + \cos\theta_s}}{2\sqrt{\varepsilon_s}} \quad \text{for} \quad \varepsilon_s > \zeta^{2/3}. \tag{9}$$

Note that G_+ is always smaller than G_-. Consequently, in the second subrange of the parameter G, the "outer" particles are trapped while the "inner" particles are transit. For brevity, transit particles from the second subrange will be referred to as "specific particles." Figure 1 shows the drift trajectories of the particles from the second subrange for $G^* = G\zeta^{-2/3} = 3$, and $x_s = \varepsilon_s \zeta^{-2/3} = 3$, $\theta_s = 0$. Figure 2 shows the trajectories for $G^* = 3.5$, i.e., the drift trajectories of the particles from the third subrange. In both figures, the dashed curve indicates the magnetic surface and the magnetic field points outward from the reader (in the direction of the ohmic current).

Note that Eqs. (5) and (6) have another solution, namely, $G = -\varepsilon_s$ at $\theta_s = 0$ and $\theta_0 = 0$. The corresponding trajectories are shown in Fig. 5 from [21]. These are the trajectories of the particles for which the quantity σ_s takes on both signs and whose longitudinal velocity component is directed along the ohmic current. Hence, we can see that the boundary between trapped and transit particles in phase space is asymmetric.

The second subrange, where the topology of the drift trajectories in phase space depends qualitatively on the sign of the particle velocity at the intersection point of the drift and magnetic surfaces in the given poloidal cross section, was first considered in [16–18]. In neoclassical theory, which assumes that $\Delta r/r \ll 1$ (where Δr is the deviation of the particle trajectory from the magnetic surface), the drift trajectories can be traced only approximately. That is why neoclassical theory fails to capture the second subrange and is capable of describing only the first and third subranges, where the outer and inner particles are either both trapped (the first subrange) or both transit (the third subrange). Let us show that it is the second subrange in which the particle motion gives rise to a new longitudinal current. If we neglect the precession velocity of the trapped particles, then we can see that their mean toroidal velocity is close to zero, so that these particles make essentially no contribution to the current. In the third subrange, the number of particles moving in either

direction is the same, so that they also do not contribute to the current.

Since the flux of specific transit particles from the second subrange in phase space is not balanced at all, it drives the longitudinal current, whose direction coincides with that of the ohmic current. The density of this asymmetry current can easily be estimated from the formula

$$j_A \sim e\langle v\rangle \delta n. \tag{10}$$

Since specific particles are near the boundary between transit and trapped particles in phase space, we have $\langle v\rangle \sim \sqrt{\varepsilon}\, v_T$. In the main part of the plasma column ($\varepsilon_s > \zeta_T^{2/3}$), the density of this group of particles can be estimated as

$$\delta n \sim n v_T \int_{G_+}^{G_-} \frac{dG}{|v_\parallel^T|} \sim \frac{\zeta_T}{\varepsilon_s} n. \tag{11}$$

We can readily see that the density δn is, in essence, determined by the difference between the densities of transit particles moving along the magnetic field (σ_+) and those moving in the opposite direction (σ_-):

$$\frac{n_u^\mp}{n} \approx \frac{1}{2}\left(1 - \sqrt{\varepsilon_s}\sqrt{1+\cos\theta_s} \mp \frac{\zeta_T}{4\varepsilon_s}\right). \tag{12}$$

Formulas (10) and (11) give

$$j_A \simeq en v_T \frac{\zeta_T}{\sqrt{\varepsilon_s}}. \tag{13}$$

Hence, the asymmetry current is associated precisely with the difference in the densities of transit particles moving along the magnetic field and in the opposite direction; this difference is, in turn, associated with the asymmetry of the boundary between trapped and transit particles in phase space. The driving force for the asymmetry current is the toroidal variations of the magnetic field, and its magnitude is proportional to the density of all of the plasma particles.

Since we assume that the temperature is constant along the drift trajectories, we can rewrite formula (13) as

$$j_A \sim \frac{cqP}{RB_0}\frac{1}{\sqrt{\varepsilon_s}}, \tag{14}$$

which implies that the magnitude of the asymmetry current is proportional to the total plasma pressure P and its density decreases toward the periphery of the plasma column.

A comparison between formula (13) and the familiar qualitative expression for the bootstrap current density,

$$j_B \sim \sqrt{\varepsilon_s}\frac{c}{B_\theta}\frac{dP}{dr}, \tag{15}$$

shows that, over the major part of the plasma column in a tokamak, the bootstrap current density is higher than the asymmetry current density. However, in the central region of the plasma column, the situation is reversed by virtue of the relationships $\langle j_A\rangle \sim 1/\sqrt{\varepsilon_s}$ and $\langle j_B\rangle \sim \sqrt{\varepsilon_s}$.

An important difference between the asymmetry current and the bootstrap current is that the first is determined by the plasma pressure (rather than by the plasma pressure gradient, as is the case with the bootstrap current).

Another way to estimate the asymmetry current density is to determine the toroidal momentum balance far from the magnetic axis ($\varepsilon_s > \zeta_T^{2/3}$). In the case at hand, transit particles moving in opposite directions have different total momenta. The rate at which the momentum is exchanged between these two particle groups is $\sim nm\dfrac{du_\parallel}{dt} \sim m\nu v_T \Delta n \sim m\nu\sqrt{\varepsilon_s}\dfrac{cT}{eB_\theta}\dfrac{n}{R}$, where ν is the particle–particle collision frequency. In turn, all of the transit particles transfer their momentum to the trapped particles at the rate $\sqrt{\varepsilon_s}\,\nu mnu_\parallel$, where $u_\parallel$ is the mean toroidal velocity of transit particles. Consequently, the toroidal momentum balance equation *for the ions* can be written as

$$m_i n_i \frac{du_{\parallel i}}{dt} = \mu_i\left(\frac{cT_i}{eB_\theta R} - u_{\parallel i}\right) + l_{ei}(u_{\parallel e} - u_{\parallel i}), \tag{16}$$

where $\mu_i = \sqrt{\varepsilon_s}\, m_i n_i \nu_{ii}$ is the ion viscosity and $l_{ei} = m_e n_e \nu_{ei}$ the electron–ion friction coefficient. The corresponding equation *for the electrons* has the form

$$m_e n_e \frac{du_{\parallel e}}{dt} = \mu_e\left(-\frac{cT_e}{|e|B_\theta R} - u_{\parallel e}\right) - l_{ei}(u_{\parallel e} - u_{\parallel i}), \tag{17}$$

where $\mu_e = \sqrt{\varepsilon_s}\, m_e n_e \nu_{ei}$ is the electron viscosity and electron–electron collisions are neglected for simplicity.

In a steady state, we have $du_\parallel/dt = 0$. Therefore, from Eqs. (16) and (17), we find the ion and electron velocities and then obtain the following expression for the asymmetry current density in the case $\sqrt{\varepsilon_s} \gg m_e/m_i$:

$$j_A = e(n_i u_{\parallel i} - n_e u_{\parallel e}) = \frac{\mu_e}{\mu_e + l_{ei}}\frac{c}{B_\theta R}(n_i T_i + n_e T_e). \tag{18}$$

For $\sqrt{\varepsilon_s} \ll 1$, we have $\mu_e \ll l_{ei}$, so that Eq. (18) becomes

$$j_A \sim \frac{e(n_e\zeta_e v_{Te} + n_i\zeta_i v_{Ti})}{\sqrt{\varepsilon_s}}. \tag{19}$$

One can easily see that expression (19) is a two-fluid analogue of formula (13). For the same ion and electron temperatures, the ions and electrons make the same contributions to the total current.

The results obtained are valid only for very low electron–ion collision frequencies. For a finite collision frequency, the contribution of the electron current is smaller than that of the ion current. The role of electron–ion collisions for different devices will be quantitatively estimated below.

We emphasize that the above analysis is valid far from the magnetic axis. Near the magnetic axis ($0 < \varepsilon_s \le \zeta^{2/3}$), the asymmetry current cannot be estimated analytically, but it can be easily estimated just at the axis ($\varepsilon_s = 0$):

$$j_A(0) \sim \frac{cqP}{RB_0}\frac{1}{\zeta_T^{1/3}}. \tag{20}$$

Note that the expression for the bootstrap current at the magnetic axis was obtained earlier in a number of papers [7–10]:

$$j_B(0) \sim \zeta_T^{1/3} Rc\left(-\frac{dP}{d\psi_0}\right). \tag{21}$$

A comparison between formulas (20) and (21) shows that, for conventional (not too peaked) plasma pressure profiles prevailing in tokamak experiments, the asymmetry current at the magnetic axis exceeds the bootstrap current. For this reason, it is important to know the radial profile of the asymmetry current over the entire plasma column.

The expression for the asymmetry current that is valid over the entire plasma column can be obtained only numerically.

3. ASYMMETRY CURRENT IN A TOKAMAK (QUANTITATIVE ESTIMATE)

The current density in an elementary plasma volume around the point with the coordinates ε_s and θ_s can be represented as [22, 23]

$$\begin{aligned}\mathbf{j}(\varepsilon_s, \theta_s) &= e\int \mathbf{v}_\parallel(\varepsilon_s, \theta_s, E, G, \sigma_s) f(\varepsilon_s, \theta_s, E, G, \sigma_s) dE dG \\ &\quad + c\nabla \times \mathbf{M},\end{aligned} \tag{22}$$

where $\mathbf{v}_\parallel$ is the longitudinal velocity of the particle guiding centers in the elementary volume, f is the distribution function of the guiding centers, and M is the total magnetic moment of the particles in the same volume. The second term in representation (22) describes the magnetization current, which can be neglected by virtue of the estimate $j_M \sim \sqrt{\varepsilon} j_A/q^2$.

In a real toroidal device, the current can be calculated quantitatively only by solving the kinetic equation. For a tokamak with circular magnetic surfaces, the familiar drift kinetic equation [24] in which the invariants of motion (E, G, J) are used as symbolic variables has a fairly simple form,

$$\frac{\omega}{qR}\frac{\partial f}{\partial \theta} = \mathrm{St}(f) + Q, \tag{23}$$

where the poloidal angular velocity ω of a particle is equal to

$$\begin{aligned}\omega &\equiv \mathbf{v}\cdot\nabla\theta \\ &= \frac{1}{qR}[v_\parallel - \zeta\cos\theta(v^2 + v_\parallel^2)/4\varepsilon\mathbf{v}].\end{aligned} \tag{24}$$

We can see that, as the magnetic axis is approached, the contribution of the drift velocity to the poloidal angular speed increases in proportion to $1/\varepsilon$.

The second term Q on the right-hand side of kinetic equation (23) describes the source ensuring that the problem is steady-state when neoclassical losses are taken into account. This source plays an especially important role in transport processes in the central region of the plasma column [25–27].

In the full range of pitch angles, the condition for the poloidal angular velocity ω to vanish, which follows from the condition $d\theta/d\varepsilon = 0$, determines the boundary such that, for the largest possible pitch angles, the trajectory of a trapped particle splits into two trajectories of transit particles. Far from the magnetic axis of the device, the quantity $qR\omega$ is close to the longitudinal velocity (3), which, in the case at hand, differs radically from the neoclassical longitudinal velocity,

$$v_\parallel = \sigma_v v\sqrt{\varepsilon_s}\sqrt{2\kappa^2 + 1 + \cos\theta}\,h^{-1/2}, \tag{25}$$

in that, in formula (3), it is important to take into account the functional dependence of the coordinate ε on both the invariants of motion and the poloidal angle θ. In formula (25), we introduced the notation $\kappa^2 = (1 + \varepsilon_s - \mu B_0)/2\varepsilon_s$. The condition for the splitting of the trapped orbit near the magnetic axis is difficult to analyze analytically (this condition was discussed in our earlier paper [21]).

At very low collision frequencies, transport processes are naturally nonlocal and cannot be directly associated with the local gradients. Since transport processes are also nondiffusive in nature, they should be described with allowance for particle and heat sources. In essence, transport processes are convective, so that it is particularly important to precisely calculate the shapes of particle trajectories, especially near the magnetic axis. In the zeroth approximation in the collision frequency, the distribution function should be found by averaging the right-hand side of Eq. (23) over particle trajectories:

$$\oint \frac{\mathrm{St}(f) + Q}{\omega} d\theta = 0. \tag{26}$$

Clearly, the steady-state distribution function so obtained is non-Maxwellian, indicating that the plasma is steady-state but thermodynamically nonequilibrium.

In the problem at hand, in contrast to conventional neoclassical theory, we are dealing with two separatrices. This circumstance may lead to a strong dependence of the distribution function on the variable G at the points $G = G_+$ and $G = G_-$ in phase space. Physically, such a dependence stems from the fact that, at a very low collision frequency, the characteristic time required for a barely transit particle to complete a revolution in the toroidal direction is too short for the particles to relax to a Maxwellian distribution [14, 28].

The explicit expression for the collision integral in terms of the invariants of motion is fairly involved [29], so that we do not write it out here. Since we failed to solve the second-order equation (23), which contains partial derivatives with respect to four variables, we restrict ourselves to obtaining quantitative estimates of the asymmetry current from information about the character of the particle motion.

The longitudinal current in a closed magnetic confinement system can be estimated from the mean poloidal velocity of the specific group of transit particles. This mean velocity can be defined as the ratio of the distance Δz the particle propagates in the toroidal direction during the time interval Δt required for it to complete a revolution in the poloidal direction to this time interval. For a tokamak, the mean velocity so defined is equivalent to the longitudinal velocity averaged over the period of the toroidal rotation of a particle along the drift trajectory (the so-called bounce-averaged longitudinal velocity) [8, 30]:

$$\langle v_\parallel \rangle = \frac{\oint v_\parallel d\tau}{\oint d\tau}, \qquad (27)$$

where $d\tau = \dfrac{d\theta}{\omega}$.

For further analyses, it is expedient to simultaneously consider two particles that move in opposite directions, pass through the same point at the magnetic surface, have the same energy, and are characterized by the same value of the parameter G. Figure 3 shows how the total (summed over σ_s) longitudinal velocity of the two particles with the same energy at the point with the coordinates $x_s = 3$ and $\theta_s = 0$ on the magnetic surface depends on the value of the parameter G^*. As may be seen from Fig. 3, specific particles from the second subrange of the full range of changes of the parameter G have the highest longitudinal velocity. The velocities of the trapped particles from the first subrange and transit particles from the third subrange are nonzero and have the same sign as the velocities of the particles from the second subrange, but, on the other hand, they are sufficiently low that their contribution to the asymmetry current can be neglected. The particles not only move in the longitudinal direction but also undergo the classical precession [20, 30]. In the Appendix, we will show that the precession velocities of the trapped and transit particles have opposite signs and that the total velocity is proportional to the gradients of the plasma pressure and safety factor. We will also show that the precession current can be neglected in comparison with both the bootstrap current at the plasma edge and the asymmetry current near the magnetic axis. In order to find the asymmetry current, we sum up the mean longitudinal velocities of the specific particles over energies, taking into account the particle velocity distribution function, and average the resulting velocities over the layer between two neighboring magnetic surfaces. Assuming that, inside the layer, the particle velocity is independent of radius and is a function of the radial coordinate ε_s of the magnetic surface under consideration, we obtain

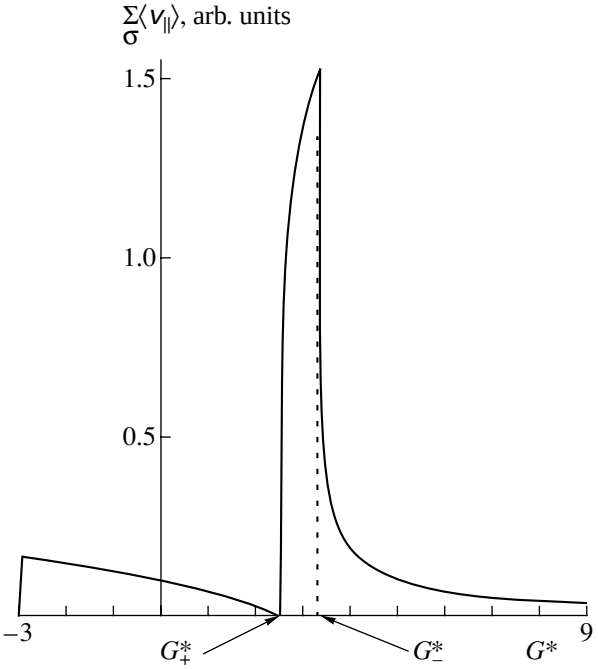

Fig. 3. Total (summed over σ_s) toroidal velocity of two particles with the same energy at the point with the coordinates $x_s = 3$ and $\theta_s = 0$ on the magnetic surface vs. parameter G^*.

$$\langle j_A \rangle = e\frac{2\pi}{l_s}\int_0^\infty E dE \int_{G_+}^{G_-} dG \oint \frac{dl_s}{|v_\parallel|_s} f \langle v_\parallel \rangle, \qquad (28)$$

where dl_s is an element of length of the poloidal cross section of the magnetic surface. In contrast to the above qualitative analysis, carried out with the help of formulas (8) and (9), the limits of integration over G are determined from the condition $\omega(\sigma_s) = 0$.

We use the following model representation for the distribution function of the specific group of transit par-

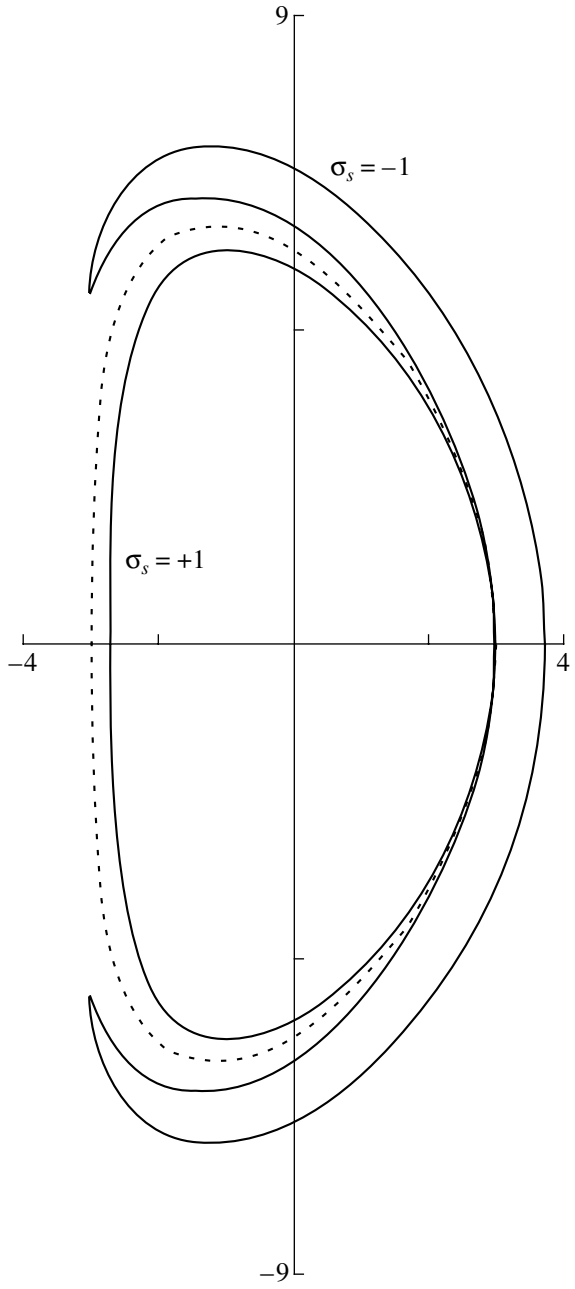

Fig. 4. Same as in Fig. 1 but for $K = 2$ and $\delta = 0.4$.

ticles from a small region in phase space:

$$f = f_M[H(G - G_+) - H(G - G_-)]. \quad (29)$$

Here, f_M is a Maxwellian particle energy distribution function and the Heaviside step function $H(x)$ is defined to be zero for $x < 0$ and to be unity for $x > 0$.

Because of the highly nonlocal character of the problem (especially near the magnetic axis), we could obtain quantitative estimates for the asymmetry current and its radial profile over the plasma column only by using numerical methods.

In order to reduce the computer time required to estimate the quadruple integral in formula (28), we applied the most accurate method of numerical integration [31]. In what follows, the numerical results obtained in our simulations will be represented as approximating formulas that are valid over the entire plasma column in the toroidal confinement systems under discussion.

3.1. Tokamak with Circular Magnetic Surfaces

For clarity, we start by presenting the particular results from computations of the asymmetry current in a tokamak with circular magnetic surfaces. The numerical results can be approximated by the expression

$$\langle j_A \rangle = 0.5 \frac{\zeta_T n e v_T}{\sqrt{\varepsilon_s + \zeta^{2/3}}}. \quad (30)$$

3.2. Tokamak with Noncircular Magnetic Surfaces

For a tokamak with noncircular magnetic surfaces, the equation describing particle trajectories can be rewritten as

$$\frac{\rho^2}{f_K(\theta)} - \frac{\rho_s^2}{f_K(\theta_s)} = \pm\sqrt{G + \rho\cos\theta} - \sigma_s\sqrt{G + \rho_s\cos\theta_s}, \quad (31)$$

where ρ is the position vector for the point at the drift trajectory, $\rho_s = \varepsilon_s f_K(\theta_s)$, $f_K = \sqrt{x^2 + y^2}$, $x = \cos\chi + \delta(\varepsilon)\sin^2\chi$, $y = K(\varepsilon)\sin\chi$, $\delta(\varepsilon) = \delta_a\varepsilon/\varepsilon_a$ is the triangularity, $K(\varepsilon) = K(0) + [K(a) - K(0)]\varepsilon/\varepsilon_a$ is the elongation of the plasma column, and the parameter χ is related to the poloidal angle θ by $\cos\theta = x/f_K$ [32].

The subscript *a* denotes values at the plasma boundary. The particle trajectories shown in Figs. 4 and 5 were calculated for the same parameter values as the trajectories in Figs. 1 and 2 but for $K = 2$ and $\delta = 0.4$. A comparison between these two pairs of figures shows that, in tokamaks with circular and noncircular magnetic surfaces, the particle trajectories are qualitatively the same.

The results from computations of the asymmetry current in a tokamak with noncircular magnetic surfaces can be approximated by the expression

$$\langle j_A^K \rangle = \frac{1.1}{(1 + 0.1\delta)(1 + 0.1K)}\langle j_A \rangle, \quad (32)$$

which implies that the asymmetry current magnitude is weakly dependent on the shape of the cross sections of the magnetic surfaces.

3.3. Asymmetry Current of Fusion α-Particles

The asymmetry current of fusion-generated α-particles was calculated in essentially the same way as in the two preceding cases. The only difference is that the distribution function f_M is replaced by the steady-state distribution function for α-particles obtained by Putvinskiĭ [29]. For our purposes here, it is convenient to represent this steady-state function in the form

$$f_\alpha(v) = \begin{cases} \dfrac{3n_\alpha}{4\pi\ln(z_0^3+1)}\dfrac{1}{z^3+1} & \text{for} \quad z \le z_0 \\ 0 & \text{for} \quad z > z_0, \end{cases} \tag{33}$$

where n_α is the α-particle density, $z_0 = v_{0\alpha}/v_*$, $v_{0\alpha}$ is the velocity of a 3.5-MeV α-particle, v_* is the velocity of α-particles at which they are equally slowed down by collisions with plasma electrons and plasma ions ($v_* \approx 1.3\times10^6\sqrt{T_e\ [\mathrm{keV}]}$ m/s), and $z = v/v_*$. The α-particle density can be estimated from the formula

$$n_\alpha = \tau_\alpha\langle\sigma v\rangle n_d n_t. \tag{34}$$

Here, τ_α is the lifetime of α-particles, $\langle\sigma v\rangle$ is the production rate of α-particles in fusion reactions, and n_d and n_t are the densities of deuterium and tritium ions.

We substitute expressions (33) and (34) into formula (28) and, for estimates, replace $G\ \zeta(v_*)$ with $\zeta_* = \zeta_T(v_*)$ in the limits of integration over G. Then, we perform the velocity integration to obtain

$$\langle j_A\rangle = 3\sqrt{\pi}en_\alpha v_*\frac{I(z_0)}{\ln|z_0^3+1|}\left(\frac{1}{l_s}\int_{G_+}^{G_-}dG\oint\frac{dl_s}{|v_\parallel|_s}\left\langle\frac{v_\parallel}{v_*}\right\rangle\right), \tag{35}$$

where

$$I(z_0) = z_0 - \frac{1}{3}\left\{\frac{1}{2}\ln\left[\frac{(1+z_0)^2}{1-z_0+z_0^2}\right] + \sqrt{3}\left[\arctan\left(\frac{2z_0-1}{\sqrt{3}}\right) - \frac{\pi}{6}\right]\right\}. \tag{36}$$

The results of numerical integration over the variables G, l_s, and τ can be approximated by the formula

$$\langle j_A\rangle = 3.2\frac{\zeta_* en_\alpha v_*}{(1+0.1\delta)(1+0.1K)\sqrt{\varepsilon_s+0.3\zeta_*^{2/3}}}\frac{I(z_0)}{\ln|z_0^3+1|}. \tag{37}$$

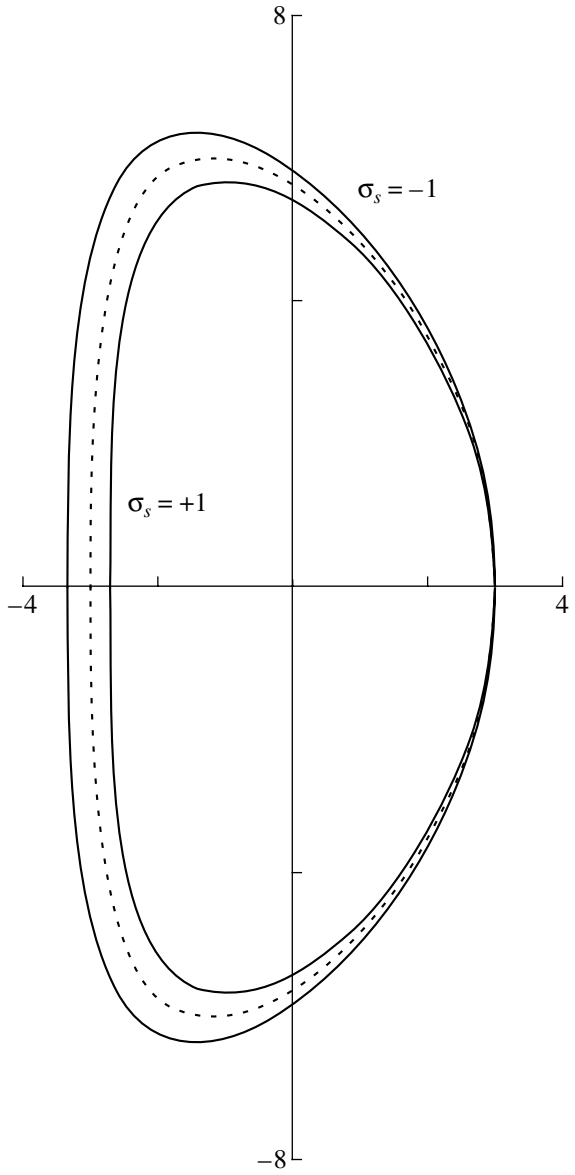

Fig. 5. Same as in Fig. 2 but for $K = 2$ and $\alpha = 0.4$.

3.4. Estimates of Noninductive Currents in a Tokamak Reactor

The results of calculations of the radial profiles of the densities of noninductive currents in the ITER-FEAT tokamak [33] are illustrated in Fig. 6. The current densities were calculated from formulas (36) and (37). In Fig. 6, curve *1* is for the total asymmetry current of plasma electrons and ions, curve *2* is for the bootstrap current, curve *3* is for the asymmetry current of α-particles, and curve *4* is for the total noninductive current. The calculations were carried out for the following radial profiles of the plasma density and electron and ion temperatures: $n = 1.05\times10^{20}[1-(\rho/\rho_a)^2]^{0.025}$ m^{-3} and $T_{e,i} = 34[1-(\rho/\rho_a)^2]^{1.8}$ keV, the remaining parameter values being $k = 1.7$, $\delta = 0.4$, $z_{\mathrm{eff}} = 1.65$, $I_p = 15.1$ MA,

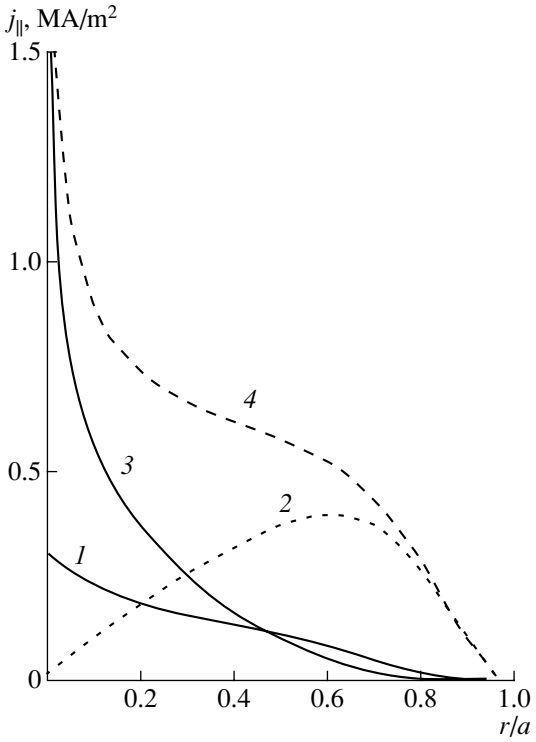

Fig. 6. Radial profiles of the densities of the noninductive currents in the ITER-FEAT tokamak: (*1*) asymmetry current, (*2*) bootstrap current, (*3*) asymmetry current of α-particles, and (*4*) total noninductive current.

and $\tau_\alpha = 15$ s. Under these conditions, the asymmetry current is 1.05 MA, the bootstrap current is 5.1 MA, and the current of α-particles is 1.1 MA. Thus, the asymmetry current of plasma electrons, plasma ions, and α-particles amounts to about 14% and noninductive currents amount to about 50% of the total plasma current. From Fig. 6, one can see that, near the magnetic axis of the device, the noninductive current is driven primarily by α-particles. In this series of computations, the collision frequency was neglected. In order to take into account the influence of the effective collision frequency on noninductive currents, we turn to the familiar expression that is usually used to calculate the bootstrap current [34]:

$$\langle j_\nu \rangle = \frac{1}{1 + 0.55\sqrt{\nu_*} + 0.45\nu_*}\langle j \rangle, \qquad (38)$$

where $\nu_* = \sqrt{2}\,Rq/(\nu\varepsilon_{\rm eff}^{3/2})$, ν is the frequency of the ion–ion collisions (for the ions) or of the electron–ion and electron–electron collisions (for the electrons), and $\varepsilon_{\rm eff} = \varepsilon_s + \zeta_T^{2/3}$ [21]. Our calculations carried out for the parameters of the ITER-FEAT tokamak show that, when the effective collision frequency is taken into account, the asymmetry current of plasma ions and the asymmetry current of α-particles both remain practically unchanged, while the contribution of the asymmetry current of plasma electrons to the total noninductive current decreases from 3.5 to 2% and the contribution of the bootstrap current decreases from 50 to 30%. We thus can conclude that taking into account the collision frequency reduces noninductive currents in a fusion plasma by a factor of approximately 1.5, mainly at the expense of a decrease in the bootstrap current.

4. ESTIMATE OF THE ASYMMETRY CURRENT IN A STELLARATOR

In a stellarator with a circular magnetic axis of radius R, the asymmetry current can be estimated using the following model expression for the magnetic field strength:

$$B = B_0[1 - \varepsilon\cos\theta - \varepsilon_h\cos(l\theta + M\phi)]; \qquad (39)$$

where $\varepsilon_h = \varepsilon_{ha}(r/a)^l$ is the helical ripple amplitude, l is the multipolarity, M is the number of magnetic field periods, and ϕ is the toroidal angle. Since the shape of the magnetic surfaces in a tokamak was found to have an insignificant impact on the asymmetry current, we restrict ourselves to considering a stellarator with circular magnetic surfaces.

By analogy with Eqs. (5) and (6) for a tokamak, the equations for the boundary between trapped and transit particles in a stellarator can be written in the form

$$\varepsilon_0^2 - \varepsilon_s^2 = -\sigma_s\zeta\sqrt{G + \varepsilon_s\cos\theta_s + \varepsilon_{hs}\cos(l\theta_s + M\phi)}, \qquad (40)$$

$$\begin{aligned}\cos\theta_0 &= -\frac{G}{\varepsilon_0} - \frac{\varepsilon_{h0}}{\varepsilon_0}\cos(l\theta_0 + M\phi)\\ &= -\frac{G}{\varepsilon_0} - \varepsilon_{ha}A^l\varepsilon_0^{l-1}\cos M\phi,\end{aligned} \qquad (41)$$

where A is the aspect ratio. If we neglect the second term on the right-hand side of Eq. (41), then, from Eqs. (40) and (41), we obtain

$$G_+ = 0 \quad \text{and} \quad G_- = \zeta^{2/3} \quad \text{for} \quad \varepsilon_s = 0, \qquad (42)$$

$$G_\pm \approx \varepsilon_s - \sigma_s\zeta\frac{\sqrt{1 + \cos\theta_s + \dfrac{\varepsilon_{hs}}{\varepsilon_s}\cos(l\theta_s + M\phi)}}{2\sqrt{\varepsilon_s}} \qquad (43)$$

$$\text{for} \quad \varepsilon_s > \zeta^{2/3}.$$

Since the stellarator is an axially asymmetric device, we must perform averaging not only over the poloidal angle θ_s but also over the toroidal angle ϕ. Calculations show that, in stellarators with $0 \le \varepsilon_h/\varepsilon \le 2$, $2 \le l \le 4$, and $4 \le M \le 10$, the asymmetry current can be estimated from formula (30), in which the safety factor q should be replaced by $1/\mu_{lM}$, where μ_{lM} is the rotational transform produced by the stellarator magnetic field.

Our estimates show that the asymmetry current in a stellarator may be of the same order of magnitude as that in a tokamak. That is why, in stellarators, in which

there are no inductive currents, the asymmetry current is, presumably, easier to reveal experimentally than in tokamaks.

Let us discuss the results of experiments in the Proto-Cleo stellarator [11] with the parameters $R = 0.4$ m, $a = 0.045$ m, $B_0 = 0.3$ T, $n = 10^{18}[1 - (\rho/a)^2]^{0.25}$ m^{-3}, $T_i = 0.05[1 - (\rho/a)^2]^2$ keV, $T_e = 0.01[1 - (\rho/a)^2]^2$ keV, and $\mu_{lm}(a) = 1$. Figure 7 compares the experimentally obtained profile of the noninductive current in the Proto-Cleo stellarator (the closed squares) with the calculated profile of the neoclassical bootstrap current (the dashed curve). The vertical bars show the experimental errors. We can see that the radial profile of the noninductive current in the region near the magnetic axis cannot be explained by neoclassical theory even at a qualitative level: the neoclassical bootstrap current is predicted to be zero in this region, but in reality the current near the axis ($R = 40$ cm) is finite.

In our opinion, this discrepancy may be resolved by incorporating the asymmetry current.

Under conditions prevailing in the Proto-Cleo stellarator, the effective collision frequency plays an important role and the asymmetry current is almost completely determined by the ion plasma component.

The Proto-Cleo is an $l = 3$ stellarator. Such stellarators usually operate with an externally imposed, correcting vertical magnetic field, which may substantially change the magnetic configuration. Since paper [11] contains no data on the rotational transform profile, we present the results of illustrative calculations carried out for several values of μ_{lM}^{eff}.

Figure 8 shows the experimental and computational data from Fig. 7 and also the radial profiles of the asymmetry current calculated for the Proto-Cleo parameters and for different values of the rotational transform: $\mu_{lM}^{\text{eff}} = 0.5$ (curve *1*), 0.2 (curve *2*), and 0.1 (curve *3*). When calculating the asymmetry current, we took into account the collision frequency. Figure 8 demonstrates quantitative agreement between the experimental data and model numerical results on the radial profile of the noninductive current near the magnetic axis of the device.

Figure 9 displays the computational results on the asymmetry current that were obtained for $\mu_{lM}^{\text{eff}} = 0.5$ without (curve *1*) and with (curve *2*) allowance for collisions. The radial profile of the bootstrap current (curve *3*) and the experimental points are the same as in Fig. 7. We can see that the actual collision frequency substantially changes the magnitude of the asymmetry current.

5. CONCLUSION

The results obtained in this study show that a new type of longitudinal electric current should exist in

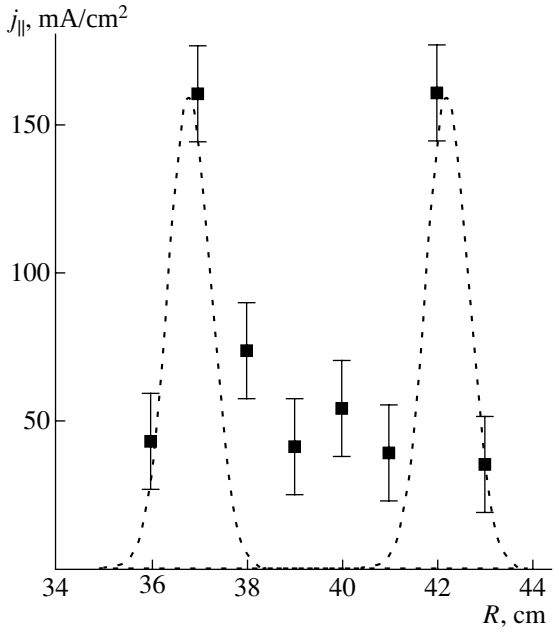

Fig. 7. Comparison between the experimentally obtained profile of the noninductive current density (closed squares) in the Proto-Cleo stellarator [11] and the calculated profile of the bootstrap current density (dashed curve).

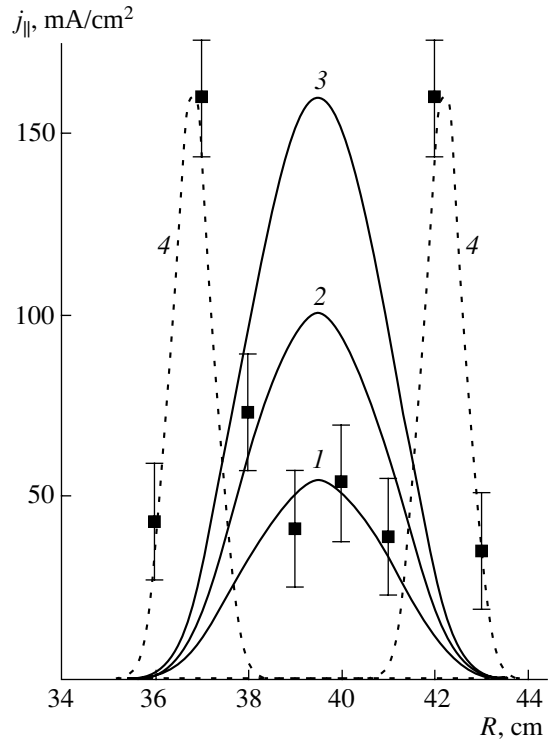

Fig. 8. Asymmetry current density vs. rotational transform for the Proto-Cleo parameters [11] and for $\mu_{lM}^{\text{eff}} = (1)$ 0.5, (*2*) 0.2, and (*3*) 0.1. The calculated bootstrap current density is shown by curve *4* and closed squares are the experimental points.

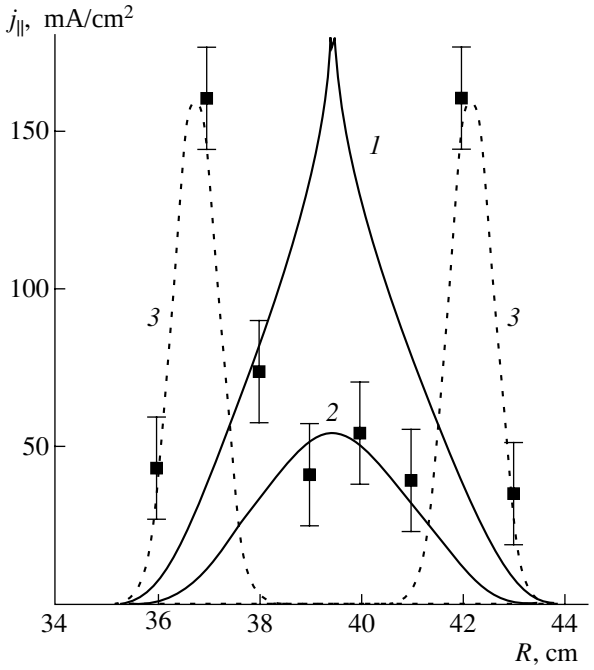

Fig. 9. Effect of the collision frequency on the asymmetry current in the Proto-Cleo stellarator [11]: (*1*) and (*2*) asymmetry current densities calculated, respectively, without and with allowance for collisions and (*3*) bootstrap current density. Closed squares are the experimental points. The adjustable parameter is $\mu_{lM}^{\text{eff}} = 0.5$.

plasmas confined in toroidal magnetic systems—the current that may be referred to as the asymmetry current because it is associated with the asymmetry of the boundary between trapped and transit particles with respect to the sign of their longitudinal velocity. This current is driven by the longitudinal magnetic field gradient, is carried by a specific group of transit particles, is proportional to the total plasma pressure, and is maximum near the magnetic axis of the device. Note that the asymmetry current can exist only in a tokamak in which the discharge duration is much longer than the energy lifetime, i.e., in a tokamak operating in a quasi-steady mode. In this case, the particle distribution function is steady-state but thermodynamically nonequilibrium. The energy fed into the plasma is partially expended on generating noninductive currents—the bootstrap current and the asymmetry current.

The asymmetry current may play an important role in any local region with a flatter plasma pressure profile and with a radial size larger than the deviation of drift trajectories from the magnetic surfaces. In ordinary tokamak discharges, these conditions are usually satisfied in the central region of the plasma column. In discharges with internal and external transport barriers, they can also be satisfied in the barrier regions.

Although the asymmetry current is relatively small in absolute value, it may help to facilitate the problem of current generation near the magnetic axis of a tokamak reactor. It is clear that, by increasing the plasma pressure in the steady operating mode, it is, in principle, possible to create fusion-grade plasmas only at the expense of noninductive currents.

ACKNOWLEDGMENTS

We are grateful to V.D. Shafranov, V.I. Ilgisonis, and V.P. Pastukhov for useful discussions and valuable remarks. This work was supported in part by the Russian Foundation for Basic Research (under the program "Leading Scientific Schools"), project no. 00-15-96526.

APPENDIX

Classical Precession Current

It is well known that, in toroidal confinement systems, the particles move along the torus with a certain mean velocity, which is called the precession velocity. In the neoclassical approximation, in which the deviation of the drift trajectories of the particles from the magnetic surface is assumed to be small in comparison with the radius r_s of the surface, we can obtain the following expression for the precession velocity at $\varepsilon_s \gg \zeta^{2/3}$ in a device with circular magnetic surfaces [23, 30, 35–38]:

$$\langle u_{pr}\rangle = \frac{\zeta_T v^2}{4 v_T \varepsilon_s}\oint\frac{(1+\varepsilon_s\varphi^2)\gamma d\theta}{\varphi}\Big/\oint\frac{d\theta}{\varphi}, \qquad \text{(A.1)}$$

where $\varphi(\kappa, \theta) = \sqrt{2\kappa^2 - 1 + \cos\theta}$, $\kappa^2 = (1 + \varepsilon_s - \mu B_0/E)/2\varepsilon_s$, $\gamma = (1 + \alpha\varphi^2)\cos\theta + S\theta\sin\theta - \alpha/2q^2$, the term $\alpha = -8\pi Rq^2(dp/dr)/B^2$ is determined by the magnetic field gradient, and $S = rd\ln r/dr$ is the magnetic shear. Assuming for estimates that the particle distribution function is Maxwellian, we can write the precession current averaged over the magnetic surface in the form

$$\langle j\rangle_{pr} = \frac{nev_T\zeta_T}{4\pi\sqrt{\pi}\sqrt{\varepsilon_s}}\int_0^\infty x^{3/2}e^{-x}dx\int_0^b d\kappa^2 \times\int_0^{2\pi}\frac{d\theta_s}{\varphi_s}\frac{\oint(1+\varepsilon_s\varphi^2)\gamma d\theta/\varphi}{\oint d\theta/\varphi}, \qquad \text{(A.2)}$$

where $x = E/T$ and $b = \kappa_{\max}^2 = (1 + \varepsilon_s)/2\varepsilon_s$. In these expressions, we neglect the deviation of the drift trajectories of both transit and trapped particles from the magnetic surface. This approximation indicates that, for trapped particles, the integral over the magnetic surface is two times smaller than the integral over the drift trajectory $\left(\int_{-\theta_*}^{\theta_*} d\theta_s/\varphi_s \approx \frac{1}{2}\oint d\theta/\varphi\right)$. In standard neoclassical theory [39], this difference implies that the

summation over σ_v should be carried out with weighting functions of 1 for transit particles and of 1/2 for trapped particles. As a result, we can reduce expression (A.2) to a far simpler form,

$$\langle j\rangle_{pr} = \left\{\frac{1}{2}\right\}\frac{ne v_T \zeta_T}{4\pi\sqrt{\pi}\sqrt{\varepsilon_s}}\int_0^\infty x^{3/2}e^{-x}dx \times \int_0^b d\kappa^2 \oint \frac{(1+\varepsilon_s\varphi^2)}{\varphi}\gamma d\theta, \quad \text{(A.3)}$$

which allows us to take the integrals over the variables θ, κ^2, and x and thus derive the desired expressions for the precession currents of the trapped and transit particles [the notation {1/2} in expression (A.3) means that the factor 1/2 refers only to trapped particles].

(i) For trapped particles, we obtain

$$\langle j_t\rangle_{pr} = -\zeta_T ne v_T F_t, \quad \text{(A.4)}$$

where

$$F_t = \frac{\sqrt{2}}{4\pi\sqrt{\varepsilon_s}}\left[1 + 2\left(2 - \frac{\pi}{3}\right)S - \frac{\alpha}{6q^2}\right]; \quad \text{(A.5)}$$

(ii) for transit particles, we obtain

$$\langle j_u\rangle_{pr} = -\zeta_T ne v_T (F_{pr} - F_t), \quad \text{(A.6)}$$

where

$$F_{pr} = \frac{1}{\varepsilon_s}\left(\frac{S}{2} + \frac{\alpha}{4q^2}\right). \quad \text{(A.7)}$$

From expressions (A.4) and (A.6), we can see that the precession current of trapped particles is completely canceled by a fraction of the precession current of transit particles and that the classical precession current is determined by the magnetic shear (the gradient of the safety factor) and by the plasma pressure gradient.

Thus, we arrive at the following expression for the total classical precession current carried by both transit and trapped particles:

$$\langle j\rangle_{pr} = -\frac{\zeta_T ne v_T}{\varepsilon_s}\left(\frac{S}{2} + \frac{\alpha}{4q^2}\right). \quad \text{(A.8)}$$

This expression implies that, for a radial safety factor profile increasing toward the plasma boundary, the precession current is directed opposite to the ohmic, bootstrap, and asymmetry currents. In operating modes with a reversed shear, the first term in expression (A.8) can cancel the second term, so that the precession current can vanish or even reverse direction.

Expression (A.8) can be rewritten in a more illustrative form:

$$\langle j_{pr}\rangle \sim -\left(\frac{S}{\sqrt{\varepsilon_s}}\langle j_A\rangle + \frac{\beta}{\sqrt{\varepsilon_s}} j_B\right), \quad \text{(A.9)}$$

where the currents $\langle j_A\rangle$ and j_B are given by formulas (14) and (15).

Hence, under the assumptions used in our analysis, the precession current is small in comparison with both the asymmetry current near the magnetic axis and the bootstrap current far from the magnetic axis. Because of this, we neglected the precession current when calculating the noninductive currents.

REFERENCES

1. R. J. Bickerton, J. W. Connor, and J. B. Taylor, Nature (London), Phys. Sci. **229**, 110 (1971).
2. B. B. Kadomtsev and V. D. Shafranov, Plasma Phys. Controlled Nucl. Fusion Res. **2**, 479 (1971).
3. A. A. Galeev and R. Z. Sagdeev, Zh. Éksp. Teor. Fiz. **53**, 348 (1967) [Sov. Phys. JETP **26**, 233 (1968)].
4. A. A. Galeev and R. Z. Sagdeev, Pis'ma Zh. Éksp. Teor. Fiz. **13**, 162 (1971) [JETP Lett. **13**, 113 (1971)].
5. R. J. Havryluk, V. Aruhasalam, M. J. Bell, *et al.*, Plasma Phys. Controlled Nucl. Fusion Res. **1**, 51 (1987).
6. V. Ya. Goloborod'ko, Ya. I. Kolesnichenko, and V. A. Yavorsky, Nucl. Fusion **23**, 399 (1983).
7. K. C. Shaing, R. D. Hazeltine, and M. C. Zarntorff, Phys. Plasmas **4**, 1375 (1997).
8. S. Wang, Phys. Plasmas **5**, 3319 (1998).
9. K. C. Shaing, Phys. Plasmas **7**, 5081 (2000).
10. K. C. Shaing, A. Y. Aydemir, R. D. Hazeltine, *et al.*, Nucl. Fusion **39**, 2103 (1999).
11. J. D. Treffert, J. L. Shohet, and H. L. Berk, Phys. Rev. Lett. **53**, 2409 (1984).
12. C. B. Forest, Y. S. Hwang, M. Ono, *et al.*, Phys. Plasmas **1**, 1568 (1994).
13. S. Ma and J. M. Dawson, Phys. Plasmas **1**, 1251 (1994).
14. W. J. Nunan and J. M. Dawson, Phys. Rev. Lett. **73**, 1628 (1994).
15. T. K. Chu, Phys. Plasmas **3**, 3397 (1996).
16. Yu. V. Gott and E. I. Yurchenko, Preprint No. IAE-6151/6 (Russian Research Centre Kurchatov Institute, Moscow, 1999).
17. Yu. V. Gott and E. I. Yurchenko, in *Proceedings of the 2nd IAEA Technical Committee Meeting on Steady-State Operation of Magnetic Fusion Devices, Fukuoka, Japan, 1999*, Vol. III, p. 796.
18. Yu. V. Gott and E. I. Yurchenko, in *Proceedings of the International Workshop "Innovative Concepts and Theory of Stellarators," Kiev, Ukraine, 2001*.
19. N. N. Bogolyubov and Yu. A. Mitropol'skii, *Asymptotic Methods in the Theory of Nonlinear Oscillations* (Gostekhizdat, Moscow, 1955; Gordon and Breach, New York, 1962).
20. A. I. Morozov and L. S. Solov'ev, in *Reviews of Plasma Physics*, Ed. by M. A. Leontovich (Gosatomizdat, Moscow, 1963; Consultants Bureau, New York, 1966), Vol. 2.
21. Yu. V. Gott and É. I. Yurchenko, Fiz. Plazmy **25**, 403 (1999) [Plasma Phys. Rep. **25**, 363 (1999)].
22. T. G. Northrop, *The Adiabatic Motion of Charged Particles* (Interscience, New York, 1963; Atomizdat, Moscow, 1967).

23. Yu. Petrov and T. S. Huang, Phys. Plasmas **7**, 4095 (2000).
24. F. L. Hinton and R. D. Hazeltine, Rev. Mod. Phys. **48**, 239 (1976).
25. R. D. Hazeltine, Phys. Plasmas **5**, 3282 (1998).
26. P. Helander, Phys. Plasmas **7**, 5081 (2000).
27. L.-G. Eriksson and F. Porcelli, Plasma Phys. Controlled Fusion **43**, R145 (2001).
28. K. C. Shaing, Phys. Plasmas **7**, 5081 (2000).
29. S. V. Putvinskiĭ, in *Reviews of Plasma Physics*, Ed. by B. B. Kadomtsev (Énergoatomizdat, Moscow, 1990; Consultants Bureau, New York, 1992), Vol. 18.
30. B. B. Kadomtsev, in *Plasma Physics and Thermonuclear Research*, Ed. by M. A. Leontovich (Akad. Nauk SSSR, Moscow, 1958; Pergamon, Oxford, 1959), Vol. III.
31. V. I. Krylov, *Approximate Calculation of Integrals* (Nauka, Moscow, 1967; Macmillan, New York, 1962).
32. Yu. N. Dnestrovskij, A. V. Melnikov, A. P. Smirnov, and A. V. Khutoretsky, Preprint No. IAE-5780/6 (Russian Research Centre Kurchatov Institute, Moscow, 1994).
33. *Technical Basis for the ITER-FEAT Outline Design* (1999), Chap. 1, Sect. 2, p. 10.
34. O. Sauter, C. Angioni, and Y. R. Lin-Lin, Phys. Plasmas **6**, 2834 (1999).
35. S. P. Hirshman, Phys. Fluids **31**, 3150 (1988).
36. B. B. Kadomtsev and O. P. Pogutse, Nucl. Fusion **11**, 67 (1971).
37. J. W. Connor, R. J. Hastie, and T. J. Martin, Nucl. Fusion **23**, 1702 (1983).
38. C. M. Roach, J. W. Connor, and S. Janjua, Plasma Phys. Controlled Fusion **37**, 679 (1995).
39. R. D. Hazeltine and P. J. Catto, Phys. Fluids **24**, 290 (1981).

Translated by I. A. Kalabalyk

Plasma Physics Reports, Vol. 28, No. 5, 2002, pp. 395–397. From Fizika Plazmy, Vol. 28, No. 5, 2002, pp. 432–435.

DUSTY PLASMA

Excitation of Dissipative Drift Turbulence in Dusty Plasmas[1]

S. Benkadda* and V. N. Tsytovich**

**LPIIM CNRS-Universite de Provence, Case 321, 13397, Marseille, Cedex 20, France*
e-mail: benkadda@newsup.univ-mrs.fr
***Institute of General Physics, Russian Academy of Sciences, ul. Vavilova 38, Moscow, 119991 Russia*
e-mail: tsytov@tp.lpi.ac.ru

Received October 25, 2001

Abstract—Drift instability in dusty plasma due to plasma density inhomogeneity and inhomogeneities of dust distributions in densities and charges is studied analytically. An explicit general expression for the growth rate of instability is derived. It is found that the growth rate of the dissipative drift instability is substantially enhanced and the threshold of the instability is lowered in the presence of dust. © *2002 MAIK "Nauka/Interperiodica".*

Drift instability in dusty plasma due to plasma density inhomogeneity and inhomogeneities of dust distributions in densities and charges can be relevant for both edge turbulence in fusion devices [1–3] and ionospheric plasmas [4, 5]. The presence of dust as a highly dissipative component in a magnetized plasma can cause the excitation of dust modified drift waves [1, 6]. These drift waves can be associated with the gradients of dust charges and dust densities and can be excited in the absence or presence of plasma density gradients. The large dissipation is caused by the collisions of plasma particles with dust grains appearing as elastic Coulomb collisions and dust capture collisions (collisions where the plasma particles recombine on dust particles). The rate of these collisions is approximately Z_dP times larger than the rate of plasma particle binary collisions, where Z_d is the dust charge in units of the electron charge and $P = n_dZ_d/n$ is the parameter proportional to the dust density n_d (n being the plasma particle density). The dust charge is usually proportional to the dust size; for dust sizes larger than 10^{-3} μm, the charges are very big ($Z_d \gg 1$; for dust grains of size on the order of 3 μm, which are most often encountered, $Z_d \approx 10^4$). The parameter P is often adjusted to the value on the order of unity. Under this condition, the dissipation is highly enhanced by the presence of dust and, therefore, any dissipative drift instability should also be very much enhanced.

In previous considerations, the effect of dissipation due to plasma particle scattering and absorption by dust grains was neglected, although this is the main effect governing the drift waves in dusty plasmas. The change of drift waves due to the contribution of dust to the quasineutrality condition in the basic state (investigated previously in [7]) has a minor effect.

We intend to show that the problem of dissipation due to dust–plasma particle elastic and inelastic collisions with allowance for both the contribution of dust to the quasineutrality condition and dust charge variations in the wave can be investigated directly. It is found that both the growth rate is enlarged and the threshold is lowered in the presence of dust. A nonlinear treatment of drift waves in dusty plasma was formulated in [6], where the linear growth rate was investigated for a particular range of parameters of the dusty plasma system. In the present note, a general analysis of the linear growth rate is performed, which allows us to find an explicit dispersion relation and its solutions.

We start with linearizing the system of nonlinear Hasegawa–Wakatani equations obtained in [6] under conditions where only the dust–plasma particle collisions are taken into account as the main dissipative process. We use the dimensionless notation of [6]:

$$t \longrightarrow \Omega_i \frac{\rho_s}{L_n} t; \quad x \longrightarrow \frac{x}{\rho_s}; \quad y \longrightarrow \frac{y}{\rho_s};$$
$$n \longrightarrow \frac{\delta n_e}{n_{e,0}} \frac{L_n}{\rho_s}; \quad \zeta \longrightarrow \frac{\delta Z_d}{Z_d} \frac{L_n}{\rho_s}; \quad \psi \longrightarrow \frac{e\phi}{T_e} \frac{L_n}{\rho_s}, \tag{1}$$

where ϕ is the electrostatic potential in the wave, Ω_i is the ion cyclotron frequency, $\rho_s = v_s/\Omega_i$ is the ion Larmor radius for the electron temperature, and δZ_d is the change of the dust charge in the drift wave. There are two parameters that determine the inhomogeneities—the parameter s, related to the gradient length of dust inho-

[1] This article was submitted by the authors in English.

mogeneity L_d, and the usual density gradient length L_n:

$$s = \frac{PL_d^{-1}}{(1+P)(1+P-PL_d^{-1})}; \quad L_d = \frac{\partial n_d Z_d}{\partial n_{i,0}}; \quad L_n^{-1} = \frac{1}{n_{i,0}}\frac{\partial n_{i,0}}{\partial x}. \tag{2}$$

The dissipative processes can be described by three coefficients—c_e (related to electron adiabaticity along the magnetic field lines), α (related to the electron capture collisions with dust grains), and β (related to the capture of both electrons and ions in collisions with dust grains) [6]:

$$c_e = \frac{v_{Te}^2 k_z^2}{\tilde{\nu}_e \Omega_i \frac{\rho_s}{L_n}}, \tag{3}$$

where k_z is the wave vector component along the magnetic field,

$$\alpha = \frac{\bar{\nu}_e}{\Omega_i \frac{\rho_s}{L_n}}, \quad \beta = \alpha(1+P)\left[1 + \frac{\nu_{ch}}{\bar{\nu}_i}\right]. \tag{4}$$

The frequencies in Eq. (4) are the dust charging frequency $\nu_{ch} = \omega_{pi} a(1+\tau+z)/\sqrt{2\pi} d_i$, the ion-dust charging collision frequency $\bar{\nu}_i = (1+P)\bar{\nu}_e = \nu_{ch} P(\tau+z)/z(1+\tau+z)$, and the frequency of the change of electron momentum in collisions with dust grains $\tilde{\nu}_e = \nu_{ch} P(\tau+z)(z+4+2z^2\exp(z)\ln(d_i/a)/3)/z(1+\tau+z)$. Here, $\tau = T_i/T_e$, $z = Z_d e^2/aT_e$, d_i is the ion Debye length, and a is the size of dust grains, which are assumed to be spherical.

The equations of [6] in the linear limit describe the modification of drift instability in dusty plasma. They are general in the sense that they take into account the most important new dissipative processes induced by dust, as well as the change of the charge balance in the initial equilibrium state induced by dust charges. This set of linear equations is

$$(i\omega k^2 - isk_y)\psi - \frac{c_e}{1+P}(\psi - n) = 0, \tag{5}$$

$$(-i\omega + \alpha + c_e)n - \alpha z\zeta + (ik_y - c_e)\psi = 0, \tag{6}$$

$$(-i\omega + \beta)\zeta = \alpha(1+P)n. \tag{7}$$

Equations (5)–(7) lead to the following dispersion relation for $\bar{\omega} = \omega/\alpha$:

$$i\bar{\omega}k^2 - is\frac{k_y}{\alpha} - \frac{c_e}{(1+P)\alpha} - \frac{c_e\left(i\frac{k_y}{\alpha} - \frac{c_e}{\alpha}\right)}{\alpha(1+P)}\left[-i\bar{\omega} + 1 + \frac{c_e}{\alpha} - \frac{z(1+P)}{-i\bar{\omega} + \beta/\alpha}\right]^{-1} = 0. \tag{8}$$

We note that Eq. (8) depends on two parameters, c_e/α and k_y/α. For $c_e \gg \alpha$, we obtain

$$i\bar{\omega}\left(k^2 + \frac{1}{1+P}\right) - \frac{k_y}{\alpha}\left(s + \frac{1}{1+P}\right) + \frac{z}{\left(-i\bar{\omega} + \frac{\beta}{\alpha}\right)} = 0. \tag{9}$$

In this limit, the parameter c_e does not enter the dispersion relation. Note that, here, both coefficients c_e and α are related to the influence of dust on the instability. The coefficient c_e describes the nonadiabaticity caused by dust, and the coefficient α describes the capture processes. In the presence of dust, the coefficient c_e is smaller by several orders of magnitude (approximately $Z_d P$ times) than that in the absence of dust. By assuming $c_e \gg \alpha$, we consider the case where the nonadiabaticity introduced by dust is much less than the effect of dust dissipation related to the charging of dust.

The quadratic equation (9) is simple to solve analytically. However, for the sake of deeper understanding, we consider the limiting cases. First of all, we can mention that, in general, the ratio β/α is on the order of unity. For the special case of small dust densities $P \ll 1$, this ratio is large:

$$\frac{\beta}{\alpha} \approx \frac{z(1+\tau+z)}{P(\tau+z)}. \tag{10}$$

In the limit $P \ll 1$, we find that the drift waves are always unstable, the instability being caused by dust only. Taking into account $P \ll 1$ and $s \ll 1$, we find

$$\omega \approx \frac{k_y}{1+k^2} + i\frac{\alpha^2 z}{\beta}. \tag{11}$$

The real part of the drift frequency is approximately the same as in the absence of dust, but the growth rate is on the order of $\bar{\omega}P \approx \nu_{ch}P^2 \approx \nu_{i,i} Z_d P^2$. Although the latter expression contains the small factor P^2, the growth rate can be substantially large if $P \gg 1/Z_d$ (we remind that Z_d is usually very large).

For P on the order of unity, the ratio β/α is also on the order of unity and the drift waves become so unstable that the real and imaginary parts of the frequency are of the same order of magnitude. This happens if

$$\frac{k_y}{\alpha}\left(s + \frac{1}{1+P}\right) \ll \frac{\beta}{\alpha}\left(k^2 + \frac{1}{1+P}\right). \tag{12}$$

In this case, there always exists an unstable root

$$\bar{\omega} = \frac{i}{2}\left(\sqrt{\frac{\beta^2}{\alpha^2} + \frac{4z}{k^2 + \frac{1}{1+P}}} - \frac{\beta}{\alpha}\right). \tag{13}$$

The figure illustrates the dependence of the growth rate $\bar{\gamma} = \gamma/\alpha = \mathrm{Im}\,\bar{\omega}$ on the wave number k and parameter P for $\tau = 0.02$ in the case of a hydrogen plasma.

For an inequality opposite to inequality (12), there is no instability: one of the roots describes simply the relaxation of dust charges ($\omega \approx -i\beta$), and another root describes a stable dust-drift wave:

$$\omega \approx \frac{k_y\left(s + \frac{1}{1+P}\right)}{k^2 + \frac{1}{1+P}} - i\frac{3\beta z\left(k^2 + \frac{1}{1+P}\right)\alpha^2}{k_y^2\left(s + \frac{1}{1+P}\right)^2}. \qquad (14)$$

An important feature is the change of the real part of the drift frequency in the presence of dust [see the first term in Eq. (14)].

We can consider the case of small and large α values and the case where both components of the wave vector are of the same order of magnitude (P is on the order or larger than unity). According to Eq. (13), the growth rate γ is on the order of α for $k \ll 1$ and decreases with the wavenumber for $k \gg 1$. For $\alpha \gg 1$, this growth rate is *very large*; for $k \ll 1$, condition (12) implies $k_y \ll \alpha$, which is always fulfilled in this case. When $k \gg 1$, condition (12) means $k \gg 1/\alpha$, which is also always fulfilled for large values of α. For $\alpha \ll 1$, the instability growth rate is again on the order of α, but, for $k \ll 1$, condition (12) gives the restriction $k_y \ll 1$. For $k \gg 1$ (where the growth rate decreases with k and, thus, is much less than its maximum value), condition (12) gives $k \gg 1/\alpha$. In this case, the value of α is approximately $Z_d P$ times larger than the correspondent expression in the absence of dust.

For $c_e \ll \alpha$, the nonadiabaticity introduced by dust dominates. Assuming that both components of the wave vector are of the same order of magnitude, we find that, for k on the order of unity and $\alpha \ll 1$, the instability is absent, but the real part of the frequency is changed substantially by dust:

$$\omega = \frac{sk_y}{k^2} - i\frac{c_e}{1+P}. \qquad (15)$$

The instability appears for $\alpha \gg 1$ and is described by Imω:

$$\omega = \frac{sk_y}{k^2} + i\frac{c_e(P(z+\tau) + z(P+1+z+\tau))}{(1+P)zP(\tau+z)}. \qquad (16)$$

Let us mention that the condition $c_e \ll \alpha$ reads $k_z^2 v_{Te}^2 \ll \bar{\nu}_e \tilde{\nu}_e \propto P^2$ and means that the parameter P should be larger than a certain value (depending on the wave vector component k_z, which is an independent variable).

This investigation shows that, in the presence of dust, the threshold for the drift instability can be much lower and the growth rate can be substantially larger than those in the absence of dust. Therefore, we expect a strong modification of turbulence in the presence of dust in the edge tokamak plasmas and ionospheric plasmas, where experimental data show evidence of dust [4].

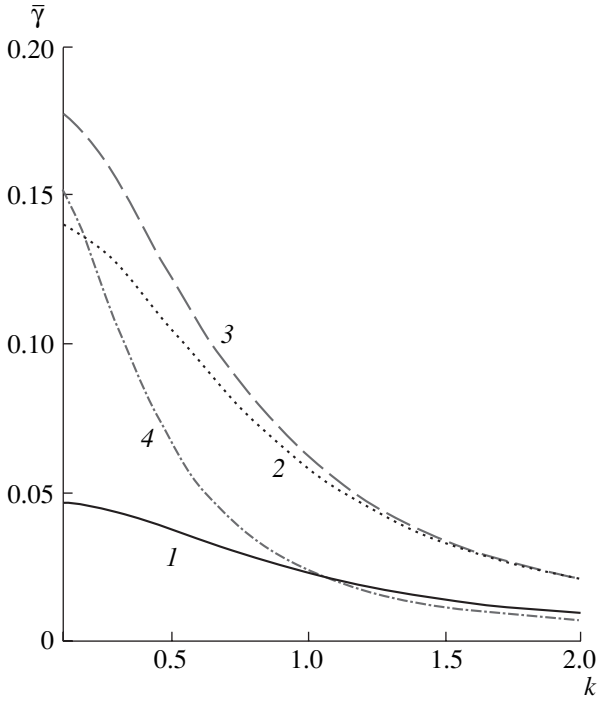

The dependence of the growth rate of dissipative drift instability $\bar{\gamma}$ in dusty plasma on the wavenumber k for different values of the parameter P: (*1*) 0.1, (*2*), 0.5, (*3*) 1, and (*4*) 5.

ACKNOWLEDGMENTS

V. N. Tsytovich would like to express his thanks for hospitality and support during his visit in 1999 to Equipe Dynamique des Systemes Complexes of CNRS-Universite de Provence (France), where this work was performed.

REFERENCES

1. S. Benkadda, V. N. Tsytovich, and A. Verga, Comm. Plasma Phys. Control. Fusion **16**, 321 (1995).
2. V. N. Tsytovich and J. Winter, Usp. Fiz. Nauk **168**, 899 (1998) [Phys. Usp. **41**, 815 (1998)].
3. W. Horton, Phys. Rep. **192**, 1 (1990).
4. S. L. Ossakow, S. T. Zalesak, and B. E. McDonald, Geophys. Res. Lett. **5**, 691 (1978).
5. R. N. Sudan, A. V. Grusinov, W. Horton, and N. Khukharkin, Phys. Rep. **95**, 95 (1997).
6. S. Benkadda, P. Gabbai, V. N. Tsytovich, and A. Verga, Phys. Rev. E **53**, 2717 (1996).
7. P. K. Shukla, M. Y. Yu, and R. Bharuthram, J. Geophys. Res. **96**, 21343 (1991).

Plasma Physics Reports, Vol. 28, No. 5, 2002, pp. 398–402. Translated from Fizika Plazmy, Vol. 28, No. 5, 2002, pp. 436–441.

PLASMA OSCILLATIONS AND WAVES

Metastable Balancing Oscillators

A. E. Dubinov and S. K. Saĭkov

All-Russia Research Institute of Experimental Physics, Russian Federal Nuclear Center, Sarov, Nizhni Novgorod oblast, 607188 Russia

Received November 22, 2001

Abstract—The problem of an oscillator performing oscillations at the top of an oscillating potential barrier is solved exactly. The conditions under which the motion is finite, quasi-finite (metastable), or infinite are determined. Examples are presented from mechanics (a Kapitsa pendulum on a solid support that oscillates in the horizontal direction), plasma physics (Bernstein–Green–Kruskal waves), and microwave electronics (metastable electrons near an oscillating virtual cathode). © *2002 MAIK "Nauka/Interperiodica".*

It is well known that the particle can undergo finite oscillatory motion (in which case it can be regarded as an oscillator) only in the presence of a restoring force. This indicates that the profile of the force field potential should have at least one local minimum.

Not so generally known is the fact that, even in a force field with the potential profile in the form of a potential barrier (with one maximum and no minima), the particle may undergo finite motion near the maximum. For this to occur, the position and/or the height of the barrier should oscillate in time. Such oscillators may be grouped into a separate class of balancing oscillators.

Here, we present an exact solution to the problem of the simplest balancing oscillator at the top of the potential barrier whose position varies periodically with time.

We consider a particle in a force field with the parabolic potential

$$U(x, t) = -a(x - \delta\cos\omega t)^2, \tag{1}$$

where a is the steepness of the parabola and δ and ω are the amplitude and frequency of the oscillations of the potential barrier.

In such a field, the equation of particle motion

$$m\frac{d^2x}{dt^2} = -\frac{\partial U(x, t)}{\partial x} \tag{2}$$

has the form

$$m\frac{d^2x}{dt^2} = 2a(x - \delta\cos\omega t), \tag{3}$$

where m is the mass of a particle.

Under the initial conditions $x(0) = x_0$ and $v(0) = v_0$, the solution to integrodifferential equation (3) is expressed in terms of elementary functions:

$$x(t) = \frac{\delta\omega_0^2\cos\omega t}{\omega^2 + \omega_0^2} - \frac{\delta\omega_0^2\cosh\omega_0 t}{\omega^2 + \omega_0^2} + x_0\cosh(\omega_0 t) + \frac{v_0}{\omega_0}\sinh(\omega_0 t), \tag{4}$$

where $\omega_0 = \sqrt{\frac{2a}{m}}$.

Let the particle be incident on an oscillating potential barrier. To be specific, we set $x_0 > \delta > 0$ and $v_0 < 0$. Using expression (4), we can determine the initial conditions under which the particle trajectory is finite, quasi-finite (metastable), or infinite and find out how the residence time τ of the particle in the interval $(-\delta, \delta)$ depends on the initial conditions.

We call the particle trajectory a "finite trajectory" if the particle oscillates in the interval $(-\delta, \delta)$ for an infinite time ($\tau = \infty$). From expression (4), we can easily see that the particle trajectory is finite when x_0 and v_0 satisfy the relationship

$$v_0 = -\omega_0\left(x_0 - \frac{\delta\omega_0^2}{\omega^2 + \omega_0^2}\right). \tag{5}$$

In this case, the terms with hyperbolic functions in expression (4) exactly cancel each other and there remains only the term with a trigonometric function, indicating that the particle will undergo periodic oscillations for an arbitrarily long time. When x_0 and v_0 values deviate slightly from those satisfying relationship (5), the particle trajectory is quasi-finite: after several oscillations, the particle will go to infinity.

Figure 1 shows the dependence of the time during which the particle oscillates in the interval $(-\delta, \delta)$ on the initial velocity v_0 for several different values of the initial coordinate x_0.

1063-780X/02/2805-0398$22.00

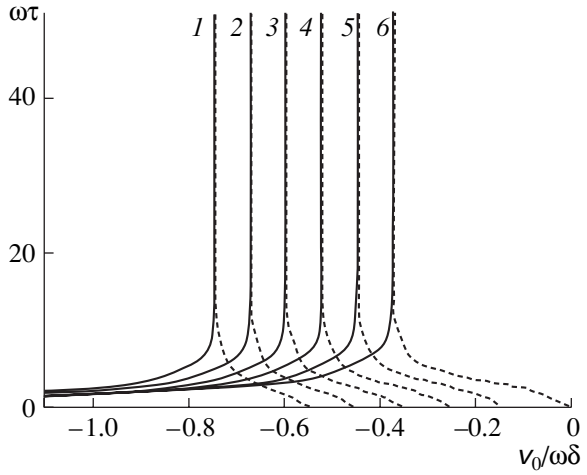

Fig. 1. Dependence of the residence time of a particle in the interval (–δ, δ) on the initial particle velocity for different initial particle coordinates: x_0/δ = (*1*) 5.5, (*2*) 5, (*3*) 4.5, (*4*) 4, (*5*) 3.5, and (*6*) 3. The dashed and solid curves correspond to reflected and transit particles, respectively.

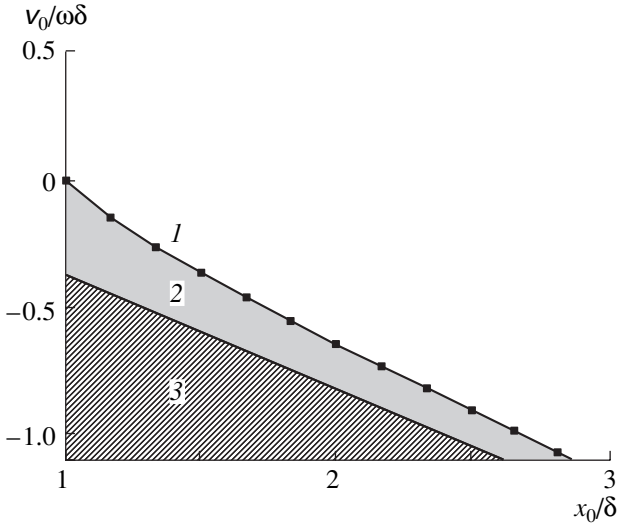

Fig. 2. Regions corresponding to different states of particle motion in the phase plane of the initial coordinates and velocities (x_0, v_0): (*1*) particles that do not reach the barrier, (*2*) reflected particles, and (*3*) transit particles.

At this point, we must make the following three remarks.

(i) The dependences shown in Fig. 1 are resonant in character.

(ii) The right (dashed) parts of the curves correspond to reflected particles and terminate at the abscissa (the latter indicates that particles with low initial velocities do not reach the barrier).

(iii) The left (solid) parts of the curves correspond to transit particles and have the following asymptotic behavior at high initial velocities:

$$\tau \approx \frac{2\delta}{v_0}. \quad (6)$$

An analysis of the solution shows that the closer the values of x_0 and v_0 to those satisfying relationship (5), the longer is the residence time of the particle within the interval (–δ, δ).

Figure 2 shows the regions corresponding to different states of particle motion in the phase plane of the initial coordinates and velocities (x_0, v_0). The plane of the initial values is divided into three regions: the particles from region *1* do not reach the barrier ($\tau = 0$), the particles from region *2* oscillate in the interval (–δ, δ) for a certain time and then are reflected back from the barrier, and the particles from region *3* oscillate in the interval (–δ, δ) for a certain time and then overcome the barrier and continue moving in the forward direction. Regions *2* and *3* are separated by the straight line determined from relationship (5), and the boundary between regions *1* and *2* was calculated numerically.

Figure 3 illustrates the motion of a quasi-finite (metastable) particle (curves *1*) against the background of oscillations of the top of the potential barrier (curves *2*).

From Fig. 3, we can see that

(i) the particle always oscillates in phase with the barrier and

(ii) the oscillatory velocity and oscillation amplitude of the barrier always exceed those of the particle.

The particle motion can also be conveniently illustrated by the phase diagram of the particle. Figure 4 shows phase diagrams for the above three characteristic states of particle motion. Figure 4a illustrates the state of finite particle motion. Figure 4b illustrates the motion of a particle that oscillates within the interval (–δ, δ) for a finite time and then is reflected from the barrier. Figure 4c illustrates the motion of a transit particle with a finite residence time within the interval (–δ, δ). Also shown in Fig. 4 is the phase diagram of the motion of the barrier (dashed circle).

Hence, we have shown the existence of finite and quasi-finite particle trajectories at the top of the potential barrier whose position varies periodically with time.

Let us present some examples of metastable balancing oscillators in different branches of physics.

1. Kapitsa pendulum. Let a mathematical pendulum consist of a mass fixed to the upper end of a thin vertical rod whose lower end is attached to the support by a pivoted mount. When the point of support vibrates with a certain frequency and amplitude, the lower position of the mass becomes unstable, while the upper position becomes stable. The stability of the upper position of a pendulum with a point of support vibrating in

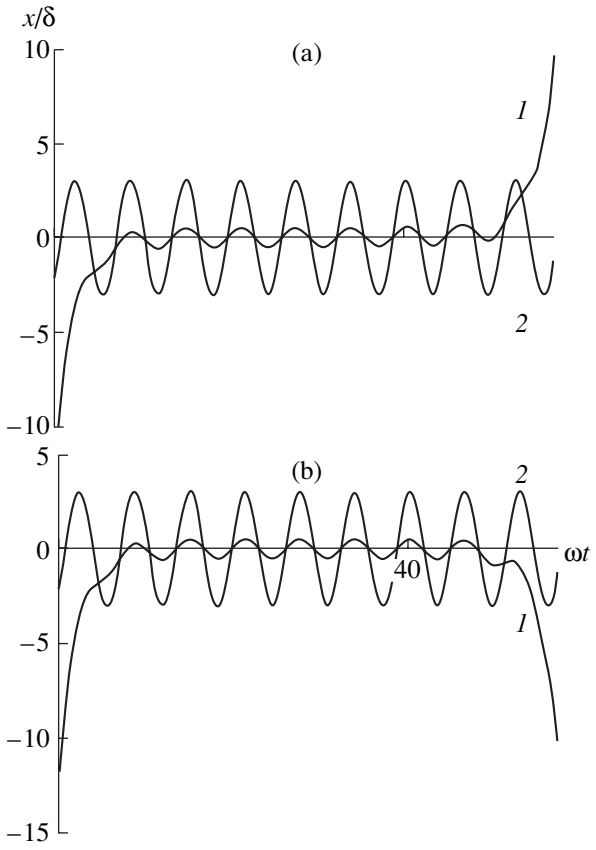

Fig. 3. Oscillations of the quasi-finite particles (curves *1*) and of the top of the potential barrier (curves *2*): (a) transit particle with $x_0/\delta = -10.8$ and $v_0/\delta\omega = 25.6$ and (b) reflected particle with $x_0/\delta = -11$ and $v_0/\delta\omega = 25.9$.

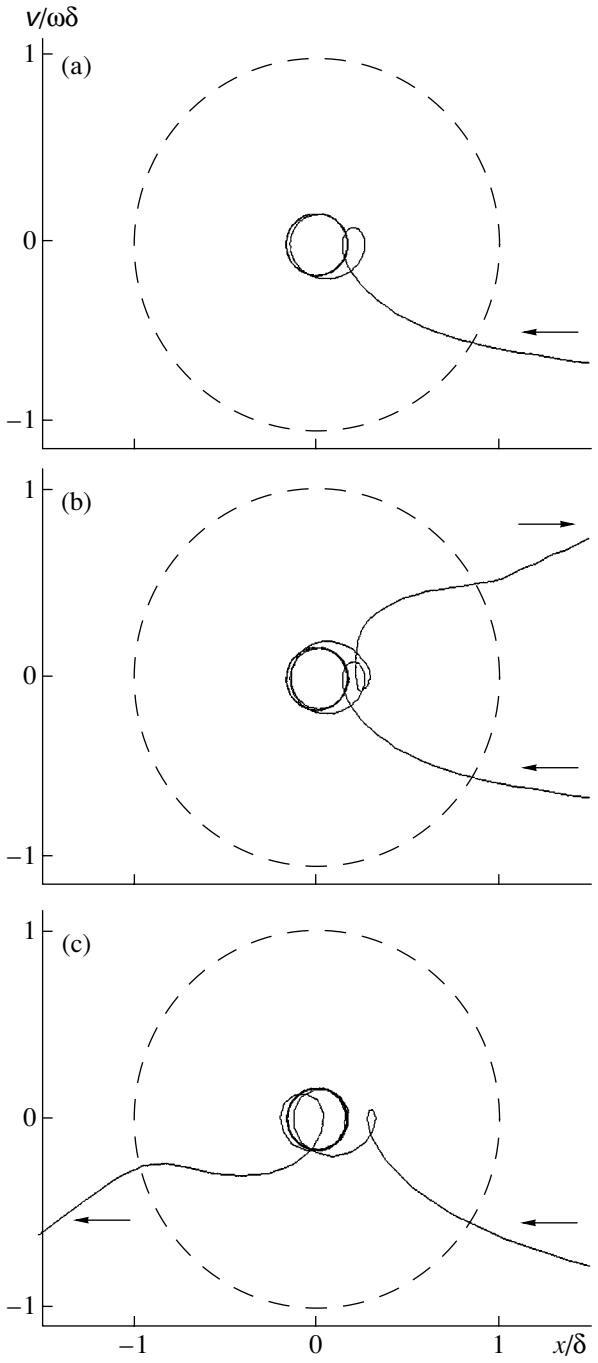

Fig. 4. Phase diagrams of the (a) trapped, (b) reflected, and (c) transit particles for different initial particle coordinates and velocities: (a) $x_0 = 4.5$ and $v_0 = -1.78884$, (b) $x_0 = 4.80069$ and $v_0 = -1.97436$, and (c) $x_0 = 5.29443$ and $v_0 = -2.55294$.

the vertical direction was first studied both theoretically and experimentally by P.L. Kapitsa [1, 2]. The dynamics of a pendulum whose point of support vibrates in the horizontal direction is described by Eq. (3) and corresponds to the behavior of a metastable oscillator.

2. Bernstein–Green–Kruskal waves in a plasma. Bernstein, Green, and Kruskal [3] studied steady nonlinear electrostatic waves in a plasma by simultaneously solving the Boltzmann and Poisson equations. In the wave's frame of reference, the wave was represented as a steady potential profile, in which case there were both transit and trapped particles in the electron and ion plasma components. If we assume that the potential profile is unsteady and oscillates in time, then there should exist metastable plasma particles concentrated near the corresponding potential barriers.

3. Metastable electrons in a vircator. In [4, 5], the dynamics of an electron beam with an oscillating virtual cathode, which divides the beam electrons into two groups (transit and reflected electrons), was studied through one-dimensional electrostatic modeling by the macroparticle method (the method of charged plane sheets). The simulations revealed a third group of electrons, called "metastable electrons." These electrons reach the virtual cathode, which plays the role of a potential barrier for them, perform several (up to 20) oscillations together with the cathode, and then pass over to the first or second group. More recently, the

existence of metastable electrons near the virtual cathode was confirmed in [6, 7]. Let us analyze the dynamics of metastable electrons in more detail.

In [4–7], this new phenomenon was merely discovered but not explained. That is why we will focus our further analysis on the following questions:

(i) What are the mechanisms responsible for the stability and trapping of metastable electrons near a virtual cathode?

(ii) Can the existence of metastable electrons be a consequence of the one-dimensional character of simulations or do they actually exist in multidimensional configurations?

(iii) Can the existence of metastable electrons be a consequence of calculations of the electrostatic part of the problem or do they actually exist in electromagnetic fields?

(iv) What is the relative number of metastable electrons in the beam?

We start by answering the first question, namely, the one about the mechanism for the stability and trapping of metastable electrons near a virtual cathode. Clearly, if the cathode were immobile, no metastable electrons would be observed, because the minimum of the electrostatic potential near the virtual cathode plays the role of a potential hump for negatively charged electrons. However, the spatial oscillations of the virtual cathode give rise to oscillations of the top of the potential energy profile. If the oscillatory velocity of the virtual cathode is higher than the electron velocity, then, for this electron, the cathode at a certain oscillation phase behaves as if it were a local potential well whose walls alternately appear and disappear.

Since a virtual cathode is an object in the electron phase space, its inertia is small and its oscillatory velocity can be higher than the velocity of certain electrons. The above metastable balancing oscillator at the top of an oscillating potential barrier is a simple example of metastable electrons in a vircator.

In order to answer the remaining three questions, we used the KARAT code (a completely self-consistent, relativistic electromagnetic particle-in-cell code) [8], which was appropriately modified in order to provide the possibility of revealing metastable electrons and calculating their number.

This was done in the following way. We chose a certain volume near the virtual cathode and calculated the residence time of each macroparticle within this volume. After running the code, we plotted the electron distribution function over the calculated residence times. Our simulations can be illustrated with the following typical example.

An equipotential cavity is a circular cylinder of radius $R = 2$ cm and length $L = 15$ cm and with conducting ends. The cavity is in a strong magnetic field ($B = 30$ kG). A monoenergetic annular electron beam with the electron energy $W = 511$ keV ($\gamma = 2$), radius $r_b =$ 1 cm, and wall thickness $\Delta r = 0.2$ cm is injected into the cavity through the left end (Fig. 5a). The limiting current of such a beam can be conveniently estimated from the familiar formula [9]

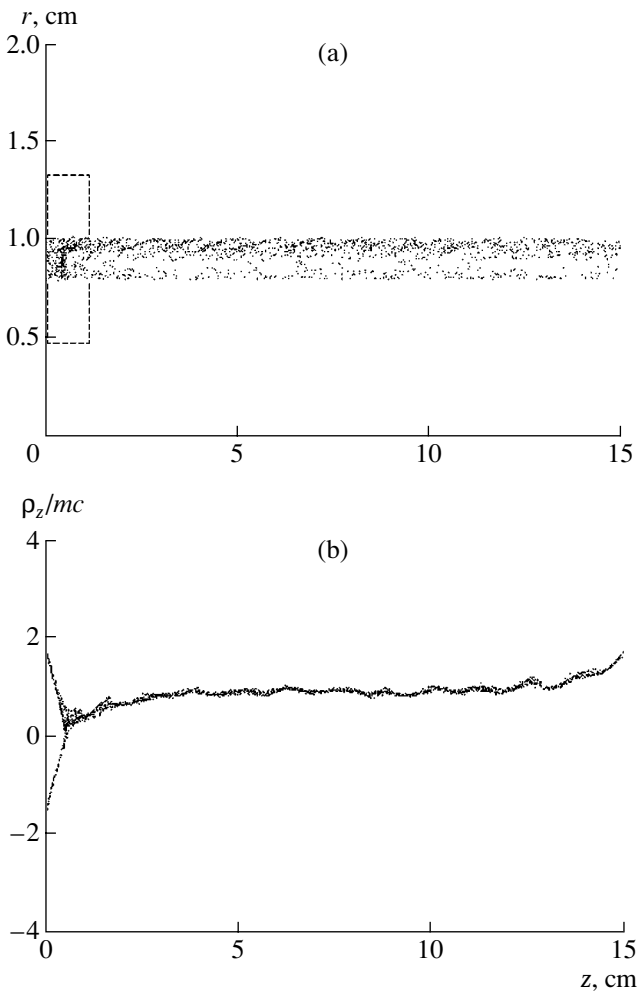

Fig. 5. Modeling of an electron beam with a virtual cathode: (a) geometry of the problem and specified dimensions (the electron distribution function was calculated over the residence times of the beam electrons in the chosen volume, which is marked by dashes) and (b) instantaneous phase diagram of the beam.

$$I_{\lim} = \frac{mc^3}{e}\frac{(\gamma^{2/3}-1)^{3/2}}{\left(\frac{\Delta r}{r_b}+2\ln\frac{R}{r_b}\right)\left(1-\operatorname{sech}\frac{\mu_1 L}{2R}\right)}, \qquad (7)$$

which gives $I_{\lim} \approx 4.82$ kA.

Figure 5b shows a representative instantaneous phase diagram of the beam at a current above the limiting current. We can see that there is a virtual cathode in the cavity. In Fig. 5a, the volume for which the residence time of the beam electrons was determined is indicated by dashes. In simulations, the total time dur-

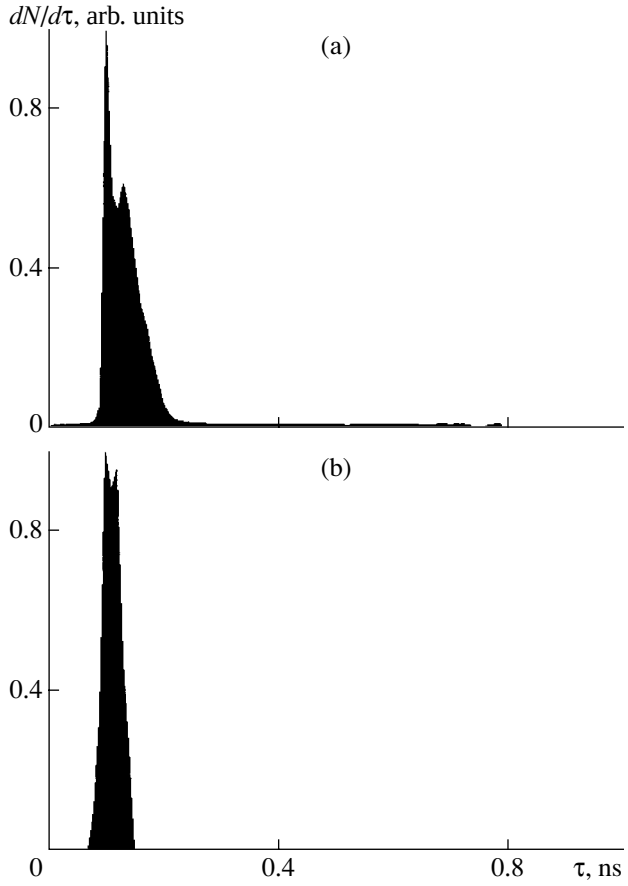

Fig. 6. Distribution function of the beam electrons over their residence times in the chosen volume for beam currents of (a) 5.15 and (b) 10 kA.

ing which the trajectories of the beam electrons were traced was 15 ns.

When the beam current was slightly above the limiting current, we revealed an appreciable quantity of metastable electrons. This is illustrated by Fig. 6, which shows the distribution functions of the beam electrons over their residence times in the chosen volume for the beam currents $I = 5.15$ (Fig. 6a) and 10 kA (Fig. 6b). A double-humped top of the distribution functions in Fig. 6 reflects the presence of transit and reflected electrons, and the long tail in the distribution function in Fig. 6a corresponds to metastable electrons. The relative fraction of metastable electrons in the beam amounts to a few tenths of a percent. When simulating the beam shown in Fig. 6b, we revealed no metastable electrons, although there remains the possibility that a small fraction of such electrons are present. A decrease in the number of metastable electrons with increasing beam current may result from two possible reasons. First, at higher beam currents, electromagnetic oscillations in the cavity are more irregular. Second, the higher the beam current, the larger is the number of beam electrons, so that, even if the number of metastable electrons remains unchanged, their relative fraction should decrease with increasing beam current.

Hence, we have revealed the mechanism by which metastable electrons appear in a virtual cathode and oscillate stably with it. The dynamics of such oscillations and their regular features have been investigated using a simple model. The existence of metastable electrons was confirmed by a completely self-consistent, two-dimensional computer modeling, which also made it possible to estimate their number.

We stress that metastable electrons oscillate in phase with the virtual cathode, thereby increasing the dipole moment of a system consisting of a virtual cathode and its image in the anode grid; consequently, by increasing the relative fraction of metastable electrons, it is possible to raise the efficiency of microwave oscillators operating with virtual cathodes (this possibility was briefly addressed in [4]).

Finally, note that the above examples do not exhaust the list of systems in which metastable balancing oscillators may exist.

ACKNOWLEDGMENTS

We are grateful to V.P. Tarakanov for helping with the work.

REFERENCES

1. P. L. Kapitsa, Zh. Éksp. Teor. Fiz. **21**, 588 (1951).
2. P. L. Kapitsa, Usp. Fiz. Nauk **44** (1), 7 (1951).
3. I. B. Bernstein, J. M. Greene, and M. D. Kruscal, Phys. Rev. **108**, 546 (1957).
4. V. E. Vatrunin, A. E. Dubinov, and V. D. Selemir, Preprint No. 31-93 (All-Russia Research Institute of Experimental Physics, Arzamas-16, 1993).
5. B. V. Alyokhin, A. E. Dubinov, V. D. Selemir, *et al.*, IEEE Trans. Plasma Sci. **22**, 945 (1994).
6. V. I. Kuznetsov and A. Ya. Énder, in *Proceedings of the Conference on the Physics of Low-Temperature Plasma, Petrozavodsk, 1995*, Vol. 2, p. 148.
7. P. V. Akimov, H. Kolinsky, V. I. Kuznetsov, *et al.*, in *Proceedings of the Conference on the Physics of Low-Temperature Plasma, Petrozavodsk, 1998*, Vol. 1, p. 513.
8. V. P. Tarakanov, *User's Manual for Code Karat* (Berkley Research Associate Inc., Springfield, 1992).
9. B. A. Al'terkop, A. Yu. Sokulin, and V. P. Tarakanov, Fiz. Plazmy **15**, 974 (1989) [Sov. J. Plasma Phys. **15**, 564 (1989)].

Translated by O. E. Khadin

Plasma Physics Reports, Vol. 28, No. 5, 2002, pp. 403–410. Translated from Fizika Plazmy, Vol. 28, No. 5, 2002, pp. 442–450.

NONLINEAR PHENOMENA

Nonlinear Oscillations of a Semiconductor Plasma with a Nonrelativistic Electron Beam

Yu. O. Averkov and V. M. Yakovenko

Institute of Radiophysics and Electronics, National Academy of Sciences of Ukraine, ul. Akademika Proskury 12, Kharkov, 61085 Ukraine

Received July 17, 2001; in final form, December 4, 2001

Abstract—Nonlinear oscillations of a semiconductor plasma with a low-density electron beam in the absence of an external magnetic field are studied in the hydrodynamic approximation. The beam is assumed to be nonrelativistic and monoenergetic. Cases are studied in which the Langmuir frequency of the electron oscillations in a semiconductor is much higher or much lower than the electron momentum relaxation rate. The self-similar solution obtained for the first case describes the damping of the nonlinear oscillations of the wave potential. Numerical analysis of the second case shows that the electric field distribution in the beam may correspond to that in a shock wave. *© 2002 MAIK "Nauka/Interperiodica".*

1. INTRODUCTION

The first investigations of nonlinear waves without allowance for thermal effects were carried out by A.I. Akhiezer, G.Ya. Lyubarskiĭ, and R.V. Polovin [1–3] about 50 years ago. They showed, in particular, that the frequency of nonlinear oscillations is independent of the oscillation amplitude only in the nonrelativistic limit. For high-intensity relativistic waves, the oscillation period increases with wave amplitude [3].

The stability conditions for electron oscillations in an unbounded cold plasma in the absence of an external constant magnetic field were investigated qualitatively by Dawson [4], who considered the cases of plane, cylindrical, and spherical symmetries. He showed that, in the one-dimensional case, the oscillations in a homogeneous plasma become unstable and that the wave front breaks when the wave amplitude becomes larger than a certain critical value. He interpreted this phenomenon as the onset of multistream plasma flows (or the phase mixing of oscillations). In the cases of cylindrical and spherical symmetries, the oscillations are anharmonic in character, so that the multistream flows will occur regardless of the oscillation amplitude. He also showed that an analogous situation takes place in an inhomogeneous plasma in the one-dimensional case.

The case of nonlinear relativistic waves was investigated by Tsytovich [5]. He considered this problem using, as an example, two identical colliding beams and determined their energy losses due to the excitation of oscillations. He showed, in particular, that, in the ultrarelativistic limit, only a small fraction of the energy of two identical colliding beams can be transferred to oscillations.

Among the first papers on the nonlinear theory of beam–plasma instabilities were papers [6–16], in which the instabilities were assumed to be suppressed mainly by the trapping of beam electrons by the plasma wave. A study was made of the interaction of both modulated and unmodulated relativistic beams with a cold collisionless plasma treated in the linear approximation. The electron beam density was assumed to be much lower than the density of plasma electrons. It was found that the efficiency of the beam–plasma interaction increases with the relativistic factor, although its linear growth rate decreases. In a monograph by Kuzelev and Rukhadze [17] and in the papers cited therein, it was shown that instabilities can be suppressed by the above mechanism only when the electron beam density is low in comparison with the plasma density. If the electron density of the beam is such that the electron plasma frequency of the beam is much higher than the maximum growth rate of hydrodynamic instability, then the instability is driven by the so-called collective Cherenkov effect (which is also called the anomalous Doppler effect for the natural oscillations of the beam). This effect can also be regarded as a resonant interaction between the plasma wave and the beam wave. According to [17], these instabilities are suppressed by the nonlinear frequency shift of the interacting waves.

There are many papers devoted to the interactions of premodulated (bunched) electron beams with plasmas [18–24]. Thus, the interaction of a monoenergetic beam with a plasma was investigated experimentally in [18, 19]. It was established that the waves excited in this interaction can propagate over much greater distances (keeping their amplitudes almost unchanged) in comparison with those in conventional beam–plasma systems with an unmodulated or a weakly modulated electron beam. Starting from the equation for the potential electric field of one-dimensional linear oscillations excited by a monoenergetic electron beam in a cold plasma, an analytic expression was derived that

1063-780X/02/2805-0403$22.00

describes the potential of the plasma wave. It was shown that the amplitude of the propagating wave remains unchanged if the electron bunches move without being deformed, which is possible only when the electric field inside the bunches vanishes and when the beam in the steady-state wave is a sequence of rectangular bunches. That the electric field vanishes inside equilibrium bunches was interpreted as being due to the superposition of the field of the excited plasma oscillations (which tends to compress the bunches) and the self-field of the bunches (which tends to expand them). As a result, regions where the wave electric field changes harmonically alternate with regions where it is zero.

The excitation of large-amplitude waves by relativistic electron beams with a partially neutralized space charge was investigated by Faĭnberg *et al.* [25, 26]. They showed that, in electron beams in which the electrons rotate in the azimuthal direction, the space charge density wave gives rise to oscillations of the beam current and, accordingly, to the magnetic self-field of the wave. In turn, this self-field initiates a self-compression force of the bunches into which the beam is broken by the wave. The self-compression force counterbalances the force of Coulomb interaction between the electrons. As a result, a wave with a large-amplitude electric field can propagate in the beam in such a way that the trajectories of the beam electrons do not intersect and the wave front does not break.

The interaction of electron beams with collision-dominated plasmas was studied in [27–29]. Ivanov *et al.* [27] used the particle-in-cell method to model the temporal evolution of the wave energy in the interaction of a monoenergetic electron beam with a collision-dominated dense plasma. The parameters of the beam–plasma system were chosen so that the collision frequency in the plasma was higher than the growth rate of the hydrodynamic instabilities in a collisionless plasma and lower than the electron Langmuir frequency. They considered the excitation of a single wave at the electron Langmuir frequency and also the excitation of a wave packet. In the first case, the wave energy in the nonlinear interaction stage oscillates and turns out to be much lower than that in a collisionless plasma. However, although the condition for the oscillations to grow at a maximum rate is violated by a decrease in the beam electron velocity, they are not completely damped because of the corresponding change in their phase. An initially monoenergetic electron beam that excites a wave packet in the plasma is thermalized in the nonlinear stage. As a result, the plasma oscillations are damped and the beam can freely propagate through the plasma without significant energy loss. The spatial evolution of the wave energy in the interaction of electron beams with collision-dominated plasmas was studies in [28, 29] for the case of excitation of a single oscillation mode. It was shown, in particular, that the dependence of the wave energy on the longitudinal (in the propagation direction of the beam) coordinate is oscillatory in character and that the wave energy in the nonlinear stage is substantially lower than that in a collisionless plasma [28]. The oscillation period in the nonlinear stage is also shorter than that in the collisionless case [29].

All of the papers cited above deal with a gaseous plasma. At the same time, it is of interest to investigate the excitation of steady-state nonlinear waves by electron beams in a solid-state plasma. Thus, the existence of nonlinear electromagnetic waves in semiconductors was addressed in many papers (see, e.g., [30–32]). The mathematical apparatus for a description of steady-state nonlinear waves of finite amplitude (domains) in semiconductors was worked out in [30, 31]. It is based on the solution of a model equation for the internal current in a semiconductor (with allowance for the diffusion current), Poisson's equation, and the continuity equation. Different nonlinear mechanisms for the onset of the envelope solitons of transverse electromagnetic waves in a semiconductor were analyzed theoretically by Bass and Khankina [32]. These mechanisms are associated with the dependence of the electron energy on the quasi-momentum in narrow band-gap semiconductors, the effect of a nonuniform high-frequency electromagnetic field, and the heating of current carriers in an external electric field.

In contrast to [27–29], in which the development of the instability was considered both in the linear and nonlinear stages, our aim here is to investigate how the dissipation in a semiconductor affects the excitation and propagation of steady-state waves in a semiconductor plasma–electron beam system. We apply the hydrodynamic approximation and assume that the beam is monoenergetic. In practice, the related phenomena can be studied experimentally, e.g., by the methods used in [33, 34] to investigate the interaction of electron beams with a solid-state plasma. We examine the following two qualitatively different cases: the first one in which the electron Langmuir frequency Ω_p in a semiconductor plasma is much higher than the electron momentum relaxation rate ν, $\Omega_p \gg \nu$, and the second one in which $\Omega_p \ll \nu$. In the first case, we obtain a self-similar solution for the wave potential. Numerical modeling of the second case with the help of the phase-plane methods shows that, in weak wave fields, the electric field distribution in the beam correspond to that in a shock wave.

2. BASIC EQUATIONS

We consider a homogeneous semiconductor and assume that there is no external magnetic field. Let the x-axis be directed along the propagation direction of a nonrelativistic monoenergetic beam moving with the velocity v_0. The nonrelativistic character of the motion of the beam electrons and the semiconductor-plasma electrons ($v, u \ll c$, where v is the beam electron velocity, u is the velocity of the semiconductor-plasma electrons, and c is the speed of light in empty space), we

restrict ourselves to considering a potential electric field ($E = -\partial\varphi/\partial x$, where φ is the electric field potential). We start with the following set of hydrodynamic equations and Poisson's equation in the one-dimensional approximation:

$$\begin{cases} \dfrac{\partial n}{\partial t} + \dfrac{\partial}{\partial x}(nv) = 0 \\ \dfrac{\partial N}{\partial t} + \dfrac{\partial}{\partial x}(Nu) = 0 \\ \dfrac{\partial v}{\partial t} + v\dfrac{\partial v}{\partial x} = \dfrac{e}{m_0}\dfrac{\partial \varphi}{\partial x} \\ \dfrac{\partial u}{\partial t} + u\dfrac{\partial u}{\partial x} = \dfrac{e}{m^*}\dfrac{\partial \varphi}{\partial x} - \nu u \\ \varepsilon_0 \dfrac{\partial^2 \varphi}{\partial x^2} = 4\pi e[(n - n_0) + (N - N_0)], \end{cases} \quad (1)$$

where n and n_0 are the electron and ion densities in the beam, N and N_0 are the perturbed and unperturbed electron densities in a semiconductor plasma, $-e$ is the charge of an electron, m_0 is the mass of a free electron, ε_0 is the dielectric constant of the crystal lattice of the semiconductor, m^* is the effective mass of an electron in a semiconductor, $v_T = = \sqrt{k_B T/m^*}$ is the thermal velocity of the conduction electrons in a semiconductor (for $\Omega_p \ll \nu$, we have $v_T \propto v_F$, with v_F being the Fermi velocity of the semiconductor-plasma electrons), k_B is Boltzmann's constant, and T is the temperature of the semiconductor lattice. The beam ions can be assumed to be immobile because the characteristic rates of change τ^{-1} of both the fields and the electron density are high in comparison with the ion Langmuir frequency Ω_i; i.e., we are working under the condition

$$\tau^{-1} \gg \Omega_i. \quad (2)$$

An immobile, positively charged crystal lattice serves as a background neutralizing the electron charge of the semiconductor plasma.

In the general case, in the equation of motion of the semiconductor-plasma electrons in set (1), we must keep the term proportional to the electron density gradient and also take into account the dependence $\nu(|E|)$ of the relaxation rate of the momentum of the semiconductor-plasma electrons on the strength of the electric field of a plasma wave. For $\Omega_p \gg \nu$, we assume that the relaxation rate is constant and corresponds to a certain characteristic electric field strength. We can expect that this assumption, which is dictated by a fairly complicated structure of the equations incorporating the $\nu(|E|)$ dependence, will yield correct order-of-magnitude results, because, in the range of the semiconductor and field parameters for which the case $\Omega_p \ll \nu$ is realized, the $\nu(|E|)$ dependence is unimportant. The necessary quantitative conditions for these assumptions will be presented at the end of the paper.

We represent the sought-for self-similar solution for the wave potential in the form

$$\varphi = \varphi(\xi), \quad \xi = x - v_{\text{ph}}t, \quad (3)$$

where v_{ph} is the phase velocity of the plasma wave ($v_{\text{ph}} \propto v_0$). Substituting representation (3) into Eqs. (1) and taking into account the above assumptions, we obtain the set of equations

$$\begin{cases} \dfrac{\partial}{\partial \xi}[n(v - v_{\text{ph}})] = 0 \\ \dfrac{\partial}{\partial \xi}[N(u - v_{\text{ph}})] = 0 \\ (v - v_{\text{ph}})\dfrac{\partial v}{\partial \xi} = \dfrac{e}{m_0}\dfrac{\partial \varphi}{\partial \xi} \\ (u - v_{\text{ph}})\dfrac{\partial u}{\partial \xi} = \dfrac{e}{m^*}\dfrac{\partial \varphi}{\partial \xi} - \nu u \\ \varepsilon_0 \dfrac{\partial^2 \varphi}{\partial \xi^2} = 4\pi e[(n - n_0) + (N - N_0)]. \end{cases} \quad (4)$$

The solutions to the continuity equation in set (4) have the form

$$n(v) = n_0 \frac{v_{\text{ph}} - v_0}{v_{\text{ph}} - v} \quad \text{for} \quad n(v_0) = n_0, \quad (5)$$

$$N(u) = N_0 \frac{v_{\text{ph}}}{v_{\text{ph}} - u} \quad \text{for} \quad N(0) = N_0. \quad (6)$$

Integrating the equation of motion of the beam electrons yields the energy conservation law

$$\frac{m_0(v - v_{\text{ph}})^2}{2} - e\varphi = \frac{m_0(v_0 - v_{\text{ph}})^2}{2} - e\varphi_0, \quad (7)$$

which leads to the following form of the dependence $v(\varphi)$:

$$v - v_{\text{ph}} = \pm\sqrt{(v_{\text{ph}} - v_0)^2 + \frac{2e}{m_0}(\varphi - \varphi_0)}, \quad (8)$$

where $\varphi_0 = \varphi(v_0)$ is a certain initial potential value.

We insert dependence (8) into Eq. (5) and obtain

$$n(\varphi) = \pm\frac{n_0(v_0 - v_{\text{ph}})}{\sqrt{(v_{\text{ph}} - v_0)^2 + \dfrac{2e}{m_0}(\varphi - \varphi_0)}}. \quad (9)$$

From physical considerations, it is clear that n and n_0 should be of the same sign. Consequently, from formulas (5) and (8), we have $v_0 > v_{\text{ph}}$ for $v > v_{\text{ph}}$ and $v_0 < v_{\text{ph}}$ for $v < v_{\text{ph}}$.

Below, the solution to the equation of motion of the semiconductor-plasma electrons and the solution to Poisson's equation will be derived separately for the cases $\Omega_p \gg \nu$ and $\Omega_p \ll \nu$, using a gallium arsenide (GaAs) semiconductor as an example.

3. SOLUTION FOR THE WAVE POTENTIAL IN THE CASE $\Omega_p \gg \nu$

The case $\Omega_p \gg \nu$ can be realized, e.g., in a heavily doped, partially compensated GaAs semiconductor at liquid helium temperatures. In this situation, the momentum of the electrons relaxes due to their scattering by the screened dipoles (in the case at hand, these are donor–acceptor complexes) [35, 36]. According to [35], in a sample with an *n*-type impurity (tellurium) concentration of about $N_i \approx 5 \times 10^{17}$ cm^{-3}, the level of compensation by a *p*-type impurity (oxygen or nickel) being 54%, the electron density is about $N_0 \approx 1.5 \times 10^{17}$ cm^{-3}. In a semiconductor with this electron density, with the lattice temperature $T = 4.2$ K, and with the electron temperature $T_e = 100$ K (in which case the electric fields are about $E \approx 50$–60 V/cm), the electron momentum relaxation rate is nearly $\nu \approx 3 \times 10^{11}$ s^{-1} [36] and the Langmuir frequency of the solid-state plasma electrons is approximately equal to $\Omega_p = \sqrt{4\pi e^2 N_0/\varepsilon_0 m^*} \approx 2.4 \times 10^{13}$ s^{-1}, where $\varepsilon_0 = 12.53$ and $m^* = 0.067 m_0$. Hence, we have $\Omega_p \approx 2.4 \times 10^{13}$ s$^{-1} \gg \nu \approx 3 \times 10^{11}$ s^{-1}.

We integrate the equation of motion of the semiconductor-plasma electrons in set (1) to obtain the energy conservation law

$$\frac{m^*(u - v_{\rm ph})^2}{2} - e\varphi + W_d = \frac{m^* v_{\rm ph}^2}{2} - e\varphi_0 + W_{d0}, \quad (10)$$

where $W_d = \nu m^* \int u d\xi$ is the energy of the dissipative losses associated with the electron–dipole scattering of the electrons and $\varphi_0 = \varphi(u = 0)$ is the same as in dependence (8). Formula (10) yields the following form of the dependence $u(\varphi)$:

$$u - v_{\rm ph} = -\sqrt{v_{\rm ph}^2 + 2\frac{e}{m^*}(\varphi - \varphi_0) + \frac{2}{m^*}(W_{d0} - W_d)}. \quad (11)$$

Here, the minus sign in front of the square-root sign is chosen because N and N_0 should be of the same sign.

Following [15], we consider the case in which the kinetic energy of the semiconductor-plasma electrons in a moving frame of reference associated with the wave is much higher than their potential energy in the wave field; i.e.,

$$\frac{m^*(u - v_{\rm ph})^2}{2} \approx \frac{m^* v_{\rm ph}^2}{2} \gg e(\varphi - \varphi_0). \quad (12)$$

This condition enables us to introduce the small parameter

$$\delta_\varphi = \frac{e\varphi^*}{m_0 v_0^2} \ll 1, \quad (13)$$

where φ^* is a certain value of the wave potential. We expand the right-hand side of dependence (11) in powers of the small parameter δ_φ and switch to the dimensionless variables

$$\psi = \varphi/\varphi^*, \quad \eta = \frac{\Omega_p}{v_0}\xi. \quad (14)$$

As a result, we obtain

$$u = -v_{\rm ph}\left(\frac{v_0^2}{v_{\rm ph}^2}\frac{m_0}{m^*}\delta_\varphi(\psi - \psi_0) + \frac{1}{m^* v_{\rm ph}^2}\left(W_{d0} - \frac{\nu}{\Omega_p} m^* v_0 \int u d\eta\right)\right) + O(\delta_\varphi^2). \quad (15)$$

Here, we assume that the dissipative correction is much smaller than $O(\delta_\varphi)$ but much larger than $O(\delta_\varphi^2)$. Applying the method of successive approximations, we find

$$u = -v_{\rm ph}\left(\frac{1}{\beta_{\rm ph}^2}\frac{m_0}{m^*}\delta_\varphi(\psi - \psi_0) + \frac{\nu}{\Omega_p}\delta_\varphi\frac{1}{\beta_{\rm ph}^3}\frac{m_0}{m^*} \times \int(\psi - \psi_0)d\eta + \frac{W_{d0}}{m^* v_{\rm ph}^2}\right) + O\left(\delta_\varphi^2, \delta_\varphi\frac{\nu^2}{\Omega_p^2}\right), \quad (16)$$

where

$$\delta_\varphi \ll \frac{\nu}{\Omega_p} \ll 1, \quad \beta_{\rm ph} = \frac{v_{\rm ph}}{v_0}. \quad (17)$$

To be specific, we set

$$\delta_\varphi = (1 - \beta_{\rm ph}^2) \ll 1. \quad (18)$$

Inserting expression (16) into solution (6) gives

$$N = N_0\left(1 - \frac{1}{\beta_{\rm ph}^2}\frac{m_0}{m^*}\delta_\varphi(\psi - \psi_0) - \frac{\nu}{\Omega_p}\delta_\varphi\frac{1}{\beta_{\rm ph}^3}\frac{m_0}{m^*} \times \int(\psi - \psi_0)d\eta - \frac{W_{d0}}{m^* v_{\rm ph}^2}\right) + O\left(\delta_\varphi^2, \delta_\varphi\frac{\nu^2}{\Omega_p^2}\right). \quad (19)$$

We substitute expressions (9) and (19) into Poisson's equation in set (4) and pass over to the dimensionless variables (14) to arrive at

$$\frac{\partial^2\psi}{\partial\eta^2} = \frac{1}{\delta_\varphi}\frac{n_0}{N_0}\frac{m^*}{m_0}\left(\frac{1}{\sqrt{1 + 2(\psi - \psi_0)}} - 1\right) - \frac{1}{\beta_{\rm ph}^2}(\psi - \psi_0) - \frac{\nu}{\Omega_p}\frac{1}{\beta_{\rm ph}^3}\int(\psi - \psi_0)d\eta - \frac{1}{\delta_\varphi}\frac{W_{d0}}{m_0 v_{\rm ph}^2} + O\left(\delta_\varphi\frac{m_0}{m^*}, \frac{\nu^2}{\Omega_p^2}\right). \quad (20)$$

Then, we differentiate Eq. (20) with respect to the dimensionless variable η and obtain

$$\frac{\partial^3\psi}{\partial\eta^3} + \frac{1}{\beta_{ph}^2}\frac{\partial\psi}{\partial\eta} + \delta_\nu\frac{1}{\beta_{ph}^3}(\psi-\psi_0) = -\delta_n\frac{1}{[1+2(\psi-\psi_0)]^{3/2}}\frac{\partial\psi}{\partial\eta} + O\left(\delta_\varphi\frac{m_0}{m^*}, \delta_\nu^2\right), \quad (21)$$

where

$$\delta_\nu = \frac{\nu}{\Omega_p}, \quad \delta_n = \frac{1}{\delta_\varphi}\frac{n_0}{N_0}\frac{m^*}{m_0}. \quad (22)$$

The initial conditions for Eq. (21) can be formulated as

$$\psi(0) = \psi_0, \quad \left.\frac{\partial\psi}{\partial\eta}\right|_{\eta=0} = \left(\frac{\partial\psi}{\partial\eta}\right)_0. \quad (23)$$

For the above parameters of the semiconductor plasma and of the wave field at $n_0 \approx 6\times10^{10}$ cm^{-3} and $\delta_\varphi \approx 1.3\times10^{-5}$ ($\beta_{ph} \approx 0.996$), we have

$$\delta_\nu \approx 0.012, \quad \delta_n \approx 2\times10^{-3}, \quad \delta_\varphi\frac{m_0}{m^*} \approx 2\times10^{-4}, \quad \delta_\nu^2 \approx 1.45\times10^{-4} \quad (24)$$

or

$$\frac{\delta_\nu}{\delta_n} \approx 6, \quad \frac{\delta_n}{(\delta_\varphi m_0/m^*)} \approx 10, \quad \frac{\delta_n}{\delta_\nu^2} \approx 14. \quad (25)$$

In accordance with relationships (25), the beam term in Eq. (21) is formally small, so that it can be regarded as a small correction and may be evaluated by successive approximations. As a result, the solution to Eq. (21) with zero on the right-hand side has the form

$$\psi^{(0)}(\eta) = C_1e^{\gamma\eta}\cos(\omega\eta) + C_2e^{\gamma\eta}\sin(\omega\eta) + C_3e^{-2\gamma\eta}, \quad (26)$$

where C_1, C_2, and C_3 are the constants of integration and

$$\gamma = \frac{1}{2\beta_{ph}}\left[\left(\frac{\delta_\nu}{2} - \sqrt{\frac{1}{27}+\frac{\delta_\nu^2}{4}}\right)^{1/3} + \left(\frac{\delta_\nu}{2} + \sqrt{\frac{1}{27}+\frac{\delta_\nu^2}{4}}\right)^{1/3}\right] > 0, \quad (27)$$

$$\omega = \frac{\sqrt{3}}{2\beta_{ph}}\left[\left(\frac{\delta_\nu}{2} + \sqrt{\frac{1}{27}+\frac{\delta_\nu^2}{4}}\right)^{1/3} - \left(\frac{\delta_\nu}{2} - \sqrt{\frac{1}{27}+\frac{\delta_\nu^2}{4}}\right)^{1/3}\right]. \quad (28)$$

Physical considerations dictate the choice $C_3 = 0$. In expressions (27) and (28), we are interested only in real roots, i.e., $\gamma, \omega \in R$. We insert solution (26) into the right-hand side of Eq. (21) and obtain the solution [37]

$$\psi(\eta) = \psi_0 + C_1e^{\gamma\eta}\cos(\omega\eta) + C_2e^{\gamma\eta}\sin(\omega\eta) - \delta_n\psi_b(\eta), \quad (29)$$

where

$$\psi_b(\eta) = \mathrm{Re}\left\{\sum_{\lambda=1}^{3}\frac{e^{s_\lambda\eta}}{2s_\lambda^2+1/\beta_{ph}^2}\int_{\eta^*}^{\eta} f(\tilde\eta)e^{-s_\lambda\tilde\eta}d\tilde\eta\right\}, \quad (30)$$

$$s_1 = -2\gamma, \quad s_2 = \gamma + i\omega, \quad s_3 = \gamma - i\omega, \quad (31)$$

$$f(\tilde\eta) = e^{\gamma\tilde\eta}\frac{(\gamma C_1+\omega C_2)\cos(\omega\tilde\eta) - (\omega C_1 - \gamma C_2)\sin(\omega\tilde\eta)}{\{1+2[C_1\cos(\omega\tilde\eta)+C_2\sin(\omega\tilde\eta)]e^{\gamma\tilde\eta}\}^{3/2}}. \quad (32)$$

In solution (29), the constants of integration C_1 and C_2, which should satisfy the initial conditions (23), can be found numerically by taking into account the fact that the quantity $(\partial\psi/\partial\eta)_0$ is related to them by

$$\left(\frac{\partial\psi}{\partial\eta}\right)_0 = C_1\gamma + \omega C_2 - \delta_n\,\mathrm{Re}\sum_{\lambda=1}^{3}\left\{\frac{C_1\gamma+\omega C_2}{(1+2C_1)^{3/2}(2s_\lambda^2+1/\beta_{ph}^2)} + \frac{s_\lambda}{2s_\lambda^2+1/\beta_{ph}^2}\int_{\eta^*}^{0} f(\tilde\eta)e^{-s_\lambda\tilde\eta}d\tilde\eta\right\}. \quad (33)$$

Figure 1 shows the numerical solution $\psi_b(\eta)$ obtained for $\eta^* = -30$, $C_1 \approx -0.01$, $C_2 \approx (\partial\psi/\partial\eta)_0 \approx 0.14$, $\gamma \approx 6\times10^{-6}$, and $\omega \approx 1$. The quantity η^* corresponds to the time at which the oscillations are completely damped. From Fig. 1, we can see that the oscillations of the wave potential are damped at a slow rate, because the ratio ν/Ω_p is small (i.e., the damping rate is low as compared to the frequency of the natural oscillations of the semiconductor plasma).

4. SOLUTION FOR THE WAVE POTENTIAL IN THE CASE $\Omega_p \ll \nu$

This case can be realized in an uncompensated semiconductor with an impurity concentration of about $N_i \approx N_0 \sim 10^{14}$ cm^{-3} at $T \approx T_e = 300$ K, the electric fields being about $E \approx 15$ V/cm. Under these conditions, the electron momentum will relax due primarily to collisions with polar optical phonons [38] with frequencies of $\nu \approx 3.5\times10^{12}$ s^{-1}, the electron Langmuir frequency being about $\Omega_p \approx 6\times10^{11}$ s^{-1}. Of course, in the case $\Omega_p \ll \nu$, it is only possible to speak of an unnatural wave in the beam–semiconductor-plasma system under consideration.

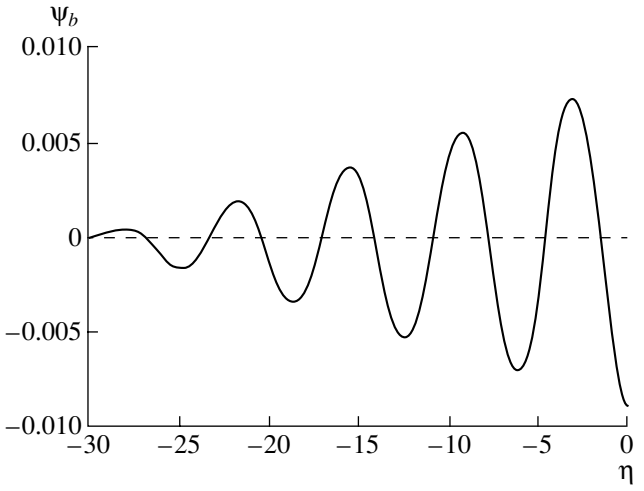

Fig. 1. Solution $\psi_b(\eta)$ for $\nu \ll \Omega_p$.

For $\nu \gg \Omega_p$, the equation of motion in set (4), specifically, the equation of motion of the conduction electrons in the semiconductor, has the solution

$$u \approx \mu \frac{\partial \varphi}{\partial \xi}, \tag{34}$$

where $\mu = e/m^*\nu$ is the mobility of the semiconductor-plasma electrons. Note that solution (34), which implies a linear dependence of the velocity of these electrons on the electric field, is valid only for weak electric fields, in which we are interested here. In the dimensionless variables (14), Poisson's equation has the form

$$\frac{\partial^2 \psi}{\partial \eta^2} = \delta_n \left(\frac{1}{\sqrt{1 + 2(\psi - \psi_0)}} - 1 \right) + \delta_\nu \frac{\partial \psi}{\partial \eta} + O\left(\frac{m_0}{m^*} \delta_\varphi \delta_\nu^2 \right), \tag{35}$$

where $\delta_\nu = \Omega_p/\nu$ and the quantities δ_n and δ_φ are the same as those in the case $\nu \ll \Omega_p$.

Investigating Eq. (35) by the phase-plane method [39] yields the singular point $P(\psi_0, \partial\psi/\partial\eta = 0)$. For $\delta_\nu^2 - 4\delta_n > 0$, the singular point $P(\psi_0, 0)$ is an unstable node, and, for $\delta_\nu^2 - 4\delta_n < 0$, it is an unstable focal point. This indicates that, in both cases, the image point in the phase plane approaches an equilibrium state as $\eta \longrightarrow -\infty$. From the condition $\delta_\nu^2 - 4\delta_n = 0$, we can obtain the following expression for the critical density n_{cr} of the beam electrons:

$$n_{cr} = \frac{\pi e^2}{\beta_{ph}^2 \varepsilon_0 \nu^2} \frac{m_0}{m^{*2}} (1 - \beta_{ph})^2 N_0^2. \tag{36}$$

For the above parameters of the semiconductor, we have $n_{cr} \approx 2.4 \times 10^8$ cm^{-3} ($\beta_{ph} \approx 0.996$). For $n < n_{cr}$ (or, equivalently, $\delta_\nu^2 - 4\delta_n > 0$), the dependence $\psi(\eta)$ is purely aperiodic (the oscillations are absent), and, for $n > n_{cr}$ (or $\delta_\nu^2 - 4\delta_n < 0$), the dependence $\psi(\eta)$ corresponds to exponentially damped oscillations.

In the vicinity of the equilibrium state $P(\psi_0, 0)$, the solutions for the wave potential and its derivative have the form

$$\psi - \psi_0 \propto \mathrm{Re}\{\exp(\lambda_{1,2}\eta)\},$$
$$\frac{\partial \psi}{\partial \eta} \propto \mathrm{Re}\{\lambda_{1,2}\exp(\lambda_{1,2}\eta)\}, \tag{37}$$
$$\lambda_{1,2} = \frac{\delta_\nu \pm \sqrt{\delta_\nu^2 - 4\delta_n}}{2}.$$

The functions $\psi(\eta)$ and $\partial\psi(\eta)/\partial\eta$ calculated for the initial conditions $\psi(0) = 0.5$ and $(\partial\psi(\eta)/\partial\eta)_0 \approx 0.15$ at $n = 10^8$ cm$^{-3} < n_{cr}$ ($\delta_n \approx 3.3 \times 10^{-3}$, $\delta_\nu \approx 0.18$) are shown in Figs. 2 and 3, respectively. The same functions calculated for the same initial conditions but at $n = 10^{11}$ cm$^{-3} > n_{cr}$ ($\delta_n \approx 3.3$, $\delta_\nu \approx 0.18$) are shown in Figs. 4 and 5, respectively. From Figs. 3 and 5, one can see that, at $n < n_{cr}$, the dependence $\partial\psi(\eta)/\partial\eta$ resembles a nonoscillating trailing edge of a shock wave, while, at $n > n_{cr}$, it has the form of an oscillating trailing edge of a shock wave.

5. DISCUSSION OF THE BASIC ASSUMPTIONS

Here, we return to the question of the applicability of the basic assumptions made during derivation of Eqs. (1). For $\nu \ll \Omega_p$, the damping rate of the wave potential is fairly small, $\gamma \approx 6 \times 10^{-6} \ll 1$. This indicates that the approximation $\nu = \text{const}$ is valid only in the range in which the amplitude of the wave potential changes insignificantly. Obviously, this is the range in which $|\eta| \sim \gamma^{-1} \sim 10^5$. Thus, the solution for the wave potential that was obtained above in the approximation $\nu = \text{const}$ is valid over a fairly wide range of η values.

For $\nu \gg \Omega_p$, the energy acquired by the semiconductor-plasma electrons in a wave field with a strength of $E \propto 15$ V/cm is about $\theta_f \approx (e/\nu)\mu E^2$, which is much lower than their thermal energy $\theta_f/k_B T \approx 10^{-6}$ (for $T = 300$ K). Consequently, the dependence of the electron momentum relaxation rate on the wave field can be neglected.

The condition for the gradient term in the equation of motion of the semiconductor-plasma electrons to be smaller than the collision term has the form

$$|\nu(|E|)u| \gg \left| \frac{v_T^2}{N} \frac{\partial N}{\partial x} \right| = \left| v_T^2 \frac{\partial \ln(N/N_0)}{\partial x} \right|. \tag{38}$$

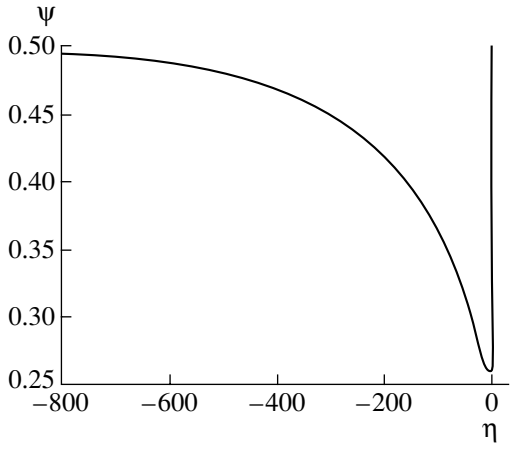

Fig. 2. Solution $\psi(\eta)$ for $\nu \gg \Omega_p$ at $n < n_{cr}$.

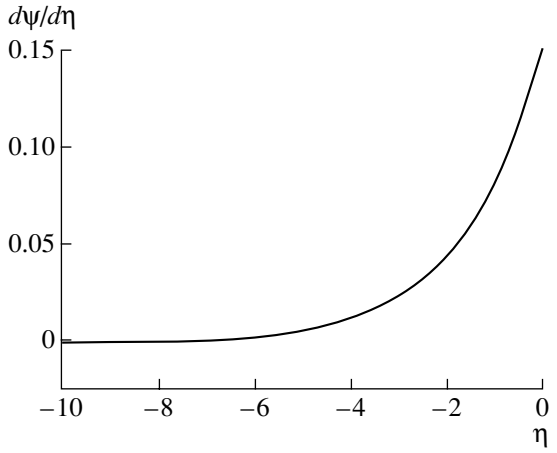

Fig. 3. Solution $\partial\psi(\eta)/\partial\eta$ for $\nu \gg \Omega_p$ at $n < n_{cr}$.

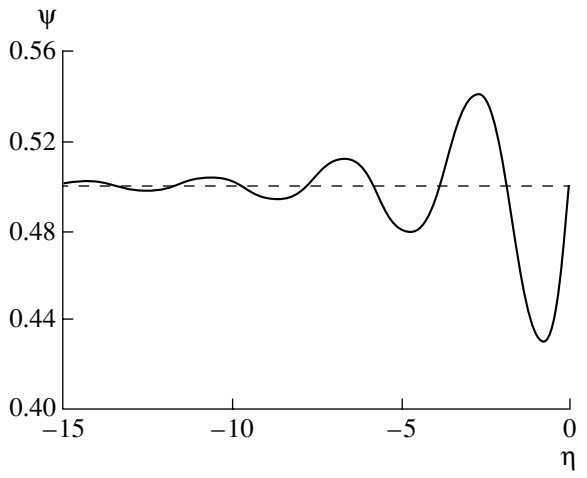

Fig. 4. Solution $\psi(\eta)$ for $\nu \gg \Omega_p$ at $n > n_{cr}$.

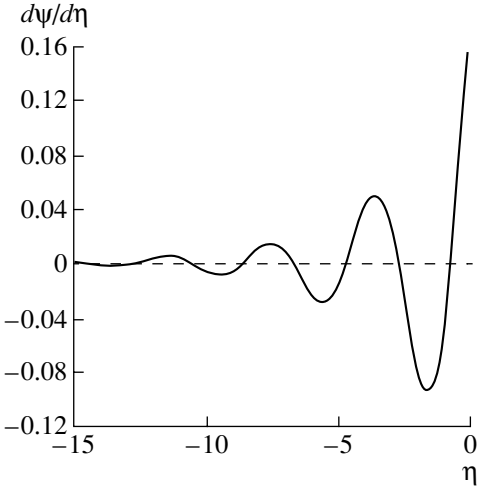

Fig. 5. Solution $\partial\psi(\eta)/\partial\eta$ for $\nu \gg \Omega_p$ at $n > n_{cr}$.

Using solution (6) and taking into account the relationship $|u/v_{ph}| \ll 1$, we find

$$\left|\frac{1}{\nu}\frac{v_T^2}{v_{ph}^2}\frac{\partial u}{\partial x}\right| \ll 1. \quad (39)$$

Estimating the drift velocity u as $u \sim \mu E$, we can rewrite inequality (39) in the form

$$\left|\frac{v_T^2}{v_{ph}^2}\frac{\mu}{\nu}\frac{\partial E}{\partial x}\right| \ll 1. \quad (40)$$

Taking into account the consequence of Poisson's equation, specifically, $\max\left|\frac{\partial E}{\partial x}\right| \approx \frac{4\pi e}{\varepsilon_0} N_0$, we finally obtain

$$\left|\frac{v_T^2}{v_{ph}^2}\frac{\mu}{\nu}\frac{\partial E}{\partial x}\right| \le \kappa = \left(\frac{v_T}{v_{ph}}\right)^2\left(\frac{\Omega_p}{\nu}\right)^2 \ll 1. \quad (41)$$

For the above parameters of the semiconductor and for $v_{ph} \approx 0.1c$ ($v_{ph} \approx 2.99 \times 10^9$ cm/s), we have $\kappa \sim 0.01$ for $\nu \ll \Omega_p$ and $\kappa \sim 10^{-6}$ for $\nu \gg \Omega_p$. Hence, we can also neglect the gradient term in the equation of motion of the semiconductor-plasma electrons in set (1).

6. CONCLUSION

The problem of the nonlinear oscillations of a semiconductor plasma with a monoenergetic low-density electron beam has been investigated in the hydrodynamic approximation. We have considered two qualitatively different cases: the first one in which the electron Langmuir frequency Ω_p in a semiconductor plasma is much higher than the electron momentum relaxation rate ν, $\Omega_p \gg \nu$, and the second one in which $\Omega_p \ll \nu$. We have shown that the case $\Omega_p \gg \nu$ can be realized in a heavily doped, partially compensated GaAs semiconductor at liquid helium temperatures in moderately

strong electric fields. In such a semiconductor, the momentum of the electrons relaxes due to their scattering by the screened dipoles, whose role is played by donor–acceptor complexes. For this case, the self-similar solution for the wave potential has been derived using perturbation theory. The case $\Omega_p \ll \nu$ can be realized in a lightly doped GaAs semiconductor in weak electric fields at room temperature. Numerical investigations of this case by using the phase-plane methods show that, in weak wave fields, the electric field distribution in the beam correspond to that in a shock wave.

ACKNOWLEDGMENTS

We are grateful to V.I. Karas' and A.A. Rukhadze for discussion of the results and useful remarks.

REFERENCES

1. A. I. Akhiezer and G. Ya. Lyubarskiĭ, Dokl. Akad. Nauk SSSR **80**, 193 (1951).
2. A. I. Akhiezer and R. V. Polovin, Dokl. Akad. Nauk SSSR **102**, 919 (1955).
3. A. I. Akhiezer and R. V. Polovin, Zh. Éksp. Teor. Fiz. **30**, 915 (1956) [Sov. Phys. JETP **3**, 696 (1956)].
4. J. M. Dawson, Phys. Rev. **113**, 383 (1959).
5. V. N. Tsytovich, Dokl. Akad. Nauk SSSR **142**, 63 (1962) [Sov. Phys. Dokl. **7**, 31 (1962)].
6. Ya. B. Faĭnberg and V. D. Shapiro, Zh. Éksp. Teor. Fiz. **47**, 1389 (1964) [Sov. Phys. JETP **20**, 937 (1964)].
7. Ya. B. Faĭnberg and V. D. Shapiro, *Plasma Physics and Problems of Controlled Nuclear Fusion* (Naukova Dumka, Kiev, 1965), p. 92.
8. R. K. Mazitov, Prikl. Mekh. Tekh. Fiz., No. 1, 27 (1965).
9. T. O'Neil, Phys. Fluids **8**, 2255 (1965).
10. Ya. B. Fainberg, Czech. J. Phys., Sect. B **18**, 652 (1968).
11. Ya. B. Faĭnberg, V. D. Shapiro, and V. I. Shevchenko, Zh. Éksp. Teor. Fiz. **57**, 966 (1969) [Sov. Phys. JETP **30**, 528 (1970)].
12. V. I. Kurilko, Zh. Éksp. Teor. Fiz. **57**, 885 (1969) [Sov. Phys. JETP **30**, 484 (1970)].
13. L. I. Rudakov, Zh. Éksp. Teor. Fiz. **59**, 2091 (1970) [Sov. Phys. JETP **32**, 1134 (1971)].
14. W. E. Drummond, J. H. Malmberg, T. M. O'Neil, and J. R. Thompson, Phys. Fluids **13**, 2422 (1970).
15. R. I. Kovtun and A. A. Rukhadze, Zh. Éksp. Teor. Fiz. **58**, 1709 (1970) [Sov. Phys. JETP **31**, 915 (1970)].
16. B. N. Breĭzman and D. D. Ryutov, Zh. Éksp. Teor. Fiz. **60**, 408 (1971) [Sov. Phys. JETP **33**, 220 (1971)].
17. M. V. Kuzelev and A. A. Rukhadze, *Electrodynamics of Dense Electron Beams in a Plasma* (Nauka, Moscow, 1990).
18. A. K. Berezin, Ya. B. Faĭnberg, L. I. Bolotin, *et al.*, Zh. Éksp. Teor. Fiz. **63**, 861 (1972) [Sov. Phys. JETP **36**, 453 (1973)].
19. A. M. Gladkiĭ, V. P. Kovalenko, and P. N. Yushmanov, Pis'ma Zh. Éksp. Teor. Fiz. **24**, 533 (1976) [JETP Lett. **24**, 491 (1976)].
20. V. P. Kovalenko and P. N. Yushmanov, Fiz. Plazmy **3**, 1284 (1977) [Sov. J. Plasma Phys. **3**, 714 (1977)].
21. A. Ts. Amatuni, M. R. Magomedov, E. V. Sekhposyan, and S. S. Elbakyan, Fiz. Plazmy **5**, 85 (1979) [Sov. J. Plasma Phys. **5**, 49 (1979)].
22. A. Ts. Amatuni, E. V. Sekhposyan, and S. S. Elbakyan, Fiz. Plazmy **12**, 1145 (1986) [Sov. J. Plasma Phys. **12**, 662 (1986)].
23. V. P. Kovalenko, Usp. Fiz. Nauk **139**, 223 (1983) [Sov. Phys. Usp. **26**, 116 (1983)].
24. Ya. B. Faĭnberg, Fiz. Plazmy **26**, 362 (2000) [Plasma Phys. Rep. **26**, 335 (2000)].
25. Ya. B. Faĭnberg, V. D. Shapiro, and V. I. Shevchenko, Pis'ma Zh. Éksp. Teor. Fiz. **11**, 410 (1970) [JETP Lett. **11**, 277 (1970)].
26. Ya. B. Faĭnberg, V. D. Shapiro, and V. I. Shevchenko, Zh. Éksp. Teor. Fiz. **61**, 198 (1971) [Sov. Phys. JETP **34**, 103 (1971)].
27. A. A. Ivanov, V. V. Parail, and T. K. Soboleva, Zh. Éksp. Teor. Fiz. **63**, 1678 (1972) [Sov. Phys. JETP **36**, 887 (1972)].
28. K. Jungwirth and L. Krlin, Plasma Phys. **17**, 861 (1975).
29. D. Winske and E. A. Jackson, Phys. Fluids **18**, 389 (1975).
30. B. W. Knight and G. A. Peterson, Phys. Rev. **155**, 393 (1967).
31. A. F. Volkov and Sh. M. Kogan, Usp. Fiz. Nauk **96**, 633 (1968) [Sov. Phys. Usp. **11**, 881 (1968)].
32. F. G. Bass and S. I. Khankina, Fiz. Tekh. Poluprovodn. (Leningrad) **18**, 353 (1984) [Sov. Phys. Semicond. **18**, 220 (1984)].
33. A. I. Borodkin, V. M. Yakovenko, G. Ya. Levin, and Yu. V. Maĭstrenko, Fiz. Tverd. Tela (Leningrad) **12**, 1515 (1970) [Sov. Phys. Solid State **12**, 1189 (1970)].
34. E. A. Kornilov, S. A. Nekrashevich, Ya. B. Faĭnberg, and N. A. Shokhovtsov, Pis'ma Zh. Éksp. Teor. Fiz. **11**, 284 (1970) [JETP Lett. **11**, 185 (1970)].
35. I. D. Voronova, Tr. Fiz. Inst. Akad. Nauk SSSR **89**, 3 (1976).
36. A. G. Samoĭlovich and M. V. Nitsovich, Fiz. Tverd. Tela (Leningrad) **5**, 2981 (1963) [Sov. Phys. Solid State **5**, 2182 (1964)].
37. E. Kamke, *Differentialgleichungen. Lösungsmethoden und Lösungen*, Bd. I: *Gewöhnliche Differentialgleichungen* (Geest and Portig, Leipzig, 1959; Fizmatgiz, Moscow, 1961).
38. E. M. Conwell, *High Field Transport in Semiconductors* (Academic, New York, 1967; Mir, Moscow, 1970).
39. A. A. Andronov, A. A. Vitt, and S. É. Khaĭkin, *Theory of Oscillations* (Fizmatgiz, Moscow, 1959), p. 916.

Translated by O. E. Khadin

Plasma Physics Reports, Vol. 28, No. 5, 2002, pp. 411–422. Translated from Fizika Plazmy, Vol. 28, No. 5, 2002, pp. 451–461.

NONLINEAR PHENOMENA

Coalescence Instability in the Electron Magnetohydrodynamics

V. P. Zhukov

Institute of Computational Technologies, Siberian Division, Russian Academy of Sciences, pr. Akademika Lavrent'eva 6, Novosibirsk, 630090 Russia

Received July 17, 2001; in final form, September 20, 2001

Abstract—The relaxation of a magnetic field perturbation periodic in two directions is studied in the electron magnetohydrodynamic approximation. It is shown that the relaxation is accompanied by the coalescence of magnetic cells. When transport coefficients are sufficiently low, the nonlinear stage of the coalescence process is independent of their values. This effect may help to explain why the duration of the crash phase of sawtooth oscillations in tokamaks is anomalously short. © *2002 MAIK "Nauka/Interperiodica".*

1. INTRODUCTION

Some processes in hot plasma cannot be described in terms of the one-fluid MHD theory. Thus, in terms of the one-fluid MHD model, the duration of the crash phase of sawtooth oscillations in tokamaks is anomalously short [1, 2]. There is, as yet, no final explanation for this disagreement with experiment.

Such problems are likely to be overcome by describing the electron dynamics more completely. MHD models capable of taking into account the effects associated with electron dynamics have been analyzed in many papers (see, e.g., [3, 4]). One of these models is the electron MHD (EMHD) model, in which the ions are treated as an immobile background and the electrons are described in hydrodynamic approximation [5]. The EMHD equations are applicable to flows with a characteristic dimension smaller than the ion dispersion length δ_i defined by $\delta_i^2 = \dfrac{m_i c^2}{4\pi Z^2 e^2 n_i}$ and with a frequency higher than the ion cyclotron frequency ω_{ci}. When electron inertia is neglected, the highest possible frequency of the flows is also restricted: it should not exceed the electron cyclotron frequency.

In this paper, the two-dimensional problem of the relaxation (reconnection) of a magnetic field periodic in two directions is studied both analytically and numerically in the EMHD approximation.

The reconnection problem in EMHD theory was considered in [6–11]. In those papers, the initial distribution of the poloidal magnetic field corresponded either to a neutral sheet or to a chain of magnetic islands stretched along the sheet. In the case of a neutral sheet, the distribution of the toroidal magnetic field depended on the same coordinate as the poloidal magnetic field (a one-dimensional magnetic configuration). In the case of a chain of magnetic islands, the toroidal magnetic field was constant. In [6–11], the stability of such one-dimensional configurations against linear perturbations was investigated analytically under the assumption that the perturbation is completely damped far from the neutral sheet. For the purposes of this article, the most important of the results obtained in [6–11] is the conclusion that, in the case of inertialess electrons in a dissipationless plasma, the initial magnetic configuration with a neutral sheet is linearly stable, while the initial configuration with a chain of magnetic islands is linearly unstable. Moreover, the stronger the magnetic field component associated with the islands, the faster the instability growth rate.

Here, the formulation of the problem is somewhat different from that used in [6–11]. The initial equilibrium distribution of the poloidal and toroidal magnetic fields is a chessboardlike set of square cells (islands) periodic in two directions. As will be shown below, the dynamics of the process under consideration is highly sensitive to the relationship between the amplitudes of the poloidal and toroidal magnetic fields. In particular, in the absence of dissipation, the initial configuration in which the toroidal magnetic field is sufficiently strong in comparison with the poloidal field is linearly stable. An equilibrium-breaking perturbation of the magnetic field is also assumed to be periodic in two directions, the period of the perturbation being an exact multiple of the period of the initial magnetic field.

Another point in which this paper differs from [6–11] is that the nonlinear stage of the instability is investigated quite thoroughly. The evolution of the magnetic configuration is traced completely, starting with the initial unstable equilibrium and ending at the final stable equilibrium, by solving the EMHD equations numerically. The results of a numerical solution of the EMHD equations are also used to determine some of the analytic dependences characterizing this evolutionary process.

1063-780X/02/2805-0411$22.00 © 2002 MAIK "Nauka/Interperiodica"

In the present paper, the problem is formulated in a way similar to that in [12]. The only difference is that Germaschewski and Grauer [12] used reduced MHD (RMHD) equations. However, the RMHD model is incapable of taking into account the toroidal magnetic field. The RMHD and EMHD models both imply that the magnetic field configuration in question is unstable against the coalescence of magnetic cells, but they give substantially different dynamic pictures of the coalescence process.

The most interesting of the results obtained in the present paper is the following. In the nonlinear stage of the coalescence of magnetic cells, the behavior of the system on scales on which most of the magnetic energy is accumulated is independent of (or, at least, depends only slightly on) the transport coefficients, provided that the coefficients are sufficiently small. In particular, for vanishing plasma resistivity and vanishing electron plasma viscosity, the coalescence lasts for a finite time. In the RMHD model [12], this time is proportional to the square root of the electrical conductivity of a plasma. The above considerations may help to explain why the duration of the crash phase of sawtooth oscillations in tokamaks is anomalously short. The tearing instability that develops in a highly conducting plasma gives rise to neutral current sheets, which are so thin that further evolution of the magnetic configuration is governed by the electron dynamics and, accordingly, is independent of the values of transport coefficients. In particular, this is true of the reconnection (crash) time.

2. MATHEMATICAL FORMULATION OF THE PROBLEM

Let the scale length of the problem be the size l of a magnetic cell, and let the characteristic poloidal magnetic field and the quantity $\omega_{ci}^{-1}\frac{l^2}{\delta_i^2}$ play the roles of the magnetic field scale and the time scale, respectively. Then, the two-dimensional ($\partial/\partial z = 0$) EMHD equations can be written as

$$\partial A/\partial t + \{H_z, A\} = \eta\Delta A - \nu\Delta^2 A, \quad (1)$$

$$\partial H_z/\partial t + \{A, \Delta A\} = \eta\Delta H_z - \nu\Delta^2 H_z, \quad (2)$$

where A is the z-component of the vector potential, H_z is the z-component of the magnetic field, η is the dimensionless plasma electrical conductivity, ν is the dimensionless electron plasma viscosity, and

$$\{f, g\} = \frac{\partial f}{\partial x}\frac{\partial g}{\partial y} - \frac{\partial f}{\partial y}\frac{\partial g}{\partial x}$$

is the Poisson bracket.

These equations have the following important property. For motions that occur in the magnetic field H_l on the scale length l, the ratio of the contributions from the nonlinearity and dissipation (the Reynolds number) is equal to $\mathrm{Re}_\nu = H_l l^2/\nu$ for a plasma with a zero conductivity and finite viscosity and to $\mathrm{Re}_\eta = H_l/\eta$ for a plasma with a zero viscosity and finite conductivity. Consequently, the Reynolds number Re_η is independent of l (a particularly important point).

The problem was solved with the initial conditions

$$A = \sin x \sin y, \quad (3)$$

$$H_z = H_0 \sin x \sin y, \quad (4)$$

in rectangular calculation region

$$0 < x < X_0 = 2\pi N, \quad 0 < y < Y_0 = 2\pi N.$$

Since the boundary conditions are periodic, N is an integer.

Below, we will show that conditions (3) and (4) correspond to an unstable equilibrium state. The motions are assumed to be driven by a small seed perturbation of the magnetic configuration satisfying these conditions. The particular shape of this perturbation is unimportant for further analysis.

Note that the coalescence of magnetic cells is favored energetically. In fact, the term $\{H_z, A\}$ in Eq. (1) can be rewritten as $(\mathbf{V}\cdot\nabla)A$, where $\mathbf{V} = (-\partial H_z/\partial y, \partial H_z/\partial x)$, so that Eq. (1) is a transport equation with dissipation. The maximum/minimum value of the solution to such an equation can only increase/decrease. Consequently, as the magnetic cells coalesce, the energy $E_p = \int_{x,}^{X_0,}\int_{y=0}^{Y_0}(\nabla A)^2\,dxdy$ of the poloidal magnetic field can only decrease, because of the increase in the cell sizes and, accordingly, the decrease in the gradients. The amplitude of the toroidal magnetic field and, accordingly, its energy can either increase or decrease during the coalescence. As will be shown below, for small amplitudes H_0, the coalescence of the cells is accompanied by a significant loss of the total energy. When the amplitude H_0 is large, the released fraction of the poloidal field energy is converted into the toroidal field energy, in which case the loss of the total energy is relatively small.

3. SMALL CALCULATION REGION ($X_0 = Y_0 = 2\pi$)

The results from a numerical solution of the problem as formulated show that the initial equilibrium state satisfying conditions (3) and (4) is unstable; moreover, the most unstable harmonics are those in which A and H_z are proportional to the linear combination of $\cos x$ and $\cos y$. A linear analysis (see Section 5) shows that, in a dissipationless plasma, these harmonics grow with the rate

$$\gamma^2 = \gamma_0^2 - \omega_0^2/2 \pm \sqrt{(\gamma_0^2 - \omega_0^2/2)^2 - \gamma_0^4}, \quad (5)$$

where $\gamma_0 = 1/2$ and $\omega_0 = H_0/2$.

For $H_0 < H_c = 2$, the real part of the growth rate, $\mathrm{Re}\gamma = (1/2)(1 - H_0^2/4)^{1/2}$, is positive, which indicates that there is an instability. For $H_0 > H_c$, the real part of γ vanishes, so that the equilibrium is stable. However, this stability is violated by dissipation.

When $H_0 < H_c$, the results obtained for the initial stage of the process by solving problem (1)–(4) numerically agree with the results of linear analysis. However, the same is not true for $H_0 > H_c$. According to linear analysis (see Section 5), the growth rate of the dissipative instability is proportional to η and ν. However, even when the harmonics $\cos x$ and $\cos y$ in the solution to problem (1)–(4) have very small amplitudes, the time scale on which they grow depends on η and ν in an irregular manner because of their nonlinear interaction with smaller scale harmonics. In the initial stage of the development of the perturbation, this interaction is weak but, at the same time, it is important because the growth rate of the dissipative instability at low η and ν is slow. Note that, for $H_0 > H_c$, the rate at which the harmonics $\cos x$ and $\cos y$ grow substantially decreases with increasing H_0. For a sufficiently large amplitude H_0, the instability does not have enough time to come into play before the initial harmonic $\sin x \sin y$ is completely damped by the conventional dissipation. The particular value of this amplitude H_0 depends on the dissipation coefficients and on the amplitude of the equilibrium-breaking perturbation. Hence, the toroidal magnetic field plays a stabilizing role.

When the harmonics $\cos x$ and $\cos y$ grow to a sufficiently large amplitude, the coalescence process becomes essentially nonlinear and proceeds at a much faster rate. An additional boundary forms in the vicinity of the adjacent corners of each pair of neighboring cells in which the magnetic field has the same sign. Then, these cells coalesce into a larger cell or into a strip. Figures 1 and 2 show the isolines of the amplitude A at different times. In order to provide a clearer insight into the coalescence process, the figures illustrate the results obtained with a calculation region whose sides are two times as long as those of the assumed region ($X_0 = Y_0 = 4\pi$). At the site of contact (reconnection) between the two cells, the plasma current becomes highly peaked (Fig. 3). Note that, in the same problem treated in the MHD approximation [12], the current density was found to evolve to a distribution characteristic of a sheet. Presumably, the appearance of the current peak instead of the current sheet is typical of the reconnection problems in which the freezing-in of the magnetic field into the plasma electrons (rather than ions) is important [13].

The nonlinear phase of the coalescence of the cells has the following important property. For sufficiently small dissipation coefficients η and ν, the behavior of the main harmonics $\cos x$, $\cos y$, and $\sin x \sin y$, which accumulate more than 80% of the total energy, is independent of the values of these coefficients and is governed by both the mutual nonlinear interaction among them and their nonlinear interaction with higher harmonics. In particular, this is also true of the time at which the cells coalesce. Instead of speaking of the limit $\eta \longrightarrow 0$ and $\nu \longrightarrow 0$, it is more correct to speak of the limits in which η can be zero and ν approaches an infinitely small (but nonzero) value. Moreover, the order in which these limits are taken is of fundamental importance: the case with $\nu = 0$ and with η smaller than a certain critical value η_c is singular: over a finite time interval, the peak current density becomes infinitely high and the peak itself becomes infinitely narrow. The critical value η_c is fairly large. Thus, for $H_0 = 0$, it is equal to 0.006. Singularities at finite plasma conductivity were also obtained by Valori *et al.* [13] in studying reconnection problems with allowance for the Hall effect. Note that, in one-fluid hydrodynamics, the plasma conductivity have a substantial impact on the scales of the main processes [12]. It should be emphasized that, in EMHD theory, the current density distribution is strongly sensitive to the values of the dissipation coefficients. The current peak evolves to a shape that ensures the dissipation of the energy flux dE/dt from large- to small-scale motions.

The singularity at $\nu = 0$ is closely associated with the fact that the Reynolds number Re_η is independent of the scale of the motion. At small η values, the energy flux from large- to small-scale motions is damped equally weakly on both large and small scales. That is why finite energy can be accumulated in the processes occurring on infinitely small scales, thereby giving rise to the singularity.

That large-scale motions are independent of ν at $\eta = 0$ is associated with the fact that, in EMHD theory, the Reynolds number Re_ν is proportional to the square of the scale, in contrast to MHD theory, in which it is linearly proportional to the scale. Consequently, in EMHD theory, it can be assumed that $\nu = 0$ on large scales.

In calculations, the smallest values of the transport coefficients were $\eta = 0$ and $\nu = 7 \times 10^{-5}$. It should be stressed that the conclusion about the independence of large-scale motions on transport coefficients was carefully checked by reducing the spacing of the numerical grid, on which the maximum number of mesh points was 300×300.

Let us consider the behavior of the energy characteristics of the process.

Figure 4 shows the time evolutions of the total energy $E_{\mathrm{tot}} = E_p + E_z$ and the energy E for different values of H_0. Here, $E_p = \int_{x,}^{X_0,} \int_{y=0}^{Y_0} (\nabla A)^2 \, dxdy$ is the energy of the poloidal magnetic field and $E_z = \int_{x,}^{X_0,} \int_{y=0}^{Y_0} H_z^2 \, dxdy$ is the energy of the toroidal magnetic field. By the energy E is meant the sum of the energy

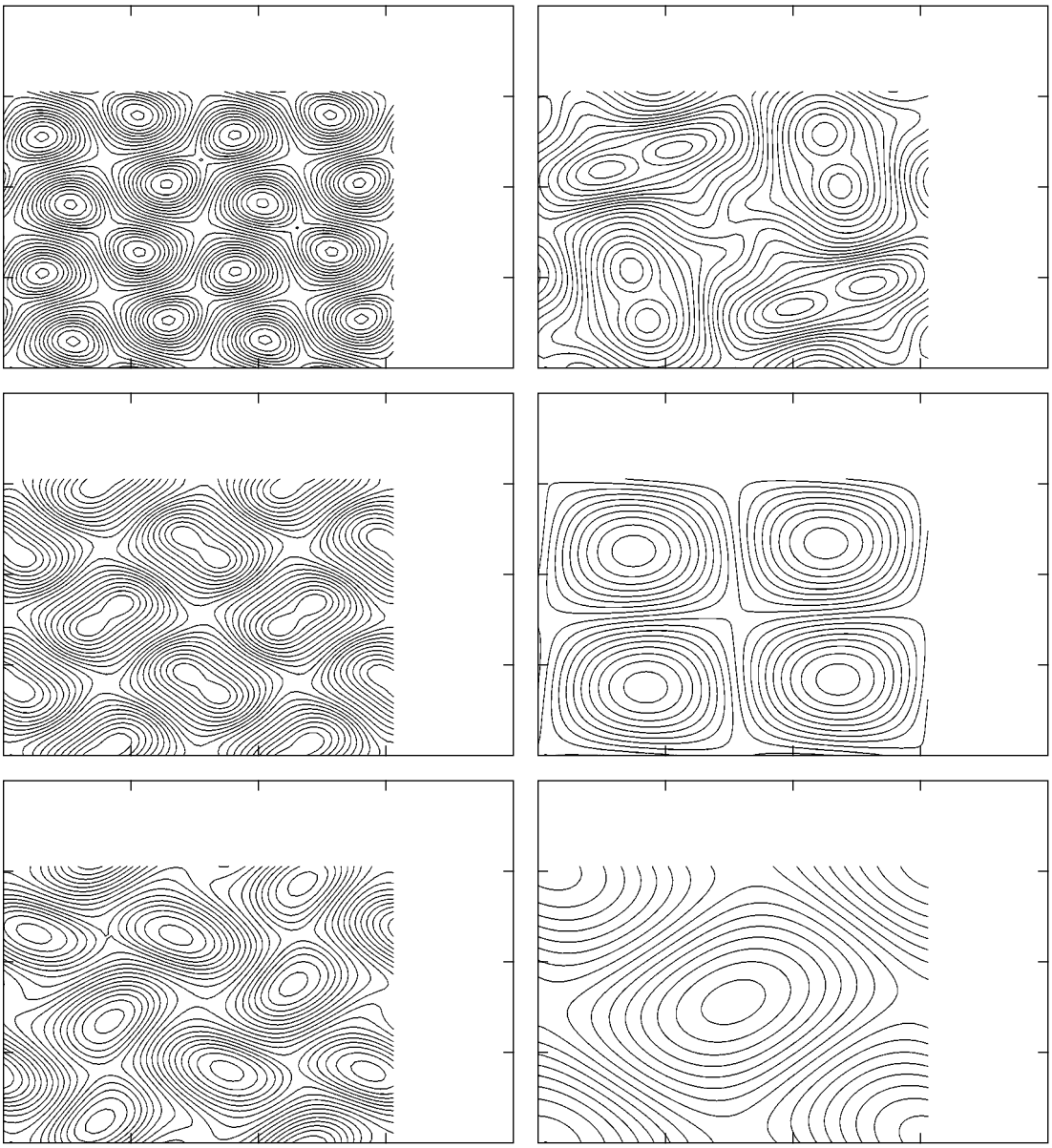

Fig. 1. Representative chain of events for the coalescence of magnetic cells (distribution of A). Shown are the events resulting in the formation of new magnetic cells. The sides of the calculation region are $X_0 = Y_0 = 4\pi$. In each column, the time increases from top to bottom, and the upper frame in the right column refers to a later time than the lower frame in the left column.

accumulated in the harmonics $\cos x$, $\cos y$, and $\sin x \sin y$ of the poloidal magnetic field and the energy accumulated in the harmonics $\cos x$ and $\cos y$ of the toroidal magnetic field. As will be shown in Section 5, the energy E plays an important role in the dynamics of the process under discussion. As may be seen in Fig. 4, the total energy decreases sharply during the nonlinear phase of the coalescence process; moreover, the larger the amplitude H_0, the smaller decrease in E_{tot}, provided that $H_0 \geq 1$. During this phase, the energy E decreases when $H_0 < 1$ and increases when $H_0 > 1$.

Also, during the coalescence process, the energy is redistributed between the toroidal and poloidal components of the magnetic field. Figure 5 shows the time evolution of the ratio E_z/E_p. At the initial instant, we have $E_z/E_p = H_0^2/2$. As a result of the coalescence of magnetic cells, this ratio increases; moreover, for $H_0 > 1$, it becomes larger than unity. Note also that, for $H_0 = 0$, the ratio E_z/E_p equals zero both before and after the coalescence; however, during the nonlinear stage of the coalescence process, the ratio E_z/E_p reaches values of order unity.

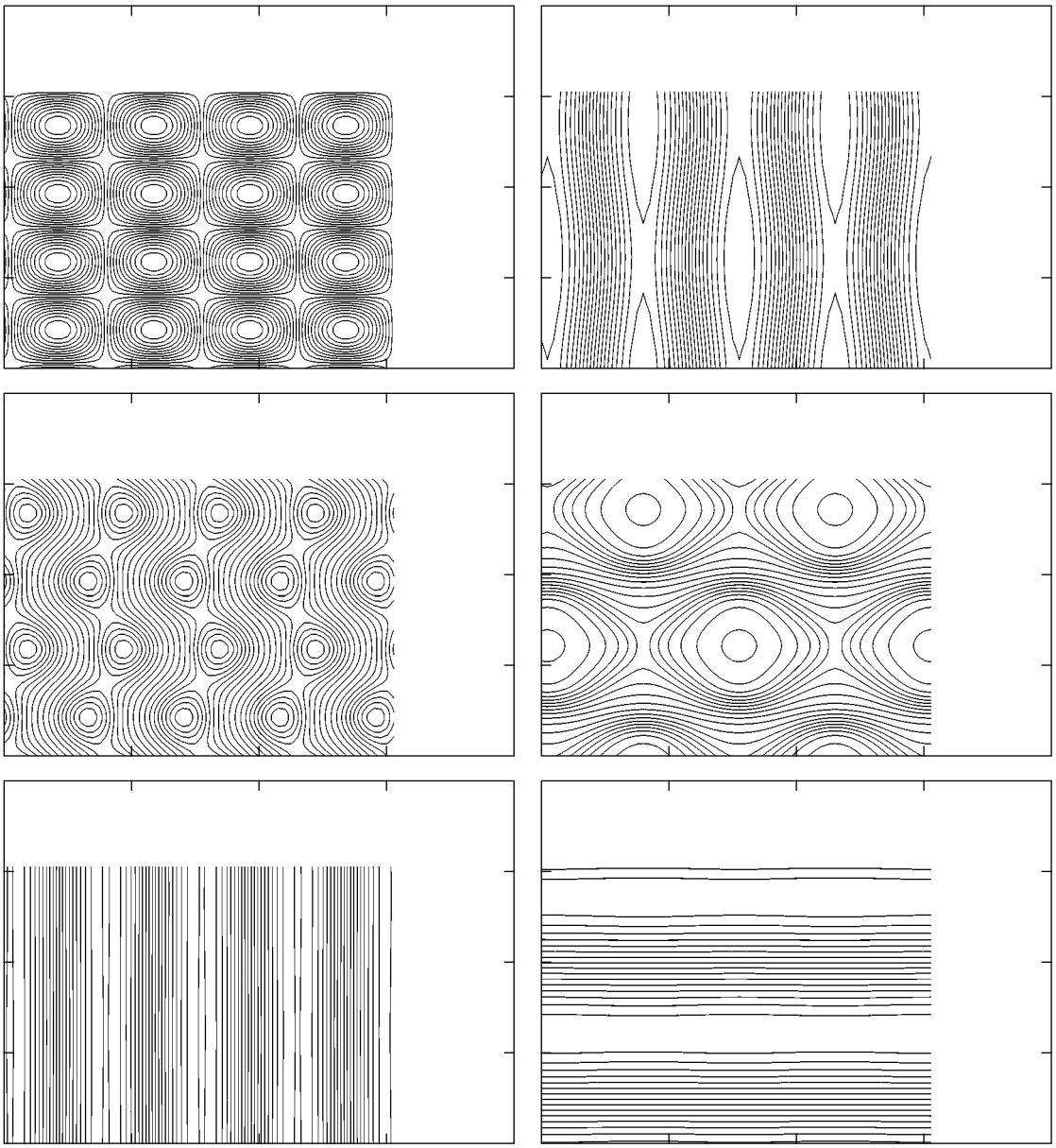

Fig. 2. Representative chain of reconnection events resulting in the formation of one-dimensional structures (strips). The sides of the calculation region are $X_0 = Y_0 = 4\pi$.

Figure 5 also shows the temporal behavior of the characteristic wavenumber defined by

$$\langle k \rangle = \left(\int_{x,\ y=0}^{X_0,\ Y_0} \int ((\nabla A)^2 + (\nabla H_z)^2) dx dy \Big/ \int_{x,\ y=0}^{X_0,\ Y_0} \int (A^2 + H_z^2) dx dy \right)^{1/2}.$$

At the initial instants, we have $k = \sqrt{2}$, which corresponds to the initial harmonic $\sin x \sin y$. After the coalescence, the harmonics $\cos x$ and $\cos y$ with the wavenumber $k = 1$ are dominant.

Note also that the coalescence dynamics differs between the cases $H_0 \ll 1$ and $H_0 \sim 1$. Figure 5 shows that, in the case of small H_0 values, the coalescence results in weakly damped oscillations. In the case $H_0 \sim 1$, the magnetic field is seen to relax to its final configuration almost immediately after the coalescence process has come to an end.

Most of the above features of the coalescence process may be clarified using the model with a small number of harmonics (see Section 5).

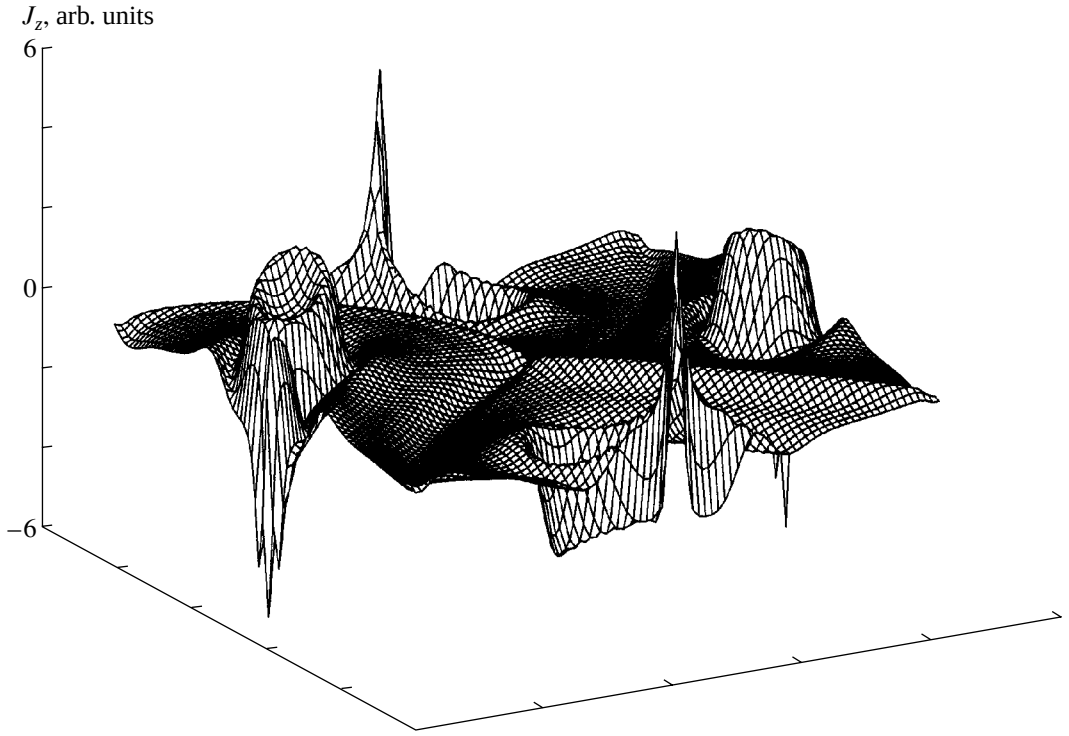

Fig. 3. Representative current density distribution in the nonlinear stage of the coalescence process. The sides of the calculation region are $X_0 = Y_0 = 2\pi$.

In a configuration that is established as a result of the coalescence of magnetic cells, the components A and H_z are linear combinations of the harmonics $\cos x$ and $\cos y$. Such a configuration calculated on the region with the sides $X_0 = Y_0 = 2\pi$ is stable. The specific structure of the configuration depends on the value of the parameter H_0 and on the symmetry properties of the equilibrium-breaking perturbation satisfying conditions (3) and (4). When the quantities A and H_z after the coalescence are proportional to the combination $\cos x \pm \cos y$ (see the second frame from the top in the left column of Fig. 1), the final configuration of magnetic cells is analogous in structure to the initial configuration. The only difference is that the final cells are $\sqrt{2}$ times larger than the initial cells and are turned through an angle of $\pi/4$ with respect to their original orientations. If this combination contains only the $\cos x$ or $\cos y$ harmonic, then the configuration established after the coalescence process is one-dimensional (see the third frame from the top in the left column of Fig. 2).

4. LARGE CALCULATION REGION

The results obtained using a calculation region with the sides $X_0 = Y_0 = 2\pi N$ (where $N \geq 2$) show that, as before, the fastest growing harmonics are those in which the components A and H_z are proportional to the linear combination of $\cos x$ and $\cos y$. Consequently, for $N \geq 2$, the formation of a configuration in the initial stage of the process proceeds in the same way as in the above case $N = 1$ and the resulting configuration corresponds to the linear combination of the $\cos x$ and $\cos y$ harmonics. If the resulting configuration is cellular, then the coalescence process repeats over and over again. We thus deal with a cascade of coalescence events, in each of which the cell side becomes larger by a factor of $\sqrt{2}$ (Fig. 1). If the configuration resulting from the first coalescence event is one-dimensional and is determined only by the $\cos x$ or $\cos y$ harmonic, then further evolution of the magnetic field proceeds through the development of a tearing instability, so that we deal with a cascade of reconnection events (Fig. 2). Note that, according to the calculated results, the instability in a one-dimensional configuration develops on a much longer time scale in comparison with that in a configuration with magnetic cells. This conclusion agrees with the results of [6–11], where it was shown that, in contrast to a configuration with magnetic islands, a one-dimensional magnetic configuration in a dissipationless plasma is linearly stable. In our analysis, the dissipation in a plasma is always assumed to be finite but low. At this point, let us make an important remark. In [6–11], a study was made of the perturbations that become completely damped far from the neutral sheet. In the case under analysis here, the perturbation is assumed to be periodic in two directions. A com-

prehensive examination of the tearing instability of neutral sheets goes beyond the scope of the present work.

The specific features of the cascades in question are determined by the value of H_0, the properties of the perturbation breaking the equilibrium conditions (3) and (4), and the size of the calculation region. Thus, if the sides of the calculation region differ from $2\pi 2^m$ (where m is an integer), then the cascade process, in which the cell side increases by a factor of $\sqrt{2}$ after each coalescence event, inevitably terminates in the corresponding stage. Further evolution proceeds in a somewhat different way. However, in all cases, the magnetic field perturbation relaxes to a stable configuration in which the components H_z and A are proportional to the linear combination of the largest scale harmonics $\cos(x/N)$ and $\cos(y/N)$.

Note that the energy of the system and the Reynolds number Re_η associated with the plasma conductivity both decrease after each reconnection event, in which case, however, the Reynolds number Re_ν associated with the electron plasma viscosity does not decrease but instead increases because of the larger characteristic length scale of each new configuration. Consequently, when $\mathrm{Re}_\nu \gg \mathrm{Re}_\eta$, there is no reason for the cascade process to terminate. In this case, it is only certain that each new coalescence event is longer than the preceding event, because the characteristic time scale of the entire process is inversely proportional to the magnetic field magnitude. When $\mathrm{Re}_\nu \ll \mathrm{Re}_\eta$, the cascade terminates after the Reynolds number Re_η reaches a value on the order of unity. Thereafter, the magnetic field is damped by conventional dissipation.

5. MODEL WITH A SMALL NUMBER OF HARMONICS

Many features of the solution of problem (1)–(4) on a calculation region with the sides $X_0 = Y_0 = 2\pi$ can be understood in terms of the model with a small number of harmonics (which will be referred to as the MSNH). In this model, the solution to the problem is approximated by the expressions

$$A = a_0 f_0 + a_1 f_1 + a_2 f_2,$$
$$H_z = b_0 f_0 + b_1 f_1 + b_2 f_2,$$

where the coefficients $a_{0,1,2}$ and $b_{0,1,2}$ depend only on time. The function $f_0 = \sin x, \sin y$ corresponds to the initial harmonic with the squared wavenumber $k_0^2 = -\Delta f_0/f_0 = 2$. The functions $f_1 = \cos x - \cos y$ and $f_2 = \cos x + \cos y$ correspond to the harmonic with the smallest wavenumber $k = 1$. The Poisson brackets of these functions have the form $\{f_1, f_2\} = 2f_0$, $\{f_0, f_1\} = f_2/2 +$ (harmonics with $k = \sqrt{5}$), and $\{f_0, f_2\} = -f_1/2 +$ (harmonics with $k = \sqrt{5}$). We can neglect the harmonics with $k = \sqrt{5}$ because they are more strongly damped by dissipation. As a result, we arrive at the following

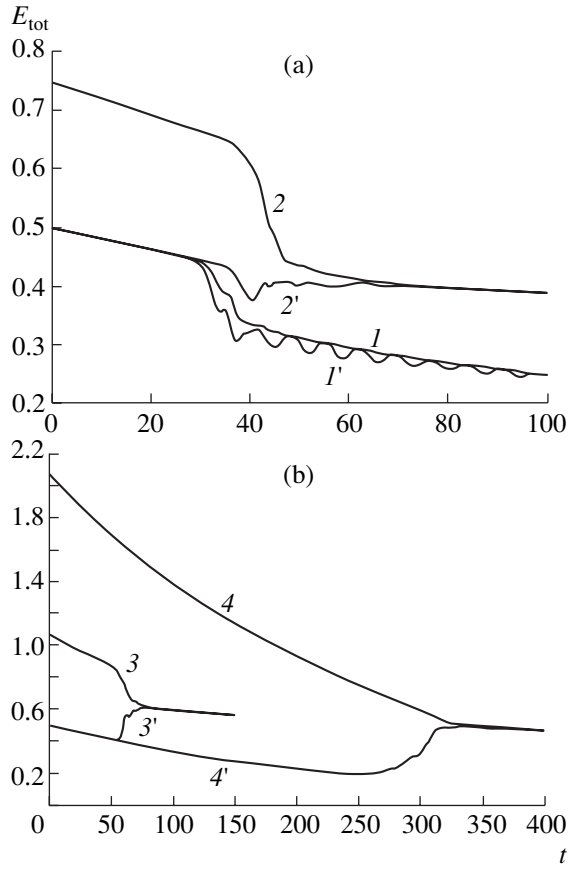

Fig. 4. Time evolutions of E_{tot} (unprimed) and E (primed) for $\eta = 0$, $\nu = 5 \times 10^{-4}$, and $H_0 = (1)$ 0, (2) 1, (3) 1.5, and (4) 2.5. The sides of the calculation region are $X_0 = Y_0 = 2\pi$.

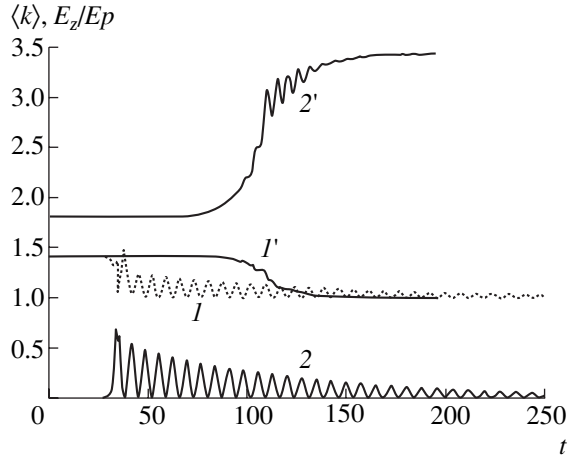

Fig. 5. Time evolutions of $(1, 1')$ $\langle k \rangle$ and $(2, 2')$ E_z/E_p for $\eta = 0$, $\nu = 5 \times 10^{-4}$, and $H_0 = (1)$ 0 and (2) 1.9. The sides of the calculation region are $X_0 = Y_0 = 2\pi$.

equations (in which the superior dot denotes differentiation with respect to time):

$$\dot{a}_1 + a_0 b_2/2 - b_0 a_2/2 = -(\eta + \nu)a_1, \quad (6)$$

$$\dot{a}_2 - a_0 b_1/2 + b_0 a_1/2 = -(\eta + \nu)a_2, \quad (7)$$

$$\dot{b}_1 - a_0 a_2/2 = -(\eta + \nu)b_1, \quad (8)$$

$$\dot{b}_2 + a_0 a_1/2 = -(\eta + \nu)b_2, \quad (9)$$

$$\dot{a}_0 - (a_1 b_2 - a_2 b_1) = -2(\eta + 2\nu)a_0, \quad (10)$$

$$\dot{b}_0 = -2(\eta + 2\nu)b_0. \quad (11)$$

Note that the harmonics with $k = \sqrt{5}$ can be neglected only in the case of large η and ν values, which is notinteresting for our purposes here. However, as will be seen below, the model (6)–(11) is very useful for understanding the dynamics of the coalescence process. Let us examine this model in more detail.

For a dissipationless plasma, linearizing Eqs. (6)–(11) about the equilibrium state $a_0 = 1$, $b_0 = H_0$, and $a_1 = a_2 = b_1 = b_2 = 0$ yields expression (5) for the growth rate γ.

We can show that, in the linear approximation, Eqs. (6)–(11) coincide with the equations for the corresponding Fourier coefficients of the linearized problem (1)–(4) if the initial (at $t = 0$) perturbation that breaks the equilibrium conditions (3) and (4) is composed only of the $\cos x$ and $\cos y$ harmonics. The reason for this is that, applying the operator $\{f_0, \ldots\}$ to the functions $\{f_0, f_{1,2}\} \mp f_{2,1}/2$ many times, we arrive at the functions that do not contain the $f_{0,1,2}$ harmonics.

Let us now investigate the nonlinearized equations (6)–(11) by converting them into a more convenient form. It should be noted that these equations have the dissipationless integral of motion

$$E = a_0^2/2 + a^2 + b^2, \quad (12)$$

where

$$a^2 = a_1^2 + a_2^2, \quad b^2 = b_1^2 + b_2^2. \quad (13)$$

In problem (1)–(4), the quantity E is the sum of the energies $E_p(1) = a^2$ and $E_p(\sqrt{2}) = a_0^2/2$ (accumulated in a poloidal magnetic field in the harmonics with the wavenumbers $k = 1$ and $\sqrt{2}$, respectively) and the energy $E_z(1) = b^2$ (accumulated in the $k = 1$ harmonics of the toroidal magnetic field). In the absence of higher harmonics, the total magnetic energy is equal to $E_{\text{tot}} = E + E_z(\sqrt{2})$, where $E_z(\sqrt{2}) = b_0^2/4$ is the energy accumulated in the $k = \sqrt{2}$ harmonic of the toroidal magnetic field.

Using the integral of motion (12) and the quantities

$$\alpha = a_1 b_2 - a_2 b_1, \quad \beta = a_1 b_1 + a_2 b_2, \quad (14)$$

we rewrite Eqs. (6)–(10) in the form

$$\dot{a}_0 - 2\alpha = -2(\eta + 2\nu)a_0, \quad (15)$$

$$\dot{\beta} + b_0\alpha/2 = -2(\eta + \nu)\beta, \quad (16)$$

$$\dot{\alpha} + a_0(a_c^2 - a_0^2)/4 - b_0\beta/2 = -2(\eta + \nu)\alpha, \quad (17)$$

$$\dot{E} = -2\eta(1 + a_0^2/a_c^2)E - 2\nu(1 + 3a_0^2/a_c^2)E, \quad (18)$$

$$a_c^2 = 2E. \quad (19)$$

Equations (11) and (15)–(19) constitute a closed set of equations. In the dissipationless case, we can draw the following analogy: these equations are equivalent to the set of equations describing the two-dimensional motion of a charged particle with coordinate a_0 and velocity 2α in one direction and velocity 2β in another. The particle moves in a constant uniform magnetic field that is oriented in the third direction and whose strength is proportional to $b_0 = H_0 = \text{const}$ and also in the potential $U(a_0) = -(a_c^2 - a_0^2)^2/8$. The potential U takes on its minimum value $-a_c^4/8$ on the line $a_0 = 0$ and its maximum value 0 is on the lines $a_0 = \pm a_c$. For $a_0 \longrightarrow \pm\infty$, we have $U \longrightarrow -\infty$.

By way of analogy, we can readily write the following dissipationless integrals of motion, which correspond to the energy W and generalized momentum P of the above charged particle:

$$W = 2(\alpha^2 + \beta^2) - (a_c^2 - a_0^2)^2/8, \quad (20)$$

$$P = \beta + H_0 a_0/4. \quad (21)$$

Formulas (12)–(14) put integrals (20) and (21) in the form

$$W = -(a^2 - b^2)^2/2, \quad (22)$$

$$P = a_0 b_0/4 + a_1 b_1 + a_2 b_2. \quad (23)$$

According to these expressions, the energy is nonpositive, $W \le 0$, and is proportional to the square of the energy difference $E_p(1) - E_z(1)$ and the generalized momentum P is equal to the fraction of the helicity $H = \int A H_z dx dy$ that is contained in the $k = 1$ and $k = \sqrt{2}$ harmonics.

We are interested in solving problem (6)–(11) rather than problem (15)–(17). Accordingly, we must impose certain restrictions on the possible solutions to problem (15)–(17) in order to single out a class of solutions that are worth considering, because the parameter a_c and the initial values of the quantities α, β, and a_0 are not arbi-

trary. Formula (12) implies that the quantity a_0 is restricted to the values $|a_0| \le a_c$; moreover, as $|a_0| \longrightarrow a_c$, the quantities α and β tend to zero by virtue of formula (20) and the condition $W \le 0$.

The case $a_c - |a_0| \ll a_c$ corresponds to a magnetic configuration in which the initial harmonic $\sin x \sin y$ dominates over the $k = 1$ harmonics. The case $|a_0| \ll a_c$ corresponds to a configuration that is dominated by the $k = 1$ harmonics and forms after the coalescence of magnetic cells. The reason for this is that the magnetic energy accumulated in the $k = \sqrt{2}$ harmonics is equal to $a_0^2/2$ and the energy accumulated in the $k = 1$ harmonics is equal to $a_1^2 + a_2^2 + b_1^2 + b_2^2 = E - a_0^2/2 = (a_c^2 - a_0^2)/2$.

The time evolution of a_0 can be easily understood by drawing an analogy with the motion of a charged particle in the magnetic field b_0 and the potential U. Clearly, the coordinate a_0 of the moving particle oscillates between minimum ($a_{\min}$) and maximum ($a_{\max}$) values. In the absence of a magnetic field ($b_0 = 0$), we have $a_{\min} = -a_{\max}$. The magnetic field b_0 turns the particle and forces it to drift along the lines U = const, thereby diminishing the difference $a_{\max} - a_{\min}$. Consequently, the initial equilibrium $|a_0| = a_c$, which is unstable in a weak magnetic field b_0, becomes stable in a sufficiently strong field b_0.

In order to analyze the temporal behavior of a_0 in more detail, we eliminate β in formula (20) using formula (21). Since the quantities W and P remain unchanged with time, we will arrive at the equation relating a_0 to the time derivative $\dot{a}_0 = 2\alpha$. For brevity, we restrict ourselves to considering the case with the initial values $\alpha = \beta = 0$ (and, accordingly, $a_1 = a_2 = b_1 = 0$) and

$$a_0(t = 0) = a_c\sqrt{1 - \epsilon},$$

where the quantity ϵ is related to the ratio between the energy W and the depth U of the potential well by

$$\epsilon^2 = 8|W|/a_c^4. \tag{24}$$

Then, the desired equation relating a_0 to $\dot{a}_0$ can be written as

$$4\dot{a}_0^2 + H_0^2(a_c\sqrt{1 - \epsilon} - a_0)^2 - (a_c^2 - a_0^2)^2 + \epsilon^2 a_c^4 = 0. \tag{25}$$

Setting $\dot{a}_0 = 0$ gives the equation for $a_{\min}$ and $a_{\max}$. Using this equation, we can easily show that $a_{\max} = a_0$ ($t = 0$).

For $H_0 < H_c = 2a_c$ (or, more precisely, $H_c - H_0 \gg a_c\sqrt{\epsilon}$) and $\epsilon \ll 1$, we obtain $a_{\max} \approx a_c$ and $a_{\min} \approx a_c - H_0$. The coordinate a_0 evolves in time as follows. For a fairly long time, on the order of $\gamma^{-1}\ln[(a_{\max} - a_{\min})/(a_0(t = 0) - a_c)] \gg 1$, the coordinate a_0 remains close to a_c (the particle is in a state close to equilibrium). Then, the coordinate a_0 deviates substantially from a_c, $a_c - |a_0| \sim a_c$, on a time scale that can be estimated from Eq. (25) as $(H_0^2 + 2a_c^2)^{-1/2}$.

For $H_0 > H_c$ (or, more precisely, $H_0 - H_c \gg a_c\sqrt{\epsilon}$) and $\epsilon \ll 1$, the period of motion is estimated to be $(H_0^2 - H_c^2)^{-1/2}$, in which case $a_{\min}$ is equal to

$$a_{\min} = a_{\max}\left(1 - \frac{H_c^2}{H_0^2 - H_c^2}\epsilon\right).$$

Consequently, unlike in the previous case, the amplitude of the motion is $a_{\max} - a_{\min} \ll a_c$ and depends sensitively on the initial value of a_0, thereby indicating that the motion is stable.

Let us consider the influence of dissipation. Since, in problem (1)–(4), the ratio a_0/a_c determines which of the harmonics is dominant, we analyze how the dissipation influences the quantity a_0/a_c. This influence can be characterized by the quantity ϵ defined in formula (24). Using Eqs. (6)–(9) and (18), we obtain

$$\dot{\epsilon} = 4(\eta + 3\nu)(a_0^2/a_c^2)\epsilon,$$

which indicates that, under the action of dissipation, the quantity ϵ increases with time. Consequently, the ratio a_0/a_c undergoes damped oscillations and approaches zero.

Recall that the case $H_0 > H_c$ and $\epsilon \ll 1$ corresponds to the onset of a dissipative instability. It is convenient to explain the mechanism for this instability by again drawing an analogy with the motion of a charged particle in the potential U and in the magnetic field b_0.

In the presence of dissipation, the particle velocity is lower than without dissipation. Consequently, the magnetic field b_0 cannot bring the particle back into its initial position. Accordingly, the particle rotates around the center $(a_{\min} + a_{\max})/2$, which moves toward the minimum in the potential U. A more important point is that dissipation increases the radius $(a_{\max} - a_{\min})/2$ of rotation of the particle. When the radius of rotation becomes comparable to a_c, the particle occurs in the region of large gradients of U and continues moving toward the position $a_0 = 0$ at a higher velocity.

In the case at hand ($H_0 > H_c$ and $\epsilon \ll 1$), we have $(a_{\max} - a_{\min})/a_c \sim (H_c/b_0)^2\epsilon$. From Eqs. (6)–(11) and (19), we obtain the following equation for the ratio b_0/H_c:

$$\frac{d(b_0/H_c)}{dt} = -\eta\left(1 - \frac{a_0^2}{a_c^2}\right)(b_0/H_c) - \nu\left(1 - \frac{3}{4}\frac{a_0^2}{a_c^2}\right)(b_0/H_c).$$

Using this equation and the equation for $\dot{\epsilon}$, we find that the ratio $(a_{max} - a_{min})/a_c$ increases at the rate $2(\eta + \nu) + (2\eta + 10.5\nu)a_0^2/a_c^2 \approx 4\eta + 12.5\nu$.

Now, we again turn to problem (1)–(4). In what follows, by the quantities a_0, b_0, α, etc., we mean the related functions of the corresponding Fourier coefficients in the Fourier series expansion of problem (1)–(4). The temporal behavior of these quantities can be described by Eqs. (11) and (15)–(19) with the additional terms that accounts for the interaction with the perturbation harmonics that are neglected in the MSNH. The results from the numerical solution of problem (1)–(4) show that the effect of this interaction on the solution to Eqs. (11) and (15)–(19) is analogous to the effect of additional dissipation. The latter, however, not merely changes the coefficients η and ν but plays a fundamentally important role. In essence, the MSNH correctly describes the solution to problem (1)–(4) only in the linear stage, when $H_0 < H_c$. For $H_0 > H_c$, the MSNH and the model with additional dissipation disagree quantitatively even in the initial stage of the evolution. This disagreement can be explained by the fact that the effect of higher harmonics, being small, is at the same time important, because, at low transport coefficients, the growth rate of the dissipative instability is slow. The MSNH implies that, in the nonlinear stage, the magnetic perturbation undergoes weakly damped oscillations from the initial magnetic configuration to a configuration corresponding to the linear combination of the cos$x$ and cos$y$ harmonics and back again. As time elapses, the latter configuration becomes dominating. However, the solution to problem (1)–(4) shows that the magnetic perturbation undergoes such oscillations only when $H_0 \ll H_c$; moreover, the oscillations are damped at a significantly faster rate than predicted by the MSNH. When the amplitude H_0 is not too small, the perturbation undergoes no oscillations and rapidly evolves to the final configuration. Nevertheless, below, we will show that the results obtained in the MSNH provide a clear insight into the regular features of the evolution of the magnetic configuration in the nonlinear stage in problem (1)–(4).

An analysis of the numerical solution to problem (1)–(4) shows that, in the nonlinear stage of the coalescence process, the quantities a_0, b_0, etc., change in such a way that the energy W becomes as close as possible to the minimum value of the potential, $\min U = -a_c^4/8$, under the condition of conservation of the helicity P and at a prescribed energy, $R^2 = a_0^2/2 + b_0^2/4 + a^2 + b^2$, accumulated in the $k = 1$ and $k = \sqrt{2}$ harmonics after the coalescence. In other words, as a result of coalescence, the parameter ϵ (24) reaches its maximum under the condition $P = \text{const}$, in which case the energy R is an unknown quantity and is to be calculated from other considerations. Although the energy R is unknown, the condition for ϵ to be maximum makes it possible to quantitatively describe energy redistribution resulting from the coalescence of the magnetic cells. Let us illustrate this point.

First, we turn to the conservation of the helicity P. Note that, in most of the calculation versions, the change in P in the nonlinear stage is not too large and reaches 20% only in rare cases. However, just before and just after the nonlinear stage of the coalescence process, the values of P were found to be essentially the same. Note also that the fraction of the generalized particle momentum P associated with the helicity contained in the $k = 1$ and $k = \sqrt{2}$ harmonics corresponds to more than 90% of the total helicity H. Using expression (23), we can reduce the conservation condition for P to the form

$$a_0 b_0/4 + a_1 b_1 + a_2 b_2 = \bar{a}_0 \bar{b}_0/4. \tag{26}$$

Here, the quantities with and without the superscript "–" are taken, respectively, at the times just before and just after the nonlinear stage. Condition (26) was derived taking into account the fact that, initially, the $k = \sqrt{2}$ harmonics dominate.

Let us analyze the consequences of the condition for ϵ to be maximum. We use expressions (12), (22), and (24) and Eq. (19) to rewrite this condition as

$$\epsilon^2 = \frac{(a^2 - b^2)^2}{(a_0^2/2 + a^2 + b^2)^2} = \max. \tag{27}$$

Taking into account relationships (13), we arrive at the following representations for the coefficients a, b, a_0, and b_0 in "spherical" coordinates R, ψ, ξ_a, ξ_b, and φ:

$$a = R\cos\psi\cos\xi_a, \quad a_0 = \sqrt{2}R\cos\psi\sin\xi_a,$$

$$b = R\sin\psi\cos\xi_b, \quad b_0 = 2R\sin\psi\sin\xi_b,$$

$$a_1 b_1 + a_2 b_2 = ab\cos\varphi.$$

In these coordinates, conditions (26) and (27) can be rewritten as

$$\begin{aligned} \chi\sin(2\psi) &= \bar{a}_0\bar{b}_0/(2R^2), \\ \chi &= \cos\xi_a\cos\xi_b\cos\varphi - (\sin\xi_a\sin\xi_b)/\sqrt{2}, \\ \epsilon^2 &= \frac{(\cos^2\psi\cos^2\xi_a - \sin^2\psi\cos^2\xi_b)^2}{(\cos^2\psi + \sin^2\psi\cos^2\xi_b)^2} = \max. \end{aligned} \tag{28}$$

The extremum of $\epsilon^2\{\xi_a, \xi_b, \psi[\chi(\xi_a, \xi_b, \varphi)]\}$ is reached at the points satisfying the equations

$$\partial\epsilon^2/\partial\xi_{a,b} + (\partial\epsilon^2/\partial\psi)(\partial\psi/\partial\chi)(\partial\chi/\partial\xi_{a,b}) = 0,$$

$$(\partial\epsilon^2/\partial\psi)(\partial\psi/\partial\chi)(\partial\chi/\partial\varphi) = 0.$$

Since $\partial\chi/\partial\varphi$ is proportional to $\sin\varphi$, $\partial\epsilon^2/\partial\xi_{a,b}$ is proportional to $\cos\xi_{a,b}\sin\xi_{b,a}$, and $\partial\chi/\partial\xi_{a,b} = -(\sin\xi_{a,b}\cos\xi_{b,a} + (\cos\xi_{a,b}\sin\xi_{b,a})/\sqrt{2})$, one of the solutions for which this extremum is reached is $\sin\xi_a = \sin\xi_b = \sin\varphi = 0$. Accordingly, we have $a_0 = b_0 = 0$. It is an easy matter to show that this solution corresponds to the maximum of ϵ. Consequently, after the coalescence, the $k = \sqrt{2}$ harmonics, which dominated before the coalescence, disappear, whereas the $k = 1$ harmonics become dominant.

In terms of the "particle–magnetic field b_0–potential U" system, the results obtained indicate that the system evolves to the most stable steady state and that the generalized particle momentum is conserved during the evolution. Clearly, this state corresponds to a particle at the bottom of the potential well ($a_0 = 0$). In order for the generalized momentum (21) to be conserved, the particle should move along the bottom ($\beta \neq 0$). The magnetic field b_0 acts to turn the moving particle. To prevent this effect, it is necessary that the magnetic field vanish ($b_0 = 0$).

Substituting $\xi_a = \xi_b = \varphi = 0$ into relationships (28) yields the equation

$$\sin^2(2\psi) = [a_0^- b_0^-/(2R^2)]^2. \quad (29)$$

After the coalescence, we have $a_0 = b_0 = 0$; consequently, $R^2 = a^2 + b^2 = E$. Since we also have $E^- = (a_0^-)^2/2$ before the coalescence, we can rewrite Eq. (29) in the form

$$\sin^2(2\psi) = (b_0^-/a_0^-)^2(E^-/E)^2. \quad (30)$$

We can see that, in order for Eq. (30) to have a solution in the case $b_0^-/a_0^- \approx H_0 > 1$, the energy E after the coalescence should exceed that before the coalescence. Above, we have shown that this is actually the case.

Equation (30) has two solutions: $\psi = \psi_*$ and $\psi = \pi/2 - \psi_*$, where $\psi_* = (1/2)\arcsin(|b_0^-/a_0^-|(E^-/E))$. Accordingly, after the coalescence, the ratio of the energies of the toroidal and poloidal magnetic fields, $E_z/E_p = b^2/a^2 = \tan^2\psi$, can be either larger or smaller than unity. Calculations show that $E_p > E_z$ for $H_0 < 1$ and $E_z > E_p$ for $H_0 > 1$. The ratio E_z/E_p increases monotonically as H_0 increases. The monotonic dependence of E_z/E_p on H_0 can also be obtained from Eq. (29) with allowance for the numerical data on the value of R^2.

The fact that, after the coalescence of the magnetic cells, the magnetic perturbation undergoes weakly damped oscillations when $H_0 \ll 1$ and does not oscillate at all when $H_0 \sim 1$ can be explained in terms of the motion of a charged particle in the magnetic field b_0 and the potential U. When $H_0 \sim 1$, the magnetic field b_0 acts to oppose the particle motion toward the bottom of the potential well, thereby trying to prevent the particle from crossing the line $a_0 = 0$. However, because of the interaction with small-scale harmonics, the magnetic field b_0 falls off to zero and the particle approaches the bottom (where the coordinate a_0 has a zero value). Consequently, the magnetic field b_0 cannot force the particle to move away from the bottom of the well, as in the case with $b_0 = \text{const}$. As a result, the particle moves gradually from the point $a_0 \approx a_c$ toward its final position $a_0 = 0$. In the absence of a magnetic field, the particle crosses the line $a_0 = 0$ with a nonzero velocity, but its relative energy $\epsilon^2 8|W|/a_c^4$ becomes slightly lower than that at the initial instant. We thus deal with the damped oscillations of a particle about the minimum of U.

6. CONCLUSION

We have shown that, in the EMHD model, the configuration of magnetic cells that is periodic in two directions is unstable against the coalescence of the cells. Numerical simulations on a calculation region whose sides exceed the period of the cells revealed a cascade of reconnection events, in each of which the characteristic scale of a newly formed configuration increases by a factor of $\sqrt{2}$.

The most interesting feature of the coalescence process is that, in the EMHD model (unlike in the MHD model), the dynamics of the cells where most of the magnetic energy is accumulated is independent of the dissipation coefficients, provided that the coefficients themselves are sufficiently small. In particular, the time scale on which the cells coalesce remains finite or, at least, increases very slowly as η and ν tend to zero. On the other hand, the dissipation coefficients have a substantial impact on the distribution of the electric current density during the reconnection process: the current density is redistributed in such a way as to dissipate the energy flux from large- to small-scale motions. The independence of the reconnection time on the dissipation coefficients in EMHD theory can explain the anomalously short duration of the crash phase of sawtooth oscillations in tokamaks.

ACKNOWLEDGMENTS

I am grateful to V.P. Lakhin and S.S. Moiseev for suggesting the problem. This work was performed under the EURATOM-FOM Association agreement with financial support from the Netherlands Organization for Scientific Research, project no. 074-006.015.

REFERENCES

1. H. Soltwisch, Plasma Phys. Controlled Fusion **34**, 1669 (1992).
2. D. Biskamp, Phys. Plasmas **4**, 1964 (1997).

3. S. V. Bulanov, F. Pegoraro, and A. S. Sakharov, Phys. Fluids B **4**, 2499 (1992).
4. D. Biskamp, E. Schwarz, and J. F. Drake, Phys. Plasmas **4**, 1002 (1997).
5. A. S. Kingsep, K. V. Chukbar, and V. V. Yankov, in *Reviews of Plasma Physics*, Ed. by B. B. Kadomtsev (Énergoizdat, Moscow, 1987; Consultants Bureau, New York, 1990), Vol. 16.
6. A. V. Gordeev, Fiz. Plazmy **1**, 259 (1975) [Sov. J. Plasma Phys. **1**, 139 (1975)].
7. A. V. Gordeev, Fiz. Plazmy **3**, 556 (1977) [Sov. J. Plasma Phys. **3**, 314 (1977)].
8. A. V. Gordeev, Fiz. Plazmy **3**, 1159 (1977) [Sov. J. Plasma Phys. **3**, 644 (1977)].
9. S. V. Basova, S. A. Varentsova, A. V. Gordeev, *et al.*, Fiz. Plazmy **17**, 615 (1991) [Sov. J. Plasma Phys. **17**, 362 (1991)].
10. A. V. Gordeev, Nucl. Fusion **10**, 319 (1970).
11. A. V. Gordeev, A. S. Kingsep, and A. V. Rudakov, Phys. Rep. **243**, 215 (1994).
12. K. Germaschewski and R. Grauer, Phys. Plasmas **6**, 3788 (1999).
13. G. Valori, H. J. de Blank, J. Rem, and T. J. Schep, in *Proceedings of the Joint Varenna–Lausanne Workshop on the Theory of Fusion Plasmas, 1998.*

Translated by O. E. Khadin

Plasma Physics Reports, Vol. 28, No. 5, 2002, pp. 423–431. Translated from Fizika Plazmy, Vol. 28, No. 5, 2002, pp. 462–470.

SOLID-STATE PLASMA

Analytic Approximations for Describing the Interaction of Charged Particles with the Emitter of a Radioisotope Current Source

M. V. Altaĭskiĭ, V. M. Balebanov, N. S. Erokhin, N. N. Zol'nikova, L. A. Mikhaĭlovskaya, and S. S. Moiseev

Institute for Space Research, Russian Academy of Sciences, Profsoyuznaya ul. 84/32, Moscow, 117810 Russia
e-mail: nerokhin@mx.iki.rssi.ru

Received October 26, 2001; in final form, November 21, 2001

Abstract—Approximate formulas for the modeling of the interaction of fast alpha particles and suprathermal electrons with solid-state plasmas of the emitter films in a secondary-electron-emission radioisotope current source are derived. The approximate formulas are used to estimate the characteristic interaction parameters, in particular, the effective stopping power of the composite material of the emitter, the ranges of alpha particles, the optimum thickness of the emitter, and the maximum possible number of binary current cells. The results obtained can be used to optimize the parameters of a prototype model of such a source and to analyze its current–voltage characteristic. They can also be applied in Monte Carlo modeling of the generation of suprathermal electrons by fast ion fluxes in a solid-state plasma and ion flux–induced fast nonequilibrium secondary electron emission from metallic and dielectric films. © *2002 MAIK "Nauka/Interperiodica".*

1. INTRODUCTION

The method of direct conversion of nuclear energy into an electrical one holds great promise for many applications, e.g., for scientific investigations in deep-space missions (to provide electric energy sources in onboard equipment), for the self-contained power supply of equipment in the Earth's hardly accessible areas, as well as in microelectronics and medicine. The question as to how this method can be implemented in a secondary-emission radioisotope current source (SERICS) was thoroughly discussed, e.g., by Balebanov *et al.* [1]. According to [1], the characteristic feature of the SERICS battery is the power-law distribution of suprathermal electrons produced during the propagation of fast ions from a radioisotope source in a solid-state plasma of an emitter consisting of a large number of thin metal layers alternating with insulating layers, e.g., in the form of grids. The high efficiency of the electric-current generation by an ion flux in the SERICS battery stems from the onset of nonequilibrium secondary electron emission. In order to develop and fabricate a prototype model of the SERICS, it is necessary to carry out some additional investigations, which include among other things a more detailed analysis of the processes of the slowing down of fast alpha particles in the emitter (in particular, refinement of the estimates for the ranges of these particles in a multilayer system of binary current cells), the determination of both the possible thicknesses of the metal films and the maximum possible number of binary current cells, direct calculations aimed at confirming the efficiency of the secondary electron emission from metal films of optimum thickness, the refinement of the previously obtained efficiency of converting nuclear energy into electrical energy, and the determination of the service time of the emitter under the alpha-particle fluence conditions characteristic of SERICS batteries.

The objective of this paper is to obtain approximate formulas for an analytic description of the interaction of fast alpha particles and suprathermal electrons with the emitter layers. The formulas are derived on the basis of the summarized data presented in a monograph by Pucherov *et al.* [2] and with the use of the data reported by Shimizu and Ding [3]. The formulas obtained are then used to calculate, in particular, the effective stopping power of the composite material of the emitter, the ranges of alpha particles, and the maximum possible number of binary current cells. In the continuous slowing-down approximation, using the transport equation with the approximate formulas derived here makes it possible to investigate the energy and pitch angle distributions of alpha particles and also the mean energy loss of the fast ion flux as a function of the depth to which the ions penetrate into the emitter.

2. APPROXIMATE FORMULAS FOR THE INELASTIC INTERACTIONS OF ALPHA PARTICLES WITH THE EMITTER

The main factor governing inelastic energy loss of fast ions is the stopping power of the medium penetrated by them. It is proposed that the role of the ionizing radiation in a SERICS will be played by alpha particles with an initial energy E_0 of about 3–10 MeV.

1063-780X/02/2805-0423$22.00 © 2002 MAIK "Nauka/Interperiodica"

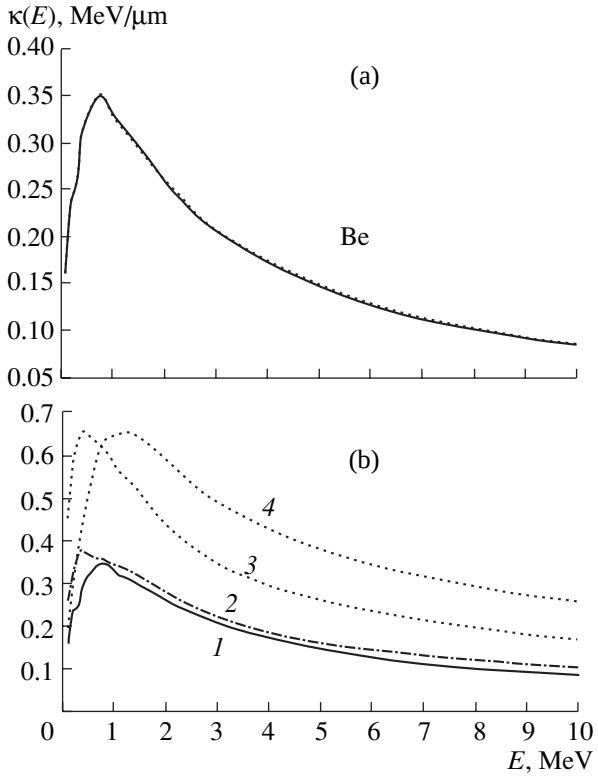

Fig. 1. (a) Plots of the stopping power of a beryllium film for alpha particles: the dotted curve is for the analytic approximation of κ calculated from formulas (2) and (3) and the solid curve is reconstructed from the basic data. (b) Analytic approximations of the stopping powers for alpha particles of (*1*) Be, (*2*) Al, (*3*) Si, and (*4*) Cu films.

Thus, a ^{210}Po alpha-particle source produces alpha particles with an initial energy of 5.3 MeV. The most comprehensive collection of data on the mass stopping power $\kappa_1(E)$ of different substances is presented in the form of the tables in monograph [2] for the fast ion energies from 100 keV to 100 MeV. Note that, in [2], the mass stopping power $\kappa_1(E)$ is given in units of MeV cm^2/g. However, in the analysis of ionization processes in the solid-state plasma of the emitter of a SERICS, it is more convenient to use the stopping power $\kappa(E)$ of substances, which is measured in units of MeV/μm. The functions $\kappa_1(E)$ and $\kappa(E)$ are related by the formula $\kappa(E) = \kappa_1(E)\rho \times 10^{-4}$, where ρ is the density of the emitter material in units of g/cm^3. When constructing analytic approximate formulas for $\kappa(E)$, we start with the following asymptotic expressions for the stopping power at low and high energies of fast ions [4]:

$$\begin{aligned} \kappa(E) &\sim (1/E_\alpha)\ln(DE_\alpha), \quad v_\alpha \gg v_B, \\ \kappa(E) &\sim E_\alpha^{1/2}, \quad v_\alpha \ll v_B, \end{aligned} \tag{1}$$

where $v_B = e^2 Z_\alpha^{2/3}/\hbar$, D is a constant, Z_α is the charge of an ion, and $\hbar$ is Planck's constant. In this section, the alpha-particle energy E_α is expressed in MeV. When analyzing an SERICS, we will also need an expression for the stopping power of substances in the energy interval $E_\alpha \in$ (100 keV–10 MeV).

One can readily see that the asymptotic expressions (1) are satisfied by the basis functions of the form $(1/E)\ln[F(E)]$, where $F(E) = 1 + (AE^{3/2})/[1 + BE^{1/2}]$ and the constants A and B determine the position of the maximum of the stopping power in the first approximation. Consequently, the most general analytic representation of the stopping power $\kappa(E)$ (in MeV/μm) is provided by the function

$$\kappa(E) = CS(E)M(E)L(E)(1/E)\ln[F(E)], \tag{2}$$

where C is a constant and the correcting functions $S(E)$, $M(E)$, and $L(E)$ make it possible to obtain the best agreement between the results of calculations by formula (2) and the data presented in [2], in particular, to reconstruct the plot of the function $\kappa(E)$ in all detail (including breaks in the plot).

In view of the accuracy of the data presented in monograph [2], function (2) appears to be quite suitable for approximating the stopping power $\kappa(E)$ in our analysis (the approximate plot of the function deviates at certain points from the corresponding values in the tables presented in [2] by no more than 5%).

Now, we determine function (2) for different substances. First, we turn to the slowing-down process in beryllium ($\rho_{Be} = 1.8477$ g/cm^3, $Z_t = 4$, and the atomic weight $A_t = 9.013$). With allowance for expressions (1), the constants A, B, and C in formula (2) should be set at $A = 5.79$, $B = 1$, and $C = 0.2196$, in which case the correcting functions are described by the expressions

$$\begin{aligned} S(E) &= \{1 + 0.01/[\cosh(20(E-1.6))]\} \\ &\quad \times \tanh[10(E+0.03)], \\ M(E) &= \{1 + 0.12/[1 + 6(E-0.8)^2]\} \\ &\quad \times \{1 - 0.032/\cosh[10(E-1.1)]\} \\ &\quad \times \{1 - 0.11/\cosh[30(E-0.3)]\} \\ &\quad \times \{1 + 0.01/\cosh[15(E-1.2)]\}\tanh(E+0.58), \\ L(E) &= 1 + \{0.04/[1 + 0.9(E-1)^2]\} \\ &\quad + \{0.06/[1 + 0.8(E-2)^2]\} \\ &\quad + \{0.03/[1 + 0.9(E-3)^2]\} \\ &\quad + \{0.06/[1 + 0.9(E-4)^2]\} \\ &\quad + \{0.023/[1 + 0.9(E-5)^2]\} \\ &\quad + \{0.04/[1 + 0.7(E-1.5)^2]\} \\ &\quad + \{0.03/[1 + 0.6(E-6)^2]\} \\ &\quad - \{0.01/[1 + 0.6(E-7)^2]\}. \end{aligned} \tag{3}$$

The stopping power of beryllium for alpha particles is illustrated in Fig. 1a, in which the dotted curve is the plot of function (2) with allowance for expressions (3) and the solid curve is reconstructed from the summarized data presented in [2].

For copper (ρ_{Cu} = 8.96 g/cm^3, Z_t = 29, and A_t = 63.54), we set A = 3.5, B = 1.5, and C = 0.8439, the correcting functions being

$$M(E) = \tanh(E + 0.985)\tanh[6.5(E + 0.0074)] \times \{1 - 0.01/[1 + 10(E - 0.7)^2]\} \times \{1 - 0.01/[1 + 2(E - 2.7)^2]\} \times \{1 - 0.012/\cosh[14(E - 0.6)]\},$$

$$S(E) = 1.033\{1 + 0.005/[1 + 10(E - 1.1)^2]\} \times \{1 - 0.005/[1 + 10(E - 1.2)^2]\}(E + 0.65)/(E + 1), \quad (4)$$

$$L(E) = 1 + \{0.13/[1 + 0.6(E - 1.2)^2]\} - \{0.3/[1 + 15(E - 0.3)^2]\} + \{0.03/[1 + 8(E - 0.8)^2]\} - \{0.0002/[1 + 8(E - 1.1)^2]\} - \{0.04/[1 + 15(E - 1)^2]\} - \{0.01/[1 + 0.5(E - 5)^2]\}.$$

The stopping power $\kappa_{Cu}(E)$ of copper for alpha particles, calculated from formula (2) with expressions (4), is given in Fig. 1b.

We also present analytic approximations for the stopping powers of aluminum and silicon for fast alpha particles. For aluminum (A_t = 26.98, Z_t = 13, and ρ_{Al} = 2.6989 g/cm^3), the constants A, B, and C are equal to A = 3.598, B = 1, and C = 0.3049 and the correcting functions $S(E)$, $M(E)$, and $L(E)$ are described by the expressions

$$S(E) = 1 + \{0.08/[1 + 6(E - 0.4)^2]\} + \{0.011/[1 + (E - 1.6)^2]\} + \{0.014/[1 + 2(E - 1.4)^2]\} - \{0.039/\cosh[20(E - 0.95)]\} + W(E),$$

$$W(E) = \{0.012/[1 + 1.5(E - 3.8)^2]\} - \{0.01/\cosh[15(E - 0.55)]\} + \{0.013/\cosh[15(E - 0.3)]\} + \{0.008/\cosh[15(E - 1)]\}, \quad (5)$$

$$M(E) = \{1 - 0.045/\cosh[8(E - 0.6)]\} \times \{1 - 0.006/\cosh[20(E - 5)]\} \times \{1 - 0.01/\cosh[2(E - 5)]\},$$

$$L(E) = \{1 - 0.0632/\cosh[15(E - 0.1)]\} \times \{1 + 0.01/[1 + 0.5(E - 7)^2]\}.$$

The stopping power of aluminum, calculated from formula (2) with expressions (5), is given in Fig. 1b.

For a silicon film (ρ_{Si} = 2.328 g/cm^3, Z_t = 14, and A_t = 28.09), the constants are A = 2.9, B = 1.885, and C = 0.6307 and the correcting functions have the form

$$S(E) = 1 + \{0.42/[1 + 1.2(E - 0.5)^2]\} + \{0.05/[1 + 0.5(E - 1.9)^2]\} - \{0.05/[1 + 2(E - 0.7)^2]\} + \{0.045/[1 + 2(E - 1.5)^2]\} + \{0.012/\cosh[(E - 4.7)]\},$$

$$M(E) = 1 - \{0.01/\cosh[10(E - 0.8)]\} + \{0.014/\cosh[10(E - 0.2)]\} - \{0.015/\cosh[E - 10]\} + \{0.01/\cosh[E - 6.5]\}, \quad (6)$$

$$L(E) = 1 - \{0.0295/\cosh[15(E - 1.05)]\} - \{0.015/\cosh[13(E - 0.6)]\} + \{0.019/\cosh[20(E - 0.4)]\} - 0.0605\{1 - \tanh[10(E - 0.1)]\}.$$

Substituting expressions (6) into formula (2) and carrying out the necessary manipulations, we obtain the stopping power of silicon as a function of the energy of alpha particles. The plot of this function is shown in Fig. 1b. From Fig. 1b, we can see that the characteristic features (such as local extremes and breaks) of the plots of the stopping power $\kappa(E)$ are fairly well described by the above approximate formulas.

The energy losses of a flux of fast alpha particles propagating through an emitter consisting of thin ($l_f < 0.1$ μm) alternating beryllium and copper films are determined by the effective stopping power of this composite material:

$$\kappa_{eff}(E) = [l_{Be}\kappa_{Be}(E) + l_{Cu}\kappa_{Cu}(E)]/(l_{Be} + l_{Cu}).$$

For beryllium and copper films of equal thickness, the calculated energy dependence of the effective stopping power of the emitter is depicted in Fig. 2a. The analytic formula (2) for $\kappa_{eff}(E)$ corresponds to the parameter choice A = 1.4, B = 0.6, and C = 0.6069 with the correcting functions

$$S(E) = \{1 - 0.01/\cosh[10(E - 1.4)]\} \times \{1 - 0.021/\cosh[1.1(E - 5.7)]\} \times \{1 - 0.03/\cosh[0.7(E - 8.4)]\} \times \{1.12 - 0.11\tanh[20(E - 0.2)]\} \times \{1 + 0.006/\cosh[0.5(E - 6)]\} \times \{1 + 0.005/\cosh[0.5(E - 8)]\} \times \{1 - 0.006/\cosh[E - 4.3]\} \times \{1 - 0.013/\cosh[E - 10]\} \times \{1 - 0.005/\cosh[18(E - 1)]\},$$

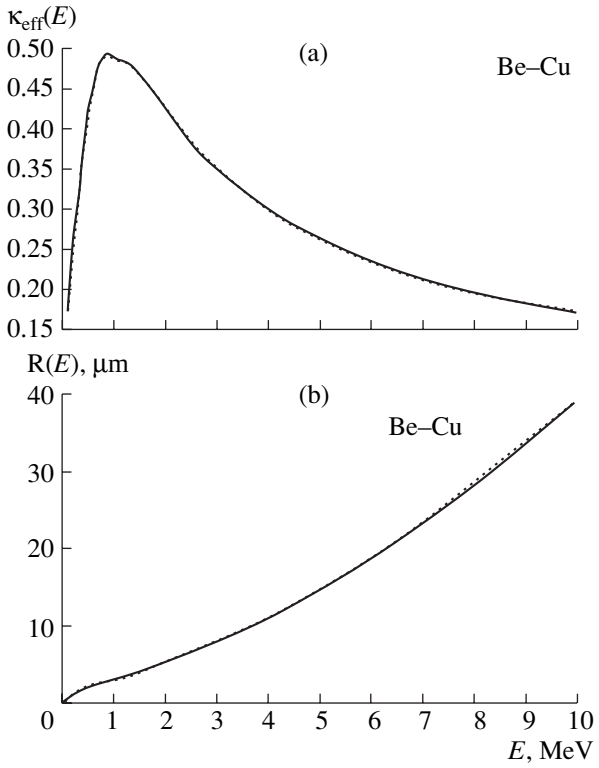

Fig. 2. (a) Effective stopping power for alpha particles of an emitter composed of beryllium and copper films of equal thickness. (b) Range of alpha particles in an emitter composed of beryllium and copper films of equal thickness.

$$M(E) = \{1 - 0.316/\cosh[3(E-0.1)]\} \quad (7)$$
$$\times \{1 - 0.031/\cosh[12(E-0.9)]\}$$
$$\times \{1 + 0.015/\cosh[6(E-1.7)]\}$$
$$\times \{1 - 0.2205/\cosh[20(E-0.1)]\}$$
$$\times \{1 - 0.01/\cosh[15(E-0.8)]\},$$
$$L(E) = 1 + \{0.1/[1 + 0.1(E-3)^2]\}$$
$$+ \{0.23/\cosh[2(E-1)]\} + \{0.06/\cosh[2(E-2.1)]\}$$
$$+ \{0.125/\cosh[5(E-0.4)]\}$$
$$+ \{0.1/\cosh[5(E-0.8)]\}$$
$$- \{0.053/\cosh[10(E-1.1)]\}.$$

Using formulas (2) and (7), we can readily calculate the actual range of alpha particles in the composite material of an emitter consisting of beryllium and copper films of equal thickness ($l_{Be} = l_{Cu}$):

$$R(E) = \int_0^E dE'/\kappa(E'). \quad (8)$$

Note that the effective range (8) is a nonlinear function of the stopping powers of copper and beryllium. Some of the calculated values of the effective range $R(E)$ are given in the table. In particular, the range of an alpha particle with an energy of 5 MeV at the entrance to the emitter is 14.4 μm. Consequently, for a 0.05-μm-thick individual film in a binary current cell of the emitter, the alpha particle can propagate through, at most, 144 binary Be–Cu layers.

The effective range $R(E)$ (in micrometers) in the composite material of an emitter with the stopping power $\kappa_{eff}(E)$ is described by the following analytic approximate expressions:

$$R(E) = D_1 X(E) H(E) E^2/\ln[F_1(E)],\ D_1 = 1.0423,$$
$$X(E) = \{1 + 0.89/\cosh[0.4(E-0.6)]\}$$
$$\times \{1 + 0.029/\cosh[8(E-0.28)]\}$$
$$\times \{1 - 0.11/\cosh[5(E-1.35)]\}$$
$$\times \{0.9158 + 0.0873\tanh[0.5(E-6)]\},$$
$$H(E) = \{1 + 0.396/\cosh[2(E-0.5)]\} \quad (9)$$
$$\times \{1 - 0.045/\cosh[1.2(E-3)]\}$$
$$\times \{1 - 0.0064/\cosh[2(E-3.5)]\}$$
$$\times \{1 - 0.033/\cosh[3(E-2.2)]\}$$
$$\times \{1 - 0.012/\cosh[1.5(E-7.6)]\},$$
$$F_1(E) = 1 + (A_1 E^{3/2})/[1 + B_1 E^{1/2}],\ A_1 = 1.4,\ B_1 = 0.6,$$

where the energy E of an alpha particle is in units of MeV. The plot of the effective range (9) is displayed in Fig. 2b.

In order to analyze the dynamics of the energy and pitch angle distributions of alpha particles in a flux propagating through a solid-state plasma of the emitter (e.g., by using the transport equation in the continuous slowing-down approximation [5]), it is also necessary to know the function $E(R)$ inverse to the function defined by formula (8), i.e., to carry out the transformation $R(E) \longrightarrow E(R)$. In this way, we obtain with reasonable accuracy the following analytic expression for the function $E(R)$ at energies of $E \le 10$ MeV:

$$E(R) = Y(R)/U(R),$$
$$Y(R) = R^2\{1 + 1.7\tanh[0.4R]\}$$
$$\times \{1 - 0.002\tanh[0.08(R-14)]\}, \quad (10)$$
$$U(R) = 8\{1 + 0.4R^{1.31}\}$$
$$\times \{1 + 0.05\tanh[0.04(R-25)]\},$$

where the effective range R of alpha particles in the composite material of the emitter is in units of μm.

Hence, the important features of inelastic interactions of the fluxes of fast alpha particles from a radioisotope source in an emitter consisting of thin metal films in an SERICS are reasonably well described by

the above analytic formulas (2)–(10) with allowance for both the features of the plot of the stopping power of the emitter and the ranges of alpha particles in a wide energy interval.

3. APPROXIMATION FOR THE STOPPING POWER OF THE EMITTER MATERIAL FOR SUPRATHERMAL ELECTRONS

Inelastic energy losses of alpha particles in the emitter are associated primarily with the ionization of substance of the films and the generation of a tail of suprathermal (fast) electrons. Suprathermal electrons can be divided into two groups [6, 7]: true secondary electrons with energies $E < 50$ eV and so-called δ-electrons with energies 50 eV $\le E \le E_m$, where the maximum energy E_m is related to the instantaneous energy E_α of an alpha particle by $E_m = 2722$ eV (E_α/5 MeV).

In order to derive approximate formulas describing the stopping power of the emitter material and the mean free paths of fast electrons in a wide energy interval, we can use, e.g., the data from [3], including those on particle losses due to the excitation of plasmons (for true secondary electrons, these losses can be significant). For copper, silicon, gold, and silver films, in which we are interested here, the stopping powers $\kappa(E)$ can be approximated by analytic expressions that are quite similar to the above formulas. Thus, for the stopping power κ_{Cu} (in units of eV/Å) of copper films for suprathermal electrons, we can obtain the approximate expression

$$\kappa_{Cu}(E) = 10^{-3}\{1 - 0.109/[1 + 20(\log(E/103500))^2]\}F_1(E)G_1(E), \quad (11)$$

where

$$F_1(E) = \{1 + 0.25/[1 + 15(\log(E/21))^2]\} \times \{1 + 0.17/[1 + 40(\log(E/49))^2]\}\{1 + 0.17/[1 + 50(\log(E/12.7))^2]\},$$

$$G_1(E) = \{1 - 0.42/[1 + 200(\log(E/3.67))^2]\} \times \{1 - 0.065/[1 + 25(\log(E/260))^2]\}\{1 - 0.08/[1 + 20(\log(E/2239))^2]\}(1 + E/2)^{3.2}/(1 + E/58)^{3.9},$$

and the energy E (in eV) of suprathermal electrons lies in the range 3.43 eV $\le E \le$ 103.5 keV.

The stopping power of silicon films for suprathermal electrons with energies 6.76 eV $\le E \le$ 105.9 keV is approximated by the expression

$$\kappa_{Si}(E) = 1.4 \times 10^{-4}\{[1 + (E/3)]^{4.4}/[1 + (E/49)]^{5.2}\} \times F_2(E)G_2(E)K_2(E), \quad (12)$$

Ranges of alpha particles in an emitter with the stopping power $\kappa_{eff}(E)$

E, MeV	R, μm	E, MeV	R, μm	E, MeV	R, μm
0.1	0.564	2.6	6.650	5.1	14.806
0.2	1.026	2.7	6.917	5.2	15.193
0.3	1.381	2.8	7.193	5.3	15.586
0.4	1.677	2.9	7.472	5.4	15.983
0.5	1.934	3	7.760	5.5	16.385
0.6	2.165	3.1	8.045	5.6	16.792
0.7	2.381	3.2	8.340	5.7	17.203
0.8	2.587	3.3	8.638	5.8	17.618
0.9	2.790	3.4	8.941	5.9	18.039
1	2.994	3.5	9.249	6	18.463
1.1	3.200	3.6	9.561	6.1	18.892
1.2	3.406	3.7	9.879	6.2	19.325
1.3	3.613	3.8	10.2	6.3	19.762
1.4	3.822	3.9	10.526	6.4	20.203
1.5	4.035	4	10.857	6.5	20.648
1.6	4.250	4.1	11.193	6.6	21.098
1.7	4.468	4.2	11.533	6.7	21.551
1.8	4.690	4.3	11.877	6.8	22.009
1.9	4.917	4.4	12.227	6.9	22.471
2	5.150	4.5	12.581	7	22.937
2.1	5.387	4.6	12.940	7.1	23.408
2.2	5.629	4.7	13.303	7.2	23.883
2.3	5.876	4.8	13.672	7.3	24.362
2.4	6.129	4.9	14.050	7.4	24.846
2.5	6.387	5	14.423	7.5	25.334

where

$$F_2(E) = \{1 + 0.98/[1 + 20(\log(E/46))^2]\} \times \{1 + 50(\log(E/24))^2\}\{1 + 1.16/[1 + 30(\log(E/36))^2]\}\{1 - 0.1/[1 + 30(\log(E/14.12))^2]\},$$

$$G_2(E) = \{1 + 0.49/[1 + 40(\log(E/28))^2]\} \times \{1 + 0.2/[1 + 30(\log(E/80))^2]\} \times \{1 - 0.2/[1 + 30(\log(E/218))^2]\} \times \{1 + 0.08/[1 + 30(\log(E/35080))^2]\},$$

$$K_2(E) = \{1 - 0.12/[1 + 20(\log(E/431))^2]\} \times \{1 - 0.3/[1 + 70(\log(E/8.3))^2]\} \times \{1 - 0.1/[1 + 200(\log(E/40))^2]\},$$

and the energy E is in units of eV.

The stopping power of silver films for suprathermal electrons with energies 4.365 eV $\le E \le$ 103.5 keV is

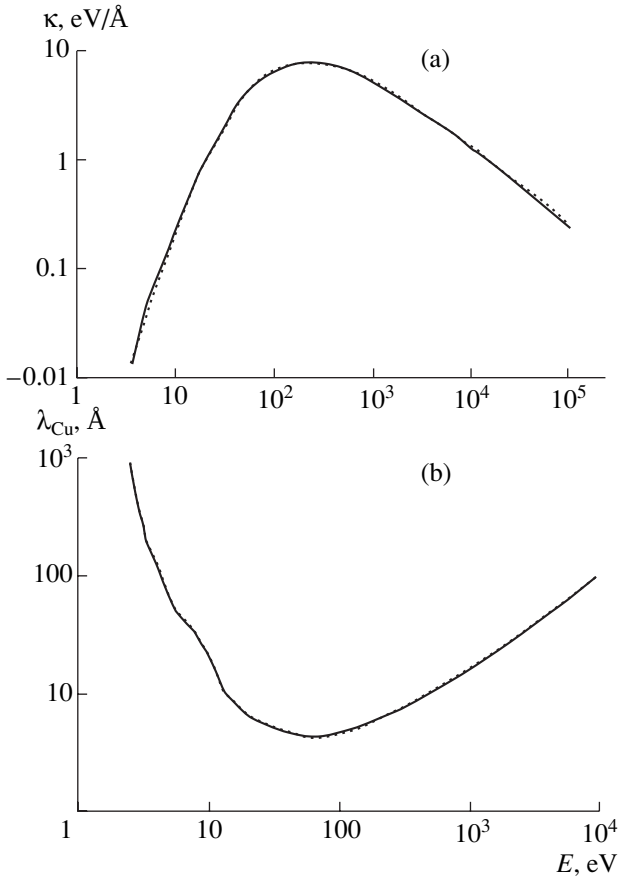

Fig. 3. (a) Stopping power of copper for suprathermal electrons. The dotted curve is for the analytic approximation. (b) Range of suprathermal electrons in copper. The dotted curve is for the analytic approximation.

approximated by the expression

$$\kappa_{Ag}(E) = 6\times10^{-4}\{[1+(E/1.8)]^{3.4}/[1+(E/60)]^{4.2}\} \times F_3(E)G_3(E)K_3(E), \quad (13)$$

where

$$F_3(E) = \{1-0.75/[1+200(\log(E/4.36))^2]\} \times \{1+0.4/[1+40(\log(E/8.5))^2]\} \times \{1+0.47/[1+50(\log(E/5.6))^2]\} \times \{1-0.08/[1+30(\log(E/26.6))^2]\},$$

$$G_3(E) = \{1+0.25/[1+100(\log(E/13))^2]\} \times \{1-0.33/[1+20(\log(E/40))^2]\} \times \{1-0.18/[1+15(\log(E/716))^2]\} \times \{1+0.08/[1+30(\log(E/15.3))^2]\},$$

$$K_3(E) = \{1-0.06/[1+20(\log(E/1603))^2]\} \times \{1+0.1/[1+50(\log(E/177))^2]\} \times \{1-0.1/[1+40(\log(E/20890))^2]\} \times \{1-0.07/[1+20(\log(E/45710))^2]\};$$

and E is in units of eV.

The stopping power of gold films for suprathermal electrons with energies 3.02 eV ≤ E ≤ 102.3 keV is approximated by the expression

$$\kappa_{Au}(E) = 10^{-3}\{[1+(E/1.2)]^{2.6}/[1+(E/80)]^{3.3}\} \times F_4(E)G_4(E)K_4(E), \quad (14)$$

where

$$F_4(E) = \{1-0.5/[1+50(\log(E/3.311))^2]\} \times \{1-0.12/[1+50(\log(E/23.7))^2]\} \times \{1+0.17/[1+50(\log(E/180))^2]\},$$

$$G_4(E) = \{1-0.18/[1+10(\log(E/668))^2]\} \times \{1+0.22/[1+50(\log(E/108))^2]\} \times \{1-0.17/[1+50(\log(E/39))^2]\},$$

$$K_4(E) = \{1-0.023/[1+40(\log(E/14))^2]\} \times \{1+0.08/[1+50(\log(E/75))^2]\} \times \{1-0.1/[1+20(\log(E/103500))^2]\},$$

and E is in units of eV.

In order to illustrate the accuracy of approximate formulas (11)–(14), Fig. 3a shows the plots of the stopping power of copper. The dotted curve is calculated from formula (11), and the solid curve is reconstructed from the data of [3]. The two curves are seen to coincide almost completely. It should be noted that, in expressions (11)–(14), the electron energy is measured from the Fermi energy.

The approximate expression for the stopping power κ_{Be} of beryllium films can be derived by using the data of [6], which refer to electron energies of 100 eV ≤ E_e ≤ 20 keV. For convenience, we introduce the normalized electron energy $y = E_e/(100\ \text{eV})$, in terms of which we obtain

$$\kappa_{Be} = a(y)(4.8665/y)\ln(1+1.368y^{1.5}), \quad (15)$$

where

$$a(y) = [1.638 - 0.638\tanh(y/15)]\{1-0.206/\cosh[0.4(y-6)]\} \times \{1-0.1/\cosh[0.3(y-15)]\} \times \{1+0.083/\cosh[3(y-1)]\}.$$

Using the data of [3, 6], it is also an easy matter to derive approximate formulas for the mean free path λ of fast electrons with respect to inelastic losses. This range is used to estimate the probability for secondary electrons to escape from the films. Thus, using the data of [6], we obtain the following approximate expression

for the mean free path λ_{Be} (in angstroms) of secondary electrons with energies 100 eV < E < 20 keV in beryllium:

$$\lambda_{Be} = (21 + 1.17y)[1.5 - 0.5\tanh(0.1y)]c(y), \quad (16)$$

where

$$c(y) = \{1 + 0.02/[1 + 0.2(0.1y - 15)^2]\} \times \tanh(0.07y)\{1 - 0.06/[1 + 0.5(0.1y - 3)^2]\} \times \{1 - 0.05/[1 + 0.05(y - 20)^2]\} \times \{1 + 0.01/[1 + 0.04(y - 100)^2]\},$$

$$y = E(\text{eV})/100.$$

Also, using the data of [3], we can see that the mean free path (with respect to inelastic collisions) of secondary electrons with energies 2.54 eV ≤ E ≤ 10 keV in copper is described by the approximate formula

$$\lambda_{Cu} = 1.65[1 + (E/60)]^{0.8}[1 + (2.64/E)]^{8.8} \times P_1(E)P_2(E)P_3(E), \quad (17)$$

where

$$P_1(E) = \{1 + 0.27/[1 + 400(\log(E/8.38))^2]\} \times \{1 - 0.2/[1 + 400(\log(E/3.45))^2]\} \times \{1 + 0.2/[1 + 200(\log(E/2.54))^2] + 0.3/[1 + 300(\log(E/10.66))^2]\},$$

$$P_2(E) = \{1 - 0.11/[1 + 400(\log(E/4))^2]\} \times \{1 - 0.06/[1 + 400(\log(E/2.9))^2]\} \times \{1 - 0.16/[1 + 300(\log(E/3.29))^2]\} \times \{1 + 0.108/[1 + 120(\log(E/7.73))^2]\},$$

$$P_3(E) = \{1 - 0.19/[1 + 10^3(\log(E/2.71))^2]\} \times \{1 - 0.065/[1 + 300(\log(E/5.34))^2]\} \times \{1 + 0.08/[1 + 200(\log(E/29.89))^2] + 0.06/[1 + 400(\log(E/3.68))^2]\}.$$

Recall that, in formula (17), the mean free path is in units of Å and the electron energy is in units of eV. The plot of function (17) is shown by the dotted curve in Fig. 3b, in which the solid curve corresponds to the data of [3].

Using the data on suprathermal electrons with energies 4.84 eV ≤ E ≤ 8.93 keV [3], we obtain the following approximate expression for the electron mean free path (in units of Å) with respect to inelastic collisions in silicon:

$$\lambda_{Si} = 2.2[1 + (E/60)]^{0.85}[1 + (4.84/E)]^{8.6} \times U_1(E)U_2(E)U_3(E), \quad (18)$$

where

$$U_1(E) = \{1 - 0.06/[1 + 40(\log(E/43.3))^2]\} \times \{1 - 0.73/[1 + 4(\log(E/25))^2]\} \times \{1 - 0.2/[1 + 200(\log(E/5.97))^2] + 1.8/[1 + 20(\log(E/11))^2]\}\{1 - 0.39/[1 + 100(\log(E/21))^2]\}\{1 - 0.02/[1 + 100(\log(E/27))^2]\},$$

$$U_2(E) = \{1 - 0.11/[1 + 100(\log(E/70))^2]\} \times \{1 - 0.15/[1 + 400(\log(E/4.84))^2]\} \times \{1 - 0.45/[1 + 200(\log(E/18.44))^2]\} \times \{1 - 0.08/[1 + 50(\log(E/113.7)^2]\},$$

$$U_3(E) = \{1 + 0.14/[1 + 800(\log(E/16.2))^2] + 0.45/[1 + 50(\log(E/15)^2]\} \times \{1 + 0.02/[1 + 70(\log(E/34))^2]\} \times \{1 - 0.2/[1 + 100(\log(E/7.13))^2]\} \times \{1 - 0.1/[1 + 1400(\log(E/17))^2] + 0.04/[1 + 30(\log(E/25)^2]\},$$

and the energy E is in units of eV.

Note that the data of [3] were obtained with allowance for inelastic electron losses due to plasmon excitation in a solid-state plasma.

The above approximate expressions (11)–(18) provide a sound basis for the calculations (and the relevant express-evaluations) of the interaction of suprathermal electrons with the emitter films in a radioisotope current source.

4. ELECTRON EMISSION

Here, we briefly discuss analytic approximations describing fast ion–induced electron emission from the emitter films. These approximations are important, in particular, for the analysis of the current–voltage characteristic of a radioisotope current source.

Let Δ be the integral yield of secondary electrons from the film per bombarding ion. Note that, according to, e.g., monograph [7], the integral yield Δ is almost entirely (up to 90%) contributed by the group of true secondary electrons. In [7], the representative secondary electron emission spectrum $d\Delta/dE$ at energies of E < 10 eV was presented for the case of irradiation of a 150-nm-thick gold film by alpha particles from the ^{252}Cf isotope. The spectrum is peaked at an energy of about $E \approx 0.7$ eV, the characteristic spectrum width being about 2 eV. In dimensionless units, the spectrum $d\Delta/dE$ of low-energy (0.295 ≤ E ≤ 9.167 eV) electrons emitted from the film is described by the following ana-

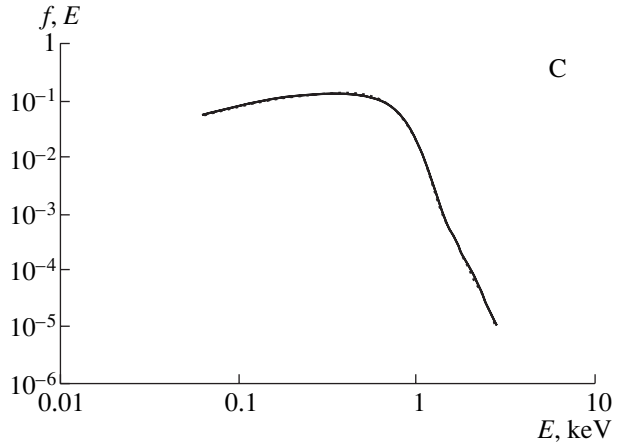

Fig. 4. Emission spectrum $f(E) = Ed\Delta/dE$ of the secondary electrons produced by alpha particles in a carbon film.

lytic approximate expression in the form of a power-law-like distribution with the correcting functions:

$$\frac{d\Delta}{dE} = C_1 F_1(E) E^{0.6}/(1 + 0.51E^2), \quad (19)$$

where

$$F_1(E) = 1 + \{1.42/\cosh[0.8(E - 0.02)]\} + \{0.17/\cosh[2(E - 0.73)]\} + \{0.029/\cosh[6(E - 0.98)]\} + \{0.118/[1 + 0.8(E - 2.1)^2]\} + \{0.088/[1 + 0.3(E - 7)^2]\}$$

and the energy is expressed in units of eV. In formula (19), the normalizing factor C_1 for the target material and bombarding ions under consideration is chosen [7] so as to satisfy the condition $\Delta = 6$.

For a wide interval of higher energies (63 eV $\le E \le$ 2825 eV), the secondary electron emission spectrum is presented in Fig. 3.7a from [7] for the case of irradiation of a carbon film with a mass thickness of 2 μg/cm^2 by 1.92-MeV alpha particles (the detection angle being 42°). The analytic approximation of the dimensionless characteristic $f(E) = Ed\Delta/dE$ presented in [7] has the form

$$f(E) = 0.834 R_1(E) W_1(E) X_1(E) E/(1 + 12.34E^8), \quad (20)$$

where

$$R_1(E) = 0.55\{1 - 0.15\tanh[10(E - 0.537)]\} \times \{1 - 0.14/[1 + 10(E - 0.537)^2]\} \times \{1 - 0.27/[1 + 16(E - 0.25)^2]\},$$

$$W_1(E) = \{1 - 0.7\tanh[5(E - 0.25)]\} \times \{1 + 0.91/[1 + 4(E - 0.963)^2]\} \times \{1 + 0.4/[1 + 2(E - 2.45)^2]\} \times \{1 + 0.25/[1 + 12(E - 0.875)^2]\} \times \{1 - 0.13/[1 + 14(E - 1.7)^2]\},$$

$$X_1(E) = 1 + \{0.05/\cosh[4(E - 1.1)]\} + \{0.093/\cosh[4(E - 2.82)]\} + \{0.082/\cosh[3(E - 2.11)]\}\{0.13/\cosh[4(E - 2.45)]\} - \{0.36/\cosh[3(E - 1.46)]\}.$$

For convenience, the electron energy in formula (20) is expressed in units of keV. The approximate formula (20) corresponds to a power-law-like spectrum of the secondary electron emission. The plot of function (20) in logarithmic variables ($\log f(E)$, $\log E$) is depicted in Fig. 4, in which the power-law parts of the secondary electron emission spectrum can easily be distinguished.

To conclude this section, we should make the following remarks. First, in a way similar to what we did when deriving the above formulas, it is also possible to obtain analytic approximate expressions for the integral yield Δ of secondary electrons from the emitter film as a function of both the energy of a fast ion and the angle θ at which it is incident on the film. The dependence on the incidence angle is very important for calculating the secondary electron emission in a radioisotope current source for actual pitch angle distributions of the alpha particles. Second, it is usually assumed (see, e.g., [7]) that the yield of secondary electrons is proportional to $1/\cos\theta$, i.e., that it is determined by the energy released by a fast ion in ionization processes at distances from the film surface that are on the order of the depth from which the secondary electrons are emitted. Since the penetration depth of alpha particles into the emitter of an SERICS is, in turn, proportional to $\cos\theta$, the integral yield of secondary electrons from the films is independent of their pitch angle distribution [8]. The construction of approximate formulas for Δ on the basis of the available experimental data and with allowance for the pitch angle distribution of alpha particles will make it possible to clarify the role played by their oblique incidence on the emitter films in both the electric-current generation in a radioisotope current source and the electric-current distribution over depth in the emitter. Finally, we note that taking into account the pitch angle distribution of alpha particles leads to more realistic estimates of both the maximum possible number of binary current cells and the efficiency of converting nuclear energy into electrical energy. Thus, the results of calculations carried out in [8] show that, for an isotropic distribution of fast ions over the directions of their momenta, the integral (over energy and pitch angles) ion flux density decreases with depth z according to the law $j_z(z)/j_z(0) = 1 - (z/R_b)^2$, where R_b is the range of an ion with the energy E_b at the entrance to the emitter. For an isotropic distribution $N_0(\theta, E_b) \sim \cos^2\theta$ of fast alpha particles incident on the emitter surface, we arrive at a far slower rate at which alpha particles are stopped in the emitter: the integral flux density

decreases with depth according to the law $j_z(z)/j_z(0) = 1 - (z/R_b)^4$. It is necessary to keep in mind that the effective range of alpha particles in the composite material of the emitter should be calculated in terms of the effective stopping power $\kappa_{\text{eff}}(E)$.

5. CONCLUSION

The results obtained in this paper are as follows.

(i) Based on the summarized data from experimental measurements and numerical calculations, we have constructed approximate formulas for the stopping powers of beryllium, copper, aluminum, and silicon films for fast alpha particles over a wide energy interval (from 100 keV to 10 MeV). We have also derived analytic approximations for both the effective stopping power of the binary current cells of beryllium–copper films for alpha particles and the ranges of alpha particles in the composite material of the emitter of a radioisotope current source.

(ii) We have obtained analytic approximations for the stopping power of the emitter for suprathermal electrons generated by fast alpha particles and for their ranges (with respect to inelastic processes) over a wide energy interval.

(iii) We have considered analytic power-law-like approximations for the secondary electron emission induced by fast alpha particles in carbon films (at low energies of the secondary electrons) and in gold films (in a wide interval of higher energies of the secondary electrons).

(iv) The approximate formulas constructed here reflect the characteristic features of the plots of the functions under consideration. The results obtained can be used, in particular, to model inelastic interactions of alpha particles and suprathermal electrons with the emitter of a radioisotope current source, to analyze the current–voltage characteristic of the source and the efficiency with which it generates the electric current, and to optimize the parameters of SERICS batteries.

ACKNOWLEDGMENTS

We are grateful to V.A. Sakovich, V.I. Karas', and V.P. Vagin for a fruitful discussion of the problems considered in this paper. This work was supported in part by the Russian Foundation for Basic Research, project no. 00-02-16279.

REFERENCES

1. V. M. Balebanov, V. I. Karas', I. V. Karas', *et al.*, Fiz. Plazmy **24**, 789 (1998) [Plasma Phys. Rep. **24**, 732 (1998)].
2. N. N. Pucherov, S. V. Romanovskiĭ, and T. D. Chesnokova, *Tables of Mass Stopping Power and Ranges of Charged Particles with Energies of 1–100 MeV* (Naukova Dumka, Kiev, 1975).
3. R. Shimizu and Z. J. Ding, Rep. Prog. Phys. **55**, 487 (1992).
4. Y.-H. Ohtsuki, *Charged Beam Interaction with Solids* (Taylor and Francis, London, 1983; Mir, Moscow, 1985).
5. M. V. Altaĭskiĭ, V. M. Balebanov, N. S. Erokhin, and S. S. Moiseev, Preprint No. Pr-2019 (Institute for Space Research, Russian Academy of Sciences, Moscow, 2000).
6. A. F. Akkerman, M. Ya. Grudskiĭ, and V. V. Smirnov, *Secondary Electron Radiation from Solids under the Influence of Gamma-Rays* (Énergoatomizdat, Moscow, 1986).
7. V. P. Kovalev, *Secondary Electrons* (Énergoatomizdat, Moscow, 1987).
8. V. M. Balebanov, N. S. Erokhin, N. N. Zol'nikova, *et al.*, Preprint No. Pr-2036 (Institute for Space Research, Russian Academy of Sciences, Moscow, 2001).

Translated by O. E. Khadin

Plasma Physics Reports, Vol. 28, No. 5, 2002, pp. 432–443. Translated from Fizika Plazmy, Vol. 28, No. 5, 2002, pp. 471–483.

PLASMA–WALL INTERACTIONS

Energy Balance in the Interaction of Intense High-Temperature Plasma Flows with Solid Targets

N. I. Arkhipov, V. P. Bakhtin, S. G. Vasenin, A. M. Zhitlukhin, S. M. Kurkin, V. M. Safronov, and D. A. Toporkov

Troitsk Institute for Innovation and Fusion Research, Troitsk, Moscow oblast, 142092 Russia

Received October 24, 2001

Abstract—The energy balance in the interaction of intense ($W \approx 7$ MW/cm^2, $Q \approx 130$ J/cm^2) flows of a high-temperature ($T_e + T_i \approx 0.7$ keV) deuterium plasma with targets made of different materials (graphite, tungsten, copper, etc.) is studied experimentally. It is shown that radiation plays a decisive role in the interaction energy balance: a plasma layer arising near the surface of the eroded target reemits most of the plasma-flow energy into the surrounding space. No more than 50 J/cm^2 reaches the surface. Then, this energy is expended primarily on the target heating and only a small fraction (less than 3 J/cm^2) is spent on the evaporation of the target surface layer. It is shown that, for targets made of high-Z materials, the energy reaching the surface is transferred predominantly by radiation. © *2002 MAIK "Nauka/Interperiodica".*

1. INTRODUCTION

The formation of a surface shielding layer is a salient feature of the interaction of intense plasma flows with solid surfaces. In the initial stage of the interaction, the density of the heat flux onto the surface almost coincides with the power density of the incident plasma flow and, in existing plasma devices, can attain tens of MW/cm^2. In a short time t_m, the surface temperature increases to the boiling (or sublimation) temperature, and the target material begins to evaporate and ionize intensively. This results in the formation of a plasma layer, which substantially decreases the heat load on the target. For this reason, this layer is called the "shielding" layer and the phenomenon itself is known as "vapor shielding." The time t during which the shielding layer is formed depends on the heat flux density W and the properties of the target material. In the order of magnitude, this time coincides with the beginning of intense surface evaporation, $t \approx t_m$. Using the data on the thermophysical properties of materials, we obtain that, at a typical flux density of $W = 10$ MW/cm^2, this time is equal to $t_m = 0.15$ μs for graphite, $t_m = 0.9$ μs for copper, and $t_m = 1.2$ μs for tungsten.

After the shielding plasma layer is formed, it protects the target surface from the direct action of the plasma flow, thus playing the role of a buffer taking over the energy flux. Further, some fraction of this energy goes for target heating, some fraction is spent to increase the shielding layer mass (i.e., to evaporate and ionize the target material and to heat the produced plasma), and, finally, some fraction is radiated from the shielding layer into the surrounding space. The evaporated material efficiently shields the surface only when the energy of the bombarding particles is not too high and their deceleration length Λ in the surface plasma layer is shorter than the layer thickness H. Otherwise, most of the particle energy is spent on the surface erosion, as in the case, e.g., of targets irradiated with high-energy electron or ion beams. As for plasma devices, the characteristic particle energies in such devices are substantially lower than in the beams and the plasma–target interaction region is usually wider. The latter circumstance decreases the mass loss from the surface layer due to the transverse layer expansion beyond the interaction region. Because of the lower particle energy and the decrease in the plasma layer mass loss, the condition $\Lambda < H$ usually holds in the interaction of intense plasma flows with solid surfaces, so that the surface layer is actually shielding.

In this paper, we present the experimental data obtained in the 2MK-200 facility at the Troitsk Institute for Innovation and Fusion Research. These data allowed us to analyze the energy balance in the interaction of deuterium plasma flows with targets made of different materials (copper, tungsten, graphite, etc.). The characteristic feature of this device is the presence of a strong magnetic field $B_0 = 25$ kG normal to the surface of a target irradiated with a plasma, which makes it possible to suppress the transverse mass loss from the shielding layer. With a rather short ($\tau \approx 20$ μs) plasma pulse with ion energies of $E_i \leq 1$ keV, the target irradiation conditions were produced such that, for all the materials under study, the shielding layer had time to form. This layer was found to govern the dynamics of the interaction process and to determine the contribution from each energy transfer channel to the total energy balance.

1063-780X/02/2805-0432$22.00 © 2002 MAIK "Nauka/Interperiodica"

2. EXPERIMENTAL SETUP

The 2MK-200 facility is a long cusp trap (LCT) [1], which is filled with a plasma by means of two coaxial pulsed plasma guns (Fig. 1). When two high-speed ($V = 4 \times 10^7$ cm/s) deuterium plasma bunches propagating in the opposite directions meet in the central part of the device, they are decelerated and thermalized, thus producing a high-temperature plasma with $\beta \approx 1$ (calculated by the external magnetic field) and an energy of up to 40 kJ. Plasma particles leave the confinement system mainly due to diffusion into the skin layer (a transition layer between the plasma with $B_{in} \ll B_{ex}$ and the external magnetic field $B_{ex} \approx 20$ kG). Then, they move along the magnetic field and escape though the annular slots of two cusps. The strong magnetic field in the annular slot ($B_0 = 25$ kG) prevents the high-β plasma from escaping. For this reason, only the magnetized skin plasma leaves the confinement system through the annular slot.

3. PARAMETERS OF THE PLASMA FLOW

The plasma flows out through the annular slot (i.e., through the maximum-field region located at a distance of R_s = 16–18 cm from the system axis; see Fig. 1) along the magnetic field lines. The magnetic field has only the radial component in this region. Downstream from the slot (in a so-called expander), the magnetic force lines diverge gradually in the azimuthal and axial directions and meet the wall of the vacuum chamber at a distance of 25 cm from the annular slot.

Table 1 shows the plasma parameters near the annular slot at different times. The flow half-width is $d_0 = 1.1$ cm and varies slightly with time, and the effective flow duration is $\tau \approx 20$ μs. The data on the plasma density, electron and ion temperatures, plasma pressure, and magnetic field were obtained from interferometry, Thomson laser scattering, and the measurements with a pressure gauge and magnetic probes, respectively [1–3].

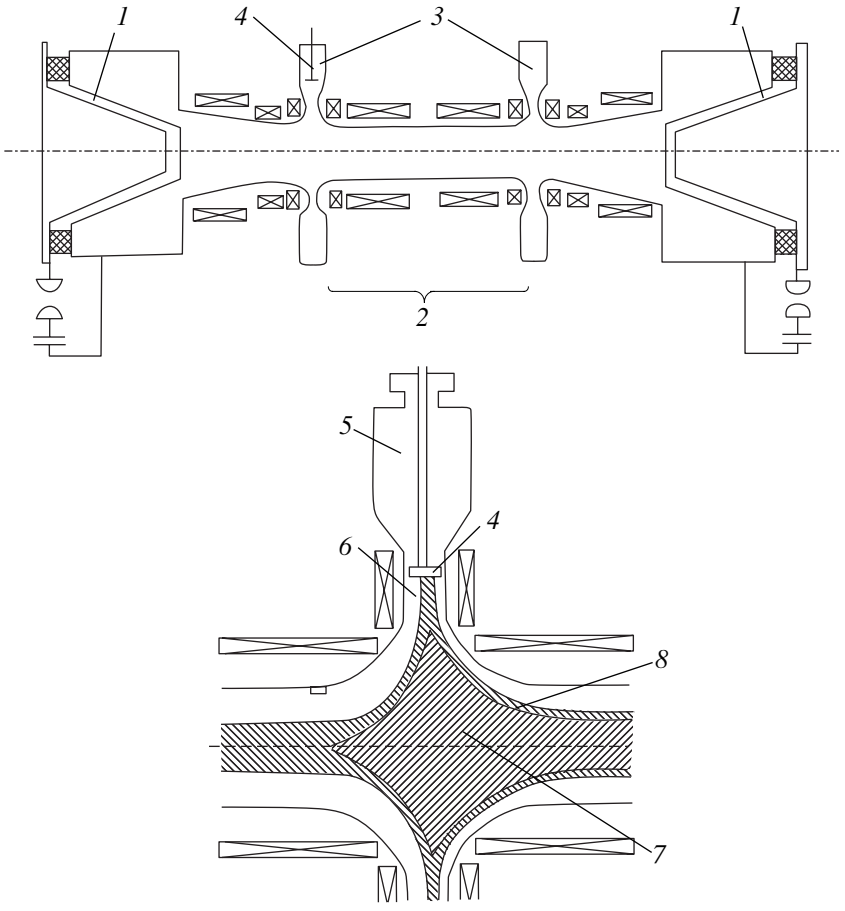

Fig. 1. Schematic of the 2MK-200 facility: (*1*) plasma guns, (*2*) LCT, (*3*) cusps, (*4*) target, (*5*) expander, (*6*) annular slot, (*7*) LCT plasma with $\beta \approx 1$, and (*8*) skin plasma.

Table 1

	$t \approx 1$ μs	$t \approx 5$ μs	$t \approx 20$ μs
n_e, 10^{-15} cm^{-3}	0.6	4	10
T_e, eV	120	140	90
T_i, eV	800	600	120
P, atm	1	5	3
β	0.04	0.2	0.12

The energy density Q in the plasma jet flowing out of the confinement system decreases as the distance R from the system axis increases. The decrease in Q is related to the expansion of the plasma flow in both the azimuthal (proportionally to $1/R$) and axial (the increase in the flow width) directions. The energy of the plasma flow was measured by a calorimeter, which was a copper cylinder 75 mm in length and 25 mm in diameter. The calorimeter was placed at a sufficiently large distance from the annular slot, $R > 28$ cm, where the shielding effect did not disturb the results of the flow energy measurements. From the calorimeter data and the flow width, measured with magnetic probes and pressure gauges, we calculated the plasma flow energy density at the distances $R = 16$–40 cm from the system axis. Near the annular slot, the calculated energy density was $Q = 130$ J/cm^2, which corresponded to an average power density of $W = 7$ MW/cm^2. Consequently, the energy of the plasma flowing out of the annular slots of two cusps amounts to $4\pi R_s d_0 Q = 30$ kJ, which agrees satisfactorily with the total plasma energy in the confinement system (~40 kJ), taking into account that a fraction of energy is lost through the axial cusp slots and some fraction is lost due to diffusion across the magnetic field toward the liner wall. At distances of $R =$ 24, 28, and 33 cm, the energy density decreased to 80, 46, and 21 J/cm^2, respectively.

The targets intended for irradiation with a plasma were inserted into the cusp in the radial direction and could be positioned at different distances R from the system axis. All the experiments described in this paper, except for an experiment with a wire mesh target and an additional experiment with graphite, were conducted at the normal incidence of the plasma flow onto the target.

4. EXPERIMENTAL RESULTS

Under our experimental conditions, the energy transferred to the shielding layer can be expended on the following processes: a fraction of energy reaches the surface and is spent on heating the target and evaporating a thin layer on its surface, and the remaining energy should be either radiated from the shielding layer into the surrounding space or stored in this layer as internal plasma energy. A significant role of radiation motivated the use of relevant diagnostics such as radiation calorimetry and soft X-ray (SXR) spectrometry. In addition, we measured the target heating and studied the erosion craters on the target surface. Using these diagnostics, we could clarify the role of each of the above processes in the total energy balance.

4.1. Radiative Losses from the Shielding Layer

In order to investigate the role of radiative losses in the interaction energy balance, we used radiation calorimetry and SXR spectrometry.

4.1.1. Radiation calorimetry. To determine the integral (over the spectrum and time) radiative losses from the surface plasma layer, we used a highly sensitive thermocouple radiation calorimeter [4], in which an aluminum-oxide film served as a calorimeter receiver. The measured absorption coefficient of this coating is no less than 98% for the radiation in the range 4 Å $< \lambda < 12$ μm, except for the VUV spectral region $200 < \lambda < 2000$ Å, in which absolute calibration was not performed. For the latter region, the theoretical estimates of the absorption coefficient give the value ≥85% [4].

The arrangement of the radiation calorimeter is shown in Fig. 2. The collimator axis was adjusted to a point located at a distance of $R_0 = 18$ cm from the system axis. By displacing the target along the radius R from shot to shot, we could collect the radiation from the plasma layer regions lying at the distance $X = R - R_0$ from the target surface. The spatial resolution of the collimator along the X-axis was $\delta = 0.5$ cm. In the transverse direction (i.e., along the system axis), the calorimeter viewing field was equal to 31 mm, which was substantially larger than the plasma flow width.

As targets, we used tungsten, copper, or graphite (the POCO brand) samples up to 5 cm long. As was shown previously in [2], the shielding layer plasma moves primarily along the magnetic field lines. Consequently, the radiating region is limited in two directions perpendicular to the magnetic field: in one direction, the size is limited by the target length L, and, in the other direction, it is limited by the layer thickness d, which can vary for different targets within the range 12–25 mm. The size of the radiating region along the third coordinate is determined by the parameters of the shielding layer and, as will be shown below, depends strongly on the charge number Z of the target material. Note that the width of the shielding layer was larger than that of the deuterium plasma flow and could vary with distance from the target, $d = d(X)$. Nevertheless, in all cases, the calorimeter collected radiation over the entire layer width. Consequently, when recalculating the radiated energy from the calorimeter readings, the knowledge of the layer thickness is only required if the radiation is not volume in character. Such a correction was made only when calculating the radiation from a tungsten plasma.

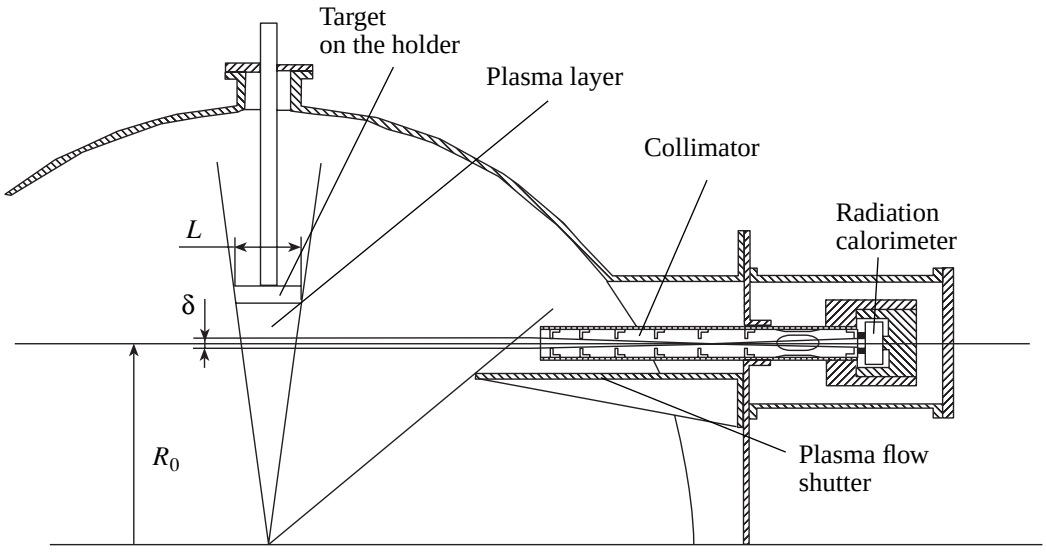

Fig. 2. Layout of radiation calorimetry.

When analyzing the plasma radiative characteristics, it is convenient to use a reduced quantity in intermediate calculations, namely, the emittance per unit volume ε. Hereinafter, when using the notation ε, we mean that the corresponding data are calculated for an optically transparent plasma. When dealing with a nonzero optical thickness, we will use the quantity ε_{eff}. In the final form, it is more convenient to use the quantity εd (or $\varepsilon_{\text{eff}} d$), which is proportional to the calorimeter signal and does not depend on the layer width.

Tungsten. Curve *1* in Fig. 3 shows the quantity εd as a function of the distance X from a tungsten target of length $L_1 = 5$ cm. It is seen that, most of the energy is radiated from the first 2–3 cm of the surface layer. In order to analyze the shape of the radiative loss curve not only qualitatively, but also quantitatively, we should have information on the optical plasma thickness. This is important for recalculating the calorimeter energy to the energy radiated by the layer in all directions. To estimate the optical thickness, we carried out an experiment with a target of length $L_2 = 2.2$ cm (Fig. 3, curve *2*). Curves *1* and *2* almost coincide for the distances $X > 1$ cm. This points to the fact that, at such distances, the plasma is almost transparent for radiation at the wavelengths characteristic of radiative losses. Near the target ($X < 7$ mm), the curves differ substantially, which indicates that it is necessary to take into account the finite optical thickness of the plasma layer. The required direct measurements of the radiating layer thickness $d(X)$ were performed with an SXR spectrograph and will be described in detail in Section 4.1.2.

Let us consider the radiating layer as a superposition of a volume source and a surface source. The radiative

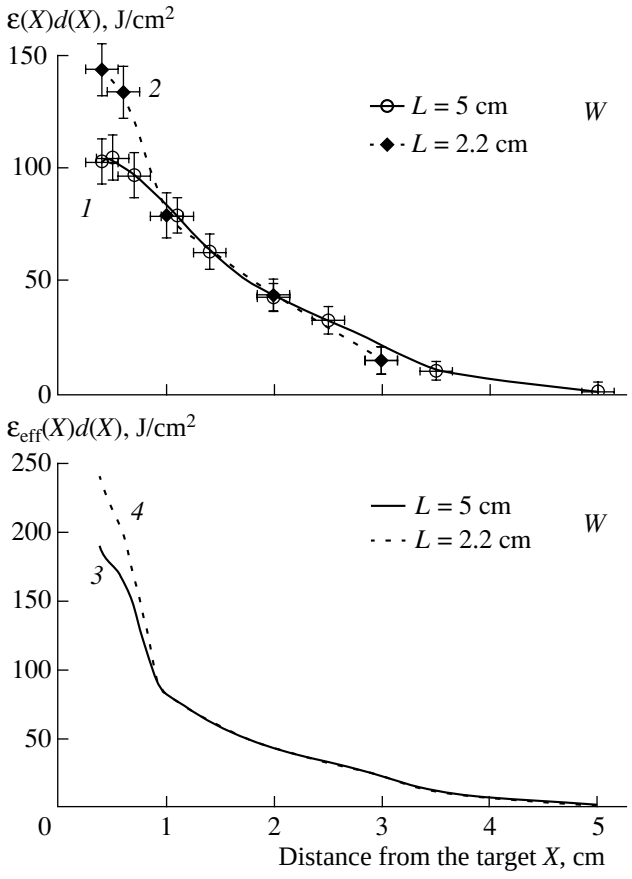

Fig. 3. Radiative losses from the plasma near a tungsten target calculated (*1*, *2*) under the assumption that the plasma optical thickness is zero and (*3*, *4*) taking into account the finite plasma optical thickness. The target length L is equal to 5 cm for curves *1* and *3* and 2.2 cm for curves *2* and *4*.

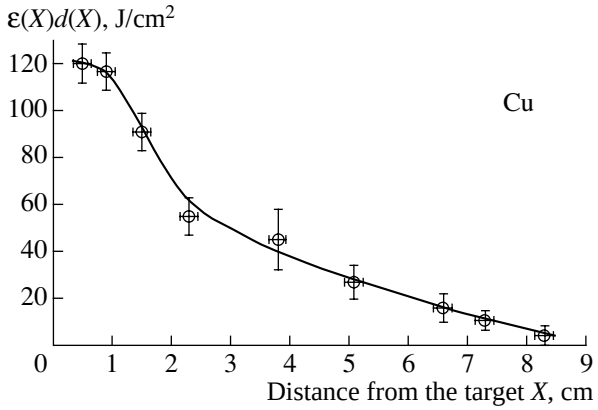

Fig. 4. Radiative losses from the plasma near a copper target 4 cm long. The curves are calculated under the assumption that the plasma optical thickness is zero.

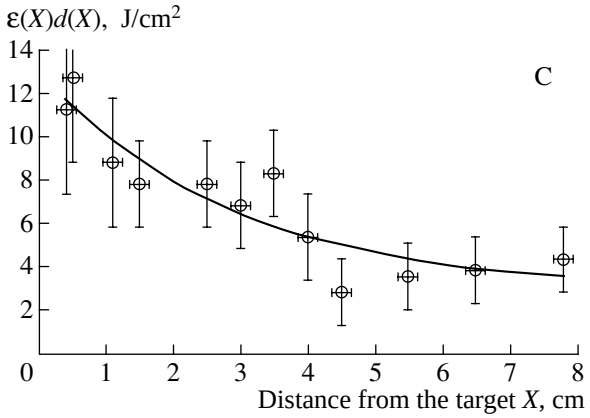

Fig. 5. Radiative losses from the plasma near a graphite target 5 cm long. The curves are calculated under the assumption that the plasma optical thickness is zero.

loss power from a layer of thickness dX is equal to

$$dE(X) = dE_V(X) + dE_S(X) = \varepsilon_V(X)dV + K(X)dS$$
$$= \varepsilon_V(X)Ld(X)dX + K(X)2(L + d(X))dX,$$

where $\varepsilon_V(X)$ is the emittance per unit volume of the first source and $K(X)$ is the surface emittance of the second source. It is assumed that ε_V and K are independent of the target length. We define the effective emittance ε_{eff} as $dE(X) = \varepsilon_{\text{eff}}(X)Ld(X)dX$. Then, we obtain

$$\varepsilon_{\text{eff}}(X) = \varepsilon_V(X) + \frac{2(L + d(X))}{Ld(X)}K(X). \qquad (1)$$

The energy received by the calorimeter from a layer of thickness dX is equal to

$$dA = dA_V + dA_S = \frac{\Omega}{4\pi}dE_V$$
$$+ \frac{\Omega}{\pi}\frac{d}{2(L + d)}dE_S = \frac{\Omega}{4\pi}Ld\left(\varepsilon_V + \frac{4}{L}K\right)dX,$$

where Ω is the collimator angular aperture.

The emittance ε calculated for an optically thin plasma is given by the equality $dA = \frac{\Omega}{4\pi}\varepsilon Ld dX$. Consequently, we have $\varepsilon(X) = \varepsilon_V(X) + \frac{4}{L}K(X)$. Denoting $\varepsilon(X)$ for targets of length L_1 and L_2 as $\varepsilon_1(X)$ and $\varepsilon_2(X)$, we obtain a set of two equations from which it follows

$$\begin{cases} \varepsilon_V(X) = \dfrac{\varepsilon_1(X)L_1 - \varepsilon_2(X)L_2}{L_1 - L_2}, \\ K(X) = \dfrac{L_1L_2(\varepsilon_2(X) - \varepsilon_1(X))}{4(L_1 - L_2)}. \end{cases} \qquad (2)$$

Curves *3* and *4* in Fig. 3 show the results of calculations of $\varepsilon_{\text{eff}}(X)d(X)$ by formulas (1) and (2). In comparison with curves *1* and *2*, respectively, the profiles become steeper; more than one-half of the energy is now radiated from the first centimeter of the plasma layer. At distances of $X < 7$ mm, about two-third of the energy is radiated by the "surface source" and one-third is radiated by the "volume source." When analyzing the energy balance, the energy density Q in a deuterium flow should be compared with the quantity $Q_{\text{rad}} = \frac{1}{d_0}\int\varepsilon_{\text{eff}}(X)\,d(X)dX$, i.e., the energy radiated by the plasma layer per unit area of the flow cross section. For a tungsten target, we have $Q_{\text{rad}} = 240$–280 J/cm^2.

Copper. The emittance of the copper plasma, as well as that of the tungsten plasma, has a pronounced peak near the target surface (Fig. 4). The maximum value $\varepsilon(X)d(X) = 120$ J/cm^2 is comparable with the corresponding value for a tungsten target. At the same time, the half-width of the curve for copper is nearly two times as large as that for tungsten and amounts to $\Delta X = 3$ cm. As a result, the radiative losses from the copper plasma layer are substantially greater. Calculations show that, without taking into account radiation trapping, these losses are equal to $Q_{\text{rad}} = 350$ J/cm^2.

POCO Graphite. The emittance of the carbon plasma (near a graphite target of length $L = 5$ cm) is much lower than the emittance of the tungsten or copper plasmas (Fig. 5). The peak near the surface is less pronounced. As the distance from the surface increases, the value of $\varepsilon(X)d(X)$ decreases by a factor of about 3; at $X \approx 4$ cm, it arrives at a plateau 4 J/cm^2 high, which continues at least to $X \approx 8$ cm. Moreover, the measurements show that, even for $X = 12.5$ cm (when $R = 30.5$ cm and the deuterium flow energy density is as low as $Q = 30$ J/cm^2), the radiative losses still are significant: $\varepsilon(X)d(X) \approx 3$ J/cm^2.

The data obtained confirm that the shielding layer near the graphite surface can be divided into two regions: a dense plasma ($n_e \geq 10^{17}$ cm^{-3}) near the surface ($X < 1$ cm) and a plasma corona, i.e., the region of a relatively rare plasma, which rapidly flows away from the surface and whose density and temperature are always nearly uniform (e.g., at $t \approx 8$ μs, the corona density and temperature are $n_e = 5 \times 10^{16}$ cm^{-3} and $T_e =$ 80 eV [2, 3]). A plateau on the emittance curve corresponds to the plasma corona.

Unfortunately, because of a low level of the valid signal against the background measured in the absence of a target, we could not obtain the data on the optical thickness of the plasma layer by shortening the target length, as was done for tungsten. To roughly estimate the character of the generation of the radiation received from the layer $X < 4$ cm, we carried out a separate experiment in which the normal to the target was inclined at an angle of 30° to the plasma flow axis. In this case, the target surface irradiated with a plasma was facing the calorimeter and we measured the radiation from different regions of the plasma layer lying over the target.

Because of the target inclination, the density of the energy flux onto the surface varied only by 14%, so that we could use the data presented in Fig. 5 in our analysis. In this experiment, the expected curves of the surface layer brightness should depend on the assumed radiation source. If radiation is surface in character, then the target inclination would have no effect on the calorimeter readings. If radiation is volume in nature, then the calorimeter readings near the target would be smaller because the plasma volume viewed by the calorimeter is narrower. In particular, we should consider the third characteristic situation with a thin ($\Delta X <$ 0.5 cm) intensively radiating layer adjacent to the target. In this case, the radiation is emitted from the layer surface, whereas the bulk plasma ($0.5 < X < 4$ cm) radiation is volume in character. The latter case deserves a particular consideration, because it is necessary to verify the assumption of [3] that a substantial fraction of the shielding layer energy can be reemitted by lithium-like carbon ions in the region of the first radiation maximum of a carbon plasma, which corresponds to a plasma temperature of ~5 eV [5]. In the experiments described in this paper, such a temperature, according to [3], can be attained only in the region lying no farther than 2 mm from the surface. If such a thin, intensively radiating layer does exist, then most of the energy should be radiated from its face parallel to the exposed target surface. When a graphite target is in the horizontal position, the calorimeter does not "sight" this radiation and the method for recalculating the radiative losses from the calorimeter signal, which was used to draw Fig. 5, can give a significantly underestimated value of the radiative loss power. A small turn of the target makes the bright face visible. As the target surface is approached, the calorimeter readings will first almost coincide with those for a horizontal target; however, they will increase rapidly when the bright face will fall into the calorimeter viewing field.

The calorimeter signals indicate that, at short ($X <$ 2 cm) distances from the target, the plasma radiation can be associated with a surface source; further, the experimental points better fit the curve calculated for a volume source. In any case, the existence of an optically thin layer adjacent to the target surface was not proved experimentally. The fact that, at distances of about 2–3 cm from the target, the radiation generation gradually takes the features of surface radiation does not lead to significant errors in determining the radiative losses from a horizontal target because, in this case, the area of the front face (parallel to the target surface) of the optically thick layer adjacent to the target is three to six times smaller than the area of the side faces (it is the radiation from these side faces that is measured in the case of a high plasma optical thickness).

Using the data presented in Fig. 5, we can determine the radiative loss power. If only the first 7 cm of the shielding layer are taken into account and the plasma optical thickness is assumed to be small, the radiative losses can be estimated as $Q'_{\text{rad}} = \frac{1}{d_0}\int_0^{7\text{ cm}} \varepsilon(X)\, d(X) dX \approx$ 40 J/cm^2. Assuming that the plasma within the first 2.5 cm radiates as a surface source, we obtain the upper estimate $Q'_{\text{rad}} < 70$ J/cm^2.

4.1.2. SXR spectroscopy. The radiative losses in the short-wavelength spectral region were measured by an SXR spectrograph with a 5000-line/mm gold transmission grating. The geometry of the experiments is similar to that in Fig. 2. Targets with a length of $L = 5$ cm and width of 3.5 cm were positioned at $R = 18.5$ cm. The spectra were measured at different distances X from the target. The spectrograph viewed the region $R = 12$–19 cm. Along the system axis, the spectrograph was adjusted to the center of the plasma flow. The spatial resolution of the spectrograph was 2.5 mm along the X-axis and 2 mm along the system axis, the spectral resolution was 1.5 Å, and the linear dispersion was 13 Å/mm. The spectral interval $10 < \lambda < 400$ Å was analyzed. The time-integrated spectrum was recorded directly on a Kodak 101-01 X-ray film. The time-resolved spectra were obtained with the help of a single-frame camera based on a microchannel plate (MCP). The X-ray emission was converted into the visible image with the help of a pulsed MCP camera [6] and recorded on a Kodak 2484 film. The time resolution of the measurements was 100 ns.

Figures 6 and 7 show the integrated (over the spectral region $\lambda < 400$ Å) plasma brightness in front of tungsten and graphite targets. The curve in Fig. 6 was obtained by analyzing the time-integrated spectrum, and the curve in Fig. 7 is obtained by integrating seven

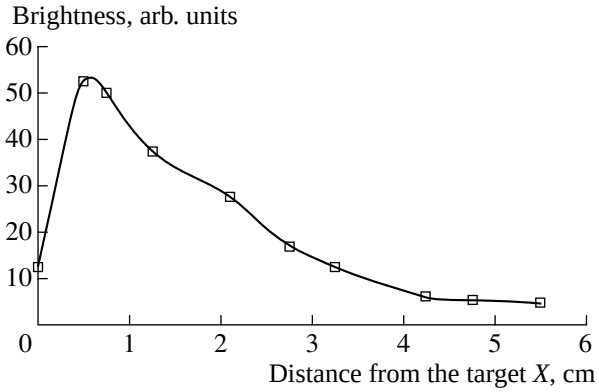

Fig. 6. Plasma brightness integrated over the spectral region $\lambda < 400$ Å near a tungsten target.

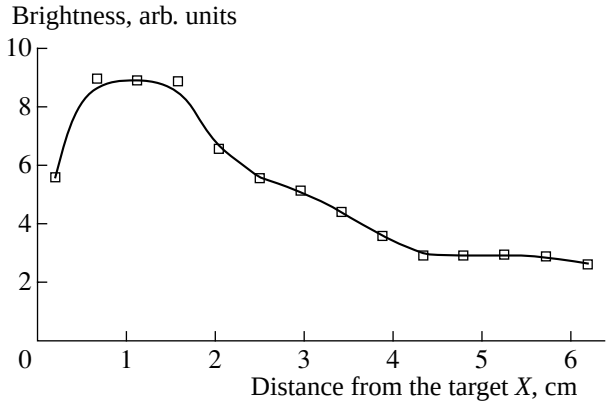

Fig. 7. Plasma brightness integrated over the spectral region $\lambda < 400$ Å near a graphite target.

instantaneous spectra of a carbon plasma at different times $t = 2$–13 μs.

In the case of an optically thin plasma, the surface brightness is proportional to the plasma emittance. In view of this fact, we can compare curve *1* in Fig. 3 with the curve in Fig. 6 and also the curves in Figs. 5 and 7. A comparison shows that, for both materials, the behavior of the corresponding curves at distances of $X >$ 0.5 cm is very similar. Hence, for both tungsten and graphite, the radiative losses in the range $\lambda < 400$ Å are proportional to the radiative losses integrated over the spectrum. Closer to the surface, at distances of $X < 0.2$–0.4 cm, the short-wavelength radiative losses decrease, which is probably due to the fact that the temperature drops sharply and, consequently, the spectrum shifts toward longer wavelengths. At the same time, it is probable that the integrated radiative losses near the surface $X < 0.3$ cm also have a tendency to decrease. This assumption does not contradict the data from radiation calorimetry, because the spatial resolution of the method (5 mm) does not permit accurate measurements in the immediate vicinity of the target. However, because of the small thickness of this region, the behavior of the radiative loss curve within it cannot substantially influence the calculated value of the energy radiated from the plasma layer, even in the case of a tungsten plasma.

To determine the width of the shielding layer near a tungsten target, the spectrograph was turned through 90°. In this case, we measured the spectra by varying the spatial coordinate along the system axis at a fixed distance from the axis $R_0 = 16$ cm. Then, in a series of successive shots, the target was placed at different radii R, which allowed us to determine the shielding layer width as a function of the distance $X = R - R_0$ from the target surface. It turned out that the width d of the radiating region was 25 mm near the surface and, then, decreased gradually as the distance from the target increased. At $X = 25$ mm, it became comparable with the width of a free deuterium flow, $d_0 = 11$ mm. In the foregoing, this result was used to calculate the radiative losses from a tungsten plasma.

4.1.3. Experiment with a mesh target. In this experiment, we used a 5×5-cm stainless-steel wire mesh as a target. The mesh was mounted in the holder so that its normal was at an angle of $\alpha = 55°$ to the axis of the plasma flow. (In other words, the target shown in Fig. 2 was turned in the figure plane in the counterclockwise direction through an angle of $\alpha = 55°$.) The mesh was made of stainless steel, the mesh cell size was 0.7 mm, and the mesh transmittance was $T = 80\%$. Interferometer measurements [2] demonstrated that, when such a mesh was used instead of a solid stainless-steel target, the parameters of the shielding layer, such as the formation time, the geometric dimensions, and the electron plasma density did not change. It may be suggested that the meshy structure of the target affects only slightly the processes occurring in the plasma layer. Consequently, the radiation fluxes near the target also change slightly in this case. The plasma observed through the mesh has the same characteristics as the plasma in front of the mesh wires at a distance of $X = 0.3$ mm from them (which is about one-half of the cell size). Thus, using the mesh target, we could determine the energy characteristics of radiation at a distance of $X \approx 0.3$ mm from the target.

The radiation calorimeter measured radiation from the front side (A) (i.e., the surface facing the plasma) and rear side (B) of the mesh. The energy radiated from unit area (normal to the measurement direction) of the source within unit solid angle (i.e., the surface brightness) was equal to $W_A \approx 8$ J/(cm^2 sr) for the front side and $W_B \approx 5.7$ J/(cm^2 sr) for the rear side of the mesh (taking into account the effective mesh transmittance $T_{eff} = 75\%$ in the measurement direction). The difference between W_A and W_B indicates that the plasma in front of the target surface cannot be considered optically thin.

If radiation is surface in character, then the energy density transferred by photons onto the mesh surface is

equal to $Q_{rad} = \pi W_B \approx 18$ J/cm^2. It is reasonable to compare the value of Q_{rad} with the energy density absorbed by the target Q_h. For $R = 24$ cm, when the plasma flow energy density is close to the density of the energy flux incident onto the inclined mesh target, the energy density absorbed by a solid stainless-steel target is equal, as will be shown below, to $Q_h = 21$ J/cm^2. Consequently, we have $Q_{rad} \approx Q_h$; i.e., the energy transferred by photons to the $X = 0.3$ mm plane almost coincides with the energy reaching the surface of the stainless-steel target.

Most likely, the energy is transferred to the surface predominantly by photons. A mechanism alternative to radiative transfer is electron heat conduction. For heat conduction to ensure the power flux with a density on the order of 1 MW/cm^2 (which is equivalent to 20 J/cm^2 for 20 μs) from the plane $X = 0.3$ mm onto the surface, the electron temperature at a distance of $X = 0.3$ mm should be no lower than 10 eV. Here, we assume that the thermal conductivity is classical; otherwise, the required temperature would be even higher. However, even at $T_e = 10$ eV, the plasma density would be no higher than $\frac{P}{T_e} = 4 \times 10^{17}$ cm^{-3}, where $P \approx 6$ atm is the plasma pressure in the shielding layer. On the other hand, the interferometric measurements [2] show that, for high-Z targets, the plasma density at distances of $X < 1$ mm from the target surface is at least 10^{18} cm^{-3}. Hence, we can conclude that the electron heat conduction cannot ensure such a high power flux as that transferred to the plane $X = 0.3$ mm by radiation. Therefore, radiation transfer plays a decisive role in the energy transfer onto the surface of the irradiated stainless-steel target. For other high-Z materials, the energy transfer mechanism is probably the same. This is confirmed by the fact that all of the studied characteristics of the shielding layer are similar near targets made of such materials.

4.2. Surface Erosion

To determine the energy expended on the target surface erosion, we inspected the surface profiles of graphite, tungsten, and copper targets (the graphite target was inspected after 40 shots, and the tungsten and copper targets were inspected after 18 shots). The graphite erosion crater was ~8 μm deep, which corresponded to an erosion rate of 0.2 μm/shot. The half-width of graphite erosion craters was 6 mm, and the full width (at a level of 0.1) was 11 mm. The erosion profile for tungsten was much wider; its full width exceeded 20 mm, which may be explained, probably, by the action of radiation from the shielding layer. Because of a complicated relief of the crater bottom, which consists of many sharp peaks and cavities, we can only evaluate the average thickness of the eroded material, which amounts to ~3 μm, i.e., 0.15 μm/shot. A substantial (≈100 μm) depth of the crater on the copper target is explained primarily by the splashing of a copper melt. Comparing the erosion crater volume with the volume of the material pressed out onto the target edges, we can roughly estimate the evaporated material thickness. This is no larger than 10 μm; i.e., the erosion rate is ≤0.5 μm/shot. The energy required to evaporate a layer of this thickness is equal to $Q_{vap} = 1.5$ J/cm^2 for tungsten, $Q_{vap} = 2$ J/cm^2 for graphite, and $Q_{vap} \le 3$ J/cm^2 for copper.

4.3. Target Heating

We measured the energy spent on the heating of targets made of tungsten, copper, stainless steel (the 12X18H9T brand), aluminum, or graphite (the EK-98 brand). For this purpose, a target made of a given material and shaped as a cylinder 10 mm in height and 25 mm in diameter was placed at different radii R and the change in its temperature after irradiation and uniform heating was measured. The target diameter was equal to the diameter of the integral calorimeter measuring the plasma flow energy Q. The cylindrical surface of the target was screened from the plasma flow. The data obtained are listed in Table 2, which presents the energy density Q_h[J/cm^2] spent on heating and a fraction of this energy in the total energy balance Q_h/Q.

The analytical solution of a model problem of heat transfer in a homogeneous slab shows that, when the heat flux W acts on the sample surface (we assume that $W(t) = \text{const}$), the flux $W_h(t)$ directed inward the sample is equal to

$$W_h(t) = \begin{cases} W, & t \le t_m = \dfrac{\pi}{4}\rho\kappa c\left[\dfrac{T_{max} - T_0}{W}\right]^2, \\ \dfrac{2}{\pi}W \arcsin\sqrt{\dfrac{t_m}{t}}, & t > t_m, \end{cases} \quad (3)$$

where ρ is the mass density, κ is the thermal conductivity, c is the specific heat (we assume that $\kappa(T) = \text{const}$ and $c(T) = \text{const}$), T_{max} is the maximum attainable (boiling or sublimation) temperature, and T_0 is the initial surface temperature.

Table 2

	R = 18 cm, Q = 130 J/cm^2	R = 24 cm, Q = 80 J/cm^2	R = 28 cm, Q = 46 J/cm^2	R = 33 cm, Q = 21 J/cm^2
W	48 (37%)	46 (58%)	29 (63%)	20 (100%)
Cu	39 (30%)	29 (36%)	20 (43%)	21 (100%)
Stainless steel	24 (18%)	21 (26%)	16 (35%)	10 (50%)
Al	26 (20%)	20 (25%)	15 (33%)	7 (33%)
Graphite	17 (13%)	16 (20%)	12 (26%)	9 (43%)

Table 3

	Θ	Q_h/Θ		
		R = 18 cm	R = 24 cm	R = 28 cm
W	1	48	46	29
Cu	0.86	45	34	23
Stainless steel	0.29	83	72	55
Al	0.45	58	44	33
Graphite	0.36	47	44	33

For $t \gg t_m$, we have

$$W_h(t) \approx \sqrt{\frac{\rho\kappa c}{\pi}}\frac{T_{\max} - T_0}{\sqrt{t}}. \quad (4)$$

According to formula (4), the energy absorbed by a target depends on its thermalphysical characteristics as $Q_h \propto \sqrt{\rho\kappa c}\,(T_{\max} - T_0)$. Using the values of thermalphysical constants calculated from the literature data [7–10] averaged over the temperature interval 300 K–$T_{\max}$ (at P = 5 atm), we obtain the following ratios of the absorbed energy in different materials: W : Cu : stainless steel : Al : graphite = 1 : 0.86 : 0.29 : 0.45 : 0.36. The factor Θ introduced in this way allows us to represent the data of Table 2 in a form convenient for comparison (see Table 3).

For each target position R = 18, 24, and 28 cm, the value of Q_h/Θ is nearly the same for all of the materials, except for stainless steel. Therefore, the experimental data obtained, as a whole, agree well with model formula (4) for each energy density Q = 130, 80, and 46 J/cm^2. Only the stainless-steel target absorbs significantly higher (by 70%) energy than that predicted by the model. One of the possible reasons is that the surface layer of the stainless-steel target is modified so that the initial concentration of chromium atoms in it decreases as compared to the initial concentration equal to 18%. As a result, the thermalphysical characteristics of the surface layer can become close to those for pure iron, which might substantially increase the power transferred via heat conduction from the surface.

The experimental fact that Q_h decreases as Q decreases is explained by a specific feature of our plasma device; namely, as Q decreases, the time of the shielding layer formation t_{form} becomes comparable with the plasma flow duration τ. The fact that Q_h indeed decreases can easily be demonstrated as follows. Let us consider two limiting cases, $\tau \gg t_m$ (the shielding layer forms instantaneously) and $\tau = t_m$ (the thermal evaporation begins only by the end of the plasma pulse). In the former case, it follows from formula (4) that $Q_h = \int_0^\tau W_h(t)dt \approx \sqrt{\frac{4\rho\kappa c}{\pi}}(T_{\max} - T_0)\sqrt{\tau}$. The latter case, according to formula (3), we have $W_h = W = \sqrt{\frac{\pi\rho\kappa c}{4\tau}}(T_{\max} - T_0)$ and, consequently, $Q_h = W_h\tau \times \sqrt{\frac{\pi\rho\kappa c}{4}}(T_{\max} - T_0)\sqrt{\tau}$. Hence, in the latter case, the target absorbs about one-fourth of the energy absorbed in the former case. In the real experiment, the heat flux W varies significantly with time; however, the tendency of Q_h to decrease with increasing t_{form} should remain under these conditions too.

As Q decreases, the time it takes for the target surface to be heated to the temperature $T_{\max}$ increases rapidly and becomes longer than the plasma pulse. The measurements carried out with tungsten and copper targets at Q = 21 J/cm^2 (the calculated heating times are t_m = 110 and 70 μs, respectively) show that no shielding layer is formed in this case and the targets absorb all the energy flux that fall onto them. This follows from the fact that the Q_h values are the same for both targets and that Q_h for each target coincides with Q. (The latter fact, if considered separately, could not be a proof that the energy is totally absorbed, because the energy incident on the target can be somewhat different from the energy Q of the free flow; see Section 5 for details.) This means that, under our experimental conditions, the accommodation coefficient of the deuteron energy is close to unity even for such a heavy element as tungsten, which has the minimum energy accommodation coefficient at a given deuteron energy [11, 12].

At a somewhat shorter calculated heating times, e.g., for t_m = 24 μs (a tungsten target at Q = 46 J/cm^2) or t_m = 23 μs (an aluminum target at Q = 21 J/cm^2), the irradiated surface absorbs no more than 50–65% of the energy, which indicates the existence of a shielding layer under these conditions. The appearance of metal vapor in this case is probably due not to thermal evaporation, but to the bombardment of the heated surface by high-energy deuterons of the plasma flow. (At $Q \geq$ 100 J/cm^2, the collisional sputtering by deuterons also takes place, but it is not dominant.) The sputtering occurs at energies higher than the threshold energy $E_{thr} \approx \frac{U_o M_a}{4M_i}$ [13], where U_0 is the bonding energy of surface atoms, M_a is the atomic mass, and M_i is the mass of the bombarding ion. As an example, for Al and W, we have U_0 = 3.3 and 8.8 eV, respectively. The threshold energy for these materials is in the range E_{thr} = 20–200 eV, which is substantially lower than the characteristic energy of plasma flow deuterons, $E \approx$ 0.3–0.8 keV, so that the sputtering can take place. As the target is heated, the efficient sputtering of the surface by bombarding ions begins when the surface temperature reaches a value of $T^* \approx U_0/40$; then, the sputtering coefficient increases exponentially [12, 14]. For different materials, the time t^* it takes for their surface to be heated to the temperature T^* varies from $0.05t_m$ for alu-

minum to $0.21t_m$ for graphite. In addition, it is necessary to take into account the time required for the sputtered atoms to be produced in an amount sufficient for the shielding effect. Most likely, in the experiments under discussion, the plasma pulse duration was longer than the total time of the shielding layer formation; consequently, only a fraction of the heat flux reached the surface.

Hence, the observed dependences of the heating energy density Q_h on the plasma flow energy density Q and the target material can be explained on rather simple assumptions that the heat is transferred into the target through heat conduction and that, as Q decreases, the sputtering (rather than evaporation) becomes a dominant mechanism for the production of atoms forming the shielding layer.

5. ENERGY BALANCE

The results obtained allows us to conclude that the radiative losses make the main contribution to the energy balance. Most of the energy is radiated even in the stage when the plasma column temperature is relatively high and the energy is supplied by the plasma jet flowing out of the LCT. Let us demonstrate this. As an example, we consider a plasma at a distance of $X = 3$ cm from the graphite target at the instant $t = 25$ μs from the beginning of interaction. At that time, we have $T_e \approx T_i \approx$ 20 eV and $n_e \approx 10^{16}$ cm^{-3} [3]. The energy density contained in the plasma column is $\varepsilon_p < \frac{3}{2}(n_eT_e + n_iT_i) + \sum_j n_j \sum_{k=1}^{\langle Z_j\rangle(T_e)} E_{kj} + \frac{1}{2}\sum_j n_j E_{(\langle Z_j\rangle(T_e)+1)j}$, where n_j is the density of the jth plasma ion species, $n_i = \sum_j n_j$, E_{kj} is the bonding energy of the kth outer electron of the jth element, and $\langle Z_j\rangle$ is the average ion charge number of the jth element. The third term is introduced into the formula in order to take into account (by the order of magnitude) the maximum possible contribution from excited levels to the potential energy. This can be important when considering a recombining plasma. To estimate the maximum plasma energy, we will use the overestimated data on the carbon content in the plasma column: $n_C = n_D$ [15], from where, taking into account that $\langle Z_C\rangle = 4$, we have $n_C \approx 2 \times 10^{15}$ cm^{-3} and $n_D \approx 2 \times 10^{15}$ cm^{-3}. Calculations yield $\varepsilon_p < 0.18$ J/cm^3. An analysis of the experimental data (Fig. 5) shows that the radiative losses from the graphite plasma are about 30 times higher than the plasma energy. Hence, the target plasma is a peculiar kind of converter, which does not store the deuterium flow energy, but converts it into radiation while the energy is supplied from the plasma jet.

As was already mentioned above, for both tungsten and graphite, the radiative losses in the range $\lambda < 400$ Å are proportional to the total radiative losses integrated over the entire spectrum. From the available experimental data, we cannot determine the proportionality factor. However, calculations performed for our experimental conditions show that this factor is close to unity [15, 16]; i.e., it is the short-wavelength range $\lambda < 400$ Å that determines the radiative losses from the target plasma at all distances (maybe except for a narrow layer adjacent to the surface).

Comparing the values of Q and Q_{rad}, we can notice the large difference between them. Note that, for tungsten and copper, we have $Q < Q_{\text{rad}}$, whereas for graphite, we have $Q > Q'_{\text{rad}} + Q_h$.

The fact that $Q < Q_{\text{rad}}$ for heavy elements indicates that either the emitter has some peculiarities not taken into account in our consideration or its characteristics are affected by the presence of a target in the plasma flow. In principle, for targets made of high-Z materials, the energy that falls into the radiation calorimeter from the shielding layer may include the additional radiation energy from the secondary plasma produced on the target area that is unaffected by the plasma flow but is exposed to an intense radiation of the layer itself. We have conducted additional experiments with collimation diaphragms that provided different spatial resolution along the device axis. These experiments showed that, in the presence of the secondary plasma, the losses can be somewhat overestimated, but not higher than by 10–15% and only at $X < 1$ cm. Deserving more attention is the second assumption that, in the presence of a target, the energy density of the plasma jet increases at the azimuthal angles where the target is positioned. The energy flow in the annular slot can become strongly inhomogeneous in the azimuthal direction. However, because of the small angular size of the target, the lifetime and parameters of the LCT plasma change insignificantly in the presence of a target and the power density averaged over azimuthal angles also changes only slightly.

In our opinion, the increase in the energy flux onto the target is due to the decrease in the space charge of trapped electrons in the expander (as was shown in [17], this space charge can efficiently suppress the secondary electron emission). The existence of the space charge was confirmed by the direct measurements of the floating potential in the expander [1]. For a substantial fraction of trapped electrons to be produced in the expander, it is necessary that the plasma flow strongly expand before it meets the expander wall or the target. When the target is located near the annular slot, the potential difference between the target and the skin plasma along the magnetic field line turns out to be much less than that between the wall and the skin plasma (along another field line). If the wall and the target are under the same potential, this results in the generation of an electric field drawing the ions onto the magnetic field lines that meet the target. In this case, the energy density Q transferred to the shielding layer var-

ies more strongly with R than is expected from the consideration of the parameters of a free plasma flow. At large distances from the annular slot (e.g., at $R >$ 28 cm), the potential difference in the skin layer between the field lines arriving at the wall and the target is small and the energy transferred to the shielding layer is close to the flow energy. As the annular slot is approached, the potential difference increases rapidly; as a result, at R = 18 cm, Q increases by a factor of 2–3 in comparison with the value calculated for a free jet.

Probably, there are another reasons why the energy transferred to the shielding layer can be underestimated. For example, when the target is positioned near the annular slot, the increase in the electron heat flux due to the increase in the gradient of the electron temperature can be of importance. In our opinion, such an underestimate actually took place because there is no other way to bring in accordance the energy losses from the shielding layer (e.g., for a copper target, $Q_{\text{rad}} \geq$ 350 J/cm^2) and the energy transferred to the layer.

For a graphite target, the thickness of the efficiently radiating layer is significantly larger than for targets made of high-Z materials. This explains why Q'_{rad}, which is the power density of radiative losses from the region ΔX_1 = 7 cm, does not coincide with $Q - Q_h$. In order to radiate the deficient energy $Q - Q'_{\text{rad}} - Q_h \approx$ 300 J/cm^2 (assuming that $Q \approx 350$ J/cm^2), it is necessary that the thickness of the radiating layer be $\Delta X_2 \approx 1$ m. According to [2], the propagation velocity of the corona front is equal to $\sim 4 \times 10^6$ cm/s; hence, the corona of this size, indeed, has time to form for $\Delta t \approx 25$ μs. However, at such a corona size, its most part would fall into the skin region adjacent to the LCT plasma with $\beta \approx 1$ and the high concentration of carbon ions in the corona would result in the intense interaction between the LCT plasma and the corona. The effect of this interaction on the energy transfer to the first seven centimeters of the visible shielding layer is difficult to predict. In this case, the processes associated with the plasma outflow from the LCT and the processes accompanying the interaction of the plasma with the target become closely interrelated and the confinement system can no longer be regarded as an energy source independent of the shielding layer when analyzing the energy balance.

6. CONCLUSION

In this paper, we have presented the results of experiments on studying the energy balance in the interaction of intense high-temperature plasma flows with solid targets. In the experiments, we used a thermalized plasma jet flowing out of an LCT filled with a plasma by means of two high-power pulsed plasma guns. The basic parameters of the free plasma flow are the following: $n_e = 5 \times 10^{15}$ cm^{-3}; T_e = 120 eV; T_i = 600 eV; Q = 130 J/cm^2; and the effective duration is $\tau \approx 20$ μs, which corresponds to an average power density of W = 7 MW/cm^2. When a target is introduced into the flow, a shielding plasma layer is formed near the target surface. The energy flux density transferred to the surface plasma increases several times and, for targets made of high-Z materials, can attain W = 20 MW/cm^2 (which corresponds to Q = 0.3–0.4 kJ/cm^2). Most likely, such an increase in the power density is related to the increase in heat losses from the confinement system in the presence of a target. For low-Z materials, which are characterized by the existence of an extended shielding layer, it is hardly possible to calculate the power transferred to the layer because of the presence of a long corona and, accordingly, a strong effect of the latter on the skin plasma parameters in the confinement system.

The energy transferred to the shielding layer is distributed as follows. Some fraction of the energy, Q_{vap}, reaches the surface of the irradiated target and is expended on the evaporation of the target material, and another fraction, Q_h, is spent on the heating of the noneroded part of the target. For all the materials under study, the energy spent on evaporation is low, $Q_{vap} <$ 4 J/cm^2, which allows one to speak of the shielding properties of the surface plasma layer. The energy spent on the target heating, Q_h, is transferred from the surface through heat conduction and, with the known thermalphysical properties of the material, can be easily calculated. For each material, there is a limiting energy that can be expended on heating at a given duration of the heating pulse. Under our experimental conditions, this energy is equal to $Q_{h\max} \approx 50$ J/cm^2 for tungsten and $Q_{h\max} \approx 20$ J/cm^2 for graphite. As the plasma flow energy density decreases to $Q \leq Q_h$, the shielding layer can still form, but the mechanism for its formation changes from evaporation to sputtering.

A separate experiment with a target made of a stainless-steel wire mesh has shown that, through a plane 0.3 mm distant from the target surface, the energy is mainly transferred by radiation. Estimates show that heat conduction is of minor importance, so that the energy reaching the surface is also transferred predominantly by radiation. Presumably, a similar energy transfer mechanism is also dominant for other high-Z materials. For low-Z materials (e.g., graphite), this conclusion was not proved, because we observed a large electron temperature gradient immediately near the surface [3].

For all of the materials under study, the radiative energy losses play a dominant role in the interaction energy balance: the shielding layer reemits most of the energy supplied by the plasma flow. The spatial distribution of the radiating regions is different for materials with different Z values. Near the tungsten target, the intensively radiating region of width $\Delta X \approx 1.5$ cm is adjacent to the surface. The radiation intensity in this region decreases rapidly with distance from the surface, and the surface radiation gradually changes to the volume radiation. The radiating copper plasma layer lies

farther from the surface, and its characteristic width is $\Delta X \approx 3$ cm. In other respects, the character of radiative losses is very similar to that in the case of a tungsten target. Near the graphite target, the radiative loss curve first smoothly falls with distance from the surface and, at $X \approx 4$ cm, arrives at a plateau. It is the plateau region corresponding to the plasma corona that reemits most of the energy of the deuterium flow. The low emittance of the plasma corona is balanced by its large length (this length is, at least, $\Delta X > 10$ cm, and, according to indirect evidence, it can attain a value of $\Delta X > 50$ cm). For high-Z materials, no radiating plasma corona was observed in the experiments.

A comparison of the experimental data with the results of calculations [15, 16] under our experimental conditions allows us to conclude that radiative losses occur mostly in the SXR spectral region. Hence, we can conclude that the shielding layer plasma near a solid target is an efficient converter of the plasma flow energy into SXR emission. The data obtained show that, for creating a high-power broadband SXR source, the interaction of intense plasma flows with targets made of high-Z materials is of most interest. In this case, it is possible to obtain compact, intensively radiating plasma objects.

REFERENCES

1. N. I. Arkhipov, A. M. Zhitlukhin, V. M. Safronov, and Yu. V. Skvortsov, Fiz. Plazmy **20**, 868 (1994) [Plasma Phys. Rep. **20**, 782 (1994)].
2. N. I. Arkhipov, V. P. Bakhtin, S. G. Vasenin, *et al.*, Fiz. Plazmy **25**, 263 (1999) [Plasma Phys. Rep. **25**, 236 (1999)].
3. N. I. Arkhipov, V. P. Bakhtin, S. G. Vasenin, *et al.*, Fiz. Plazmy **24**, 340 (1998) [Plasma Phys. Rep. **24**, 309 (1998)].
4. B. A. Bryunetkin, V. D. Gladkov, O. V. Kopistko, *et al.*, in *Methods for Studing Spectral and Relaxation Characteristics of Atoms and Ions* (NPO VNIIFTRI, Moscow, 1990).
5. R. Clark, J. Abdallah, and D. Post, J. Nucl. Mater. **220–222**, 1028 (1995).
6. D. A. Toporkov, N. I. Arkhipov, S. G. Vasenin, *et al.*, Prib. Tekh. Éksp., No. 1, 128 (1998).
7. *Handbook of Physical Properties of Steels and Alloys Used in Nuclear Engineering*, Ed. by B. E. Neĭmark (Énergiya, Moscow, 1967).
8. *Handbook of Thermodynamical Properties of Individual Substances*, Ed. by V. P. Glushko (Nauka, Moscow, 1977–1984), Vols. 1–4.
9. Y. S. Touloukian, R. W. Powell, C. Y. Ho, *et al.*, *Thermophysical Properties of Matter (TPRC Data Series)* (IFI Plenum, New York, 1970), Vols. 1, 2.
10. *Handbook of Physical Quantities*, Ed. by I. S. Grigoriev and E. Z. Meilikhov (Énergoatomizdat, Moscow, 1991; CRC, Boca Raton, 1997).
11. M. F. A. Harrison, in *Applied Atomic Collision Physics*, Vol. 2: *Plasmas*, Ed. by H. S. W. Massey, E. W. McDaniel, and B. Bederson (Academic, New York, 1984; Énergoatomizdat, Moscow, 1987).
12. Yu. V. Martynenko, A. I. Ryazanov, O. B. Firsov, and Yu. N. Yavlinskii, in *Reviews of Plasma Physics*, Ed. by M. A. Leontovich and B. B. Kadomtsev (Énergoatomizdat, Moscow, 1982; Consultants Bureau, New York, 1987), Vol. 12.
13. J. Bohdansky, J. Roth, and H. Bay, J. Appl. Phys. **51**, 2861 (1980).
14. Yu. V. Martynenko, in *Advances in Science and Technology, Ser. Plasma Physics*, Ed. by V. D. Shafranov (VINITI, Moscow, 1982), Vol. 3.
15. H. Wuerz, N. Arkhipov, V. Bakhtin, *et al.*, Fusion Technol. **32** (1), 45 (1997).
16. N. G. Karlykhanov, Yu. V. Martynenko, Yu. I. Matveenko, *et al.*, Fiz. Plazmy **22**, 998 (1996) [Plasma Phys. Rep. **22**, 903 (1996)].
17. I. K. Konkashbaev, I. S. Landman, and F. R. Ulinich, Zh. Éksp. Teor. Fiz. **74**, 956 (1978) [Sov. Phys. JETP **47**, 501 (1978)].

Translated by N. F. Larionova

Plasma Physics Reports, Vol. 28, No. 5, 2002, pp. 444–452. Translated from Fizika Plazmy, Vol. 28, No. 5, 2002, pp. 484–492.

LOW-TEMPERATURE PLASMA

Microwave Plasma Torch for Analytical Spectrometry

D. V. Vlasov, K. F. Sergeĭchev, and I. A. Sychev

Institute of General Physics, Russian Academy of Sciences, ul. Vavilova 38, Moscow, 119991 Russia

Received October 17, 2001

Abstract—A microwave argon plasma torch is used to excite the spectra of various materials admixed to the working gas. It is shown that this torch is a very efficient tool for detecting extremely low impurity concentrations in the sample material. An important advantage of the method is the simplicity of testing liquid and dusty samples. The torch design and the device for spectral analysis created at the Institute of General Physics are described. The parameters of the torch plasma are estimated. These estimates agree satisfactorily with the observations of other authors. The spectroscopic studies of impurities in distilled water with the use of a plasma torch showed that the sensitivity of this technique is no worse than 10^{-9}, which is comparable with the sensitivity of inductively coupled plasma devices. © *2002 MAIK "Nauka/Interperiodica".*

1. INTRODUCTION

To produce high-temperature plasma jets, ac or dc arc discharges and gas-plasma torches, exploiting the energy of exothermic reactions, are usually used. Thus, the combustion of hydrogen in the fluorine atmosphere at 10 atm proceeds at a temperature of 4800 K. It is difficult to achieve higher temperatures by means of chemical reactions, because the flame gas is dissociated and, then, ionized. For this reason, the methods for producing high-temperature plasmas in arc torches are usually based on the ohmic heating of the conducting ionized medium, because, in this case, it is possible to attain higher temperatures due to the higher specific energy released in the discharge. For example, temperatures of up to 50000 K were achieved in electric arcs. However, the arcs are not usually used in spectroscopy, because the working gas is strongly contaminated by the vapor of the electrode material undergoing strong erosion. For this reason, RF and microwave discharges are more appropriate for spectroscopy, because they can operate without electrodes; as a result the plasma produced is much more pure.

An RF electrodeless discharge excited in a gas jet flowing out into the atmosphere was implemented by Reed [1] in 1960. This type of discharge is usually referred to as an inductively coupled plasma (ICP) torch. A substantial advantage of this torch is related to injecting the gas tangentially to the wall of a cylindrical quartz tube. Due to the swirling of the gas flow, the discharge is stabilized and is separated from the tube wall. In a similar device providing a 40-kW power deposition in a discharge excited in an air (argon) flow at atmospheric pressure inside a 6-cm-diameter quartz tube at a gas flow rate of up to 1 l/s, temperatures of the effluent plasma of up to 10 000 K were achieved by Yakushin [2]. A theoretical model describing the operation of the ICP torch was proposed by Raĭzer [3], who showed that the processes occurring in the plasmatron are very similar to the combustion in a usual chemical torch. Both models are based on solving the problem of the propagation of an equilibrium discharge wave due to heat conduction or a combustion wave.

As the frequency of the field exciting an electrodeless discharge increases, not only the plasmatron dimensions can be reduced proportionally to the field wavelength, but the specific radiation power deposited in the discharge can also be increased. This circumstance is important for achieving high plasma temperatures in relatively small and inexpensive devices. Due to the progress in microwave electronics achieved in the 1960s, resulting in the development of high-power cw magnetrons, it became possible to create open-flame microwave plasmatrons in the form of a coaxial plasma torch [4]. At first, attempts were made to use such plasmatrons with a power of one to several kW to initiate plasmochemical reactions at high temperatures and to weld small-size refractory-metal pieces in the reducing atmosphere. At present, microwave plasmatrons attract much interest because of their possible applications in plasma chemistry due to the high temperature and electron density in the torch plasma [5].

In recent years, microwave plasmatrons have also found applications in high-temperature spectroscopy as sources for spectral excitation. Thus, in [6], with the help of a coaxial cavity positioned at the edge of a coaxial line fed from a microwave source with a power of 100–300 W at a frequency of 2.45 GHz, a short flame with an electron temperature of 5500 K, an electron density of $\sim 10^{14}$ cm^{-3}, and a gas temperature of ~4000 K was obtained in an argon jet flowing from the cavity into the atmosphere.

2. DESIGN OF THE MICROWAVE TORCH

The design of the microwave torch is shown in Fig. 1. The key element of the torch is a waveguide–

1063-780X/02/2805-0444$22.00

coaxial junction with the transformation coefficient and the voltage standing-wave ratio both close to unity. The rectangular waveguide has a 45×90 mm cross section. The radii of the coaxial feeder of the torch are a = 10 mm and b = 2.5 mm. The feeder impedance, estimated by the formula

$$Z_c = 60\varepsilon_d^{-1/2}\ln(a/b) \quad (1)$$

is equal to $Z_c = 83\ \Omega$. The central tube of the coaxial feeder passes through the rectangular waveguide and, then, through a tunable coaxial stub. The tube is connected to a working-gas balloon via a reduction gearbox. A quartz tube is pasted with a heat-resistant hermetic sealing compound to the shielding tube of the coaxial line in the gap between the feeder and the stub, so that the volume filled with the working gas is isolated from the cavity and the magnetron. The inner tube, through which the working gas is fed, ends with a nozzle forming a plasma jet. In the design of a torch described in [4], the nozzle was made of a refractory metal and the outer tube of the coaxial line was cooled with water. Below, it will be shown that these measures are undertaken merely to protect the torch unit from heat fluxes emergent from the objects treated with the torch. This is not necessary if the torch flame is directed upward, in the direction of the convective flux of the gas heated by the torch. In this case, the nozzle can be made of a metal that has a relatively low melting temperature, because the torch plasma, unlike the arc discharge, does not touch the nozzle itself. In our case, the conical nozzle is made of copper. The torch coaxial feeder is hermetically fixed into a flange that can be connected to a vacuum chamber with quartz windows for the radiation output. The chamber is intended for preventing the penetration of air into the torch flame region when operating with flammable gases. In addition to the torch unit described above, the device also includes a feeding rectangular waveguide connected to the magnetron unit through a protecting ferrite isolator or a circulator. Experiments showed that the microwave torch is, in fact, a load matched to the magnetron, so that the isolator (circulator), which is one of the most expensive components of the transmission line, may be excluded. As a high-voltage power source for the magnetron, we used a modified supply unit for an electric-discharge pump, to which a 5-kV 100-μF capacitor was added to smooth the voltage ripples of the divider bridge circuit. This allowed us to achieve the continuous mode of magnetron operation instead of the pulsed mode used commonly in microwave ovens, in which the amplitude modulation by the rectified mains voltage attains 100%. We also added a filament transformer provided with a high-voltage insulation of its secondary winding.

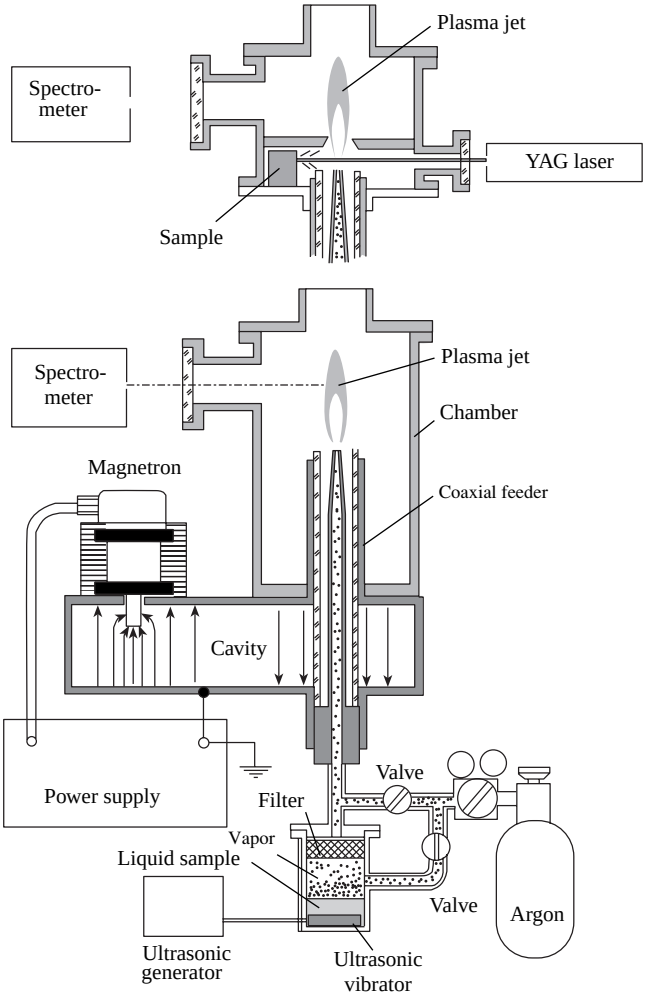

Fig. 1. Design of the microwave torch. The sampling of the material evaporated by a YAG laser (at the top) and the layout of the microwave excitation of the torch and the sampling of liquid with the help of an ultrasonic evaporator (at the bottom).

3. CHARACTERISTIC FEATURES OF THE PLASMA JET PRODUCED BY THE MICROWAVE TORCH

Figure 2 presents photographs of the plasma jet produced by the coaxial microwave torch operating with argon. The gas outflow rate varied from 10 to 50 sccm. The continuous magnetron power was ~850 W. Spectral measurements showed the absence of copper lines in the green spectral region. This allows us to conclude that the copper impurities introduced by the nozzle into the discharge plasma are negligible. When a thin copper wire was inserted into the plasma jet, it was melt, and we observed a characteristic green luminescence of copper. The radius and length of the plasma core were ≈0.1 and ≈1 cm, respectively. As the argon outflow rate was varied, we observed that, at low outflow velocities (<1 m/s), the plasma jet transformed into an interelectrode arc discharge or quenched, whereas at high out-

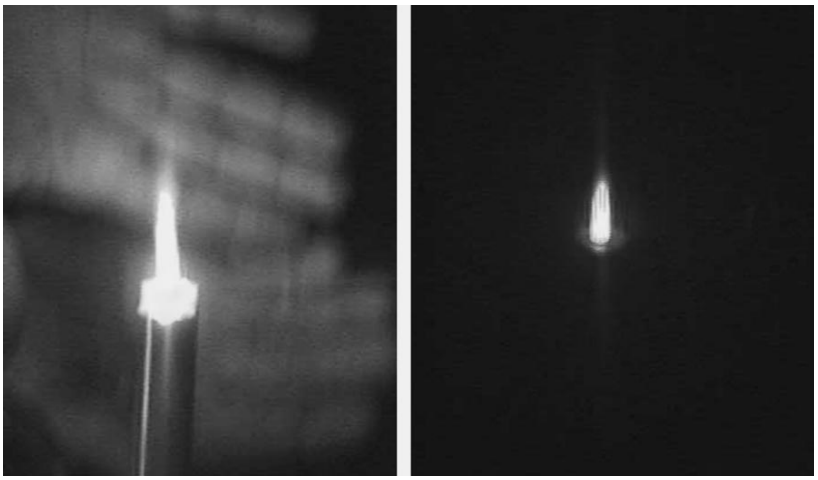

Fig. 2. Photographs of the plasma jet at the outlet from the coaxial line: without filters (on the left) and with a UF-2 filter (on the right).

flow velocities (>>1 m/s), it continued to burn and varied only slightly in size. The fact that the torch unit was heated insignificantly during a long operation time indicates that the heat transfer from the plasma jet to the torch is insignificant. Thus, we can conclude that the slow-combustion regime is realized in the jet, when the heat-conduction wave propagating towards the nozzle is continuously carried away by forced convection in the gas flow. The microwave radiation power scattered by the plasma jet into the surrounding space is relatively low because the intensity of the microwave background at a distance on the order of several tens of centimeters from the jet does not exceed the sanitary standard. This means that the microwave-power absorption coefficient in the plasma jet is close to unity, which, in turn, provides a way of estimating the jet plasma parameters.

4. ESTIMATES OF THE JET PLASMA PARAMETERS

The equivalent circuit of the plasma torch, which contains no special components matching the torch unit to the magnetron, consists of an active resistance and a capacitive reactance connected in parallel. The capacitive reactance is compensated for by tuning the unit, so the active resistance R plays a decisive role in the torch operation. For the optimum power transfer to the load (flame), it is necessary that the impedances of the coaxial line and the plasma jet be equal to each other,

$$Z_c = R\ [\Omega]. \tag{2}$$

The parameters of the jet plasma were estimated as follows. Proceeding from the impedance matching condition (2) and the observed geometric dimensions of the jet, namely, its characteristic length L and radius ρ, we determine the average conductivity of the plasma:

$$\sigma = L/(R\pi\rho^2)\ [\Omega^{-1}\ \mathrm{m}^{-1}], \tag{3}$$

which is related to the electron density n_e and the electron collision frequency ν in the gas (plasma) by the known relationship

$$\sigma = e^2 n_e/m\nu, \tag{4}$$

where e and m are the electron charge and mass, respectively. Here, we use the electrostatics approximation, which is applicable when the electron collision frequency substantially exceeds the angular frequency of the electromagnetic field and the plasma jet length is shorter than the electromagnetic wavelength:

$$\begin{aligned} \nu &\gg \omega = 2\pi f, \\ L &\le \lambda/2\pi = c/\omega. \end{aligned} \tag{5}$$

To calculate the average density n_e, we should know the electron–atom collision frequency ν_a, which depends on both the pressure (i.e., the neutral density) in the gas surrounding the plasma jet and the electron temperature T_e. If the discharge is excited in argon atmosphere under normal conditions and the electron temperature is in the range $0.5 < T_e < 5$ eV, then, according to [6], the dependence $\nu_a(T_e)$ can be approximated by the formula

$$\nu_a\ [\mathrm{s}^{-1}] = 3.3 \times 10^9 p\ [\mathrm{torr}]\ T_e\ [\mathrm{eV}] = 6 \times 10^{10} T_e/T_g, \tag{6}$$

where $p = N_g k T_g$ is the gas pressure, N_g is the atom density, and T_g is the gas temperature in the plasma jet. The physical parameter determining the frequency ν_a is the density N_g, rather than the pressure p. In the transverse direction, the plasma jet is in equilibrium with the surrounding atmosphere: $N_0 T_0 = N_g T_g$. Hence, expression (6) is represented in the form where ν_a is inversely pro-

portional to T_g. In high-temperature discharges, the energy is lost predominantly via radiation:

$$P_r = \varepsilon(T_g)\sigma_0 T_g^4 S, \quad (7)$$

where $\varepsilon(T_g)$ is the emissivity factor, $\sigma_0 = 5.67 \times 10^{-8}$ W/(m^2 K^4) is the Stefan–Boltzmann constant, and $S = 2\pi\rho l$ is the radiating area. Assuming that the input microwave power absorbed in the discharge, P_0, is converted mainly (accurate to the factor ε) into blackbody radiation with the power P_r, we determine T_g:

$$T_g = [P_0/(\varepsilon\sigma_0 S)]^{1/4}. \quad (8)$$

On the other hand, the plasma conductivity in a medium with a high degree of ionization is determined by electron–ion collisions,

$$\nu_{ei} = 2.9 \times 10^{-6} Z N_i \ln\Lambda T_e^{-3/2}, \quad (9)$$

where N_i (in cm^{-3}) is the plasma ion density, Z is the ion charge number, T_e is in eV, and $\ln\Lambda = 5$–20 is the Coulomb logarithm. Most likely, the conductivity in a high-pressure discharge is determined by the frequency ν_a; however, it should be kept in mind that the collision frequency ν_{ei} can also play an important role.

Expressions (3)–(8) allow us to find the dependence $n_e(T_e)$:

$$\begin{aligned} n_e\ [\mathrm{m}^{-3}] &= 2.1 \times 10^{18} \sigma T_e/T_g \\ &= 2.1 \times 10^{18} (T_e/T_g) L/(Z_c \pi \rho^2). \end{aligned} \quad (10)$$

To determine n_e and T_e, we should have one more equation relating these quantities. For estimates not pretending to a high accuracy, we can use the Saha equation [6], which is applicable for an equilibrium plasma with a low degree of ionization ($n_e \ll N_g$) and ions with $Z = 1$:

$$n_e^2\ [\mathrm{m}^{-6}] \approx 4.8 \times 10^{21} (g_+/g_a) N_g T^{3/2} \exp\{-(I/kT)\}, \quad (11)$$

where T [K] is the equilibrium temperature of the medium,

$$T_e = T_i = T_g; \quad (12)$$

$(g_+/g_a) = 6$ for noble gases; and I is the ionization energy (for argon, we have $I = 15.8$ eV). Actually, high-pressure microwave discharges are nonequilibrium and the electron temperature is always higher than the gas temperature. Consequently, when T_e is estimated by the Saha equation (11) in which n_e is determined by expression (10), such an estimate will inevitably result in nonequilibrium temperature values, $T_e > T_g$.

The estimate for T_g obtained by assuming the emissivity factor to be in the range $0.5 \le \varepsilon \le 1$ gives the probable gas temperature range $4000 \le T_g \le 4800$ K. The electron temperature is estimated at $T_e \approx 0.55$ eV $\approx$ 6400 K, which is higher than T_g by a factor of ~1.5. In this case, the electron density that should ensure the optimum conductivity of the jet plasma is equal to $n_e \approx 10^{20}$ m^{-3}. The calculations of the electron collision frequencies by formulas (6) and (9) demonstrated the correctness of the assumption that electron–neutral collisions are dominating: $\nu_a \approx 2.5 \times 10^{11}$ s^{-1}, whereas $\nu_{ei} \le 10^{10}$ s^{-1}.

Let us consider the characteristics of a microwave propagating through the plasma with the above parameters. For this purpose, we will use the formulas presented in [7] for calculating the propagation and attenuation constants ($\beta = 2\pi/\lambda_p$ and α, respectively), as well as the skin depth δ for the case of the normal incidence of a plane wave on a half-space filled with a homogeneous plasma (here, λ_p is the microwave wavelength in the plasma). In the case under consideration, two inequalities are satisfied: $n_e \gg n_c\nu_a/\omega$ and $\nu_a \gg \omega$, where $n_c = m\omega^2/(\varepsilon_0 e^2)$ is the critical plasma density for a given frequency $\omega = 2\pi f$ and ε_0 is the permittivity of a vacuum. Quantitatively, we have n_c [m^{-3}] $= 1.24 \times 10^{16} f^2$ [GHz]. In this case, complicate formulas can be reduced to the form:

$$\beta \approx \alpha \approx (\omega/c)[n_e\omega/(2n_c\nu)]^{1/2}, \quad (13)$$

$$\delta = 1/\alpha. \quad (14)$$

Substituting the above plasma parameters into these formulas, we obtain $\beta \approx \alpha \approx 4.2$ cm^{-1}. From here, we determine the wavelength in the plasma $\lambda_p = 2\pi/\beta \approx 1.5$ cm; over this length, the power is attenuated by a factor of $e^2 = 7.4$. The skin depth to which the field penetrates into the plasma is $\delta \approx 0.24$ cm. These estimates, obtained for a wave propagating in a homogeneous plasma, are close to the observed longitudinal ($L \sim 1$ cm) and transverse ($\rho \sim 0.1$ cm) plasma jet dimensions in spite of the fact that the formulas obtained can hardly be applied to a nonuniform plasma waveguide along which a damped surface mode propagates. Note that the plasma jet can be neither longer (because of microwave power absorption) nor wider (because of the finite depth to which the microwave field penetrates into the plasma).

Let us estimate the convective energy losses caused by the gas flow. The energy density per unit length of the plasma jet is equal to $W_1 = \pi\rho^2 N_g k T_g$, and the power carried away by the jet is

$$P_c = W_1 v\ \mathrm{W}, \quad (15)$$

where v is the gas flow velocity. For the argon flow velocity in the range 1–10 m/s, the convective losses are estimated at $P_c \approx 5$–50 W, which is no more than 6% of the input power. This also indirectly confirms our previous assumption that the power losses from the plasma jet are caused primarily by radiation.

Now, we consider the discharge ignition conditions. The limiting (breakdown) microwave power that can be

transmitted through the coaxial waveguide not filled with a dielectric can be calculated by the formula

$$P_{br} = 8.3 \times 10^{-3} E_{br}^2 b^2 \ln(a/b) \text{ W}. \quad (16)$$

Here, a and b are in cm and E_{br} [V/cm] is the breakdown electric field near the central conductor, where the field is maximum. The value of E_{br} for air at atmospheric pressure is equal to 29 kV/cm. The corresponding power value is $P_{br} \approx 600$ kW. For argon at atmospheric pressure, we have $E_{br} \approx 17$ kV/cm and $P_{br} \approx 200$ kW. This power value is several orders of magnitude higher than the power level at which breakdown occurs at the outlet from the coaxial waveguide. The actual field strength at the central conductor of the coaxial line is ~0.54 kV/cm at a microwave power of 850 W. It is probable that a sharp nozzle edge, which locally increases the electric field, plays a certain positive role, resulting in the reduction of the breakdown power. However, it seems that this effect is not a unique reason why the breakdown field strength decreases. A resonance occurring in the waveguide itself before breakdown can also contribute to this effect. Before breakdown, a rectangular waveguide loaded with a matched coaxial line is a high-Q cavity for the lowest H_{10} mode with a wavelength of $\lambda_g = 16.7$ cm. Since the field in this cavity is enhanced by a factor of several tens, the electric field strength at the outlet from the coaxial line can increase to the breakdown value. This is possible if the length the rectangular waveguide L is a multiple of the half-wave,

$$L = n\lambda_g/2 = n \times 8.35 \text{ cm}.$$

If this equality is not satisfied or in the presence of a ferrite circulator, it is necessary to force the torch ignition by creating a spark at the edge of the coaxial line. However, when operating without a ferrite circulator, the self-breakdown and the subsequent stable discharge in the continuous mode were achieved due to the resonant enhancement of the field, provided that the length of the feeding waveguide was chosen properly. When the waveguide dimensions did not satisfy the resonance condition or in the repetitive mode of magnetron operation with the modulation by the ac mains voltage, we did not achieve a reproducible ignition of the discharge even with the help of an artificial spark because, in this case, such a spark should be produced for each magnetron pulse.

To find out whether or not the above jet plasma parameters in an argon discharge at atmospheric pressure can be regarded as unique, we consider previous experiments conducted with different gases flowing through a quartz tube passing through a waveguide in the direction of the applied electric field [8, 9]. In [8], the discharge was excited by the field with a wavelength of $\lambda = 12$ cm in a waveguide with a 7.2×3.4 cm cross section. The tube radius was ≈1 cm, and the discharge radius was ≈0.5 cm. The input power was 1–2 kW. In this case, the temperature in air at atmospheric pressure was ≈4000 K; in nitrogen, it was ≈5000 K. By matching the discharge plasma load to the source, the authors managed to deposit up to 80–90% of the microwave energy in the plasma. In [9], a waveguide with the same cross section and a quartz tube of radius 0.8 cm were used. Nitrogen at atmospheric pressure was studied. The measurements of the vibrational and rotational temperatures, as well as the measurements of the electron density, showed that the nitrogen plasma was close to the equilibrium state. The temperature was ≈6000 K and depended only slightly on the power. In contrast, in a similar experiment with a microwave discharge in argon [10], the electron temperature was equal to ≈7000 K and appreciably exceeded the gas temperature, which was equal to ≈4500 K. This is explained by the fact that, in atomic gases, there are no losses of the electron energy through the impact excitation of molecular vibrations.

To understand the effects occurring in the torch discharge, it is important to know whether or not the local thermodynamic equilibrium (LTE) is reached in the discharge. The complete thermodynamic equilibrium is rather an ideal model applicable to a closed plasma system with a homogeneous temperature distribution. In a real situation, the complete thermodynamic equilibrium is not realized because of the finite dimensions of the gas-discharge plasma. In such a plasma, there exist heat, radiation, and charge fluxes disturbing the spatial homogeneity and the thermal equilibrium. Nevertheless, under certain assumptions, it makes sense to say about the LTE. For the LTE to occur in a collisional plasma, it is necessary to satisfy the following conditions [11]:

(i) the frequency of collisions with heavy particles should be sufficient for the electrons to lose the excess energy acquired from the external electric field;

(ii) the ionization and recombination processes should proceed in the plasma volume, and the diffusion of charged particles from the volume should be negligible; and

(iii) the deactivation of excited atoms should occur via quenching in collisions, and the emitted photons should be absorbed in the plasma volume and do not leave the plasma.

A factor disturbing the equilibrium is the external electric field. Due to the interaction with this field, the electron temperature T_e differs from the temperatures of heavy particles, T_g and T_i. As a criterion of the permissible excess of T_e over T_g and T_i, we can use the inequality [11]

$$(T_e - T_g)/T_e = (m_a/4m_e)(\lambda_e eE)^2 (1.5kT_e)^{-2} \ll 1, \quad (17)$$

where λ_e is the electron mean free path (here, we assumed that $T_g = T_i$). This inequality implies that the energy gained from the field over the mean free path ($\lambda_e eE$) should be substantially lower than the electron thermal energy $1.5kT_e$.

For the LTE model to be applicable, the admissible spatial inhomogeneity of the temperatures and the densities of different particles, T_s and n_s, should satisfy the inequalities

$$\lambda_s \nabla T_s T_s^{-1} \ll 1, \quad \lambda_s \nabla n_s n_s^{-1} \ll 1, \tag{18}$$

which imply that the mean free paths of the particles should be shorter than the characteristic lengths at which their temperatures and densities vary. Estimates show that, for the jet plasma, the LTE condition (17) is not satisfied, because the left-hand side of the inequality is two orders of magnitude larger than the right-hand side, which explains the large difference between the electron and atom temperatures. In contrast, conditions (18) can easily be satisfied.

For a plasma satisfying the LTE requirements, the criterion of a permissible deviation from equilibrium reduces to the condition for the electron density to be no less than a certain value [12] (provided that the deviation from the Boltzmann distribution does not exceed 10%):

$$n_e \geq 1.6 \times 10^{18} T_e^{1/2} (eU_{p,q})^3 \text{ m}^{-3}, \tag{19}$$

where $U_{p,q}$ is the energy difference between the levels p and q such that radiative transitions between them can result in the deviation from the equilibrium. When studying a low-temperature plasma, an intermediate situation is most frequently encountered in which the plasma can be optical thick in certain spectral regions and, simultaneously, optically thin in other regions. Thus, the low-temperature gas-discharge plasma in noble gases is transparent in the UV region and, partially, in the visible region, whereas the line and continuum IR emission is strongly absorbed. The most strong absorption is observed in the resonance lines.

An analysis of many experimental data showed that the LTE in argon is reached at the following plasma parameters [13]:

$$n_e \geq 5 \times 10^{21} \text{ m}^{-3} \quad \text{and} \quad T \approx 8500 \text{ K}.$$

It was found that, in high-pressure plasmas, the population of the ground energy state should deviate from that prescribed by the Boltzmann distribution, whereas the equilibrium is easily reached for the upper states. Thus, for the population of the upper states to be equilibrium, it is sufficient that the density be $n_e > 3 \times 10^{20}$ m^{-3} even if there is a large difference between the electron temperature $T_e = (7–10) \times 1000$ K and the gas temperature $T_g = 2320–5400$ K [14]. At the same time, the data presented in [15, 16] show that, at pressures of $p > 5 \times 10^4$ Pa (on the order of atmospheric pressure) and electron densities of $n_e \approx 3 \times 10^{16}$ cm^{-3}, the population of the ArI ground state is several times higher than the equilibrium population.

The above considerations show that, at the given basic parameters of the jet plasma, the LTE conditions are not satisfied and that it is necessary to perform a special analysis of the emission spectra, particularly, in the UV region. One can expect that, in the presence of impurity atoms, the emission spectra from argon plasma in the IR, visible, and UV regions will be somewhat modified, which is the subject for spectroscopy studies.

5. APPLICATION OF THE MICROWAVE TORCH TO ANALYTICAL SPECTROSCOPY

The methods of the classical analytical spectroscopy, including the resonance fluorescence, are known as the most reliable, precise and sensitive tools both for scientific research and applications. Laser beams are often used to produce a plasma. A laser beam focused at the surface of a specimen generates a hot-plasma spark with a temperature on the order of 1 keV. Atoms and molecules in the plasma of the evaporated material emit the characteristic radiation. The initial temperatures of the laser-produced plasma are high enough for any element of the Mendeleev periodic table to be ionized, thus providing a means for its reliable identification. The light emitted from the laser-produced spark is collected by mirrors onto the entrance slit of a high-resolution spectrometer. The spectrum obtained in the spectrometer exit plane is detected by one or several CCD arrays. Their output signals are amplified, filtered, cleared from noise, and then are recorded in a computer with time intervals shorter than 1 ms.

Up to the present time, the pulsed laser spectroscopy, characterized by a resolution on the order 1 ppm (part per million), satisfied the requirements of the researchers and manufacturers of materials. However, as the role played by fine cleaning in the technologies for fabricating new materials and integrated circuits increased, a demand arose for a better sensitivity of analytical methods. The primary disadvantage of taking samples with the help of lasers is that the lifetime of the laser-produced plasma and, consequently, of the excited states of the sampled-material atoms is shorter than 1 μs, which significantly limits the sensitivity of the method. Obviously, the sensitivity can be improved by increasing the lifetime of the evaporated-material plasma, which can be achieved by injecting the sampled material into a steady plasma jet. In this case, it is expected that the time-integrated characteristic optical radiation from the sample should increase by several orders of magnitude.

This idea was realized in the above-mentioned ICP devices, which allowed one to improve the sensitivity of the method up to 1 ppb (part per billion). However, the ICP devices also have disadvantages. First, such devices are very expensive, primarily because of the high cost of plasma sources and a complexity of its operation. Second, the sampled material is spread over a large ICP plasma volume (of several tens of cm^3), which makes it hardly possible to improve the sensitivity even if the plasma image is focused onto the spectrometer entrance slit. Third, the ICP plasma density is

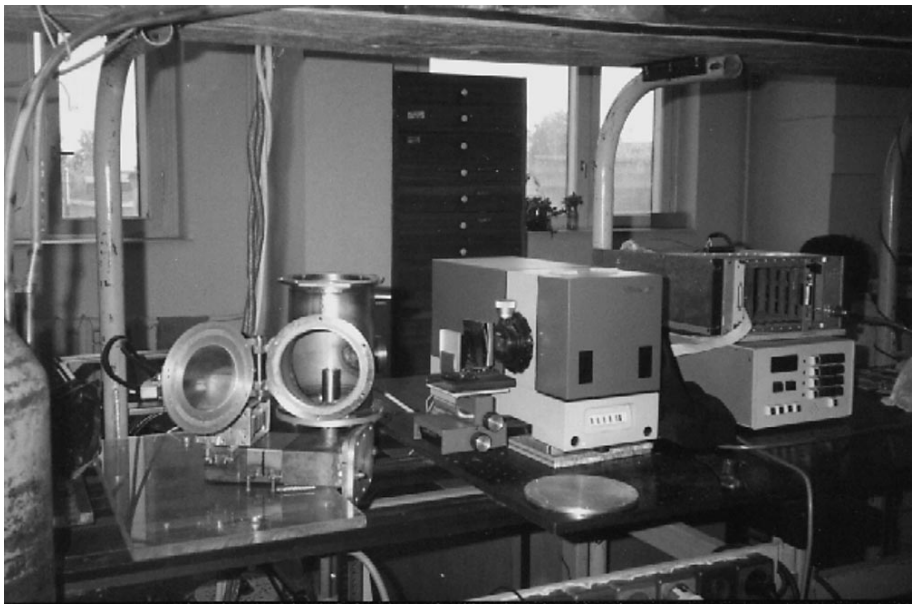

Fig. 3. View of the device for spectral analysis.

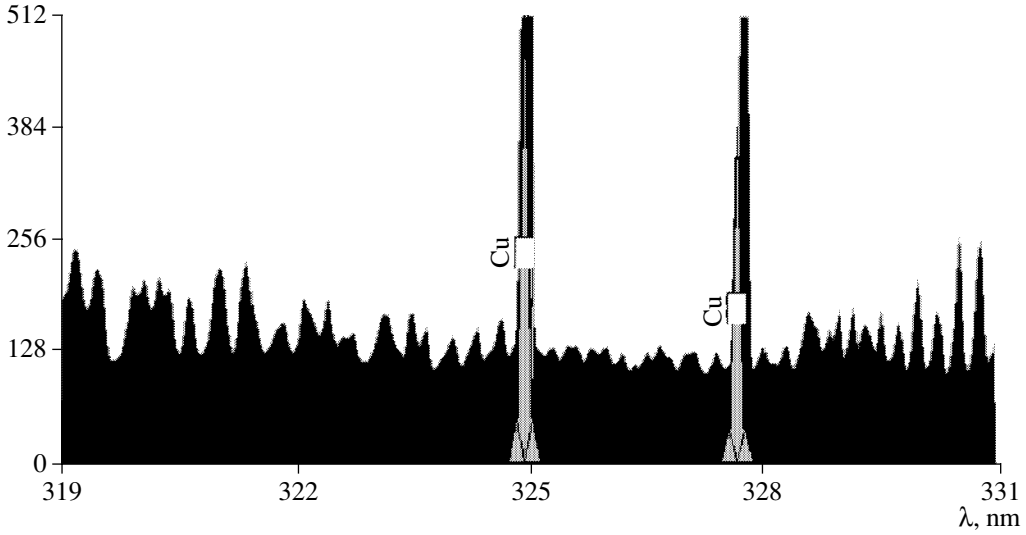

Fig. 4. Spectrum of unprocessed water (shown by dark shading). The copper lines are distinctly seen (the reference copper lines are shown by gray shading); the intensity of the lines substantially exceeds that of the copper lines observed in the working gas (argon).

several orders of magnitude lower than the density of the microwave-discharge plasma.

It follows from the above considerations that the microwave torch is a more appropriate device for solving the problem of increasing the sensitivity of spectroscopic measurements. Figure 3 demonstrates the photograph of a model laboratory device for sensitive spectroscopy with the use of a microwave plasma jet. By analogy to ICP devices, it was called microwave coupled plasma (MWCP) device. The device consists of three main units (aside from a laser). These are a microwave torch, a monochromator equipped with a CCD array for light detection, and a computer. The most expensive component is the CCD array (from 1000 to 2000 USD). A small-sized candlelike flame of the torch can be imaged easily on the monochromator entrance slit. Since the parameters of the plasma jet depend only slightly in the gas flow velocity, the sampled-material vapor content in the discharge can be varied in a wide range. A significant advantage of the method under discussion is, on the one hand, the possibility of mixing the sampled material taken from a solid target by a

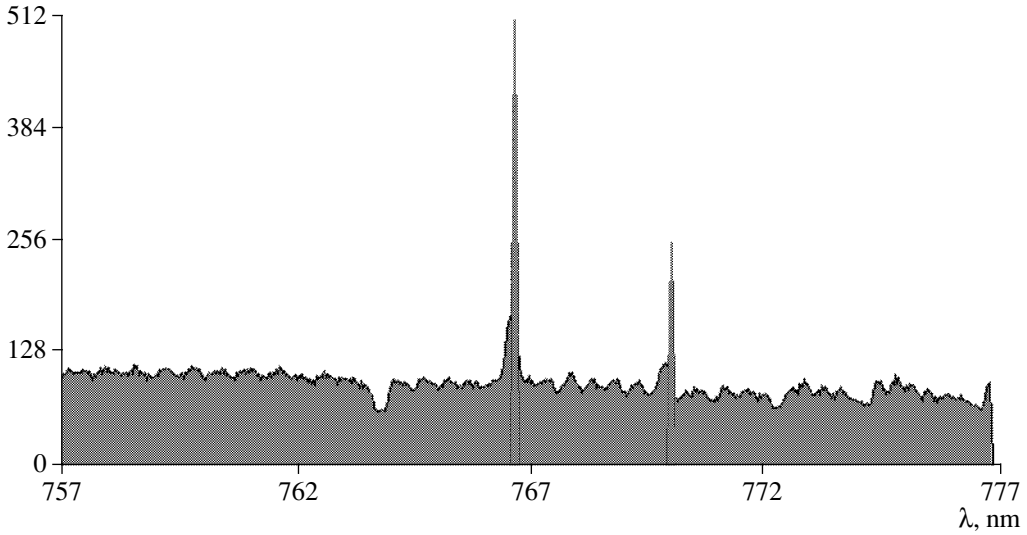

Fig. 5. Spectrum of water that is the product of combustion of hydrogen in oxygen, both prepared through electrolysis of singly distilled water (shown by gray shading). The K lines are distinctly seen in the spectrum (the reference potassium lines are shown by dark shading).

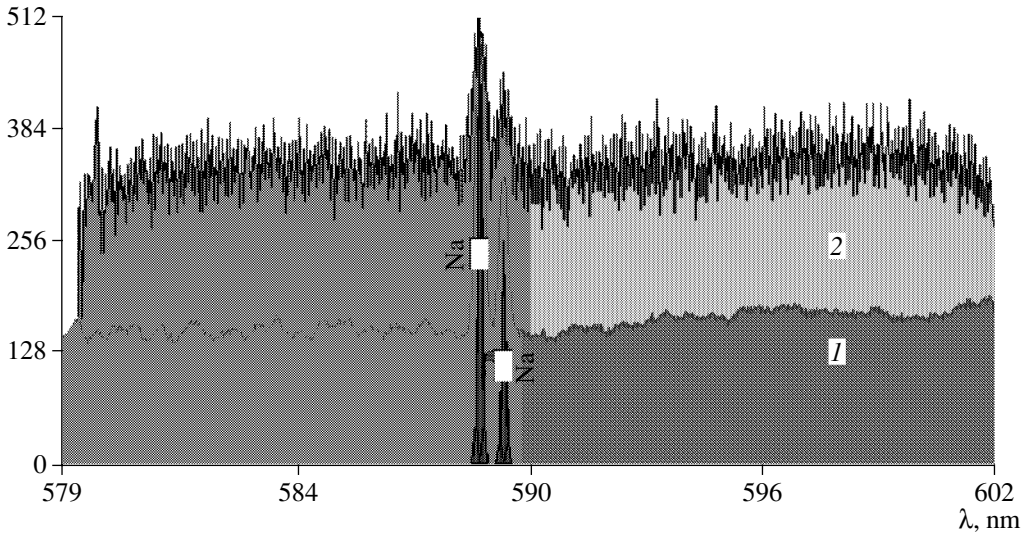

Fig. 6. Spectra of distilled water after (*1*) a single and (*2*) triple distillation. The Na lines are distinctly seen in the spectrum (the reference sodium lines are shown by dark shading); the lines decrease substantially after triple distillation, but do not disappear at all. Their level corresponds to an impurity concentration of about 1 ppb.

pulsed laser with a jet plasma of the microwave torch (as is shown at the top of Fig. 1). On the other hand, it is also possible to study dusty and liquid samples without laser evaporation, by mixing the sampled material and the working gas with the help of a nebulizer or an ultrasonic evaporator (as is shown at the bottom of Fig. 1). The device can be made portable.

To demonstrate the potentialities of the method, we performed an analysis of impurities of various elements in water, e.g., the content of Na, K, and other atoms (see Figs. 4–6). First, we studied tap water, in which we detected many elements. Then, we analyzed the water prepared through the combustion of hydrogen in the oxygen atmosphere and also water distilled up to three times. The impurity content in singly distilled water was also determined with the help of a mass-spectrometer; its level did not exceed 10^{-7}. In the spectrogram of the water prepared through the combustion of hydrogen in oxygen (Fig. 5), one can see peaks corresponding to K admixture. Note that, in the spectrogram for distilled water, even after triple distillation (Fig. 6), one can see

the Na peaks exceeding noise and indicating the presence of sodium atoms at a level of several ppb.

6. CONCLUSION

The experiments with a microwave torch have demonstrated that the sensitivity of analytical plasma spectroscopy can be significantly increased by using the technique proposed. From the physical standpoint, the use of electromagnetic radiation in the microwave range is more efficient for plasma production in comparison with RF radiation. Another advantage is the ease of fabrication and low cost of microwave torches, because they can be powered by the magnetrons of microwave kitchen ovens.

The electron density and temperature in the nonequilibrium plasma of the jet, which are the main factors determining the excitation of atomic and molecular levels of the impurities under study, require further experimental investigations. The estimates made by using the Saha equation, which is only applicable for equilibrium plasma, do not pretend to yield high accuracy because, under our experimental conditions, the discharge plasma is far from equilibrium. Nevertheless, these estimates do not contradict the observations of other authors.

ACKNOWLEDGMENTS

We thank V.A. Kuchumov for the discussion of the results obtained.

REFERENCES

1. T. V. Reed, J. Appl. Phys. **32**, 821 (1961).
2. S. V. Kononov and M. I. Yakushin, Prikl. Mekh. Tekh. Fiz., No. 6, 67 (1966).
3. Yu. P. Raĭzer, Prikl. Mekh. Tekh. Fiz., No. 3, 3 (1968).
4. H. Püschner, *Heating with Microwaves: Fundamentals, Components, and Circuit Technique* (Springer-Verlag, New York, 1966; Énergiya, Moscow, 1968).
5. S. I. Gritsinin, I. A. Kossyi, N. I. Malykh, *et al.*, in *Proceedings of the 14th International Symposium on Plasma Chemistry, Prague, 1999*, Vol. 2, p. 675; S. I. Gritsinin, I. A. Kossyi, N. I. Malykh, *et al.*, in *Proceedings of the 15th International Symposium on Plasma Chemistry, Orlean, 2001*, Vol. 4, p. 1479.
6. S. K. Wong, UTIAS Technical Note Can. No. 225.
7. V. E. Golant, *Microwave Methods for Studying Plasmas* (Nauka, Moscow, 1968).
8. L. M. Blinov, V. V. Volod'ko, G. G. Gontarev, *et al.*, in *Low-Temperature Plasma Generators*, Ed. by A. V. Lykov (Énergiya, Moscow, 1969), p. 345.
9. L. M. Baltin, V. M. Batenin, I. I. Devyatkin, *et al.*, Teplofiz. Vys. Temp. **9**, 1105 (1971).
10. L. M. Baltin, V. M. Batenin, V. R. Gol'dberg, and N. I. Tsemko, in *Low-Temperature Plasma Generators*, Ed. by A. V. Lykov (Énergiya, Moscow, 1969), p. 438.
11. W. Finkelburg and H. Maecker, *Elektrische Bögen und thermisches Plasma*, in *Handbuch der Physik*, Bd. XXII (Springer-Verlag, Berlin, 1956; Inostrannaya Literatura, Moscow, 1961).
12. *Plasma Diagnostic Techniques*, Ed. by R. H. Huddlestone and S. L. Leonard (Academic, New York, 1965; Mir, Moscow, 1967).
13. V. N. Kolesnikov, in *Physical Optics*, Ed. by D. V. Skobel'tsyn (Nauka, Moscow, 1964), Tr. Fiz. Inst. Akad. Nauk SSSR **30**, 53 (1964).
14. V. Newman, Beitr. Plasmaphys. **11**, 248 (1971).
15. G. Pichler and V. Vujnovic, Phys. Lett. A **40**, 397 (1972).
16. J. B. Shumaker and C. H. Popenoe, J. Res. Natl. Bur. Stand., Sect. A **76** (2), 71 (1972).

Translated by N. F. Larionova

Plasma Physics Reports, Vol. 28, No. 5, 2002, pp. 453–456. Translated from Fizika Plazmy, Vol. 28, No. 5, 2002, pp. 493–496.

BRIEF COMMUNICATIONS

Feasibility of Using Laser Ion Accelerators in Proton Therapy

S. V. Bulanov* and V. S. Khoroshkov**

**Institute of General Physics, Russian Academy of Sciences, ul. Vavilova 38, Moscow, 119991 Russia*

*** Institute of Theoretical and Experimental Physics, ul. Bol'shaya Cheremushkinskaya 25, Moscow, 117259 Russia*

Received November 22, 2001

Abstract—The feasibility of using laser plasma as a source of high-energy ions for the purposes of proton therapy is discussed. The proposal is based on the efficient ion acceleration observed in recent laboratory and numerical experiments on the interaction of high-power laser radiation with gaseous and solid targets. The specific dependence of proton energy losses in biological tissues (the Bragg peak) promotes the solution of one of the main problems of radiation therapy, namely, the irradiation of a malignant tumor with a sufficiently strong and homogeneous dose, ensuring that the irradiation of the surrounding healthy tissues and organs is minimal. In the scheme proposed, a beam of fast ions accelerated by a laser pulse can be integrated in the installations intended for proton therapy. © *2002 MAIK "Nauka/Interperiodica".*

Recently developed compact lasers capable of generating ultrashort pulses in the multi-terawatt and petawatt power range have found progressively wider applications [1]. Thus, it was proposed to use these lasers to create new types of charged particle accelerators [2], sources of hard X-ray and gamma radiation [3], and charged particle injectors [4], as well as to apply them to the problem of inertial confinement fusion (in the framework of the concept of fast ignition of fusion targets with the use of laser-accelerated electron [5] or ion [6] beams). The above applications are based on the fact that the nonlinear interaction of high-power laser radiation with matter is accompanied by the efficient conversion of laser energy into the energy of fast particles. The generation of collimated fast ion beams was observed in many experiments on the interaction of ultrashort laser pulses with gaseous and solid targets [7] and was thoroughly investigated using multidimensional particle-in-cell computer simulations [8]. In present-day experiments [7], the energy of fast electrons (protons) attains several hundreds (tens) of MeV. Computer simulations show that, by optimizing the parameters of a petawatt laser pulse and a target, it is possible to achieve a protons energy of about several hundreds of MeV [8].

In this paper, we discuss the feasibility of using laser plasma as a source of high-energy ions for the purposes of hadron therapy. Hadron therapy is a constituent part of radiation therapy, which makes use not only of high-energy ion beams, but also of pi mesons, neutrons, electron beams, and X-ray and gamma radiation to irradiate cancer tumors (for details, see [9] and the literature cited therein). Generally, surgical removal, chemotherapy, and radiation therapy are applied in parallel to treat cancers. In developed countries, the radiation therapy is applied to more than one-half of oncological patients. After more than 40 years of experimental research, clinical centers of proton therapy (PT), intended for the treatment of up to 1000 patients per year, are now being actively developed. Three such centers have already been put into operation; in the nearest future, there will be nine PT centers [10]. Each of them is equipped with a special medical proton accelerator, from where proton beams are delivered to three to five treatment rooms. A mandatory and the most expensive attribute of such centers is the Gantry system for the multiple-field irradiation of the lying patient (Fig. 1a).

Proton therapy has a number of advantages. First, a proton beam is insignificantly scattered by atomic electrons, which reduces the irradiation of healthy tissues located on the side of the tumor. Second, the deceleration length of protons with a given energy is fixed, which allows one to avoid undesirable irradiation of healthy tissues behind the tumor. Third, the presence of a sharp maximum of proton energy losses in tissues (the Bragg peak) provides a substantial increase in the radiation dose in the vicinity of the beam stopping point (see, e.g., [9]). Up to the present time, conventional particle accelerators (synchrotrons, cyclotrons, and linacs) have been used to produce proton beams with the required parameters. The use of laser accelerators seems to be very promising because of their compactness and additional capabilities of controlling the proton beam parameters.

There are two versions of using laser accelerators. In the first version, a conventional accelerator is replaced with a laser one. In the second version, which seems to be more attractive, laser radiation is delivered to a target, where it is converted into fast ions. The target is situated directly at the entrance to the treatment room, which is especially important for the design of the Gan-

1063-780X/02/2805-0453$22.00

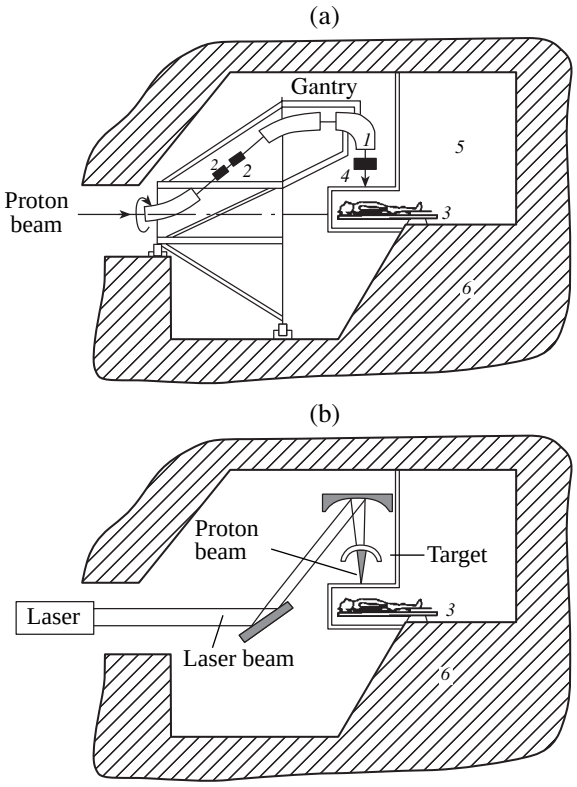

Fig. 1. (a) Conventional Gantry system: (*1*) deflecting magnets, (*2*) quadrupole lenses, (*3*) positioner, (*4*) dose delivery system and dose monitoring, (*5*) treatment room, and (*6*) concrete protection; (b) personal laser accelerator.

try system. Note that the Gantry system is not only expensive, but also very large (6–8 m in diameter and 10–12 m in length) and heavy (100 t or higher) facility. The weight and cost of the system are mainly determined by a powerful and very precisely made magneto-optical system rotating as a single entity. The use of the second version will allow one to both simplify the system and substantially reduce its cost. In this case, the central accelerator, the beam transportation channels, and the larger part of the Gantry magnetic system become unnecessary. One of the possible engineering solutions is shown in Fig. 1b.

The requirements for the main parameters of a medical proton beam (a beam intensity of $(1–5) \times 10^{10}$ proton/s and a maximum proton energy of 230–250 MeV) can easily be satisfied with the use of modern acceleration technique. At the same time, the other two requirements—the beam must be highly monoenergetic, $\Delta\mathcal{E}/\mathcal{E} \le 10^{-2}$, and the duty-factor (the useful time fraction of a pulsed beam) should be no worse than 0.3 (otherwise, the repetition rate must be no lower than several Hz)—are rather difficult to satisfy.

A comparison of the ion energy spectrum required for medical applications ($\Delta\mathcal{E}/\mathcal{E} < 10^{-2}$) with that observed in laboratory and numerical experiments on the interaction of laser radiation with matter shows that the available ion spectra are far from being monoenergetic. It follows from [7, 8] that, at energies lower than the maximum energy ($\mathcal{E} < \mathcal{E}_{max}$), the energy distribution is quasi-thermal with the effective temperature T several times lower than $\mathcal{E}_{max}$. Such a spectrum is unacceptable for medical purposes, because it does not ensure an essential increase in the radiation dose in a local area and will cause an unacceptably intense irradiation of healthy tissues.

In order to improve the quality of a proton beam, it can be "cut" into narrow beams in energy space. However, in this case, the conversion efficiency of laser energy into the energy of fast particles is significantly reduced and, what is more important, the number of the beam particles decreases. A more promising approach is related to the use of multilayer targets. Thus, it was proposed to use a foil target consisting of high-Z atoms and covered with a thin hydrogen-containing film (see Fig. 2a). When the target is irradiated with an ultrashort laser pulse, heavy atoms are partially ionized and their electrons escape from the foil, thus creating the charge-separation electric field. Because of their large inertia, the heavy ions remain at rest, while the more mobile protons are involved in the process of acceleration. The energy spectrum of protons accelerated in the charge-separation field near the target surface can be found from the continuity condition for the particle flux in energy space, namely, $N(\mathcal{E}) = n_0(x_0)|dx_0/d\mathcal{E}|$. Here, the energy $\mathcal{E}$ is a function of the Lagrangian coordinate x_0, $N(\mathcal{E})$ is the differential particle energy spectrum, and $n_0(x_0)$ is the initial spatial distribution of the particles. We can see that, in order to produce a highly monoenergetic proton beam, it is necessary that the hydrogen layer thickness Δx_0 be small (i.e., the function $n_0(x_0)$ should be highly localized in x_0 space) and/or the derivative $|d\mathcal{E}/dx_0|$ should vanish at a certain point x_m. In the vicinity of this point, the function $\mathcal{E}(x_0)$ can be represented as $\mathcal{E}(x_0) = \mathcal{E}_{max} - \alpha(x_0 - x_m)^2/4$. It follows from here that, in the vicinity of the maximum energy, the particle energy spectrum has the form $N(\mathcal{E}) = n_0/\alpha^{1/2}(\mathcal{E}_{max} - \mathcal{E})^{1/2}$. The necessary conditions for this acceleration regime can be ensured by using a two-layer target with a hydrogen-containing film deposited on the front side of the foil, as is shown in Fig. 2b. Note that, when preparing this paper, we become acquainted with the recently published paper [10], in which the increase in the efficiency of ion acceleration in the interaction of laser radiation with two-layer targets was demonstrated experimentally.

The characteristic energy of protons accelerated in the charge-separation electric field $E \approx 2\pi n_0 Zel$ in the region of size $R_\perp$, equal to the laser spot radius, can be estimated in the order of magnitude as $\mathcal{E}_{max} = 2\pi n_0 Ze^2 l R_\perp$ and the energy spectrum width as $\Delta\mathcal{E} =$

$2\pi n_0 e^2 \Delta x_0 R_\perp$. Here, n_0 is the density of high-Z ions in the foil, Ze is their electric charge, l is the foil thickness, and Δx_0 is the thickness of the hydrogen-containing film. It is assumed that the intensity of laser radiation is sufficiently high for all the electrons to be blown out of the laser-irradiated region under the action of the ponderomotive pressure. For this purpose, it is necessary that the dimensionless amplitude of the laser field $a = eE/m_e\omega c$ be larger than $a_c = l/d_e$, where E is the laser field strength, ω is the laser frequency, e and m_e are the charge and mass of an electron, and $d_e = c/\omega_{pe}$ is the collisionless skin depth. For a laser wavelength of about 1 μm and a foil thickness of 5 μm, the threshold field amplitude is $a_c = 50$; i.e., the laser intensity is $I = 5 \times 10^{21}$ W/cm^2, which corresponds to the petawatt power range [1]. It follows from [8] that, in this case, the energy of fast protons attains several hundreds of MeV, which is sufficient for PT. As was noted above, the flux of accelerated protons in a beam should be no less than $(1–5) \times 10^{10}$ proton/s, which is achievable, because, in experiments of [7, 8], the number of accelerated protons attained a value of 10^{12}–10^{13} proton/pulse. To ensure such a number of fast particles, it is sufficient that the thickness of the solid-state hydrogen-containing film on the target surface be about 1 μm at a laser spot diameter of about 10 μm. In addition, the parameters of a proton beam can be controlled by varying the target geometry (as was shown in [8], the protons accelerated from the surface of a convex foil target are focused into its center of curvature). Note that the high quality of the proton beam (the smallness of the ratio $\Delta\mathscr{E}/\mathscr{E}$) is of fundamental importance not only for medical applications, but also for charged particle injectors [4] and the problem of fast ignition of fusion targets with the use of laser-accelerated ion beams [6].

As the fast ion beam propagates through a tissue, it loses energy. The energy loss rate is equal to $d\mathscr{E}/dx = K/\mathscr{E}^2$ (see, e.g., [11]), where the K factor logarithmically depends on the proton energy. Figure 3 shows the profiles of the energy deposited by proton beams with different energy distributions. Curve *1* corresponds to the distribution $N(\mathscr{E}) = n_0\theta(\mathscr{E}_{max} - \mathscr{E})\theta(\mathscr{E} - \mathscr{E}_{min})$, where $\mathscr{E}_{max}$ and $\mathscr{E}_{min}$ are the maximum and minimum proton energies in the beam, $\theta(\xi) = 1$ at $\xi > 0$, and $\theta(\xi) = 0$ at $\xi < 0$ (for the given distribution, $(\mathscr{E}_{max} - \mathscr{E}_{min})/\mathscr{E}_{max} = 0.1$). In curve *2*, which corresponds to the energy spectrum $N(\mathscr{E}) = n_0\theta(\mathscr{E}_{max} - \mathscr{E})\theta(\mathscr{E} - \mathscr{E}_{min})/(\mathscr{E}_{max} - \mathscr{E})^{1/2}$, we can see a pronounced peak of energy losses. For comparison, Fig. 3 also shows the profiles of the energy deposited by monoenergetic and quasi-thermal proton beams. Curve *3* corresponds to a monoenergetic beam: $N(\mathscr{E}) = n_0\delta(\mathscr{E}_{max} - \mathscr{E})$. We can see the Bragg peak of energy losses in the vicinity of the beam stopping point. Curve *4* corresponds to the energy distribution of the form $N(\mathscr{E}) = n_0\theta(\mathscr{E}_{max} - \mathscr{E})\exp(-\mathscr{E}/2T)^{1/2}$, where $T = \mathscr{E}_{max}/2$ is the effective temperature. It is this distribution that is usually used to approximate the fast proton energy spectra observed in laboratory and numerical experiments on the interaction of laser radiation with non-optimized targets. It is clear that this distribution is unacceptable and it is necessary to use optimized multilayer targets.

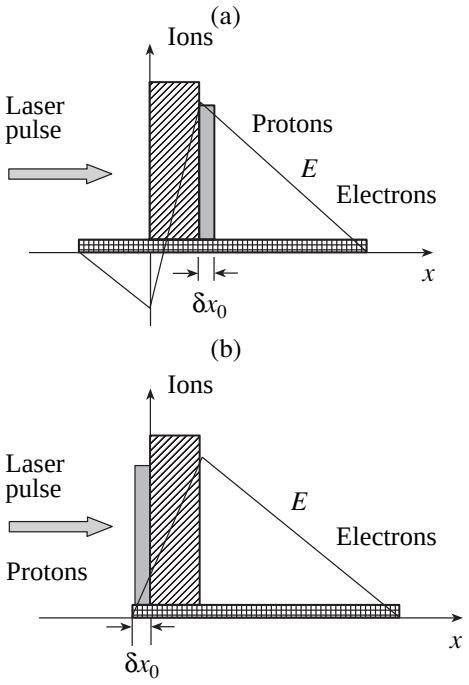

Fig. 2. Two-layer target: a thin hydrogen-containing film is deposited on (a) the rear side and (b) the front side of a foil consisting of high-Z atoms.

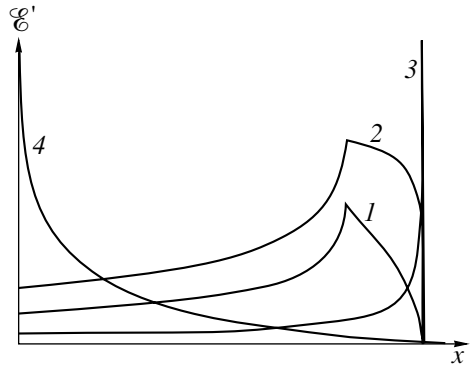

Fig. 3. Energy deposition profiles for beams with different energy distributions.

The future of hadron therapy is related to the creation of specialized oncological centers equipped with modern diagnostics and medical accelerators. Cities with a population of two to three million inhabitants need centers with four treatment rooms. For smaller cities, centers with one treatment room are required; however, to create such centers based on conventional accelerators and existing Gantry systems is inexpedient

from the economical standpoint. At the same time, the creation of such centers in medium-sized hospitals would expand the range of PT applications and, a very important point, would made it possible to bring medical centers closer to patients. One of the solutions to this problem is the creation of relatively inexpensive specialized medical laser proton accelerators having relatively small dimensions (2–3 m) and weighting no more than several tons. In fact, this can substantially simplify the design and reduce the cost of PT centers. The use of multilayer targets with various shapes and structures provides additional possibilities for controlling the parameters of fast ion beams, such as the energy spectrum, the number of particles, the focal length, and the size of the region where the proton energy is deposited.

As concerns the low repetition rate of the proton pulses, there are two possible solutions to this problem. At present, the repetition rate of the required ultra-high-power (petawatt) laser pulses is rather low. The repetition rate of proton pulses can be increased by implementing an assembly of lasers shooting at a single target in succession. It is also possible to accelerate the bunch of protons repeatedly, each time increasing the energy of protons by several MeV. This may be achieved with sequentially positioned targets and lower power lasers, which nowadays have a sufficiently high repetition rate.

REFERENCES

1. G. A. Mourou, P. J. C. Barty, and M. D. Perry, Phys. Today **51**, 22 (1998); M. D. Perry and G. Mourou, Science **64**, 917 (1994); G. Mourou, Z. Chang, A. Maksimchuk, *et al.*, Fiz. Plazmy **28**, 14 (2002) [Plasma Phys. Rep. **28**, 12 (2002)].
2. T. Tajima and J. M. Dawson, Phys. Rev. Lett. **43**, 267 (1979); K. Nakajima, D. Fisher, T. Kawakubo, *et al.*, Phys. Rev. Lett. **74**, 4428 (1995); A. Modena, Z. Najimudin, A. E. Dangor, *et al.*, Nature **337**, 606 (1995).
3. N. H. Burnett and G. D. Enright, IEEE J. Quantum Electron. **26**, 1797 (1990).
4. K. Krushelnik, E. L. Clark, R. Allot, *et al.*, IEEE Trans. Plasma Sci. **28**, 1184 (2000).
5. M. Tabak, J. Hammer, M. E. Glinsky, *et al.*, Phys. Plasmas **1**, 1626 (1994).
6. M. Roth, T. E. Cowan, M. H. Key, *et al.*, Phys. Rev. Lett. **86**, 436 (2001); V. Yu. Bychenkov, W. Rozmus, A. Maksimchuk, *et al.*, Fiz. Plazmy **27**, 1076 (2001) [Plasma Phys. Rep. **27**, 1017 (2001)].
7. G. S. Sarkisov, V. Yu. Bychenkov, V. T. Tikhonchuk, *et al.*, Pis'ma Zh. Éksp. Teor. Fiz. **66**, 787 (1997) [JETP Lett. **66**, 828 (1997)]; A. Maksimchuk, S. Gu, K. Flippo, *et al.*, Phys. Rev. Lett. **84**, 4108 (2000); E. L. Clark, K. Krushelnick, M. Zepf, *et al.*, Phys. Rev. Lett. **85**, 1654 (2000); S. P. Hatchett, C. G. Brown, T. E. Cowan, *et al.*, Phys. Plasmas **7**, 2076 (2000); A. J. Mackinnon, M. Borghesi, S. Hatchett, *et al.*, Phys. Rev. Lett. **86**, 1769 (2001).
8. T. Zh. Esirkepov, Y. Sentoku, K. Mima, *et al.*, Pis'ma Zh. Éksp. Teor. Fiz. **70**, 80 (1999) [JETP Lett. **70**, 82 (1999)]; S. V. Bulanov, N. M. Naumova, T. Zh. Esirkepov, *et al.*, Pis'ma Zh. Éksp. Teor. Fiz. **71**, 593 (2000) [JETP Lett. **71**, 407 (2000)]; Y. Sentoku, T. V. Lisseikina, T. Zh. Esirkepov, *et al.*, Phys. Rev. E **62**, 7271 (2000); H. Ruhl, S. V. Bulanov, T. E. Cowan, *et al.*, Fiz. Plazmy **27**, 411 (2001) [Plasma Phys. Rep. **27**, 363 (2001)].
9. V. S. Khoroshkov and E. I. Minakova, Eur. J. Phys. **19**, 523 (1998).
10. J. Badziak, E. Woryna, P. Parys, *et al.*, Phys. Rev. Lett. **87**, 215001 (2001).
11. R. B. Miller, *Introduction to the Physics of Intense Charged Particle Beams* (Plenum, New York, 1982; Mir, Moscow, 1984).

Translated by A. S. Sakharov